Grid-forming control to achieve a 100% power electronics interfaced power transmission systems

Taoufik Qoria

► To cite this version:

Taoufik Qoria. Grid-forming control to achieve a 100% power electronics interfaced power transmission systems. Electric power. HESAM Université, 2020. English. NNT : 2020HESAE041 . tel-03078479

HAL Id: tel-03078479

https://pastel.hal.science/tel-03078479v1

Submitted on 16 Dec 2020

HESAM UNIVERSITÉ

Arts et Métiers Sciences et Technologies

ÉCOLE DOCTORALE SCIENCES ET MÉTIERS DE L'INGÉNIEUR
L2EP - Campus de Lille

THÈSE

présentée par : **Taoufik QORIA**
soutenue le : **5 Novembre 2020**

pour obtenir le grade de : **Docteur d'HESAM Université**

préparée à : **École Nationale Supérieure d'Arts et Métiers**
Spécialité : **Génie Electrique**

Grid-forming control to achieve a 100% power electronics interfaced power transmission systems

"Nouvelles lois de contrôle pour former des réseaux de transport avec 100% d'électronique de puissance"

THÈSE dirigée par :
Prof. KESTELYN Xavier

Co-dirigée par :
Prof. GUILLAUD Xavier

et Co-encadrée par :
Dr. GRUSON François

Jury

M. Thierry Van Cutsem	Professor, University of Liege, Belgium	Président
M. Wang Xiongfei	Professor, Aalborg University, Denmark	Rapporteur
M. Marco Liserre	Professor, Université de Kiel, Germany	Rapporteur
M. Stéphane Clenet	Professor, ENSAM, France	Examinateur
Mme. Maryam Saeedifard	Associate Professor, Georgia Tech, USA	Examinatrice
M. Jon Are Wold Suul	Associate Professor, NTNU, Norway	Examinateur
M. Xavier Guillaud	Professor, École Centrale de Lille, France	Examinateur
M. François Gruson	Associate Professor, ENSAM, France	Examinateur
M. Thibault Prevost	Engineer, RTE, France	Invité

THÈSE

This project has received funding from the European Union's Horizon 2020 research and innovation program under grant agreement No 691800. This report reflects only the author's views and the European Commission is not responsible for any use that may be made of the information it contains.

To my parents and my brothers ...

To my wife ...

To my little daughter Sarah QORIA ...

Acknowledgements

This doctoral thesis summarizes the research activities conducted during my time as a PhD student at the Electrical Engineering and Power Electronics Laboratory (L2EP) of ENSAM ParisTech Paris from January 2017 to November 2020. There are many people to thank for their help and support during this period.

First, I would like to express my deepest gratitude to my advisors Prof. Xavier Guillaud, Prof. Xavier Kestelyn and Dr. François Gruson for giving me the opportunity to pursue my PhD at L2EP. They have been exemplary advisors who provided me with a lot of support, guidance and freedom in my research.

I feel happy and honored that this PhD could add values to the practice, but I know it would not be possible without the support of my advisor Prof. Xavier GUILLAUD, who believed in me and valued my work. My gratitude also goes to Dr. Philippe Delarue for allowing me to be an active part of L2EP during my master studies. My next thanks go to Dr. Riad Kadri and Dr. Hicham Fakham for their immense support. They were of incredible importance to me, both as friends and colleagues.

Special thanks go to Prof. Wang Xiongfei from Aalborg University Denmark and Prof. Marco Liserre from university de Kiel Germany for being reviewers of this thesis. I appreciate the time they spent on reading the thesis and providing valuable comments that helped me improving the quality of the final manuscript. Other special thanks go to Prof. Thierry Van Cutsem from Liege University Belgium, Dr. Maryam Saeedifard from Georgia Tech USA, Dr. Jon Are Wold Sul from NTNU Norway, Prof. Stephane Clenet from ENSAM ParisTech and Eng. Thibault Prevost from RTE Paris for being examiners of this thesis. I really appreciated the rich scientific exchange with them during the defense.

I would also like to thank Dr. Frederic Colas who was not directly my advisor but always was ready to help me out. I extend my thanks to all members of the MIGRATE consortium, both the research and industry partners. In particular, I would like to thank our close collaborators at RTE, ETH and University College Dublin, as well as all members of the project management team. Furthermore, I acknowledge the financial support from the European Union’s Horizon 2020 research and innovation.

As it is hard to name everyone individually, I would like to thank every member of the L2EP for the greatest 4 years we spent together. Special thanks go to my office mates, Ebrahim, Artur, Nnaemeka, Quentin, Martin and Pierre. Other special thanks go to Agatha Williams-Kelly from University of Edinburgh and my colleague Artur Avazov from Centrale Lille for the time they devoted to read this thesis and improving its quality.

Last but not least, I would like to express my deepest gratitude to my family, my parents and my wife for their endless love, support and understanding. They have no idea about my work, but always encourage me to pursue my own dream.

Abstract

The rapid development of intermittent renewable generation and HVDC links yields an important increase of the penetration rate of power electronic converters in the transmission systems. Today, power converters have the main function of injecting power into the main grid, while relying on synchronous machines that ensure all system needs. This operation mode of power converters is called "Grid-following". Grid-following converters have several limitations: their inability to operate in a standalone mode, their stability issues under weak grids and faulty conditions and their negative side effect on the system inertia.

To meet these challenges, the grid-forming control is a good solution to respond to the system needs and allow a stable and safe operation of power system with high penetration rate of power electronic converters, up to a 100%. Firstly, three grid-forming control strategies are proposed to guarantee four main features: voltage control, power control, inertia emulation and frequency support. The system dynamics and robustness based on each control have been analyzed and discussed. Then, depending on the converter topology, the connection with the AC grid may require additional filters and control loops. In this thesis, two converter topologies have been considered (2-Level VSC and VSC-MMC) and the implementation associated with each one has been discussed. Finally, the questions of the grid-forming converters protection against overcurrent and their post-fault synchronization have been investigated, and then a hybrid current limitation and resynchronization algorithms have been proposed to enhance the transient stability of the system. At the end, an experimental test bench has been developed to confirm the theoretical approach.

Keywords: Power converters, Grid-forming control, Power system dynamics, Small-signal stability analysis, Current limitation, Transient stability

Résumé

Le développement rapide de la production d'énergie renouvelable intermittente et des liaisons HVDC entraîne une augmentation importante du taux de pénétration des convertisseurs statiques dans les réseaux de transport. Aujourd'hui, les convertisseurs statiques ont pour fonction principale d'injecter une puissance dans le réseau tout en s'appuyant sur des machines synchrones qui garantissent tous les besoins du système électrique. Ce mode de fonctionnement est appelé «Grid-following». Les convertisseurs contrôlés en Grid-following ont plusieurs limitations: leur incapacité à fonctionner en mode autonome, leurs problèmes de stabilité dans des réseaux faibles et en cas de défaut ainsi que leur effet négatif sur l'inertie équivalent du système. Pour relever ces défis, le contrôle en Grid-forming est une bonne solution pour répondre aux besoins du système électrique et permettre un fonctionnement stable et sûr du système même avec un taux de pénétration des convertisseurs statique de 100%. Tout d'abord, trois stratégies de contrôle en Grid-forming sont proposées pour garantir quatre fonctionnalités principales: contrôle de tension, contrôle de puissance, émulation d'inertie et le support de la fréquence. La dynamique et la robustesse du système basées sur chaque contrôle ont été analysées et discutées. Ensuite, selon la topologie du convertisseur, la connexion avec le réseau AC peut nécessiter des filtres et des boucles de contrôle supplémentaires. Dans le cadre de cette thèse, deux topologies de convertisseur ont été envisagées (VSC à 2-niveaux et VSC-MMC) et l'implémentation associée à chacune a été discutée. Enfin, les questions de la protection des convertisseurs Grid-forming contre les surintensités et leur synchronisation post-défaut ont été étudiées, puis, des algorithmes de limitation de courant et de resynchronisation ont été proposés pour améliorer la stabilité transitoire du système. Un banc d'essai a été développé pour confirmer les approches théoriques proposées.

Mots clés : Convertisseur DC/AC-AC/DC, Grid-forming contrôle, Dynamiques des systèmes électriques, stabilité petit-signaux, Limitation de courant, Stabilité transitoire

Contents

V. Current limitation and transient stability 107

VI. Experimental Validation of the Grid-Forming Converters 135

List of Figures

List of Tables

I. Introduction to a power system based 100% power electronics

I.1 Context and motivation

Toward a 100% Renewable Electrical Grid: The transition to a renewables-based energy system is already under way. The last decade has seen the cost of renewable energy decline continuously, making it cost-competitive compared to conventional energy in many parts of the world. Since 2009, the module prices for solar photovoltaics (PV) have fallen by around 80%, while wind turbine prices have declined by 30-40%, making the business case for renewable energy stronger than ever before (IRENA, 2017) [1]. The most crucial benefits of transitioning to a 100% renewable energy system is the resulting large reduction of greenhouse gas (GHG) emissions. To achieve this global warming limit, the IPCC (Intergovernmental Panel on Climate Change) highlights the need for a rapid energy transformation based on a significant increase of renewables (IPCC, 2018). Several countries already come close to achieving this goal. Iceland, for instance, supplies 100% of its electricity needs with either geothermal or hydropower. Other countries that have electric grids with high fractions of renewables based on hydropower include Norway (97%), Costa Rica (93%), Brazil (76%), and Canada (62%). Hydropower plants have been used for decades to create a relatively inexpensive renewable energy, but these systems are limited by natural rainfall and geographic topology. In many countries, most good sites for large hydropower resources have already been developed, which requires a transition to intermittent renewable energy sources (IRES) (i.e., wind and solar photovoltaic systems). Countries such as Denmark, Ireland, and Germany have massively installed intermittent renewable energy systems and are operating with annual penetrations of more than 20% at the national level [2]. Some scenarios from the European Wind Energy Association show that over the next ten years, wind energy could meet one-fifth of the electricity demand in Europe by 2020, one-third by 2030, and half by 2050 [3]–[5].

A number of studies have excluded nuclear, carbon capture and storage technologies to investigate whether power systems could rely on 100% renewable energy sources, such as those for Denmark, Netherlands, Germany, France, Ireland, Portugal [6]–[10]. Although the first trends do not indicate the feasibility of a 100% renewable power, due to intermittent generation of the power sources, however, the residual demand not supplied by the IRES can be compensated by one of the dispatchable generation technologies, storage systems or the inertia stored in the mechanical part of the wind turbines.

A power system based 100% intermittent renewable energy is still a subject to investigate. Nevertheless, a scenario with an area of the present power system supplied occasionally with 100% intermittent renewable sources is of high likelihood. Actually, since wind and photovoltaic generations are concentrated where the wind blows and the sun shines respectively, a large area of the power transmission system may lose the last synchronous link connecting it to the rest of the system as illustrated by Figure I-1. In such a situation, the transmission grid operators must adapt their practice to run the islanded system with no synchronous generation, under sufficient reliability.

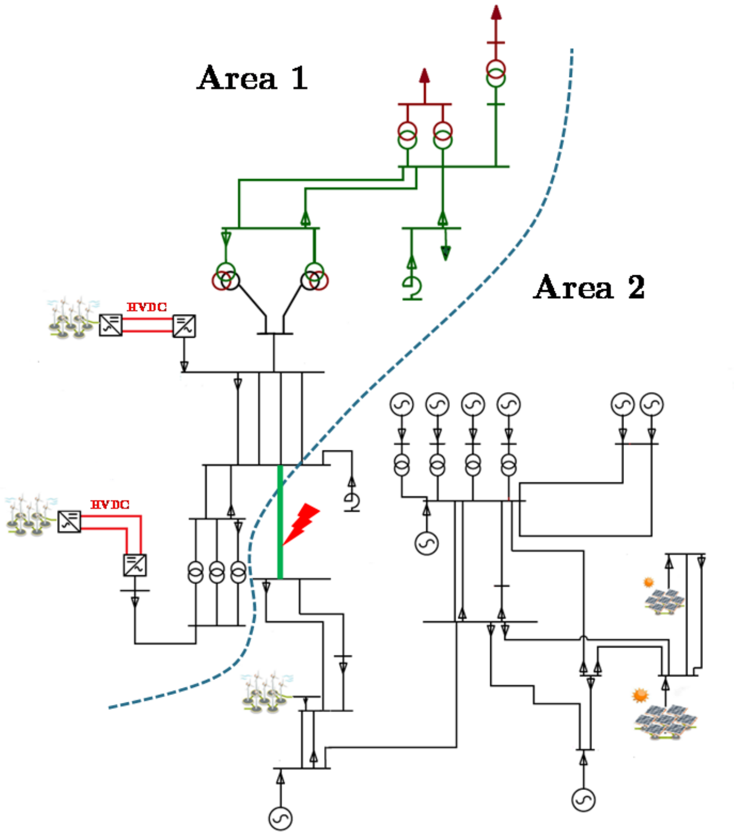

Figure I-1 - Representation of the present power system losing its last synchronous link

Apart from the issues related to the primary energy source, the management of this energy itself remains a major issue and where power electronics play a fundamental role.

Power System and Power Electronic Converters: Power electronic converters have been developed for decades with many types of applications. One of the first applications is the drive of electrical machines mainly used for industrial applications. The beginning of the renewable energy story had a moderate influence on the power electronic converters market. Very quickly, the connection of wind turbines and photovoltaics through power electronic converters becomes compulsory. In addition, some new transmission links had to be established in order to transmit the renewable energy from the area where it is generated to the area where it is consumed. Another reason is the market incentive. In Europe, ENTSO-E, the European Network of TSOs for electricity is planning the future grid with the Ten Years Network Development Plan, (TYNDP) [11], where, a lot of new HVDC links are mentioned as highlighted on the map in Figure I-2.

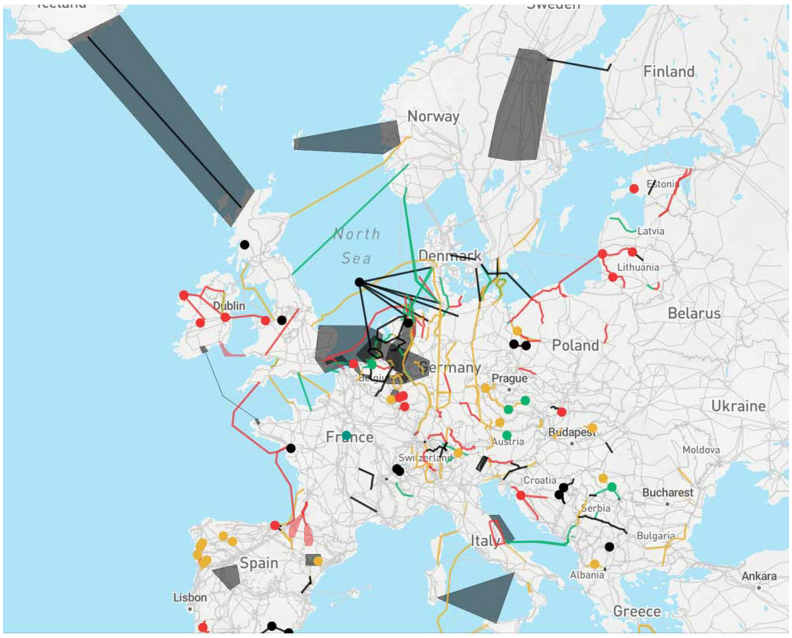

Figure I-2 - HVDC links in Europe [11]

These factors (i.e., increase of IRES and HVDC links) result in a significant increase of power electronic converters in the current power system. Two types of power converters topologies exist in the present power system: the Voltage Source Converter (VSC) based on transistor technology and Current Source Converter (CSC) based on thyristor technology, also called Line Commuted Converter (LCC). Indeed, before using transistors for the drive of DC or synchronous motor, the thyristor based-power converters were connected to a current source. Due to the operating mode of the thyristors, the current source operation mode was compulsory. When switching to transistor-based-power converters, both choices i.e., current source or voltage source were available. This choice had an influence on the type of switches, a CSC is supposed to use a switch composed of a transistor in series with a diode, whereas the VSC needs a transistor in parallel with a diode as shown on Figure I-3.

In case of a CSC, the two switches in series induce more losses than in the case of a VSC. The VSC has been chosen for its efficiency and because it is easier to manage a voltage source with a capacitor than a current source with an inductor.

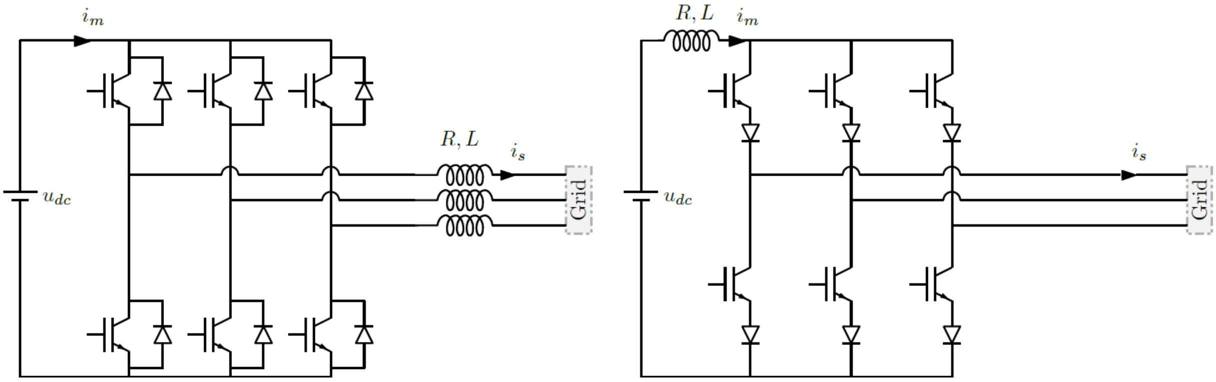

a) VSC

b) CSC

Figure I-3 - Current Source Converter versus Voltage Source Converter

A converter is always a double modulator of electrical quantities. In the case of a VSC, the DC bus voltage u_{dc} is modulated to generate a set of three voltages on the AC side, but at the same time, the AC grid currents are modulated to generate the DC current i_m . Thus, this topology could either be called “DC voltage source converter” or “AC current source converter”. The modulation is intrinsically symmetrical. However, in practical applications, only one modulation is used, i.e., the voltage modulation to control the AC currents. This is the reason why this converter is named “Voltage Source Converter”.

For high power applications, the DC bus voltage is limited by the technology of the cables. For several years, the nominal voltage for the DC cable had to be set to 320 kV between one pole and the ground. Now, some new projects are expected with higher voltage of 400 kV to 525 kV. In all cases, this voltage is supposed to put hundreds of transistors in series. Switching hundreds of transistors at the same time is extremely challenging [12], the concept of a Voltage Source Modular Multilevel Converter (VSC-MMC) is a solution to this issue. It is based on a series connection of elementary submodules, which do not switch at the same time. Submodules may use a half-bridge, full-bridge or hybrid topologies [13].

A stack of N-submodules is called an arm. Each arm is connected to an inductor (L_{arm} , R_{arm}) whose aim is to limit the derivative of the current in case of a DC fault. Each phase comprises two identical arms. One is connected to the positive pole of the DC bus and the other is connected to the negative pole of the DC bus. The combination of two arms in the same phase is called a leg. The MMC is composed of three legs (see Figure I-4). The series connection of hundreds of elementary submodules results in a quasi-sinusoidal modulated voltage waveform as shown in Figure I-4.

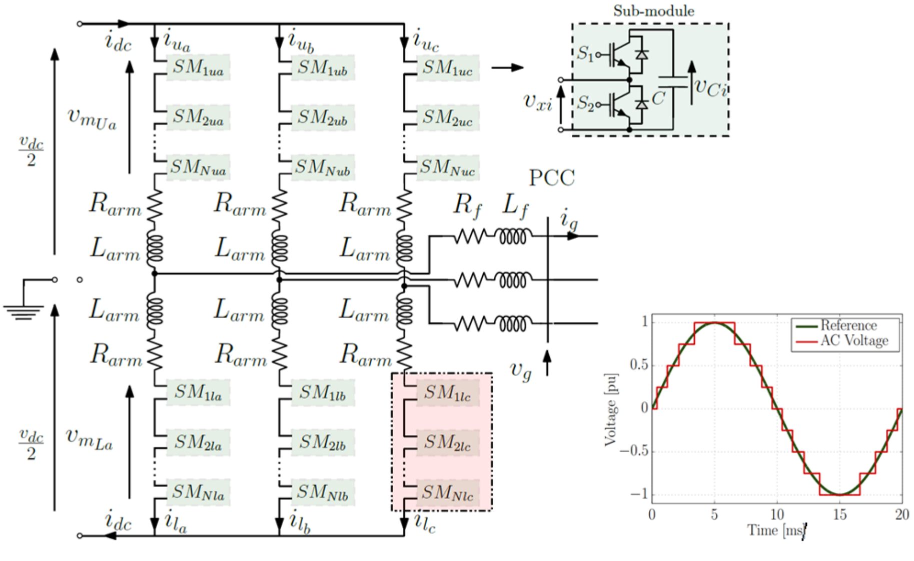

Figure I-4 - Modular Multilevel Converter

Control management of power electronic converters: When the power injected by these power converters is not negligible with respect to the nominal power of the system at the point of common coupling, the grid quantities can be significantly affected. As a consequence, power converters cannot be considered as simple devices connected to the main grid, but they will actively participate in supporting the grid and affecting its stability. Hence, it is important to monitor the grid-connected power converters by estimating their states (e.g.; angle, voltage …), and also to manage their power exchange. The fundamental aim of power converters is to inject the power coming from wind and solar or planed on HVDC links to the main grid. This aim is fulfilled through an adequate control management i.e., power converters require first to be synchronized to the main grid, then injecting the power. The purpose of the grid synchronization stage is to determine the phase angle of the grid voltage to control the power exchange between the AC and DC systems, then, the exchanged power dynamics are specified by a power control stage. Therefore, effective grid synchronization algorithms in addition to an adequate power management are key factors determining the complete control structure quality.

Conventional Grid-following Control: Today, power converters are controlled under the presumption that an AC voltage with a given magnitude and frequency is maintained at their terminals which they can simply follow to inject a controlled power. In practice, this translates into the assumption that the AC system is dominated by synchronous generators forming the instantaneous AC voltage. This control strategy is well-known as a grid-following control. If a part of the AC grid dominated by renewable energy sources is disconnected from the main AC grid due to a fault or line tripping, it will lead to a loss of synchronism because of the absence of an AC voltage to follow.

Another consequence of the increase of the grid-following based-converters proportion is the decrease of the total grid inertia [14], which induces a faster dynamic response of the frequency [15]. The low-inertia phenomenon has been already noticed in several areas, such as Ireland and UK. More details about those data are published by ENTSO-E [16]. Actually, a “Synthetic inertia” concept has been proposed for grid-following converters. However, because of the frequency estimation delay and control response time, this concept is not as efficient as a real inertia to limit the frequency derivative [17]. Moreover, since synthetic inertia control uses the frequency derivative to emulate the inertial effect, this induces more noise that may disturb the system operation and endanger the system stability.

Another limitation of grid-following converters is their inability to operate correctly under weak grid conditions and especially to respond to the fault-ride through (FRT) requirements [18]. In fact, large wind farms are usually located in remote and offshore areas. High voltage transmission systems that have long transmission distances are used to deliver wind power to main grids. Long transmission lines or cables result in a high grid impedance, and thereby, a weak AC grid. Many studies show that the operation of grid-following converters is limited and highly sensitive under weak grid conditions. Hence, an acceptable operation with desired performances cannot be guaranteed. [19]. Moreover, in case of a fault, the grid-code requires a full reactive current injection to support the AC voltage. However, in the case of an islanded wind turbine platform, where no reactive power is demanded, this may not be the right choice. Because of all these reasons and to avoid several limitations of the grid-following control, some countries such as Ireland made a choice to limit the integration of grid-following converters in their grid to 60 percent [20], [21].

To anticipate and prepare for these challenges, the way to control power converters has to be changed in order to meet system needs as with a synchronous machine.

Power Electronic Converters and System Needs: The system needs listed in Table I-1 have been guaranteed until now thanks to the physical characteristics of SGs. For instance, SGs have inertia because of their rotating mass that compensates a power imbalance during transients. Power converter devices have not got any, and therefore, they require storage systems with adequate control laws. Another example is the overcurrent capability that is larger for SG than for power electronic converters. Actually, semiconductor components could be oversized to deal with overcurrent issues. However, this engenders additional cost and weight, making the installation of station based power converters less beneficial. Moreover, power converters are currently controlled as current sources. They do not impose their own voltage like SG. Consequently, they cannot operate in standalone mode.

Table I-1 Technical needs [20]

Service	Main technical functions	Conditions
Electrical energy transport on AC line	Three-phase sinusoidal currents injection	$\omega_{min} < \omega < \omega_{max}$
Parallel load connection	Control of grid nodes RMS voltages	$V_{min} < V(i) < V_{max}$
System safety	Load-sharing between parallel generators	$\sum P_{gen}(i) = P_{load}$
Hardware Security	Overcurrent limitation	$I_{gen}(i) < I_{max}$

In the near future, power converters will dominate the AC system and replace SGs. Thus, they are asked to impose an instantaneous AC voltage at their terminals, while fulfilling the same transmission system requirements as conventional SGs. This capability of power converters is known as “grid-forming” that necessitates a change in the way the converters are controlled today.

I.2 State-of-the-art: From grid-following to grid-forming

ENTSO-E is currently working on a new version of this grid code which will embed the notion of grid-forming converters. A working group has already published a technical report document called “High Penetration of Power Electronic Interfaced Power Sources and the Potential Contribution of Grid-Forming Converters” on this topic. It defines several subtopics of concern which are to be examined.

- Creating system voltage
- Contributing to fault level
- Sink for harmonics
- Sink for unbalance
- Contribution to inertia
- System survival to allow effective operation of Low Frequency Demand Disconnection (LFDD)
- Preventing adverse control interactions

Referring to the literature, to make power converters have grid-forming capability, a droop control method also called inverse-droop control for synchronization [22] and power regulation has been proposed to imitate the parallel operation characteristics of SGs. It was originally proposed in [23] for uninterruptible power supply (UPS) systems, and has been developed into a general approach for parallel converters [24], especially in Microgrid [25]–[31] and UPS systems [32], [33]. Thereafter, several variants of droop control have been proposed to improve the system dynamics [34] and to be applied in low voltage grids, in which the line impedance is more resistive [35]. Moreover, a virtual frequency-voltage frame method is proposed to solve this problem in any given condition of line impedance R/X ratio [36]. On the other hand, P-ω droop can still be applied in LV grids by adding virtual output impedance to make the total line impedance more inductive [37]–[39], to improve the active power dynamics and to ensure a decoupling between active and reactive power [40]. Additionally, it has also been demonstrated that optimization of the droop coefficient [41] can help to enhance system stability. Contrary to the secondary and tertiary controls that need communication signals from a central controller [42] [43] [44], the primary droop control allows a power sharing in parallel operation only based on load measurements and without communication.

Despite the benefits of the droop control strategies, it still has no inertia emulation capability, which limits their applicability to small-scale power system. A low-pass filter is added to droop control allows emulating the inertial effect [45]–[47] similarly to a SG. However, this yields an oscillatory behavior of the system [46]. Therefore, another promising solution that replaces the conventional droop control has been proposed to mimic not only the steady state characteristics of SGs, but also their transient characteristics, by applying swing equation to enhance the inertia. Different implementations have been proposed in the literature such as Virtual Synchronous Generator (VSG) [47], [47]–[49], Synchronverter [50]–[54], virtual synchronous machine (VSM) [27], [45], [55]–[59] and VISMA [60], but all of them adopt the idea of controlling the converter to mimic an actual SG by using its corresponding models. In this way, a converter performs equivalent to an SG, especially in terms of inertia response [61], [62]. Therefore, the VSG can play an important role in more power electronic based power systems in the future. In recent work, it is reported that additional lead-lag unit allows the conventional droop control to contribute to total inertia of the system and improve the system damping [46], [47], and make it mathematically equivalent to the VSG [46]. However, this analogy is only true under many assumptions that have not been discussed in the literature.

Apart from the VSG and the droop control, other control laws allowing the grid-forming capability have been proposed: Virtual Oscillator (VOC) [63]–[68], matching control [10] and Inducverter [69]. It has been proven that the VOC is equivalent to conventional droop control from a small-signal sense [64], [65], [70]. However, this control may be more advantageous in the case of voltage unbalance and distortion due to its non-linear characteristic [64], [68]. The Matching control is another way to emulate the SG, by creating through the control, a link between the DC bus and the frequency, where the moment of inertia will be equivalent to DC capacitor and the DC voltage will be equivalent to the rotation speed. This technique is controlling the frequency through the variation of the DC voltage. Therefore, the control of the DC side with a proportional controller is mandatory. Thanks to the link between the DC bus and the frequency, the load sharing capability can be achieved similarly to the conventional droop control, where the droop frequency gain is equivalent to the proportional controller gain. The main drawback of such controller is the all-in-one features, i.e., (DC voltage, grid-frequency control, power sharing and the active power control) managed with only one degree of freedom. The last algorithm, the Inducverter refers to the emulation of the induction machine characteristics, where converters can be synchronized to the main grid without considering its initial frequency. However, the emulation of this control may result in some numerical issues due to the derivative action in the model of the machine.
Some of these controllers such as VSG are using the PLL, whereas, the droop control, the filtered droop control, virtual oscillator, matching control and Inducverter are not using the PLL. For some authors [20], the PLL-less option is advantageous to avoid the numerous stability issues caused by the PLL with the classical grid-following control [20], whereas, other authors affirm that the PLL has no major impact on the steady-state operation, and its utilization is limited to damping purposes [58]. Neither affirmation has been theoretically proven.

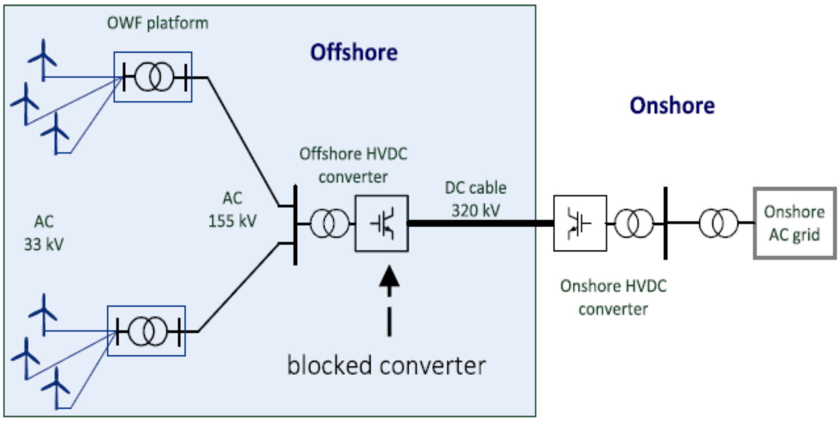

Figure I-5 - Typical configuration of OWFs connected to the main grid via HVDC-link [71]

Recently, a novel concept allowing power converters to operate in islanded mode while being a current source has been proposed in [71], [72]. The development of this control was motivated by the following reason: the blocking state of the HVDC offshore converter illustrated in Figure I-5 yields a distortion of the 155 kV point and its increase roughly by 30%. This behavior was linked especially to the way the current loop is implemented for the GSC (Grid Side Converter). This behavior has been avoided by proposing a direct AC voltage control with a transient damper for the grid current.

In control hierarchy, two different control layers for power electronic converters are characterized as depicted in Figure I-6 : The outer control is linked with the system level, and the inner control interacts with the device level.

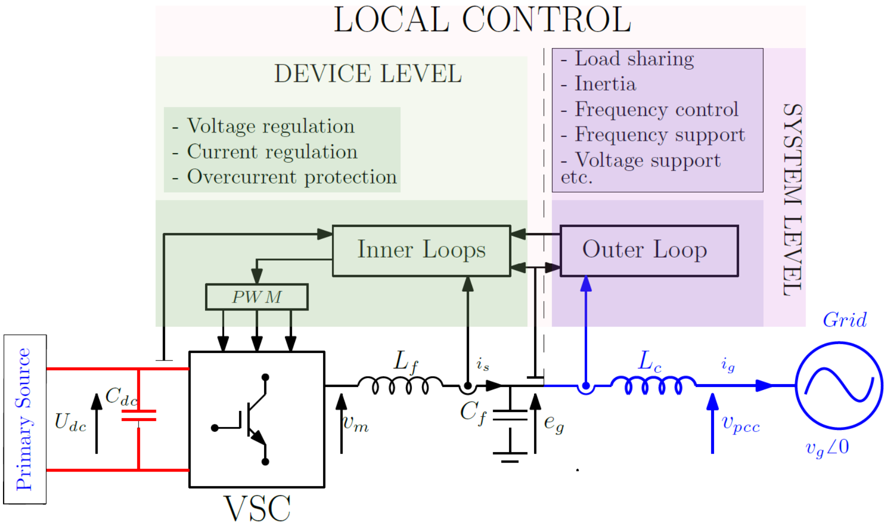

Figure I-6 - Local control hierarchy

In most of the references cited previously, except in [71], the focal points were on the outer loop control and its interaction with the system level. Other researches were mainly interested in the design and the control of the inner control loops. Actually, one common solution to control the AC voltage is based on the cascaded PI controller structure. This solution is favored for industrial applications because of the simplicity of its implementation, and also because it generates a current reference that serves to protect the converter [73]. Apart from the conventional cascaded PI controllers [28], [34], [73]–[77], other control strategies have been used such as sliding mode control for inner current loop and a mixed H_2/H_∞ for AC voltage loop [78], fractional order controller [79] and LQR technique [80]. The method in [78] aims to design a robust controller in order to achieve high performances, however, this technique is complex and requires very high computation effort. The method in [79], has been motivated by its flexibility and its high number of degrees of freedom, and finally, the method in [80] has been motivated by its simplicity. Moreover, it achieves a desired voltage bandwidth. Among the inner control strategies proposed for grid-forming converters, a few studies have discussed the control design in high power applications [73], [78], where the switching frequency is lower than 5kHz. Such conditions can result in slow dynamics [73], restrained stability regions and interactions between control loops, which can lead to an unstable system [81]. Therefore, controller parameter tuning in such conditions is still a challenge.

Contrary to 2-Level VSC, MMCs do not require an output LC filter, and therefore, no compulsory need for AC voltage regulation loops. The modulated voltage can be directly driven by a set of AC voltages. However, the MMC contains internal capacitors in each submodule, which require some internal loops to control the energy. The dynamics of these loops are close to those of the outer loop, which may cause interactions between controllers. This question has not been investigated in the literature.

Grid-forming converters are operating as a voltage source behind impedance, and thus, they are very sensitive to grid disturbances that may engender overcurrent. The current-limiting strategies of grid-forming VSCs during large disturbances have been studied in many references [22], [82]–[89]. Among these works, few references extend the current limitation studies to the large power system [87], where other events can cause overcurrent issues such as line tripping and reclosing. Two main strategies have been proposed for grid-forming converters in order to limit the current during transients. One solution is to limit the current with a current saturation algorithm (CSA) [82], [83], [88]. The second solution is the Virtual Impedance (VI) [71], [84]–[86], [90], [91]. It has been implemented to emulate the effect of physical impedance when the current exceeds its nominal value. This control strategy intended to modify the AC voltage reference in order to limit the current. Therefore, its reaction against the fault depends on the AC current as well as on the dynamics of the AC voltage regulators. For slow inner control dynamics, the virtual impedance cannot guarantee a current limitation during the fault. A feed-forward action on the modulated voltage has been proposed to deal with this issue [87]. Once the current is limited, the post-fault synchronization is of highest interest. However, the impact of the current limitation techniques on the transient stability has been marginally studied in the literature [92]–[97]. Indeed, an unstable behavior when the overcurrent protection is disabled would lead to an unavoidable trip from the main grid for safety purposes [18]. However, in future power systems, different power sources have to cope with various events and guaranty the stability. In this context, the transient stability of the system is defined as the ability of the power converter to recover the synchronism after fault clearing. The choice of the current limiting algorithm has a large influence on the transient stability. In [92], [95], the transient instability phenomenon using the CSA while keeping the droop control has been studied. To avoid this instability issue, some papers proposed to switch from voltage control, based on the droop control to current control, based on a phase-locked loop [22], [98]. These methods require a complex algorithm for fault detection and triggering conditions. Moreover, as specified by [22], fault recovery could only be achieved after a considerable retuning of the voltage controller and the power controller in order to avoid AC voltage collapse. In [84], the authors showed through time-domain simulations, the ability of the VI to ensure a better transient stability than the CSA in case of a heavy load connection. However, this result has not been theoretically investigated.

To anticipate and prepare for future challenges linked to the high penetration rate of power electronic converters in power transmission systems [16], [99], [100], several European Transmission System Operators (TSO) and universities have gathered to form a European project to work on these issues, e.g., PROMOTioN [101], MIGRATE [102], recently HVDC Inertial Provision [99], etc. Among these projects, the MIGRATE Project is interested in a high integration of power electronic converters up to a 100%. The MIGRATE project that funded this work is presented in the following paragraph.

MIGRATE Project: MIGRATE stands for ***Massive InteGRATion of power Electronic devices***. It is an EU-funded project under the framework of European Union's Horizon 2020. It gathers several partners that are presented in Figure I-7. There are 11 TSO, 12 universities and one manufacturer from 13 countries working together in this project. Their main objective is to propose innovative solutions to progressively adjust the HVAC system operations. The different objectives of the project are addressed in 8 work packages. This PhD is part of the work package 3 that aims at developing controls and operations of a grid with 100% converter-based devices.

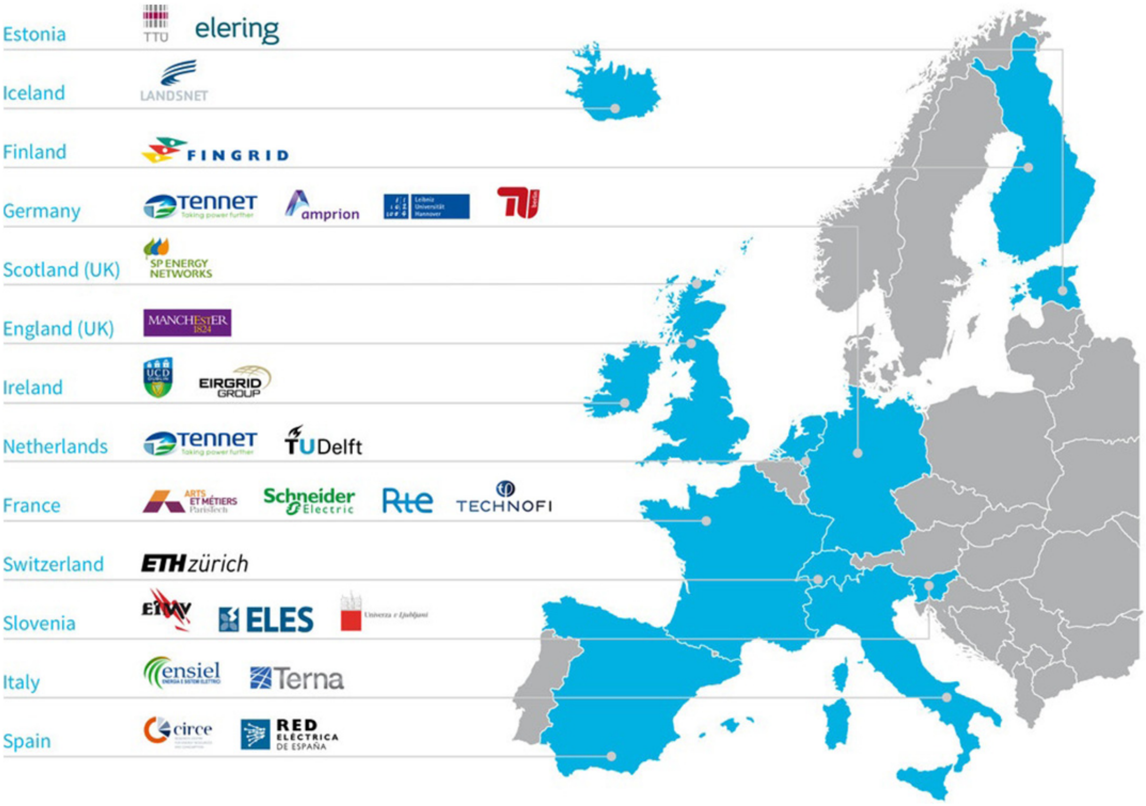

Figure I-7 - Members of MIGRATE project [102]

I.3 Contributions and contextual constraints

The main contributions of this work are listed below:

- **Chapter II:** Starting from the fundamental goal of a power converter, which aims to provide active power to the main grid, a first grid-forming control structure is derived. It consists of a robust power control loop that allows power converter to guarantee a specified active power dynamics regardless of the AC grid stiffness. In this chapter, the possible coupling between active and reactive power is highlighted and limited through a specific power controller tuning. Additionally, a transient virtual resistor is also implemented to overcome a particular resonance around the grid frequency and damp the grid current dynamics.
  The proposed control is equipped with a PLL. It is demonstrated that the use of the PLL in this control is fundamentally different from the grid-following.

- **Chapter III:** The power converter is connected to an AC system with a variable grid frequency that emulates: the swing equation, the turbine dynamics and the governor of a real synchronous machine. Based on this simple grid case, the active power and frequency dynamics of the first grid-forming solution are studied. Then, two control strategies are derived from the first solution to allow inertia emulation similarly to a SM. The first solution is a PLL based-control and the second one in a PLL-less control. The properties of each control method are highlighted and their impact on the active power and frequency dynamics are deeply analyzed along this chapter.

- **Chapter IV:** In previous chapters, the converter was connected to the AC system through an L filter. This consideration simplifies the analysis. However, its appropriateness is relative to the converter topology. In case of grid-forming 2-Level converters, the connection to the AC grid is usually done through an LCL filter. This additional LC filter requires additional voltage and control loops. In this chapter, the impact of the implementation of this filter and its control on system stability is highlighted and new control methods are proposed to improve the system stability, dynamics and guarantee the same performances reached in the previous chapters.
  In the case of Modular Multilevel Converters (MMCs), an LC filter is not required since they generate a quasi-sinusoidal output voltage. However, the main challenge with MMCs, is the energy management on their submodules. In this chapter, the impact of the grid-forming control loops on the energy stored on the MMC is briefly discussed.

- **Chapter V:** This chapter deals with current limitation in faulted conditions. Two control techniques are presented and their implementation on each inner control strategy is shown. The current limitation methods are compared and their impact on the transient stability is highlighted. Based on this comparison, a hybrid current limitation control is proposed to benefit the advantage of both methods. Additionally, a simple adaptive gain is proposed in order to improve the critical clearing time and hence, the transient stability.

- **Chapter VI:** To validate the proposed control strategies, a small-scale power converter is developed. Then, the interoperability between the proposed controls is assessed through a Power Hardware In the Loop (PHIL) simulation, where different test cases are performed.

In this thesis, some contextual constraints are considered:

- The solutions must be compatible with the highest voltage, and the highest power rating of existing VSCs.
- The secondary and the tertiary control are not discussed in the thesis.
- With no synchronous generators, the definition of system frequency is no longer linked with the rotation speed of rotors. As a consequence, frequency estimation is unclear, especially under the fundamental period or during transients. Thus, an arbitrary choice constrains the proposed solution not to rely on frequency measurements. This task is handled by another Work Package in the project.
- The source of the primary energy is neglected in this thesis.
- Harmonics, nonlinear loads and motor loads are out of the scope of this thesis.

I.4 List of publications derived from this work

The publications resulting from this thesis are listed below. The main contributions presented in this manuscript are based on the journal papers J1-J6, the conference papers C1-C13, a book chapter and different public simulation models..

J1: “Critical clearing time determination and enhancement of grid-forming converters embedding virtual impedance as current limitation algorithm” IEEE Journal of Emerging and Selected Topics in Power Electronics, 12/2019, **QORIA Taoufik**, GRUSON François, COLAS Frédéric, DENIS Guillaume, PREVOST Thibault, GUILLAUD Xavier

J2: “Current Limiting Algorithms and Transient Stability Analysis of Grid-Forming VSCs” Electric Power Systems Research (EPSR), **QORIA Taoufik**, GRUSON François, COLAS Frédéric, GUILLAUD Xavier

J3: “Classification of Droop-Based Grid-Forming Control Schemes: Application in Forced Commutated Converter-Based HVDC Systems” Electric Power Systems Research (EPSR), ROKROK Ebrahim, **QORIA Taoufik**, BRUYERE Antoine, FRANCOIS Bruno, GUILLAUD Xavier

J4: “Direct AC Voltage Control for Grid-forming Inverters” Journal of Power Electronics, **QORIA Taoufik**, LI Chuanyue Li, OUE Ko, GRUSON François, COLAS Frédéric, GUILLAUD Xavier

J5: “Coupling influence on the dq impedance stability analysis for the three-phase grid-connected inverter” MDPI Energies, 09/2019, LI Chuanyue Li, **QORIA Taoufik**, COLAS Frédéric, JUN Liang, WENLONG Ming, GRUSON François, GUILLAUD Xavier

J6: “A PLL-free grid-forming control with decoupled functionalities for high-power applications” IEEE Access, **QORIA Taoufik**, ROKROK Ebrahim, BRUYERE Antoine, FRANCOIS Bruno, GUILLAUD Xavier

C1: “Analysis of the coupling between the outer and inner control loops of a Grid-forming Voltage Source Converter” EPE2020, 09/2020 **QORIA Taoufik**, GRUSON François, COLAS Frédéric, KESTELYN Xavier, GUILLAUD Xavier

C2: “Impact of grid-forming control on the internal energy of a modular multi-level converter” EPE2020, 09/2020 ROKROK Ebrahim, **QORIA Taoufik**, BRUYERE Antoine, FRANCOIS Bruno, ZHANG Haibo, BELHAOUANE Moez, GUILLAUD Xavier

C3: “Current Limiting Algorithms and Transient Stability Analysis of Grid-Forming VSCs” PSCC 2020, 06/2020 **QORIA Taoufik**, GRUSON François, COLAS Frédéric, GUILLAUD Xavier

C4: “Classification of Droop-Based Grid-Forming Control Schemes: Application in Forced Commutated Converter-Based HVDC Systems” PSCC 2020, 06/2020 ROKROK Ebrahim, **QORIA Taoufik**, BRUYERE Antoine, FRANCOIS Bruno, GUILLAUD Xavier

C5: “Effect of Using PLL-Based Grid-Forming Control on Active Power Dynamics under Various SCR” IECON'2019-IEEE, 10/2019 ROKROK Ebrahim, **QORIA Taoufik**, BRUYERE Antoine, FRANCOIS Bruno, GUILLAUD Xavier

C6: “Power Converters Classification and Characterization in Power Transmission Systems” EPE'19, 09/2019 **QORIA Taoufik**, PREVOST Thibault, DENIS Guillaume, GRUSON François, COLAS Frédéric, GUILLAUD Xavier

C7: “Tuning of AC voltage-controlled VSC based Linear Quadratic Regulation” IEEE PowerTech19, 06/2019 **QORIA Taoufik**, LI Chuanyue Li, OUE Ko, GRUSON François, COLAS Frédéric, GUILLAUD Xavier, PREVOST Thibault

C8: “Inertia effect and load sharing capability of grid-forming converters connected to a transmission grid” 15th ACDC19, 02/2019 **QORIA Taoufik**, GRUSON François, COLAS Frédéric, DENIS Guillaume, PREVOST Thibault, GUILLAUD Xavier

C9: “Tuning of cascaded controllers for robust grid-forming Voltage Source Converter” Power Systems Computation Conference, 06/2018 QORIA **Taoufik**, GRUSON François, COLAS Frédéric, GUILLAUD Xavier

C10: “Development of a power hardware in the loop simulation of an islanded Microgrid” IECON'19, 10/2019 FAKHAM Hicham, **QORIA Taoufik**, LEGRY Martin, DUCARME Olivier, COLAS Frédéric

C11: “Modeling and Control of the Modular Multilevel Converter connected to an inductive DC source using Energetic Macroscopic Representation” EPE'18, 09/2018 **QORIA Taoufik**, GRUSON François, DELARUE Philippe, LE MOIGNE Philippe, COLAS Frédéric, GUILLAUD Xavier

C12: “Electromagnetic Transients (EMT) Model Design based on Modular Multilevel Converter Mockup” The International Conference on Power Systems Transients (IPST2019), 06/2019 BELHAOUANE Moez, ZHANG Haibo, COLAS Frédéric, KADRI Riad, **QORIA Taoufik**, GRUSON François, RAULT Pierre, DENNETIERE Sébastien, GUILLAUD Xavier

C13: “Contrôle du Convertisseur Modulaire Multiniveaux connecté à une source DC inductive” Symposium de Génie Electrique 2018, SGE 2018, 07/2018 **QORIA Taoufik**, GRUSON François, DELARUE Philippe, LE MOIGNE Philippe, COLAS Frédéric, GUILLAUD Xavier

Book Chapter: “Converter-based dynamics and control of modern power systems". Place of publication not identified: ELSEVIER ACADEMIC Press, 2020.

Data I: **T. Qoria**, U. Markovic, T. Jouini, D. Groß, G. Denis, and T. Prevost. Data underlying the research of a 3 bus model for full inverter system - Migrate WP3. 2018.

Data II: https://github.com/l2ep-epmlab/VSC_Lib

II. Synchronization and power control of a simplified VSC connected to an AC system

II.1 Introduction

The fundamental aim of a voltage source converter connected to the AC grid is to convert the DC power into an active power on the AC grid and vice versa depending on the direction of the power flow. In order to achieve this goal, power converters may behave as current injectors (grid-following) or voltage sources (grid-forming) [104]–[107]. In both solutions, the question of the synchronization and the way to manage the active power exchange with the grid plays a crucial role. Till now, the grid-following concept has been used in most applications. However, using the power converters based on the grid-forming concept may come up to be an interesting solution in certain situations.

In this chapter, a fundamental concept is first proposed in section II.2 to explain the two ways to control the power. Then, some brief recalls about the grid-following control are given in section II.3. In section II.4, which is the core of this chapter, the operating principle of a converter based on "grid-forming control" is presented. Then, its control structure for synchronization and power control is developed, while taking into account its dynamic behavior, stability and robustness aspects.

II.2 Fundamental concept for the power control with power electronic converters

II.2.1 Description of the connection of a DC bus to an AC grid

In this chapter, the simplest topology to connect a DC grid to an AC grid is considered (Figure II-1). It consists of a Voltage Source Converter (VSC) connected on one side to a DC voltage source u_{dc} and on the other side to an AC grid through an RL circuit.

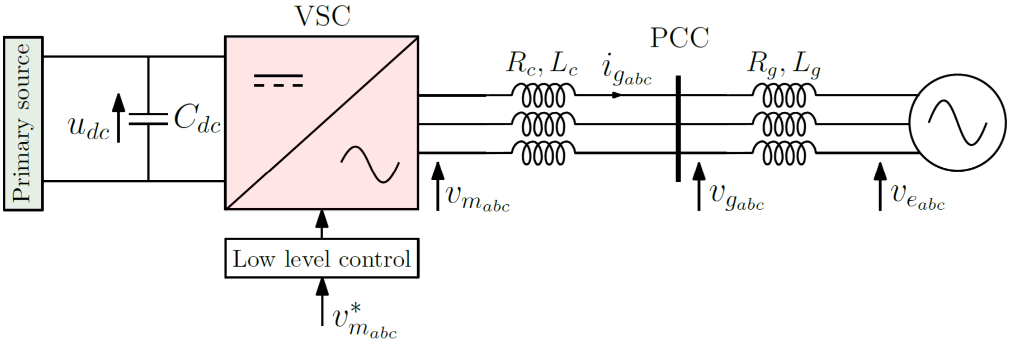

Figure II-1 - Representation of a VSC connected to an AC system

$v_{m_{abc}} = \left[v_{m_a}, v_{m_b}, v_{m_c}\right]^T$ are the modulated voltages obtained by the modulation of the DC bus voltage through the switching stage. In the following, the switching time (T_s) is supposed to be small enough to assimilate $v_{m_{abc}}$ to its average value.

The low level control is not taken into account in this chapter. It is assumed that the modulated voltage $v_{m_{abc}}$ is directly driven by a set of three-phase reference signal in the control $v^{*}_{m_{abc}}$ (i.e. $<v_{m_{abc}}>_{T_s}=v^{*}_{m_{abc}}$).

In this chapter, the power converter is assumed to be connected to the AC grid through a simple R,L filter (R_c, L_c). For high voltage applications such as power transmission systems, the resistive part is assumed to be much smaller than the impedance $L_c\omega_g\,(L_c\omega_g \gg R_c)$. This usually represents the leakage impedance of the transformer. For this kind of application, the typical value of this impedance in per-unit is around 0.15 p.u. This value is considered in the rest of this thesis.

The AC grid is assumed to be balanced. It is modeled by a Thevenin equivalent AC voltage source in series with its equivalent impedance (R_g, L_g), providing an AC voltage $v_{g_{abc}} = \left[v_{g_a}, v_{g_b}, v_{g_c}\right]^T$. The grid currents are denoted by $i_{g_{abc}} = \left[i_{g_a}, i_{g_b}, i_{g_c}\right]^T$.

Even if the model from Figure II-1 is oversimplified, this latter is used for introducing the synchronization and the power exchange principle between power converters and AC grids. Let's define the notation that will be used in the sequel,

- Frequency: Grid frequency ω_g.
  Estimated grid frequency $\tilde{\omega}_g$
  Modulated converter frequency ω_m
- Time domain angle: Grid voltage angle θ_g
  Estimated grid voltage angle $\tilde{\theta}_g$
  Modulated voltage angle θ_m
- Phasor angle: Grid voltage angle δ_g
  Estimated grid voltage angle $\tilde{\delta}_g$
  Modulated voltage angle δ_m

Table II-1 Base quantities

Base quantities	Value
S_b	S_n (rated power)
U_b	U_n (ph-ph voltage)
I_b	I_n
ω_b	ω_n
Z_b	U_n^2/S_n
L_b	Z_b/ω_b
C_b	$1/(Z_b.\omega_b)$

II.2.2 Grid impedance and stiffness

The equivalent grid impedance is related to the Short Circuit Ratio (SCR), which expresses the AC grid stiffness. The SCR is defined as the ratio of the maximum apparent power of the grid to the rated power of the interconnecting generator. The SCR is expressed as:

$$SCR = \frac{S_{ac}}{P_{dc}^{N}} \tag{II-1}$$

where S_{ac} is the short-circuit power of the AC system and P_{dc}^{N} is the rated power of the VSC station.

$$S_{ac} = \frac{U_e^2}{\omega_g^{SI} L_g^{SI}} \tag{II-2}$$

If the electrical quantities are expressed in per-unit, the SCR can be simply expressed with respect to the grid impedance,

$$SCR = \frac{1}{\omega_g L_g} \tag{II-3}$$

where ω_g is the grid frequency in per-unit (ω_g =1 p.u).
According to the IEEE standard 1204-1997 [108], a stiff grid is defined as a grid with the short-circuit ratio (SCR) $>$ 3, under this value, the grid is considered as weak or very weak if the SCR is lower than 2.
Hereinafter, modeling and control are done in per-unit.

II.2.3 Power converter controls classification and distinction

II.2.3.1 Basic concept of active power control

Before studying the dynamic behavior of the voltage source converter, a quasi-static model of the three-phase system presented in Figure II-1 is shown in Figure II-2. It aims to explain two different ways to control the power with a power converter. In this subsection, the resistor is neglected to simplify the analysis.

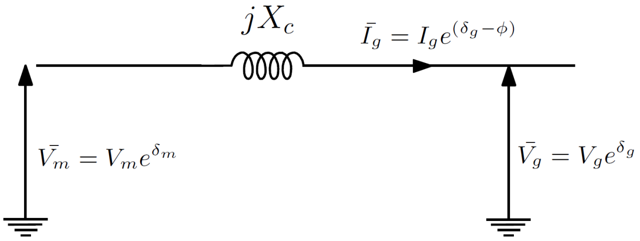

Figure II-2 - Single phase quasi static model of the VSC connected to the grid

Figure II-3 shows the phasor representation of this simple system.

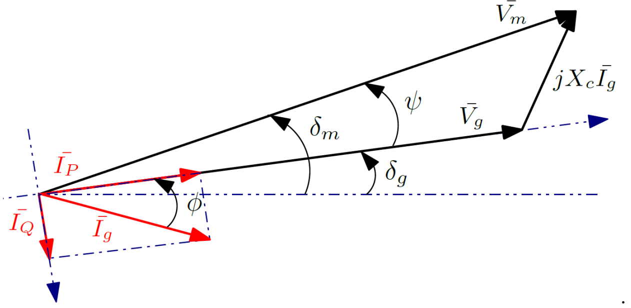

Figure II-3 - phasor representation of the studied system

Based on the phasor representation above, the active power at PCC can be expressed as,

$$P = \Re(\overline{V_g}\,\overline{I_g}^{*}) = V_g I_P = V_g I_P cos(\phi) \tag{II-4}$$

In steady state, another formulation based on the modulated voltage can be derived from this expression. Applying Kirchhoff's law on the system gives:

$$\overline{V_m} = jX_c\overline{I_g} + \overline{V_g} \tag{II-5}$$

It yields:

$$P = \Re\left(\frac{\overline{V_g}(\overline{V_m} - \overline{V_g})}{jX_c}\right) = \frac{V_m V_g}{X_c} sin(\psi) \tag{II-6}$$

The formulation of the power based on the current is the origin of the current controlled converter "grid-following". The second formulation based on the voltage is the origin of the voltage controlled converter "grid-forming".

II.2.3.2 Grid-following principle

With the first formulation of the active power, P depends on the active current. In other words, the power control is linked with the current management. Let's define P^* as the active power setpoint. From (II-4), the reference for the active current I_p^* is obtained through a simple division by the RMS PCC voltage as shown in Figure II-4. In steady state, it is assumed that $I_p^* = I_p$.

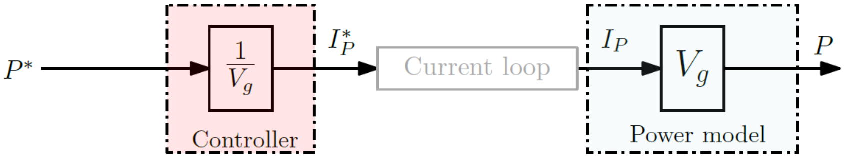

Figure II-4 - Principle of the open loop power control with the current controlled mode

A more robust control of the active power can be achieved based on the closed-loop control (Figure II-5). The inevitable inaccuracies of the model and disturbances will be compensated. Moreover, if an integral control is embedded in the controller C(s), $P = P^*$ in steady state.

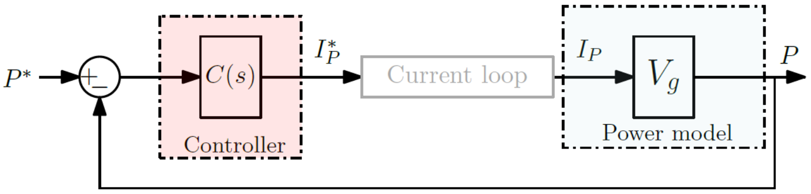

Figure II-5 - Principle of the closed-loop power control with the current controlled mode

Controlling the active current I_p means that the grid voltage magnitude and phase angle are known so that $\overline{I_p}$ is aligned with $\overline{V_g}$ as illustrated in Figure II-3. For this control concept, it can be concluded that an estimate of the grid angle is compulsory.

To sum up, for a given P^*, the current $\overline{I_g}$ is known. $\overline{V_g}$ is an external input for the system, $\overline{V_m}$ can be deduced from (II-5). In case of a change on $\overline{V_g}$, $\overline{V_m}$ has to be modified in order to keep a constant grid current in phase and magnitude. This is the origin of the name “grid-following”. In the literature, this type of control is also called “grid-feeding”.

In the same way as for the active power, similar control principle in Figure II-4 and Figure II-5 can be applied for the reactive power.

In time-domain, the general organization of a grid-following control is given in Figure II-6. It is decomposed in three main parts:

- Average value control of the active and reactive powers. The reactive power loop can be replaced by an RMS voltage loop.
- Estimation of the grid angle.
- Current control.

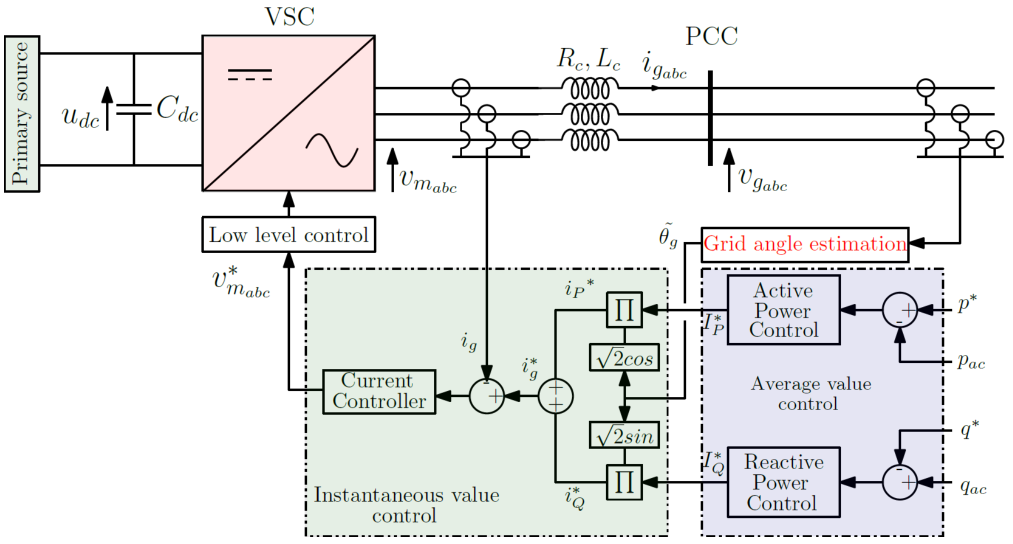

(a) Control in abc frame

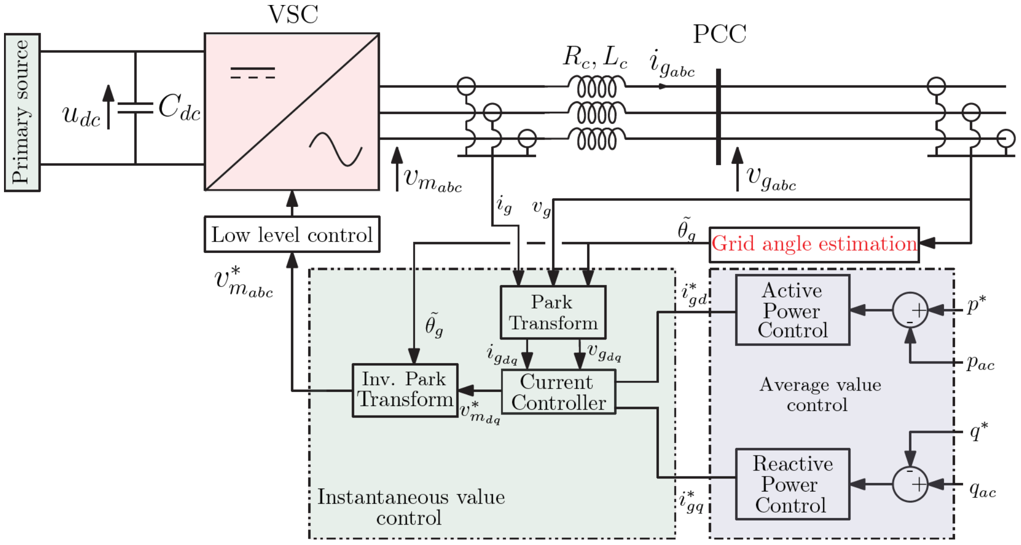

(b) Control in d-q frame

Figure II-6 - General principle of the grid-following control.

In Figure II-6.a and Figure II-6.b, the current control is implemented in (abc) and (d-q) frame, respectively. It does not change the general organization. In any case, an estimation of the grid angle is needed either to generate the three-phase sinusoidal current references or to be used in the Park transformation.

Note that the active power "P" has been replaced by the instantaneous power "p_{ac}". In a balanced three-phase system, the value of p_{ac} and P is the same, but the way to calculate it is different between phasor and EMT applications.

II.2.3.3 Grid-forming principle

Consider the second formulation of the active power in (II-6) to explain the basics of the second type of control. The active power is linked with the modulated angle δ_m and the RMS value of the modulated voltage V_m. Since it is not possible to accept a large variation on V_m, it is decided to control the active power thanks to δ_m. Hence, the control has to generate a reference for this angle δ_m^* as shown in Figure II-7. Basically, the generation of δ_m^* only needs information on the active power. Therefore, no information on the grid voltage is compulsory in the control. With this control, V_m is maintained at a given V_m^* setpoint. Since the grid angle δ_g can be considered as a disturbance, it can be compensated if an estimate of the grid angle $\tilde{\delta}_g$ is introduced in the control.

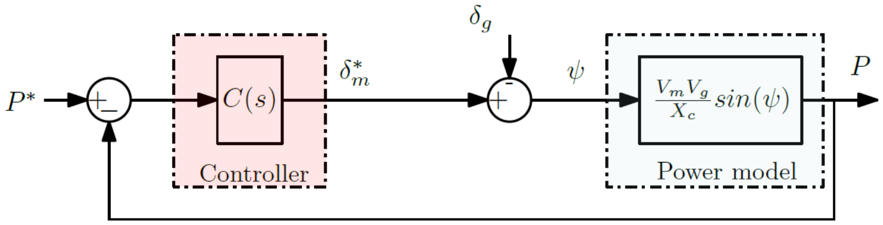

Figure II-7 - Principle of the closed-loop power control with the voltage controlled mode

The active power has to be adapted in time domain. The time domain modulated voltage angle θ_m can be deduced from the phasor modulated voltage angle δ_m (i.e., $\theta_m = \omega_m t + \delta_m$). Figure II-8 illustrate the way to generate the time-domain angle θ_m^* (Figure II-8.a in (abc) frame and Figure II-8.b in (d-q) frame).

II.2.3.4 Distinction between grid-forming and grid-following controls

The fundamental difference between grid-following and grid-forming control is linked with the way to synchronize the converter to the grid. Indeed, a grid-following based-VSC is a power converter whose injected currents are controlled with a specific phase displacement with respect to the grid voltage at the PCC. As a consequence, the knowledge of the fundamental frequency of the grid voltage is needed at any time for the correct calculation of the converter reference currents whose magnitude and angle with respect to the grid voltage phasor are properly modified by outer control loops so as to inject the required amount of active and reactive power [109].

In case of the grid-forming control, the way to synchronize is fundamentally different. The voltage magnitude is fixed freely and independently on the grid voltage, then, a self-synchronization is achieved thanks to a power control loop. An estimate of the grid angle is not compulsory. This does not mean that it cannot be used in the control. The use of this information is one of the major differences in the different types of grid-forming control as it will be discussed in this chapter and in chapter III.

This mode of synchronization is very similar to the way the synchronous generator is synchronized to the grid.

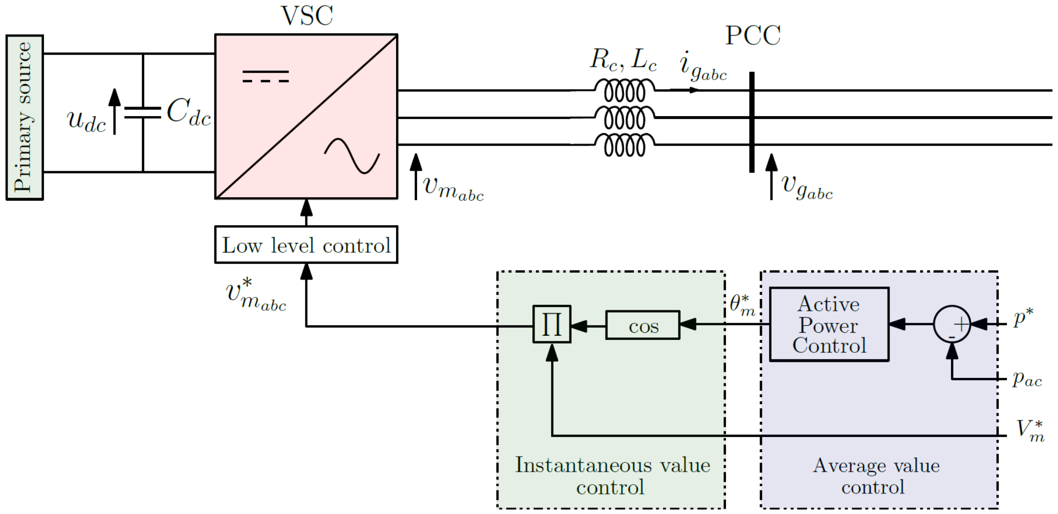

(a) Control in abc frame

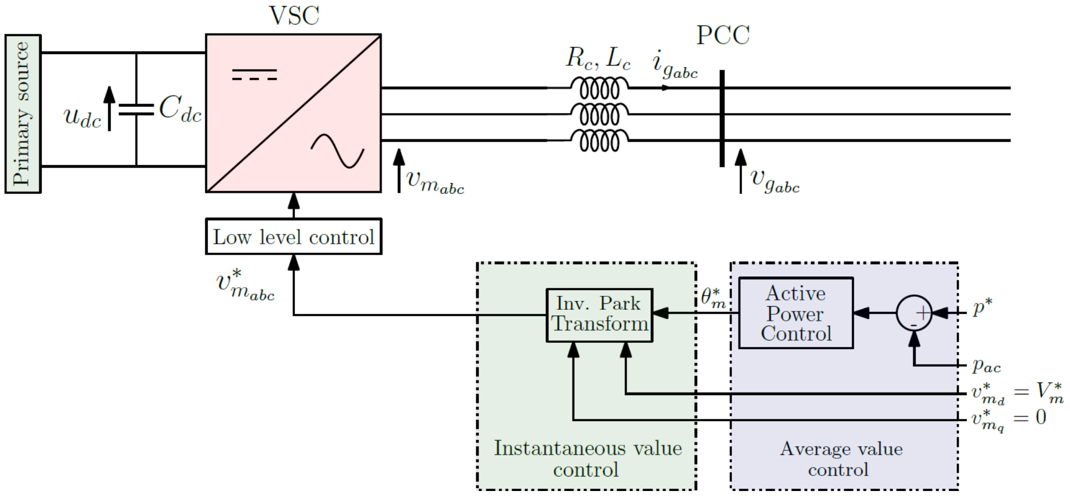

(b) Control in d-q frame

Figure II-8 - General principle of the grid-forming control.

II.3 Synchronization and power control based on grid-following control

This section recalls the principle of the grid following control, its structure and also highlights some of its limitations. The modeling and control are implemented in a *d-q* frame.

II.3.1 Synchronization based on synchronous reference frame phase-locked loop

To estimate the grid angle, a Synchronous Reference Frame Phase-Locked Loop (SRF-PLL) is often used. This control technique has been improved to operate either in balanced or unbalanced conditions [110]. However these abnormal conditions are out of the scope of this thesis. The structure of the SRF-PLL is recalled in Figure II-9.

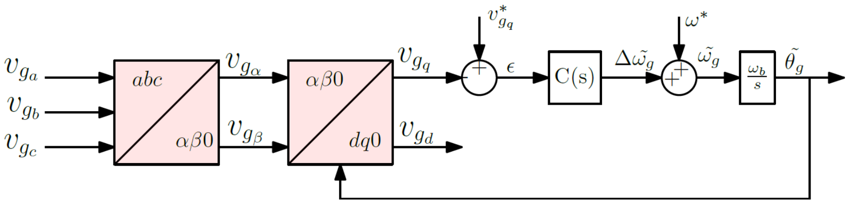

Figure II-9 - Structure of SRF-PLL

Considering a stiff AC grid ($SCR=\infty$, $v_g = v_e$), the input of the PLL is the three-phase sensed voltage signals $v_{g_{abc}}$ expressed in per-unit by the following equation:

$$\begin{pmatrix} v_{g_a} \\ v_{g_b} \\ v_{g_c} \end{pmatrix} = \begin{pmatrix} V_g cos(\theta_g) \\ V_g cos(\theta_g - \frac{2\pi}{3}) \\ V_g cos(\theta_g - \frac{4\pi}{3}) \end{pmatrix} \tag{II-7}$$

The grid voltage signals are converted to two-phase stationary reference frame signals $v_{g_{\alpha\beta}}$ (Appendix A), which is given by,

$$\begin{pmatrix} v_{g_\alpha} \\ v_{g\beta} \end{pmatrix} = \sqrt{(2/3)} \begin{pmatrix} 1 & -1/2 & -1/2 \\ 0 & \sqrt{3}/2 & -\sqrt{3}/2 \end{pmatrix} \begin{pmatrix} v_{g_a} \\ v_{g_b} \\ v_{g_c} \end{pmatrix} = \sqrt{(3/2)} \begin{pmatrix} V_g \cos(\theta_g) \\ V_g \sin(\theta_g) \end{pmatrix} \tag{II-8}$$

$v_{g\alpha}$ and $v_{g\beta}$ are directly fed into the next function which is $\alpha-\beta$ to $d-q$ rotating reference frame transformation matrix. This later is given by,

$$\begin{pmatrix} v_{g_d} \\ v_{g_q} \end{pmatrix} = \underbrace{\begin{pmatrix} \cos(\widetilde{\theta}_g) & \sin(\widetilde{\theta}_g) \\ -\sin(\widetilde{\theta}_g) & \cos(\widetilde{\theta}_g) \end{pmatrix}}_{R(\widetilde{\theta}_g)} \begin{pmatrix} v_{g_\alpha} \\ v_{g_\beta} \end{pmatrix} = \sqrt{(3/2)} \begin{pmatrix} V_g \cos(\theta_g - \widetilde{\theta}_g) \\ V_g \sin(\theta_g - \widetilde{\theta}_g) \end{pmatrix} \tag{II-9}$$

The aim of the PLL is to achieve the equality $\theta_g = \widetilde{\theta}_g$. By doing so, the following expression is obtained,

$$\begin{pmatrix} v_{g_d} \\ v_{g_q} \end{pmatrix} = \sqrt{(3/2)} \begin{pmatrix} V_g \\ 0 \end{pmatrix} \tag{II-10}$$

In order to achieve (II-10), the controller $C(s)$ used in the PLL aims to regulate v_{g_q} to its reference $v_{g_q}{}^* = 0$ in the steady state. The output of the controller $C(s)$ is the estimated grid frequency $\tilde{\omega}_g$. The estimated phase angle $\tilde{\theta}_g$ is then derived by the integration of $\tilde{\omega}_g$:

$$\tilde{\theta}_g = \omega_b \int \tilde{\omega}_g dt \tag{II-11}$$

ω_b is the base frequency in rad/s.

From (II-9) it can be seen that the system is nonlinear because of the rotational matrix $R(\tilde{\theta}_g)$. However, by assuming a small difference between the grid phase angle and the estimated one, the nonlinearity can be neglected (i.e.; $\cos(\theta_g - \widetilde{\theta}_g) \approx 1$ and $\sin(\theta_g - \widetilde{\theta}_g) \approx \theta_g - \widetilde{\theta}_g$). Based on this assumption, the control path is obtained as shown in Figure II-10.a.

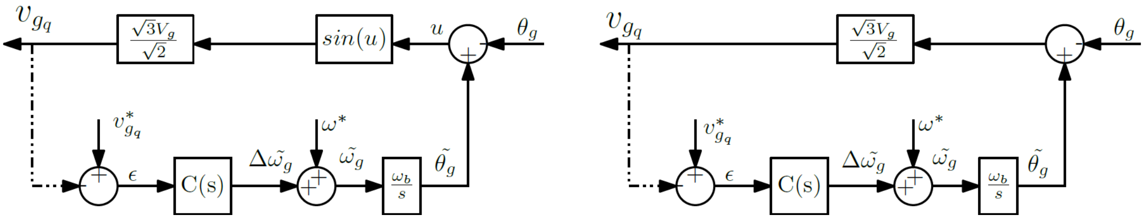

(a) Nonlinear model (b) Linearized model

Figure II-10 - Closed loop control structure for the SRF-PLL.

To avoid a steady state error between the voltage reference $v^*_{g_q} = 0$ and the measured quadratic voltage v_{g_q}, a simple Proportional-Integral (PI) controller is required,

$$C(s) = k_{p_{PLL}} + k_{i_{PLL}} / s \tag{II-12}$$

where, $k_{p_{PLL}}$ and $k_{i_{PLL}}$ are the proportional control gain and integrator gain, respectively.

From the control structure in Figure II-10.b, the transfer function of the system is expressed as follows:

$$P(s) = \frac{v_{g_q}}{v^*_{g_q}} = \frac{1 + \frac{k_{p_{PLL}}}{k_{i_{PLL}}} s}{1 + \frac{k_{p_{PLL}}}{k_{i_{PLL}}} s + \frac{1}{k_{i_{PLL}} \omega_b} s^2} \tag{II-13}$$

According to the specifications related to the damping ζ and the response time $T^R_{5\%}$, the controller gains are determined. In most cases, the PLL response time is chosen between 10ms < $T^R_{5\%}$ < 100ms. Based on these specifications, the SRF-PLL controller gains are obtained:

$$k_{p_{PCC}} = \frac{2\zeta\omega_n}{\omega_b}, \qquad k_{i_{PLL}} = \frac{\omega_n^2}{\omega_b} \tag{II-14}$$

ω_n is defined as the natural frequency of the second order system.

The SRF-PLL control in Figure II-10 is simulated considering the system and control parameters listed in Table II-2 and Table II-3, respectively. The VSC rating power is supposed to be P_n =1GW. This value corresponds to the biggest VSC connected to the power transmission system nowadays [111].

The scenario considers a change on $v_{g_q}^*$: at t=0.2 s, a step of 0.5 p.u is applied.

The simulation results are presented in Figure II-11.

One can remark that both linear and nonlinear models of the PLL have nearly the same dynamics. The response time set in the specifications is respected. However, an overshoot of 12% is noticed in the transient. It is especially linked to the zero of the transfer function in (II-13).

Table II-2 Typical system parameters

Symbol	Value	Symbol	Value
P_n	1 GW	SCR	∞
f_n	50 Hz	U_e	320 kV
L_c	0.15 p.u	R_c	0.005 p.u

Table II-3 Control parameters

Symbol	Value	Symbol	Value
$k_{i_{PLL}}$	31.83 p.u.	$T_{5\%}^R$	50ms
$k_{p_{PLL}}$	0.636 u		

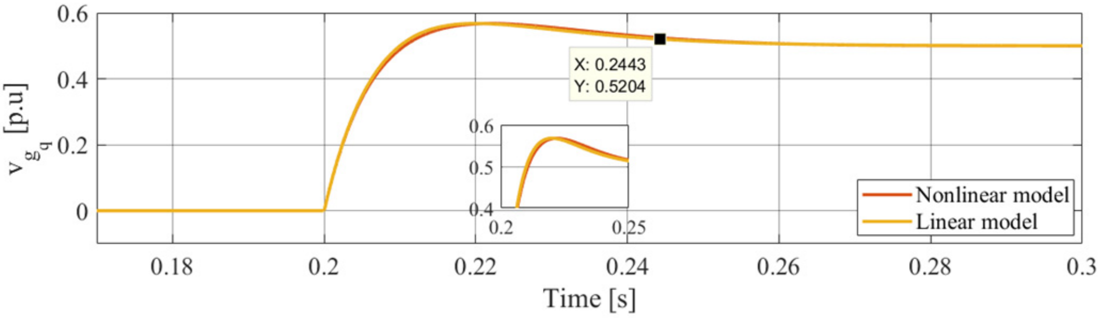

Figure II-11 - SRF-PLL dynamics.

The power converter is now synchronized to the grid. The next task consists of implementing a power control loop to allow a power exchange between both sources.

II.3.2 Grid current and power control

From the example presented in Figure II-1, it is possible to express the system dynamics in the synchronous reference frame with the following equations:

$$\frac{di_{g_d}}{dt} = \frac{\omega_b}{L_c} v_{m_d} - \frac{\omega_b}{L_c} v_{g_d} - \frac{R_c \omega_b}{L_c} i_{g_d} + \omega_g \omega_b i_{g_q} \tag{II-15}$$

$$\frac{di_{g_q}}{dt} = \frac{\omega_b}{L_c} v_{m_q} - \frac{\omega_b}{L_c} v_{g_q} - \frac{R_c \omega_b}{L_c} i_{g_q} - \omega_g \omega_b i_{g_d} \tag{II-16}$$

Conventionally, the control structure of such a system is derived from the model inversion principle, which leads to the following control scheme in Figure II-12.

In addition to the PI controllers, decoupling terms must be implemented to avoid a high transient coupling between i_{g_d} and i_{g_q}. As already mentioned, the aim is to ensure independent regulation of the active and reactive power. Usually, the grid current control for a high power VSCs applications is tuned to achieve its references in around 1-10ms. The control tuning method is similar to the one used for the SRF-PLL.

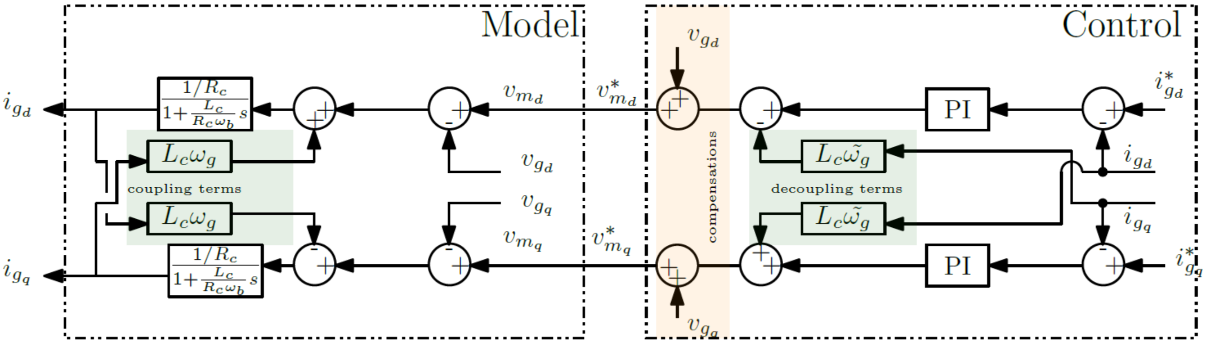

Figure II-12 - Grid-following control structure

The current references $i^*_{g_{dq}}$ in Figure II-12 can be provided by an outer power control loop. Thanks to the PLL, the grid voltage is assumed to always be aligned with the d-axis ($v_{g_q}=0$), the power control loop is defined from the following equations:

$$p_{ac}=v_{g_d}i_{g_d}+\underbrace{v_{g_q}i_{g_q}}_{\sim 0} \tag{II-17}$$

$$q_{ac}=-v_{g_d}i_{g_q}+\underbrace{v_{g_q}i_{g_d}}_{\sim 0} \tag{II-18}$$

By inverting (II-17) and (II-18), the reference $i^*_{g_d}$ and $i^*_{g_q}$ are deduced from active and reactive power references in Figure II-13.

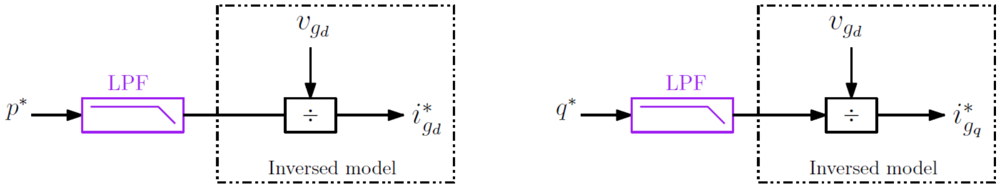

(a) (b)

Figure II-13 - Power controllers (a) Active power, (b) Reactive power.

A low-pass filter can be added to the power references in order to decouple the power response from the current response (ω_{LPF}=30rad/s equivalent to T_R^P=100 ms).

The controller performances are verified through time-domain simulations illustrated in Figure II-14.

- t=0 s, both active and reactive power references are set zero.
- t= 200 ms, a step on p^* = 0.5 p.u is applied.
- t= 600 ms, a step on q^* = 0.5 p.u is applied.

Note that the dynamic response of the system meets the specifications. Moreover, a perfect decoupling between active and reactive power is achieved.

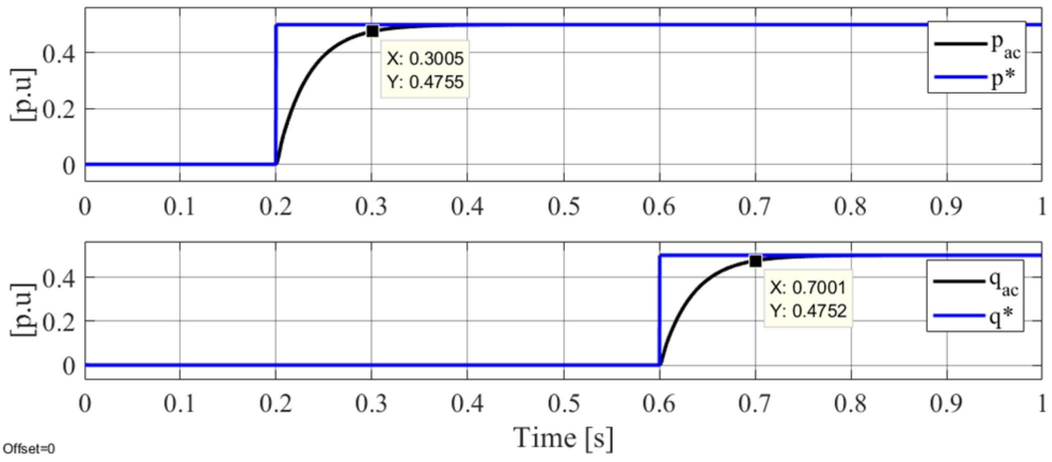

Figure II-14 - Time-domain simulation of grid-following control $(T_{5\%}^{R}=100ms)$.

Aside from the power control loops, other outer loops can be implemented to handle the needs of the AC and DC systems. These outer control structures are summarized in Figure II-15.

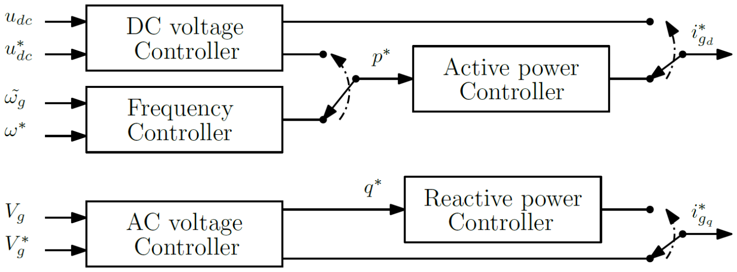

Figure II-15 - VSC outer controllers.

If a DC voltage controller is implemented, the active current injected to the AC grid is calculated in order to keep the DC voltage around its reference value u_{dc}^*. The DC voltage control is a mandatory task that should be handled at least by one of the power converters in AC/DC/AC conversion [112].

If the frequency and/or AC voltage controllers are implemented, power converters become interactive with the AC system. Hence, power converters adjust their active and reactive power or currents in order to maintain the grid frequency and voltage amplitude in an acceptable range [113], [114].

The VSC based on grid-following fulfils several functionalities in grid-connected mode and particularly when the AC grid is strong (SCR > 3). However, its operation in weak grid conditions remains one of its weakest attributes. In the next section a brief review on the static and dynamic limitations of grid-following converters in case of weak grids is recalled.

II.3.3 Grid-following control limitations under weak grids

The “weak grid” in a general context implies that the AC voltage at the point of common coupling is not stiffly constant. As already mentioned in section II.2.2, a grid is considered as weak when SCR < 3. In weak grid conditions, there are some challenges in using power converters based on grid-following control strategies [20],

[116], [117]–[119], starting with their failure to operate in full power ranges if no voltage management is considered. As it is well known, the weakness of the grid can induce some static limitations, which are independent of the type of control. First, the steady state equations of the electrical grid quantities described in Figure II-1 are derived:

$$0=\frac{\omega_b}{L_g}v_{g_d}-\frac{\omega_b}{L_g}v_{e_d}-\frac{R_g\omega_b}{L_g}i_{g_d}+\omega_g\omega_b i_{g_q} \tag{II-19}$$

$$0=\frac{\omega_b}{L_g}v_{g_q}-\frac{\omega_b}{L_g}v_{e_q}-\frac{R_g\omega_b}{L_g}i_{g_q}-\omega_g\omega_b i_{g_d} \tag{II-20}$$

$$0=\frac{\omega_b}{L_c}v_{m_d}-\frac{\omega_b}{L_c}v_{g_d}-\frac{R_c\omega_b}{L_c}i_{g_d}+\omega_g\omega_b i_{g_q} \tag{II-21}$$

$$0=\frac{\omega_b}{L_c}v_{m_q}-\frac{\omega_b}{L_c}v_{g_q}-\frac{R_c\omega_b}{L_c}i_{g_q}-\omega_g\omega_b i_{g_d} \tag{II-22}$$

The grid resistance can be neglected since X≫R. Moreover, as the AC voltage at PCC is aligned with the d-axis and the grid currents are equal to their references in steady state, (II-19) and (II-20) can be written,

$$0=\frac{\omega_b}{L_g}V_g-\frac{\omega_b}{L_g}v_{e_d}+\omega_g\omega_b i^*_{g_q} \tag{II-23}$$

$$0=-\frac{\omega_b}{L_g}v_{e_q}-\omega_g\omega_b i^*_{g_d} \tag{II-24}$$

Since the grid frequency ω_g is varying in a small range, it is assumed that ω_g =1 p.u. The current reference $i^*_{g_q}$ is set to zero for the demonstration. Based on these considerations and from (II-23) and (II-24),

$$V_g=v_{g_d}=\sqrt{V_e^2-\left(\omega_g L_g i^*_{g_d}\right)^2} \tag{II-25}$$

Based on (II-21), (II-22) and (II-25),

$$v_{m_d}=V_e \tag{II-26}$$

$$v_{m_q}=\omega_g L_c i^*_{g_d} \tag{II-27}$$

$$V_m=\sqrt{\left(v_{md}^2+v_{mq}^2\right)} \tag{II-28}$$

(II-25) and (II-28) demonstrate the dependency of the AC voltage magnitude on the converter current. Actually, an increase of the current i^*_{gd} results in a decrease of the voltage at PCC. Because of that, the active power cannot achieve its nominal value. This may have destabilizing side effect if an outer DC voltage control is implemented. Indeed, the system cannot inject the desired active power to maintain the DC voltage around its nominal value [115]. In order to transfer 1 p.u. of active power, the reactive power should be supplied to the grid. Therefore, an AC-voltage management is needed so the voltage at PCC recovers its nominal value.

In addition to static limitations, the dynamic aspects of grid-following converters should also be taken into account. Actually, in weak grid conditions, the system may become unstable because of many factors (i.e., SRF-PLL dynamics and their interactions with outer control loops). A retuning of the PLL, the outer voltage controller and the current controllers may increase a stability margin. However, this may lead to a slower dynamic response [119].

An illustrative example of the instability issue in weak grid situation is given in Figure II-17. The grid case is illustrated in Figure II-16:

- Case 1 (Figure II-17a): $SCR = [3,\ 1.2]$, T_R^{PLL} =50 ms, $k_v = [300,\ 80]$ p.u.
- Case 2 (Figure II-17b): $SCR = 1.2$, $T_R^{PLL} = [100,\ 50,\ 30]$ ms, $k_v = 80$ p.u.

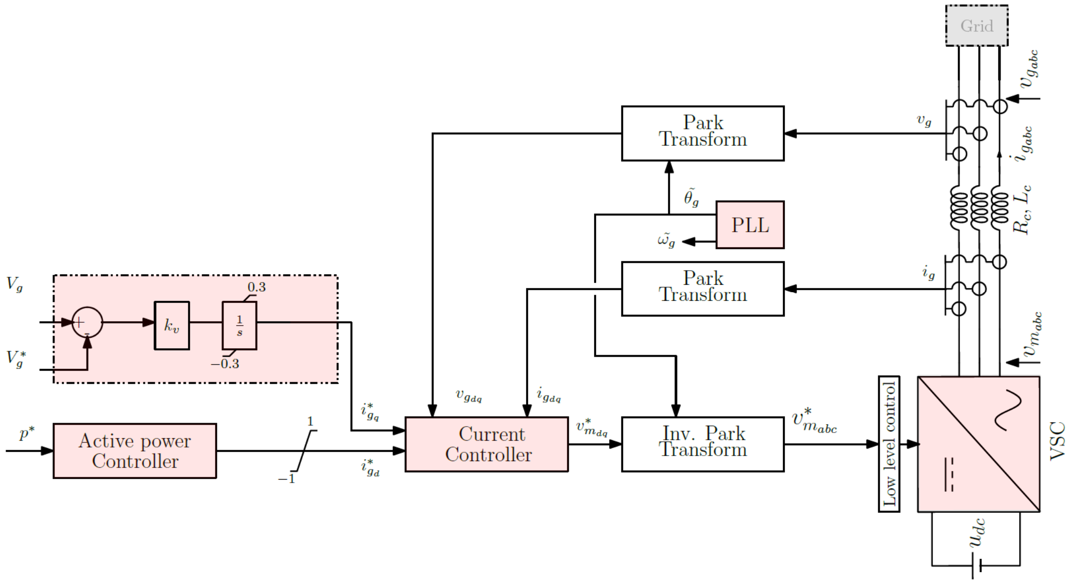

Figure II-16 - Grid-following control structure with various control configurations

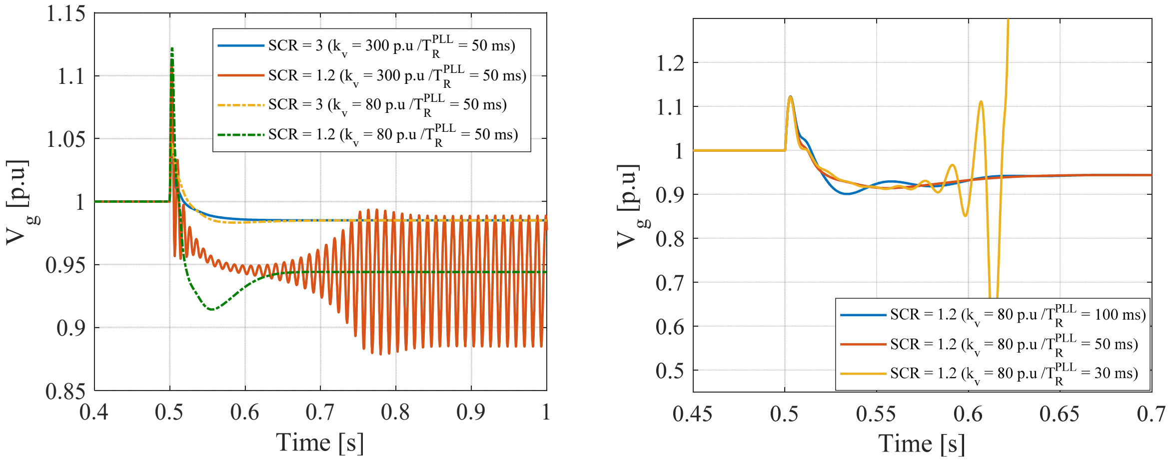

(a) Impact of AC voltage dynamics

(b) Impact of PLL dynamics

Figure II-17 - Instability phenomenon of the grid-following converter under very weak grid conditions

The results show the impact of the outer voltage loop and PLL dynamics on the system stability:

- A fast response of the voltage loop results in an oscillatory response (red curve).
- A slow, but reasonable voltage loop dynamics results in a stable system operation (green curve).
- A fast PLL dynamics leads to unstable system operation (yellow curve).

II.3.4 Summary

With the grid-following control, the grid current dynamics are fully controlled through the SRF-PLL and the inner current control loops. This leads to a fast control response of the system in case of a strong AC grid. Moreover, as the power converters are controlling the injected current directly, the converter safety against overcurrent is guaranteed. However, the grid-following control presents some drawbacks. It operates only in grid-connected mode. It may lead to small-signal instability issues and a lack of operation in full power range under weak grid conditions.

In the next section, a VSC based on grid-forming control is investigated starting with the AC voltage controlled-VSC modeling, control design, small-signal stability and robustness analysis.

II.4 Synchronization and power control based on grid-forming control

This section discusses the modeling and control aspects of the grid-forming control-based VSC. The phasor approach has been used in section II.2.3.1 to demonstrate the overall principle of the control. Some complementary features have to be added for the instantaneous control. The main concept of power exchange between AC sources is deepened. Then, the system control design is proposed, while considering the stability and robustness factors.

II.4.1 System Modeling

Continuing with the example from Figure II-1 and considering the AC grid as a stiff one $SCR = \infty$, two kinds of models can be computed (phasor or dynamic model). The behaviors of these models are compared in this section. In steady state, the imposed voltage is supposed to be balanced with a modulated frequency ω_m equal to ω_g.

II.4.1.1 Phasor modeling

The power converter is connected to the main grid through the impedance $Z_c^{\angle\phi_z}$. The power delivered to the grid through this impedance is expressed as follow:

$$S = \overline{V}_g \overline{I}^* = \frac{V_g^{\angle 0} V_m^{\angle\delta_m}}{Z_c^{\angle -\phi_z}} - \frac{V_g^{2\angle 0}}{Z_c^{\angle -\phi_z}} \qquad \text{(II-29)}$$

Since, $R_c = Z_c \cos\phi_Z$ and $L_c\omega_g = Z_c \sin\phi_Z$, the active and reactive power can be derived:

$$p_{ac} = \frac{V_g}{R_c^2 + X_c^2}\left[R_c\left(V_m \cos\left(\delta_m\right) - V_g\right) + X_c V_m \sin\left(\delta_m\right)\right] \tag{II-30}$$

$$q_{ac} = \frac{V_g}{R_c^2 + X_c^2}\left[-R_c V_m \sin\left(\delta_m\right) + X_c\left(V_g - V_m \cos\left(\delta_m\right)\right]\right. \tag{II-31}$$

The equations above show the link between the active and reactive powers (p_{ac}, q_{ac}), the voltage amplitudes V_g, V_m and the internal angle δ_m. In power transmission systems, the inductive component is higher than the resistive one (i.e. $L_c\omega_g \gg R_c$), therefore, R$_c$ can be neglected, which yields a well-known power expression already used in subsection II.2.3.1:

$$p_{ac} = \frac{V_m V_g}{L_c\omega_g}\sin\left(\delta_m\right) \tag{II-32}$$

$$q_{ac} = \frac{V_m\left(V_m - V_g \cos\left(\delta_m\right)\right)}{L_c\omega_g} \tag{II-33}$$

Considering the typical output value of the inductor $L_c\omega_g$ =0.15 p.u, and assuming a strong AC grid, the internal angle δ_m is kept sufficiently small $\delta_m \ll \pi/2$ (i.e.; the system operates in the linear area of the $p_{ac}(\delta_m)$ curve as depicted in Figure II-18) and the voltage amplitude difference remains small for all operating points. Referring to [20], the internal angle should be kept lower than $\delta_m \leq 30°$ so as the system operates in a linear area.

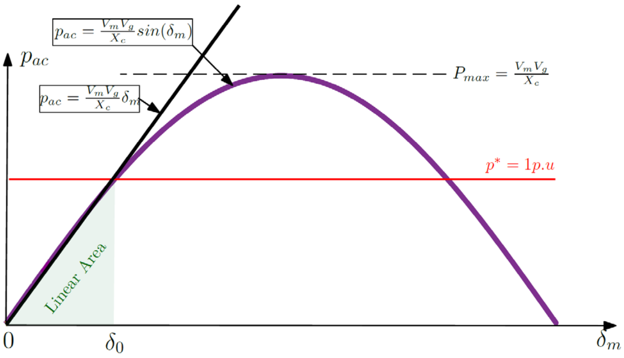

Figure II-18 - $p_{ac}(\delta_m)$ curve ($V_m = V_g = 1$ p.u)

From (II-32), (II-33) and the considering the system linearity, the simplified power expressions are obtained,

$$p_{ac} = \frac{V_m V_g}{L_c\omega_g}\delta_m \tag{II-34}$$

$$q_{ac} = \frac{V_m\left(V_m - V_g\right)}{L_c\omega_g} \tag{II-35}$$

As already explained, (II-34) and (II-35) show that the active power can be controlled through the internal angle and the reactive power through the AC voltage amplitudes. The static models are often used to analyze large power systems dominated by synchronous generators, where the power dynamics are slow. However, in power system dominated by power converters, the static models may hide some fast dynamics that affect the system performances and stability. Hence, a dynamic modeling is required.

II.4.1.2 Dynamic modeling

The dynamic model is developed in the synchronous rotating reference frame *d-q* with the d-axis chosen aligned with the AC grid voltage v_g . To put the whole system in the same control frame, the direct and quadratic parts of the converter voltage can be expressed as,

$$v_{m_d} = V_m cos(\delta_m) \tag{II-36}$$

$$v_{m_q} = V_m sin(\delta_m) \tag{II-37}$$

As a consequence, the grid current dynamics are expressed as,

$$\frac{d}{dt} i_{g_d} = \frac{\omega_b}{L_c} V_m \cos(\delta_m) - \frac{\omega_b}{L_c} V_g - \frac{R_c \omega_b}{L_c} i_{g_d} + \omega_g \omega_b i_{g_q} \tag{II-38}$$

$$\frac{d}{dt} i_{g_q} = \frac{\omega_b}{L_c} V_m \sin(\delta_m) - \frac{R_c \omega_b}{L_c} i_{g_q} - \omega_g \omega_b i_{g_d} \tag{II-39}$$

(II-38) and (II-39) are nonlinear because of the terms $\omega_g i_{g_{dq}}$, $V_m \cos(\delta_m)$ and $V_m \sin(\delta_m)$. Since the grid frequency ω_g is varying in a small range, these variations can be neglected (i.e.; $\omega_g = \omega_0 = 1$ p.u). The linear expressions of $V_m \cos(\delta_m)$ and $V_m \sin(\delta_m)$ around an operating point x_0 are given by:

$$V_m \cos(\delta_m) = -V_{m0} \sin(\delta_{m0}) \Delta\delta_m + \Delta V_m \cos(\delta_{m0}) \tag{II-40}$$

$$V_m \sin(\delta_m) = V_{m0} \cos(\delta_{m0}) \Delta\delta_m + \Delta V_m \sin(\delta_{m0}) \tag{II-41}$$

where, “Δ” and “0” denote the small derivation and the initial value, respectively.

The linear formulas of the active and reactive power from the converter side are expressed as,

$$\Delta p_{ac} = \Delta v_{m_d} i_{g_{d0}} + v_{m_{d0}} \Delta i_{g_d} + \Delta v_{m_q} i_{g_{q0}} + v_{m_{q0}} \Delta i_{g_q} \tag{II-42}$$

$$\Delta q_{ac} = \Delta v_{m_d} i_{g_{q0}} + v_{m_{d0}} \Delta i_{g_q} - \Delta v_{m_q} i_{g_{d0}} - v_{m_{q0}} \Delta i_{g_d} \tag{II-43}$$

From (II-40 - II-43) and the development in Appendix B, the active power and the reactive power are obtained in Laplace domain,

$$\begin{bmatrix}\Delta p_{ac}(s)\\ \Delta q_{ac}(s)\end{bmatrix}=\begin{bmatrix}T_{p\delta} & T_{pV}\\ T_{q\delta} & T_{qV}\end{bmatrix}\begin{bmatrix}\Delta\delta_m(s)\\ \Delta V_m(s)\end{bmatrix} \tag{II-44}$$

$$T_{p\delta}=\frac{\begin{gathered}\left[\frac{V_{m0}\left(\frac{L_c}{\omega_b}\right)^2\left(V_g\left(R_c\sin\left(\delta_{m0}\right)+L_c\omega_g\cos\left(\delta_{m0}\right)\right)-V_{m0}L_c\omega_g\right)}{\left(R_c\right)^2+\left(\omega_gL_c\right)^2}\right]s^2+\left[\frac{2R_c\frac{L_c}{\omega_b}V_{m0}\left(V_g\left(R_c\sin\left(\delta_{m0}\right)+L_c\omega_g\cos\left(\delta_{m0}\right)\right)-V_{m0}L_c\omega_g\right)}{\left(R_c\right)^2+\left(\omega_gL_c\right)^2}\right]s+\ldots\\ V_{m0}V_g\left(R_c\sin\left(\delta_{m0}\right)+L_c\omega_g\cos\left(\delta_{m0}\right)\right)\end{gathered}}{\left(\frac{L_c}{\omega_b}s+R_c\right)^2+\left(\omega_gL_c\right)^2} \tag{II-45}$$

$$T_{pV}=\frac{\begin{gathered}\left[\frac{V_{m0}\left(\frac{L_c}{\omega_b}\right)^2\left(V_g\left(-R_c\cos\left(\delta_{m0}\right)+L_c\omega_g\sin\left(\delta_{m0}\right)\right)+R_c\right)}{\left(R_c\right)^2+\left(\omega_gL_c\right)^2}\right]s^2+\left[\frac{2R_c\frac{L_c}{\omega_b}\left(V_g\left(-R_c\cos\left(\delta_{m0}\right)+L_c\omega_g\sin\left(\delta_{m0}\right)\right)\right)}{\left(R_c\right)^2+\left(\omega_gL_c\right)^2}+V_{m0}L_c/\omega_b\right]s+\ldots\\ 2R_cV_{m0}+V_g\left(-R_c\cos\left(\delta_{m0}\right)+L_c\omega_g\sin\left(\delta_{m0}\right)\right)\end{gathered}}{\left(\frac{L_c}{\omega_b}s+R_c\right)^2+\left(\omega_gL_c\right)^2} \tag{II-46}$$

$$T_{q\delta}=\frac{\begin{gathered}\left[\frac{V_{m0}\left(\frac{L_c}{\omega_b}\right)^2\left(V_g\left(-R_c\cos\left(\delta_{m0}\right)+L_c\omega_g\sin\left(\delta_{m0}\right)\right)+V_{m0}R_c\right)}{\left(R_c\right)^2+\left(\omega_gL_c\right)^2}\right]s^2+\left[\frac{2R_c\frac{L_c}{\omega_b}V_{m0}\left(V_g\left(-R_c\cos\left(\delta_{m0}\right)+L_c\omega_g\sin\left(\delta_{m0}\right)\right)+V_{m0}R_c\right)}{\left(R_c\right)^2+\left(\omega_gL_c\right)^2}+V_{m0}{}^2L_c/\omega_b\right]s+\ldots\\ V_{m0}V_g\left(R_c\cos\left(\delta_{m0}\right)+L_c\omega_g\sin\left(\delta_{m0}\right)\right)\end{gathered}}{\left(\frac{L_c}{\omega_b}s+R_c\right)^2+\left(\omega_gL_c\right)^2} \tag{II-47}$$

$$T_{qV}=\frac{\begin{gathered}\left[\frac{\left(\frac{L_c}{\omega_b}\right)^2\left(-V_g\left(R_c\sin\left(\delta_{m0}\right)+L_c\omega_g\cos\left(\delta_{m0}\right)\right)+V_{m0}R_c\right)}{\left(R_c\right)^2+\left(\omega_gL_c\right)^2}\right]s^2+\left[\frac{2R_c\frac{L_c}{\omega_b}\left(-V_g\left(R_c\cos\left(\delta_{m0}\right)+L_c\omega_g\sin\left(\delta_{m0}\right)\right)+V_{m0}L_c\omega_g\right)}{\left(R_c\right)^2+\left(\omega_gL_c\right)^2}\right]s-\ldots\\ V_g\left(R_c\sin\left(\delta_{m0}\right)+L_c\omega_g\cos\left(\delta_{m0}\right)\right)+V_{m0}L_c\omega_g\end{gathered}}{\left(\frac{L_c}{\omega_b}s+R_c\right)^2+\left(\omega_gL_c\right)^2} \tag{II-48}$$

The linearized model in (II-44) has been validated through a comparison between the static and nonlinear dynamic models. As shown in Figure II-19, a step on $\Delta\delta_m = 0.15$ rad is applied to the system at t= 1 s. The initial active power transmitted between AC sources is set to $p_{ac0} = 0$ p.u.

From (II-44) and the obtained results in Figure II-19, some remarks can be drawn,

- In steady state, by neglecting the effect of the resistor R_c, the following matrix of static transfer functions is obtained,

$$\begin{bmatrix}\Delta p_{ac}(s\sim 0)\\ \Delta q_{ac}(s\sim 0)\end{bmatrix}=\begin{bmatrix}\frac{V_{m0}V_g}{L_c\omega_g}\cos\left(\delta_{m0}\right) & \frac{V_g}{L_c\omega_g}\sin\left(\delta_{m0}\right)\\ \frac{V_{m0}V_g}{L_c\omega_g}\sin\left(\delta_{m0}\right) & \frac{V_{m0}-V_g\cos\left(\delta_{m0}\right)}{L_c\omega_g}\end{bmatrix}\begin{bmatrix}\Delta\delta_m\\ \Delta V_m\end{bmatrix} \tag{II-49}$$

  The diagonal part of the matrix above is equal to the static equations in (II-34) and (II-35). The non-diagonal part presents the coupling transfer functions between active and reactive power. In steady state and for a strong grid, the non-diagonal matrix is negligible.

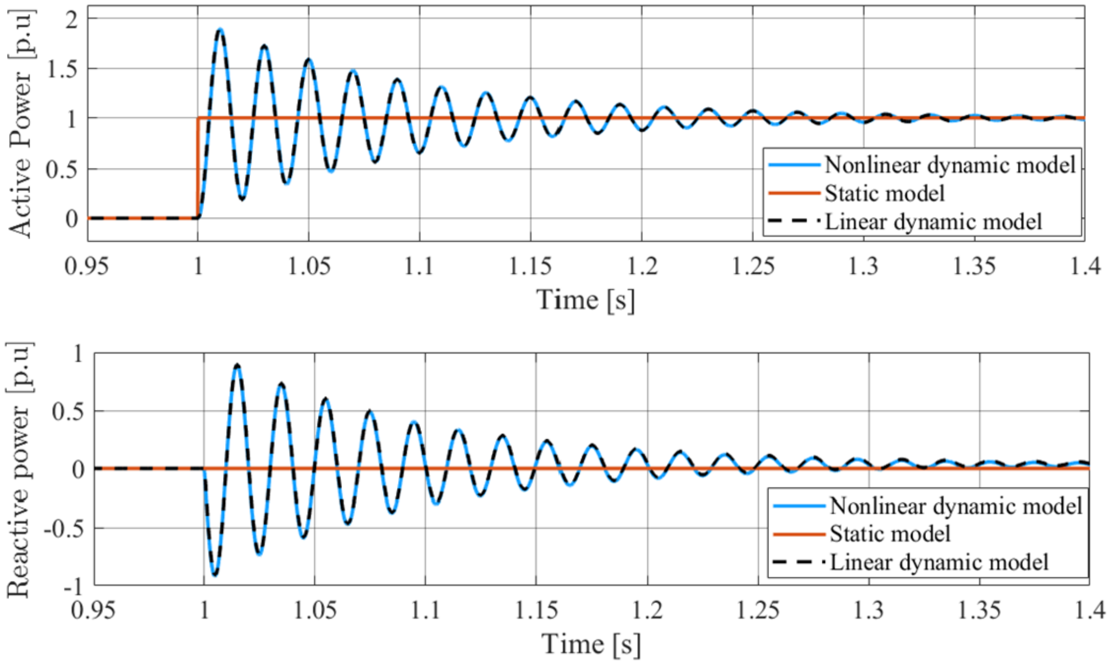

Figure II-19 - Comparison between, static, nonlinear dynamic and linearized dynamic model.

- The dynamic transfer functions in (II-44) have two resonant poles expressed as following,

$$s_{1-2} = \underbrace{-\frac{R_c}{L_c}\omega_b}_{\Re} \pm \underbrace{j\omega_g\omega_b}_{\Im} \tag{II-50}$$

These two poles are linked to the grid current dynamics $i_{g_{dq}}$. The damping of $\zeta_{s_{1-2}}$ depends mainly on L_c, R_c as shown in (II-51),

$$\zeta_{s_{1-2}} = \frac{\Re}{\sqrt{\Re^2 + \Im^2}} = \frac{R_c}{\sqrt{R_c^2 + \left(L_c\omega_g^2\right)}} \tag{II-51}$$

Using typical parameters of Table II-2, the damping of s_{1-2} is very small as illustrated through time-domain simulations in Figure II-19. From (II-51), the damping of s_{1-2} can be improved by decreasing L_c or by increasing R_c. The improvement of the damping of the resonant poles will be further discussed in the next subsection.

- During the transient, Figure II-19 shows a transient coupling between active and reactive power due to the non-diagonal transfer functions. The transient power coupling becomes higher when the system operates around the resonance frequency ω_b as shown in Figure II-20.
- (II-44) has two zeros expressed in (II-52): The zeros computation of a square transfer function is given in [120].

$$z_{1-2} = \pm\omega_g\omega_b\sqrt{\cos\delta_{m0} / \left(\frac{V_g}{V_{m0}} - \cos\delta_{m0}\right)} \tag{II-52}$$

From (II-52), one can notice that the system has two symmetrical zeros, one on the Left-Half Plan (LHP) and the second one on the Right-Half Plan (RHP). The LHP zero induces a faster system response and increases the overshoot. It can be easily compensated by the addition of poles, while, the RHP zero cannot be compensated by additional poles since the system will lead to instability. The RHP zeros introduce a time delay on the system and undershoot, which imposes a fundamental limitation on the achievable bandwidth of the feedback control. In control theory, the system with RHP zeros is called a non-minimum phase system.

The location of the RHP zeros depends mainly on the operating point (i.e.; initial voltages amplitude V_g / V_{m0} and the internal angle δ_{m0}). When the RHP zeros reach the origin $z_{1\text{-}2}$, this implies that $\delta_{m0} = \pm\dfrac{\pi}{2}$ as proved in (II-53).

$$z_{1-2} = \pm\omega_g\omega_b\sqrt{\frac{\cos\delta_{m0}}{V_g / V_{m0} - \cos\delta_{m0}}} = 0\Bigg|_{\delta_{m0}=\pm\pi/2} \tag{II-53}$$

- The weak grid is the situation where the RHP zero may reach the origin. Therefore, its effect condition is more significant because of the high impedance between AC sources.

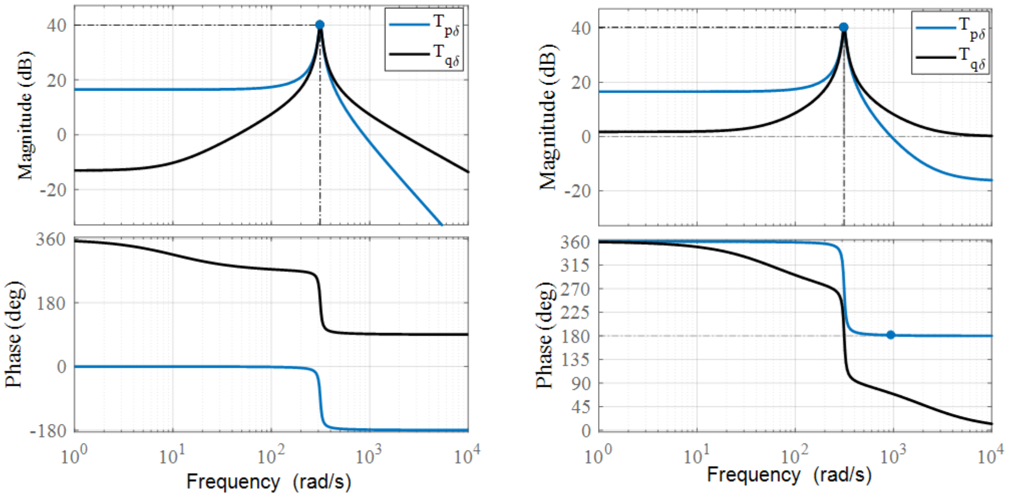

(a) (b)

Figure II-20 - Frequency response of $T_{p\delta}$ and $T_{q\delta}$ at two different operating point, (a) $p_{ac} = 0$ p.u, (b) $p_{ac} = 1$ p.u.

II.4.2 Grid current dynamics enhancement based on a TVR

As explained previously, the oscillatory modes s_{1-2} are directly linked to the impedance Z_c. A solution to damp these poles is to increase the value of R_c by adding a resistor R_V. For some efficiency reason, it is not recommended to add a real resistor in the circuit. However, the controller can be adapted to emulate a virtual resistor R_v (VR) [22], [121].

The overall idea is to adjust the voltage reference of the converter with respect to the grid current. The voltage references $v^*_{m_{dq}}$ are modified to take into account the VR:

$$v^*_{m_d} = v^{*\prime}_{m_d} - R_v i_{dg} \tag{II-54}$$

$$v^*_{m_q} = v^{*\prime}_{m_q} - R_v i_{qg} \tag{II-55}$$

Emulating a resistor effect with the control is supposed to measure the current, while the current sensor dynamics have been neglected in the following analysis. Hence, the original grid dynamic equations are modified:

$$\frac{di_{g_d}}{dt} = \frac{\omega_b}{L_c} v^{*\prime}_{m_d} - \frac{\omega_b}{L_c} V_g - \frac{(R_c + R_V)\omega_b}{L_c} i_{g_d} - \omega_g \omega_b i_{g_q} \tag{II-56}$$

$$\frac{di_{g_q}}{dt} = \frac{\omega_b}{L_c} v^{*\prime}_{m_q} - \frac{(R_c + R_V)\omega_b}{L_c} i_{g_q} + \omega_g \omega_b i_{g_d} \tag{II-57}$$

From (II-56) and (II-57), the new system modes are obtained;

$$s_{1-2} = \underbrace{-\frac{R_c + R_V}{L_c}\omega_b}_{\Re} \pm \underbrace{j\omega_g \omega_b}_{\Im} \tag{II-58}$$

Depending on the desired damping $\zeta_{s_{1-2}}$, the value of R_V is obtained,

$$R_V = \frac{\zeta_{s_{1-2}} (L_c \omega_g)}{\sqrt{1 - \zeta^2_{s_{1-2}}}} - R_c \tag{II-59}$$

The following damping has been chosen $\zeta_{s_{1\text{-}2}}$ =0.5. It corresponds to $R_V = 0.09$ p.u.

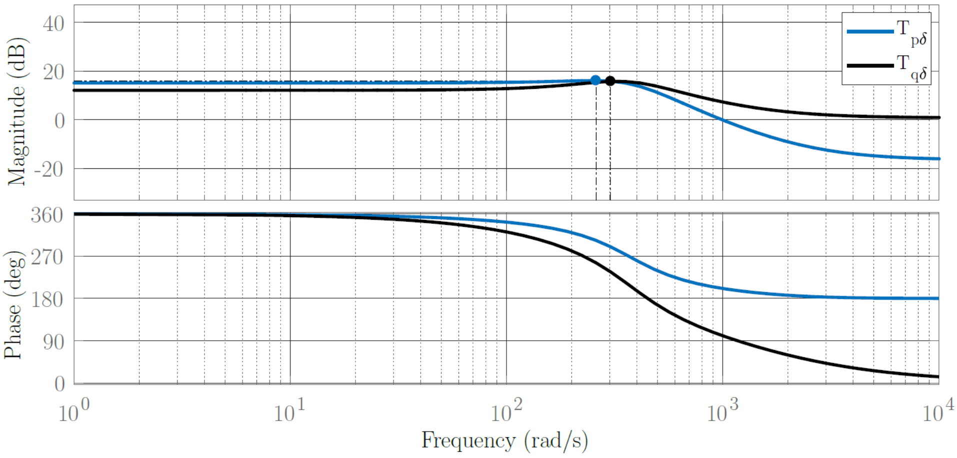

Figure II-21 - Frequency response of $T_{p\delta}$ and $T_{q\delta}$ with VR

It is clear from Figure II-21 that the damping of the system has been widely improved by introducing a virtual resistor. However, inasmuch as the AC voltage amplitude of the converter is modified with respect to the grid current, and the X_c / R_c ratio becomes much smaller than ($X_c / R_c \ll 10$), the magnitude of both $T_{p\delta}(s \sim 0)$ and $T_{q\delta}(s \sim 0)$ at low frequencies have been changed, and thereby, results in an important steady state coupling between active and reactive power.

To avoid the impact of the virtual resistor at low-frequencies, a derivative action is introduced. The filter structure in Figure II-22 allows the virtual resistor to only act during the transient. The filter bandwidth ω_{TVR} should be chosen to cover the frequency range of all the possible resonances in AC systems [121] e.g.; $\omega_b /5$.

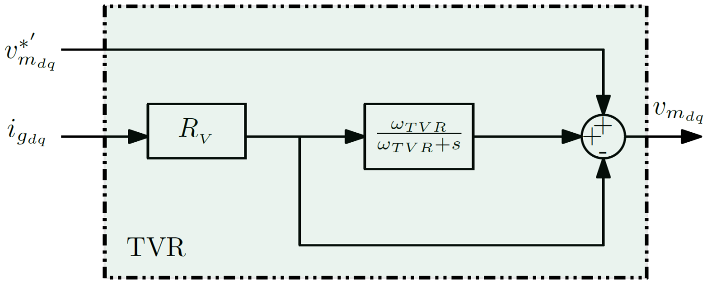

Figure II-22 - Transient virtual resistor (TVR)

The effectiveness of the transient virtual resistor is shown in Figure II-23, where the system is well damped and presents a negligible steady state power coupling.

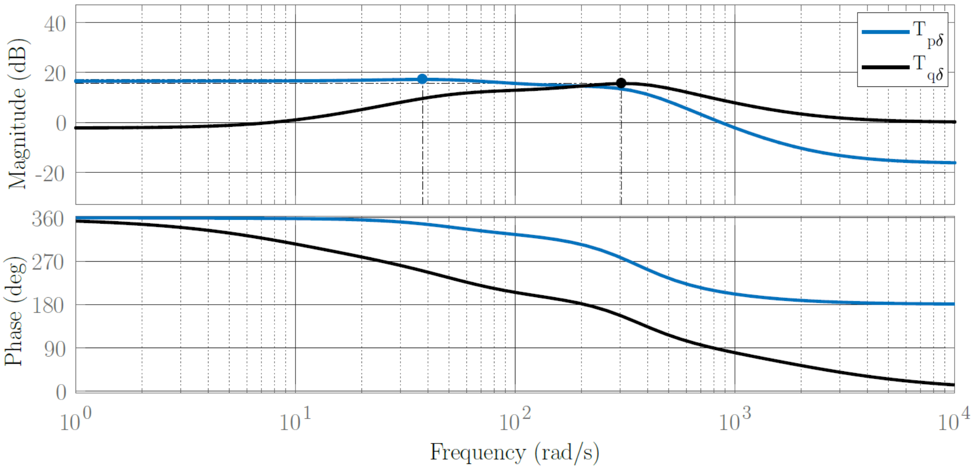

Figure II-23 - Frequency response of $T_{p\delta}$ and $T_{q\delta}$ with TVR

The TVR performances are demonstrated also through the time-domain simulations in Figure II-24. The same test case performed in Figure II-19 is applied while keeping the same scales:

- t=0 s, both active and reactive power references are set zero.
- t= 1 s, a step on $\Delta\delta_m$=0.15 rad is applied.

Compared to the results obtained in Figure II-19, note that the dynamic response of the system is widely improved. Moreover, the dynamic model with the TVR becomes closer to the static model in the frequency range of $\omega \leq$ 10 rad/s. In the next section, the active power control design is made in this frequency range of $\omega \leq$ 10 rad/s, and thus, the static model will be enough to tune the power controller.

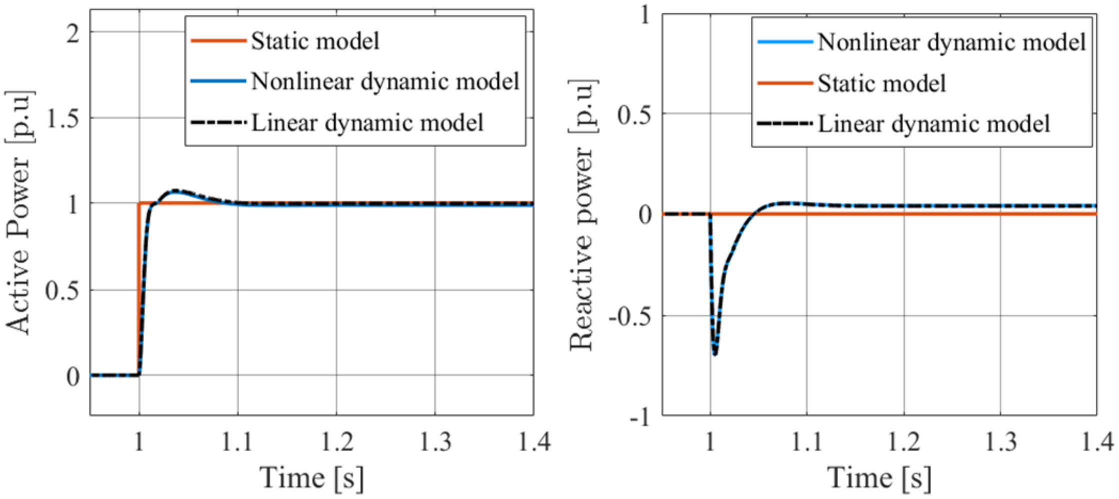

Figure II-24 - Grid current dynamics enhancement using the transient virtual resistor

II.4.3 Active power regulation

II.4.3.1 Design of the active power control

As mentioned in section II.2.3.3, in steady-state, the active power exchange is directly linked to the angle between both AC voltages. The aim of this section is to choose the type of regulator to control the angle and explain its design.

The power control structure is presented in Figure II-25.

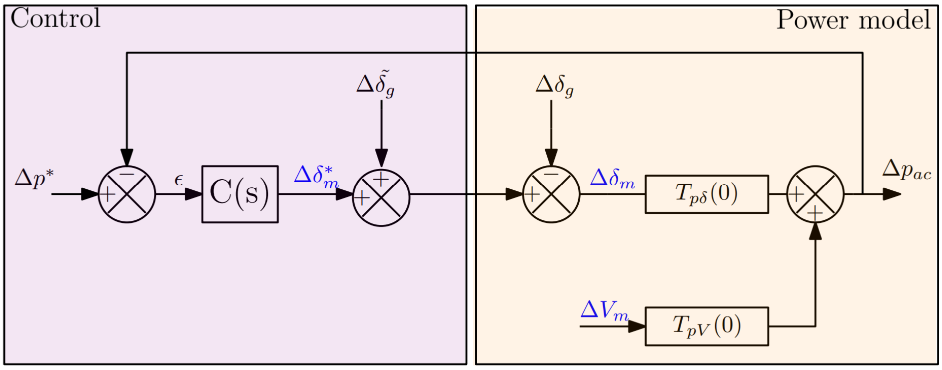

Figure II-25 - Partial model of a converter with a grid-forming control

To cancel the active power error in the steady state, a simple Integral-Controller $C(s) = k_i / s$ is needed. The compensation of the grid angle disturbance is not mandatory. Nevertheless, its use allows achieving higher dynamics performances in terms of active power setpoint tracking. Therefore, the grid angle compensation is adopted in the rest of this chapter.

From the block diagram in Figure II-25, the closed-loop transfer function is written as:

$$\Delta p_{ac} = \frac{1}{1+\dfrac{s}{k_i T_{p\delta}(0)}}\Delta p^* + \underbrace{\frac{\dfrac{s}{k_i}}{1+\dfrac{s}{k_i T_{p\delta}(0)}}\left(\Delta\widetilde{\delta_g} - \Delta\delta_g\right)}_{\sim 0} + \underbrace{\frac{\dfrac{T_{pV}(0)}{T_{p\delta}(0)k_i}s}{1+\dfrac{s}{k_i T_{p\delta}(0)}}\Delta V_m}_{\sim 0} \tag{II-60}$$

Considering a perfect estimation of $\Delta\tilde{\delta}_g$ and neglecting the static coupling transfer function $T_{qV}(0)$ found in (II-49), (II-60) can be simplified:

$$\Delta p_{ac} = \frac{1}{1+\dfrac{s}{k_i T_{p\delta}(0)}}\Delta p^* \tag{II-61}$$

The system time constant is expressed with respect to the controller gain k_i and the system parameters V_m, V_g and $L_c\omega_g$:

$$\tau = \frac{L_c\omega_g}{k_i V_m V_g} \tag{II-62}$$

In the following subsection, the design of the controller gain k_i is presented, while considering a trade-off between the active power dynamics and the transient decoupling between active and reactive power.

II.4.3.2 Transient power decoupling

Transient power decoupling for multi-inputs multi-outputs (MIMO) systems is feasible through the design of complex decoupling controllers [120]. The aim of such control structures is to ensure a fast system response in all frequency ranges. However, because of power system parametric uncertainties, a perfect power decoupling is not possible. In power transmission systems, active and reactive power dynamics are not quite fast enough (i.e., a hundred milliseconds for active power and a few seconds for reactive power), which allows the system to operate in low frequency ranges. Based on that, the power decoupling can be achieved only through an appropriate controller design. It is recalled from Figure II-23 that a transient power decoupling is achievable when the system operates in frequency ranges lower than 10 rad/s. Based on that, the time constant of the power controller is chosen such as:

$$\tau = 100\,ms \tag{II-63}$$

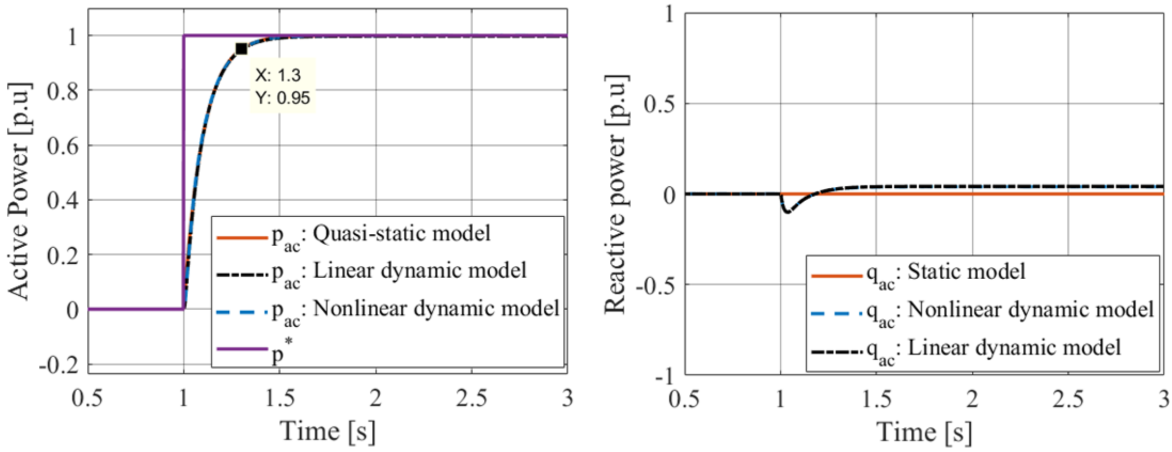

Figure II-26 - Time-domain simulation of a grid-forming active power control

The results of the active power control are gathered in Figure II-26, where it can be noticed that the quasi-static and dynamic models behave in a similar way. The coupling between active and reactive power is quite small as expected. Moreover, the specification imposed in terms of response time $T^{R}_{5\%} = 300$ ms is respected.

II.4.3.3 Active power filtering and its impact on the system dynamics

The real power measurement p_{ac} may contain unwanted noise and harmonics. Therefore, a low-pass filter is often used to avoid such disturbances as depicted in Figure II-27. It allows limiting the fast angle variations [79], filtering the frequencies at 2ω in the case of unbalanced conditions [122] and taking into account sensors delay [123].

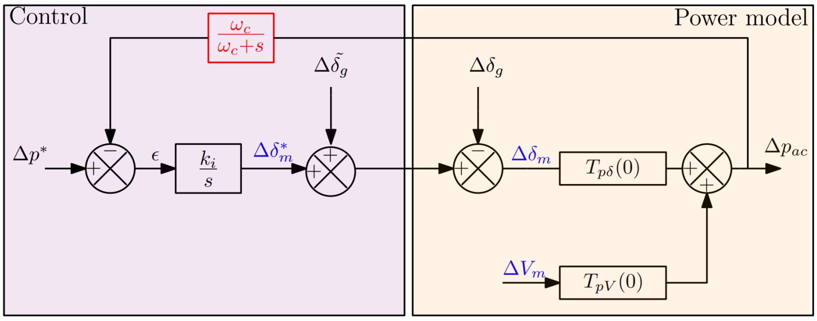

Figure II-27 - Active power feedback control including a low-pass filter

The purpose of this subsection is to study the impact of the low-pass filter and its position on the behavior of the system.

From the block diagram of Figure II-27, the closed-loop transfer function is expressed as,

$$\Delta p_{ac} = \frac{1+\dfrac{s}{\omega_c}}{1+\dfrac{1}{k_i T_{p\delta}(0)}s+\dfrac{1}{k_i T_{p\delta}(0)\,\omega_c}s^2}\Delta p^* \tag{II-64}$$

The transfer function is a 2nd order one. ζ and ω_n are expressed as,

$$\zeta = \frac{1}{2}\sqrt{\frac{L_c \omega_g \omega_c}{k_i V_m V_g}}, \qquad \omega_n = \sqrt{\frac{k_i V_m V_g \omega_c}{L_c \omega_g}} \tag{II-65}$$

From, (II-64) and (II-65), the following remarks are drawn,

- The system contains an LHP zero that depends mainly on the cut-off frequency ω_c. If the value of ω_c is very small, it increases the system rise time and induces overshoots.
- A small value of ω_c reduces also, the system damping and increases its response time, resulting in oscillations and overshoots.

The effect of the low-pass filter is illustrated in Figure II-28, where three values of cut-off frequency have been taken $\omega_c = \left[\dfrac{\omega_b}{10},\dfrac{\omega_b}{20},\dfrac{\omega_b}{30}\right]$.

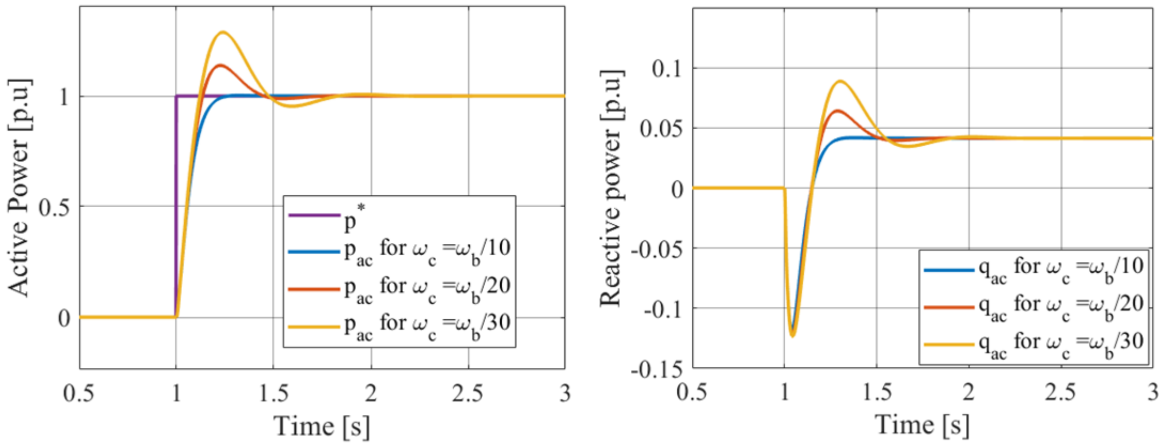

Figure II-28 - Impact of a low-pass filter introduced on the measured active power.

The zero effect could easily be compensated by introducing the low pass-filer after the comparator instead of the measured active power (see Figure II-29).

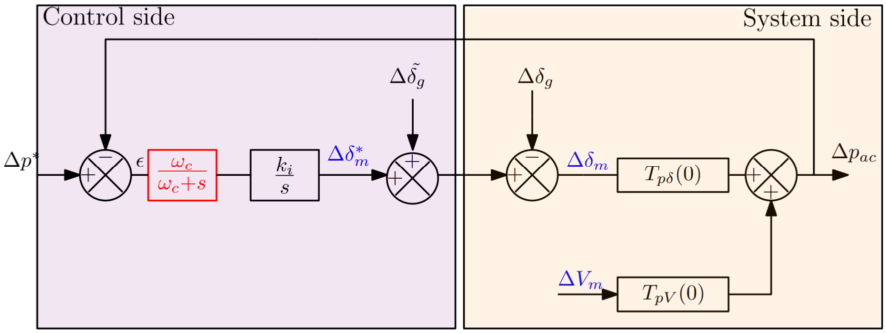

Figure II-29 - Active power feedback control including a low-pass filter

Based on the block diagram Figure II-29, the equation (II-64) is modified, and thereby, new transfer function without zero effect is deduced,

$$\Delta p_{ac} = \frac{1}{1+\dfrac{1}{k_i T_{p\delta}(0)}s+\dfrac{1}{k_i T_{p\delta}(0)\,\omega_c}s^2}\Delta p^* \tag{II-66}$$

The active and reactive power dynamics are shown in Figure II-30.

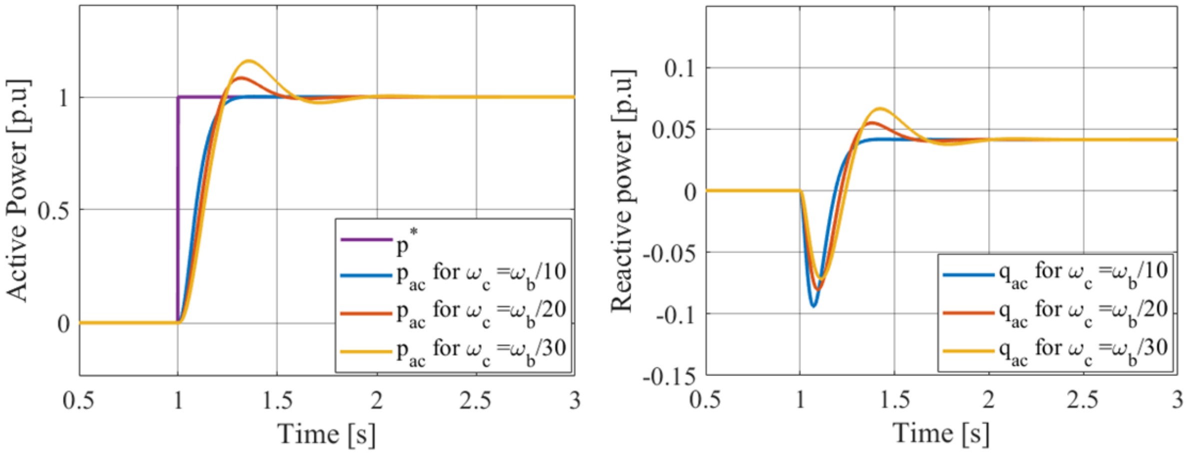

Figure II-30 - Impact of the low-pass filter position.

Compared to Figure II-28, it is possible to see that the active power overshoot caused by the LHP zero is significantly reduced. Moreover, since the LHP zero is compensated, the rise time of the active power is decreased resulting in a small power coupling.

In the next sections, the low-pass filter cut-off frequency will be set to $\omega_c = \omega_b/10$.

II.4.3.4 Study of the influence of the grid angle estimation on the system dynamics and robustness

The grid angle estimation for power converters is done through the SRF-PLL introduced in section II.3.1. The SRF-PLL can never estimate instantaneously the grid angle, but after a brief delay. Hence, this section deals with the impact of the SRF-PLL based grid-forming converter on the system stability, strength and dynamics under different SCR values.

A small-signal modeling (i.e.; Linearization) is used to analyze the eigenvalues trajectory and their characteristics. To build a state-space model, the converter side is decoupled from the grid side through the insertion of a small decoupling capacitor $C_D =$ 0.005 p.u (see Figure II-31).

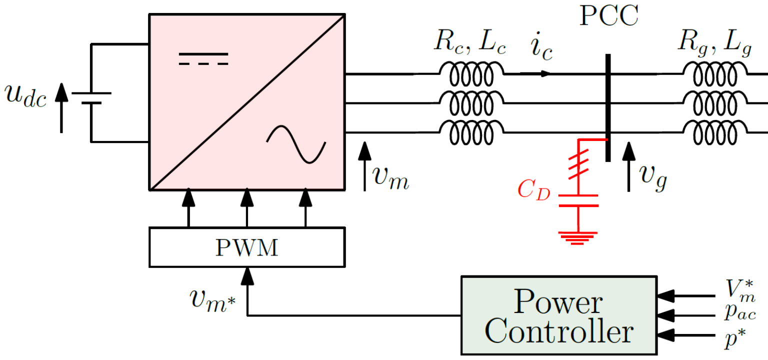

Figure II-31 - Studied system with dissociation between VSC and AC grid sides.

The nonlinear state-space model of the system including its control is given by,

$$\begin{bmatrix} \dot{x}_1 \\ \dot{x}_2 \end{bmatrix} = \begin{bmatrix} A_{11} & A_{12} \\ A_{21} & A_{22} \end{bmatrix}_{(x_i, u_j)} \begin{bmatrix} x_1 \\ x_2 \end{bmatrix} + \begin{bmatrix} B_{11} \\ B_{12} \end{bmatrix}_{(x_i, u_j)} \begin{bmatrix} u_1 \\ u_2 \end{bmatrix} \tag{II-67}$$

Where x_i and u_j are the system state variables and inputs, respectively.

$$x_i = \left[\underbrace{i_{c_d}\; i_{c_q}\; i_{g_d}\; i_{g_d}\; v_{g_d}\; v_{g_q}}_{x_1}\; \underbrace{\zeta_{PLL}\; \delta_{PLL}\; \epsilon_{p_{ac}}\; \delta_m\; \zeta_{TVR_d}\; \zeta_{TVR_q}}_{x_2} \right],\; u_j = [v_{e_d}\; v_{e_q}\; p^*\; v_{m_d}\; v_{m_q}] \tag{II-68}$$

ζ_{PLL} and δ_{PLL} are the PLL controller dynamics

$\epsilon_{p_{ac}}$ and δ_m are the low-pass filter and power controller dynamics, respectively.

ζ_{TVR_d} and ζ_{TVR_q} are the TVR dynamics.

A_{ii} and B_{ij} are the control matrix, The studied system contains nonlinearities due to the PLL and power control. Its response can be approximated around a given operating point through a linearized model.

The linear state-space matrices in (II-69) are given in Appendix C.

$$\begin{bmatrix} \dot{\Delta x_1} \\ \dot{\Delta x_2} \end{bmatrix} = \begin{bmatrix} A_{11} & A_{12} \\ A_{21} & A_{22} \end{bmatrix}_{(x_0,u_0)} \begin{bmatrix} \Delta x_1 \\ \Delta x_2 \end{bmatrix} + \begin{bmatrix} B_{11} \\ B_{12} \end{bmatrix}_{(x_0,u_0)} \begin{bmatrix} \Delta u_1 \\ \Delta u_2 \end{bmatrix} \tag{II-69}$$

In Figure II-32, the resulting linear model is compared against the nonlinear model and the simplified model in (II-66) through time-domain simulations.

- t=1 s, a power reference change of $p^* = 0.2$ p.u is applied.
- t=2 s, a power reference change of $p^* = -0.4$ p.u is applied.

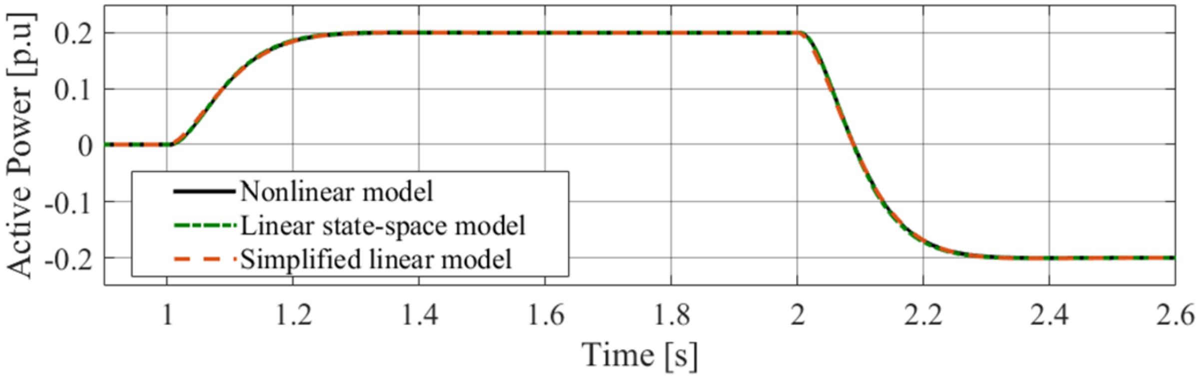

Figure II-32 - Linear state space model validation (SCR = 10 and $T_R^{PLL} = 10ms$)

In case of SCR = 10 and $T_R^{PLL} =$ 10 ms, the linearized state-space model and the simplified model in (II-66) are of high accuracy.

Indeed, the simplified model in (II-66) is independent of the SCR variation, but, it assumes a fast grid angle estimation so as $\delta_m = \tilde{\delta}_m$.

In the rest of this subsection:

- The stability of the system is assessed based on different values of the SCR and T_R^{PLL}.
- The validity and limitations of the simplified model are assessed by comparing it to the linear state-space model in the same conditions.

Let's recall first the static limitation on the active power. From (II-34), the system can operate over the full power range if the maximum impedance respects the following condition,

$$L_g \omega_g \leq \frac{V_m V_E}{p_{ac_n}} \sin(\delta_{\max}) - L_c \omega_g \tag{II-70}$$

where p_{ac_n} and δ_{max} denote the nominal active power delivered by the power converter (p_{ac_n} =1 p.u) corresponding to the maximum angle that ensures a small-signal stability ($\delta_{max} = \pm\pi/2$). From (II-70), the minimum value of the SCR is obtained,

$$SCR_{\min} = \frac{p_{ac_n}}{V_m V_e \sin\left(\delta_{\max}\right) - p_{ac_n} L_c \omega_g} \sim 1.2 \qquad \text{(II-71)}$$

The obtained value in the formula (II-71) assumes that both AC voltages are controlled around their nominal values $V_m = V_e = 1$ p.u. Otherwise, the minimum value of the SCR changes as well. Underneath this value, the power converter cannot achieve the nominal power, which leads to instability.

In Figure II-33, the evolution of the eigenvalues is drawn based on three different response times of the PLL (T_R^{PLL}=10 ms, T_R^{PLL}=50 ms, T_R^{PLL}=100 ms). The applied scenario aims to vary the SCR from "Strong grid SCR = 3" to "Very weak grid $SCR_{\min}$ = 1.2" for a unitary operating point.

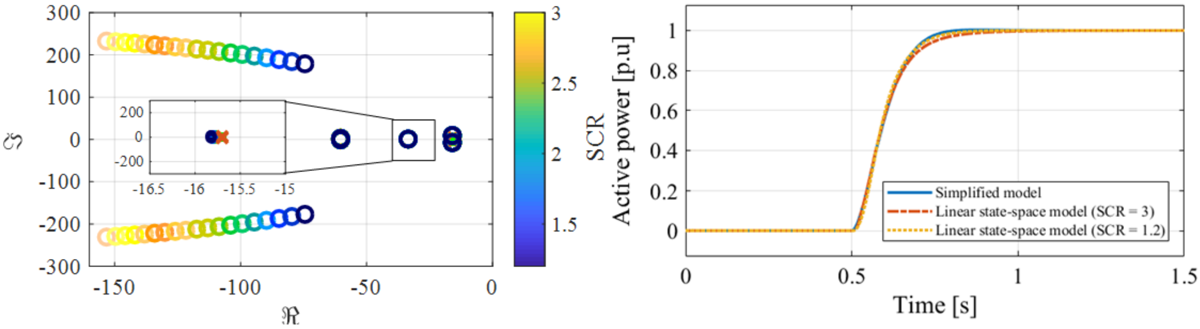

(a) T_R^{PLL}=10 ms

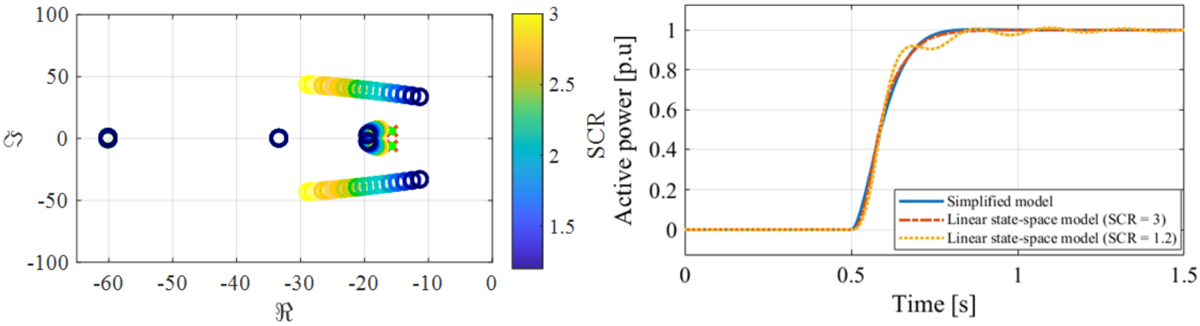

(b) T_R^{PLL}=50 ms

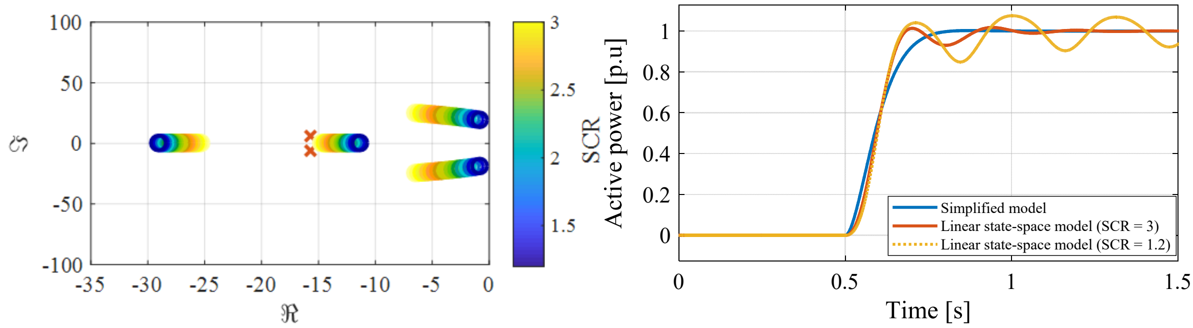

(c) T_R^{PLL}=100 ms

Figure II-33 - Active power dynamics and stability in very weak grid conditions (X) simplified model (O) Linear state-space model

The following conclusions are drawn based on the obtained results [124]:

- The system is stable for the critical SCR = 1.2 in all test cases.

- If the PLL is fast (e.g. $T_R^{PLL} < 50$ ms), the dominant dynamics are mainly linked with the states of the active power control loop. Moreover, the simplified model is accurate and it is sufficient to analyze the active power dynamics. Otherwise, the simplified model cannot always be used.
- The active power dynamics are sensitive to the PLL dynamics under very weak grid conditions, especially when $T_R^{PLL} > 50$ ms. Actually, For a PLL response time higher or equal to 50ms, there is a high interaction between the states of the power control loop and the states that are mainly linked with the PLL. For $T_R^{PLL} = 100$ ms, the states that are linked with the PLL are the dominant poles of the system.

Based on these conclusions, $T_R^{PLL} = 10$ ms is taken for the rest of this thesis.

Since the increase of the grid impedance results in an increase of the angle between AC voltages δ_m, the nonlinearity of the system becomes more important. Hence, time-domain simulations for $SCR_{\min} = 1.2$ are established in Figure II-34.a.

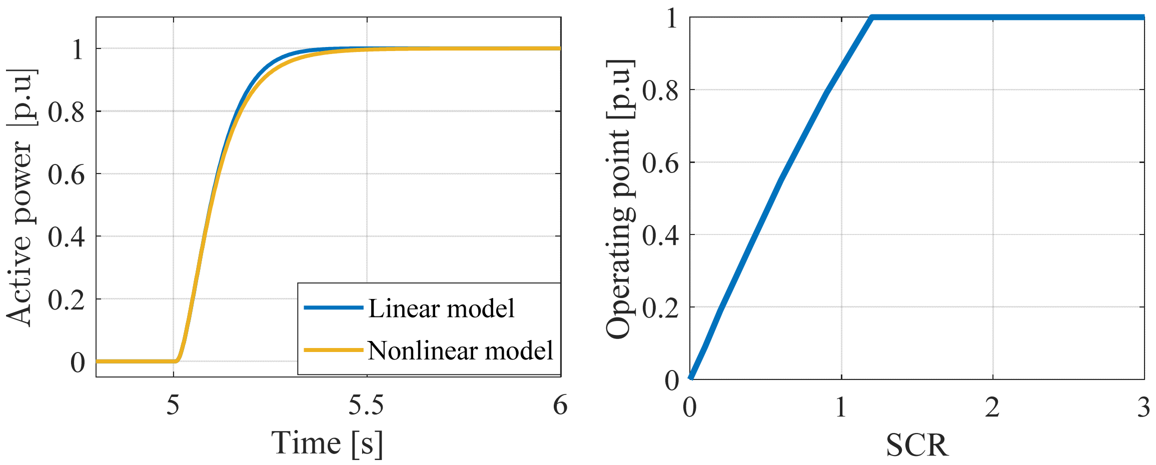

(a) (b)

Figure II-34 - (a) Comparison between linear and nonlinear models (b) SCR with respect with the operating point

From Figure II-34.a, a slight difference between the linear and the nonlinear models can be noticed in transient, but globally, the general trends are validated.

A generic graph of the SCR with respect to the operating point is depicted in Figure II-34.b.

In weak grid conditions, an important side effect should be highlighted. Actually, when the grid is stiff, the effect of the coupling transfer functions $T_{q\delta}(0)$ and $T_{pV}(0)$ have been neglected in the steady state because of the small variation of δ_m. However, when the grid is weak, the value of δ_m is not negligible anymore and especially for high operating points. If the AC voltage amplitude is kept around its nominal value, a steady state coupling between active and reactive power is considerable. The power coupling is illustrated by the vector diagram in Figure II-35.

The diagram shows that the increase of the grid impedance while keeping a constant AC voltage v_m, leads to an increase of the reactive current, and thereby, inducing a significant increase of the current magnitude I_g . This magnitude has to be monitored in order to avoid exceeding the physical current limitation of the power converter. The issues of the grid-forming VSC's overcurrent will be treated in chapter V.

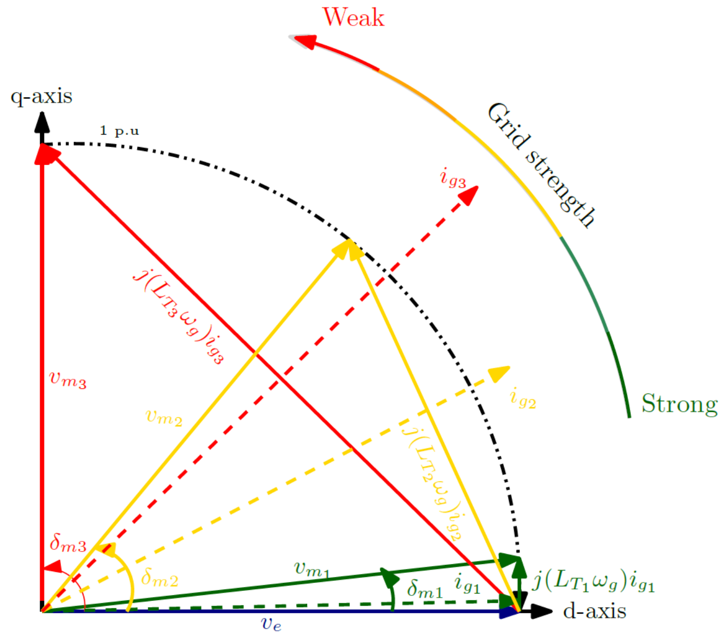

Figure II-35 - Vector diagram for power coupling in weak grids $p^* = 1$ p.u .

II.4.4 Conclusion

Reaching a high controllability level of the grid-forming converters is to deal with several factors i.e., dynamics, stability and robustness. In this chapter, a power regulator of the grid-forming converter is developed through a model-based inversion principle. The controller gains have been tuned to achieve acceptable dynamics, while ensuring an acceptable transient decoupling between active and reactive power.

To damp potential resonances around the grid frequency, transient virtual resistance has been added to the power controller. Moreover, it allows damping the grid currents in the transient, which results in a global system controllability.

Since the grid current and PLL dynamics are faster than the active power dynamics, the simplified quasi-static and dynamic models behave similarly. Consequently, the analysis of large grids may be done based on a simplified model.

From a stability and robustness point of view, the proposed control shows its ability to operate under very weak grid conditions. Indeed, it keeps the same active power dynamics in both strong and very weak grids, provided that an adequate response time of the PLL is chosen ($T_R^{PLL} < 50$ ms). However, in case of a weak grid, the grid current magnitude increases because of the steady-state coupling between active and reactive power. Therefore, the grid current magnitude has to be monitored in order to protect power converters against overcurrent.

In the next chapter, the VSC will be introduced in its environment, where the frequency is not constant anymore, thus, the converter contribution to the power system support is investigated.

III. Services provided by grid-forming VSCs to the AC system at the local level

III.1 Introduction

In the previous chapter, the VSC was connected to an infinite bus, where the frequency is assumed to be constant. In this section, the frequency is not constant anymore. The goal is to study the dynamic behavior of the VSC and its interoperability with a real AC system. Apart from the synchronization and constant power injection achieved with the control developed in chapter II ("Strategy A"), the converter must be able to contribute to the grid support. Thus, two variants of grid-forming control are derived from "Strategy A" and called "Strategy B" and "Strategy C" [125]. These strategies are introducing an inertial effect, which can help to limit the derivative of the frequency in the case of power unbalance. Depending on the variant, it is shown that the frequency droop control may be compulsory (Strategy C) or optional (Strategy A and B).

In this chapter, a systemic approach has been proposed in order to explain theoretically and in a simple manner the stability and the dynamic behavior of the system based on each of the three control strategies developed in this thesis. A recall of some of the standard analysis tools used for SG-based is given, and their validity for PE-based system is demonstrated. The main differences between both systems are also highlighted.

The association of grid-forming VSCs is assessed through different test cases. These latter allow confirming the stability and the interoperability of VSCs based on different control strategies. In addition, the focus of the transient behavior of these converters leads to a basic but interesting criterion to distinguish grid-forming and grid-following converters.

III.2 System description

Figure III-1 presents a VSC connected to an AC system formed by a linear resistive load P_{load} and an equivalent variable frequency AC grid. Different types of grid-forming controls will be analyzed (Strategy A, B, C). An outer droop control loop may be implemented to allow a frequency support of the VSC.
The equivalent AC grid consists of an AC voltage source in series with its impedance (R_g, L_g), which is driven by a model representing the dynamic behavior of a synchronous machine. It consists of a swing equation and a lead-lag filter, which is a simplified modelling of the turbine dynamics [53], [79]. A governor is added to support the grid frequency.

The notations used in this chapter are given in the following lines:

For the VSC:

- p_{vsc} and p_{VSC}^{SI} are the active power calculated from the converter side in per-unit and SI, respectively.
- ω_m is the modulated frequency of the converter.
- L_c, R_c is the connection impedance ($L_c = 0.15$ p.u, $R_c = 0.005$ p.u).
- S_{b1} is the rated power of the VSC chosen as its base power.
- R is the outer droop control gain ($R = 0.04$).

For the equivalent AC grid:

- p_g and p_g^{SI} are the active power calculated from the grid side in per-unit and SI, respectively.
- ω_e is the frequency of the grid.
- L_g, R_g is the connection impedance ($L_g = 0.15$ p.u, $R_g = 0.005$ p.u).
- S_{b2} is the rated power of the equivalent AC grid chosen as its base power.
- R_{SG} is the droop control gain ($R_{SG} = 0.04$).
- $H_{eq}, T_N, T_D, \omega_{e_n}$ are the inertia constant, the lead time constant, the lag time constant and the nominal grid frequency, respectively.

At the PCC:

- ω_g is the frequency at the load level.
- P_{load} is the instantaneous power of the load.

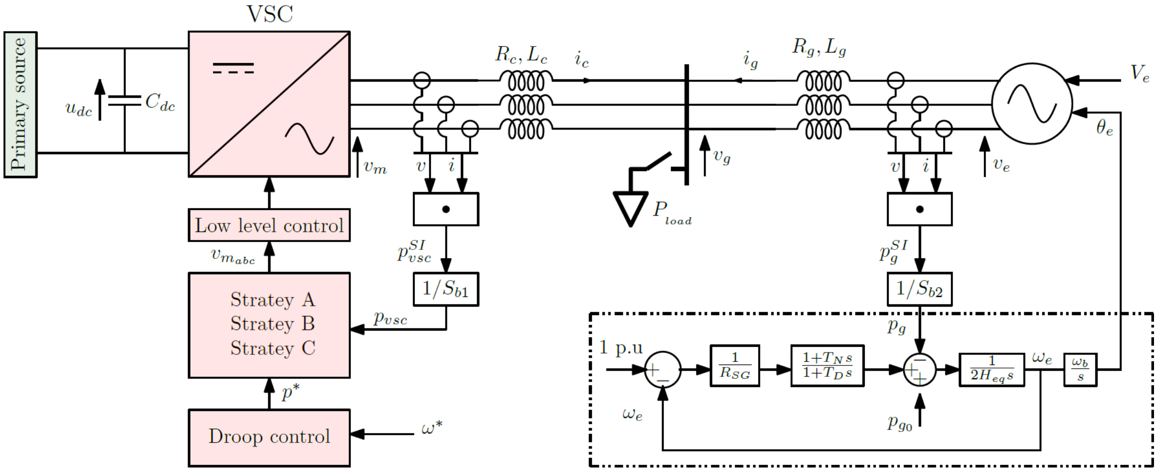

Figure III-1 - AC voltage-controlled VSC connected to an equivalent AC grid with variable frequency

The grid case in Figure III-1 is used to analyze the active power and frequency dynamics. Three different control strategies are studied under different situations.

To get into a realistic situation, the ratio between the rated powers of AC sources as given in (III-1) is taken into account. It aims to show the impact of the dominancy of the grid-forming converter over the AC grid and vice-versa.

$$PR = 100\frac{S_{b1}}{S_{b1}+S_{b2}} = 100\frac{S_{b1}}{S_T}\ [\%] \qquad \text{(III-1)}$$

In the rest of this chapter, the total power delivered by the VSC and the equivalent AC grid is of $S_T = 1000$ MW.

In this chapter, all theoretical equations neglect the PLL and grid currents dynamics. These assumptions hold true for the chosen T_R^{PLL} as proved in chapter II. Yet, they will be confirmed in each situation through time-domain simulations.

Simulation parameters are listed in Table III-1.

Table III-1 Simulation parameters

P_{n1}	500 MW	P_{n2}	500 MW
Cosϕ	0.95	Cosϕ	0.95
L_c	0.15 p.u	L_g	0.15 p.u
R_c	0.005 p.u	R_g	0.005 p.u
V_m	1 p.u	V_e	1 p.u
R	0.04 p.u	T_N	1s
R_v	0.09 p.u	T_D	6s
ω_{TVR}	60 rad/s	H_{eq}	5s
$T_{PLL5\%}^{R}$	10 ms	R_{SG}	0.04 p.u

III.3 Strategy A: Dynamic analysis of the variable-frequency system

"Strategy A" has already been studied in the first chapter for a VSC connected on a fixed frequency grid. In this section, the behavior of the grid-forming converter driven with "Strategy A" is studied in case of a variable-frequency grid.

III.3.1 System modeling and dynamic analysis

First, a small-signal analytical model of the system in Figure III-1 is built. The idea is to achieve a qualitative dynamic analysis of this system in order to have a physical explanation of the active power and frequency behavior.

The active power dynamics-based Strategy A:

The equation (III-2) recalls the 2nd order transfer function $\Delta p_{vsc} / \Delta p^*$ developed in chapter II (Equation (II-66)).

$$\Delta p_{vsc} = \frac{1}{1+(k_i K_c)^{-1}s+(K_c k_i \omega_c)^{-1}s^2}\Delta p^* \qquad \text{(III-2)}$$

where $K_c = V_m V_g / X_c$. This equation is derived in per unit – VSC base (S_{b1})

- ***Differential equations of the grid frequency:***

(III-3) describes the 2rd order equation used to drive the grid frequency,

$$-p_g = 2H_{eq}\omega_e s + \frac{1}{R_{SG}}\left(\frac{1+T_N s}{1+T_D s}\right)(\omega_e - 1) \qquad \text{(III-3)}$$

The small signal equation of (III-3) is expressed in the following:

$$-\Delta p_g = 2H_{eq}\Delta\omega_e s + \frac{1}{R_{SG}}\left(\frac{1+T_N s}{1+T_D s}\right)(\Delta\omega_e) \tag{III-4}$$

- ***Power model of the system:***

From the law of the power conservation,

$$\Delta p_g^{SI} + \Delta p_{vsc}^{SI} = \Delta P_{load} \tag{III-5}$$

with $\Delta p_{VSC}^{SI} = S_{b1}\Delta p_{VSC}$ and $\Delta p_g^{SI} = S_{b2}\Delta p_g$

III.3.1.1 Active power and grid frequency dynamics

III.3.1.1.1 Setpoint change Δp^*

As demonstrated in chapter II, the active power dynamics of the VSC in (III-2) are independent of the AC grid. The effectiveness of this statement is proved through time-domain simulations performed in Figure III-2.

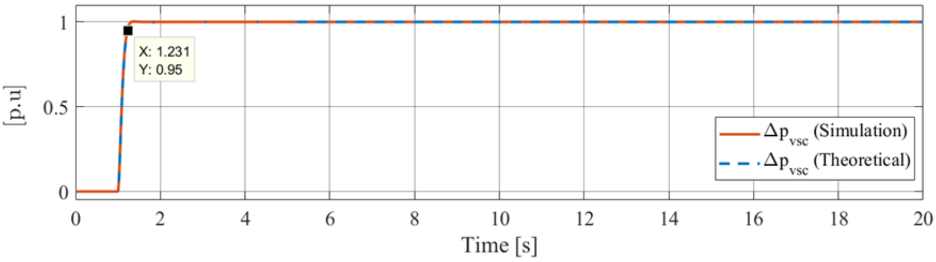

Figure III-2 - Active power dynamics with respect to the p^* setpoint change.

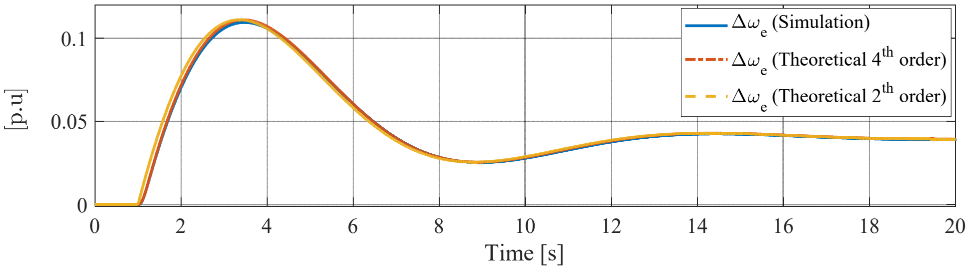

Figure III-3 - Frequency dynamics with respect to the p^* setpoint change

The active power change leads to an increase of the grid frequency. The evolution of the grid frequency with respect to the active power setpoint change is obtained from the equations in the following lines. From (III-5):

$$\Delta p_g = -(S_{b1}/S_{b2})\Delta p_{vsc} \tag{III-6}$$

with $\Delta P_{load} = 0$ p.u since no load variation is applied.

By replacing Δp_{vsc} in (III-6) by its equation in (III-2) and putting it in (III-4), the transfer function $\Delta\omega_e / \Delta p^*$ is deduced:

$$\Delta\omega_e = \frac{S_{b1}}{S_{b2}} \frac{R_{SG}(1+T_D s)}{\underbrace{\left(1+(k_i K_c)^{-1} s + (k_i K_c \omega_c)^{-1} s^2\right)}_{\alpha} \underbrace{\left(1+\left(T_N + 2H_{eq} R_{SG}\right) s + 2H_{eq} R_{SG} T_D s^2\right)}_{\beta}} \Delta p^* \quad \text{(III-7)}$$

(III-7) is a 4th order transfer function, which consists of a product of two 2nd order transfer functions α and β, respectively. The dynamic comparison between both transfer functions show that the eigenvalues of β ($\lambda_{1-2}^{\beta} = \text{-}1.17 \pm 0.553i$) are dominant against the ones of α ($\lambda_{3-4}^{\alpha} = \text{-}15.7 \pm 8.32i$). Thus, α can be neglected, which yields,

$$\Delta\omega_e = \frac{S_{b1}}{S_{b2}} \frac{R_{SG}(1+T_D s)}{\underbrace{\left(1+\left(T_N + 2H_{eq} R_{SG}\right) s + 2H_{eq} R_{SG} T_D s^2\right)}_{\beta}} \Delta p^* \quad \text{(III-8)}$$

Therefore, the frequency dynamics with respect to the active power setpoint change Δp^* can only be modeled with a second order transfer function in (III-8) as long as the frequency dynamics are slower than the active power dynamics.

The effectiveness of this theoretical approach is demonstrated through time-domain simulations performed in Figure III-3.

The results illustrate a high similarity between the simulated model, the 4th order theoretical model and the 2nd order theoretical one.

III.3.1.1.2 Load change ΔP$_{\text{load}}$

In this subsection, a load change of ΔP_{load}=500 MW is applied to the system.

When a load change is applied, the grid frequency variations are compensated in the control by the PLL, and thus, $\tilde{\omega}_g = \omega_m$, which keeps $\Delta p^* = \Delta p_{vsc} =$ 0 p.u since no variation is applied on Δp^*. Hence, it can be deduced that $\Delta P_{load} = \Delta p_g^{SI}$. Based on that, the frequency dynamics with respect to the load change can simply be obtained by replacing Δp_g by $\Delta P_{load} / S_{b2}$ in (III-4), which yields:

$$\Delta\omega_e = \text{-}\frac{1}{S_{b2}} \frac{R_{SG}(1+T_D s)}{\left(1+\left(T_N + 2H_{eq} R_{SG}\right) s + 2H_{eq} R_{SG} T_D s^2\right)} \Delta P_{load} \quad \text{(III-9)}$$

As shown in Figure III-4, simulation results almost match the developed theoretical results. Some slight differences can be noticed in the transient and steady state. They are mainly linked to the PLL and the grid current dynamics as well as to the resistive part of the filters, respectively.

The damping and the natural frequency of (III-9) are given by:

$$\zeta = \frac{1}{2} \frac{T_N + 2H_{eq} R_{SG}}{\sqrt{2H_{eq} R_{SG} T_D}}, \quad \omega_n = \sqrt{\frac{1}{2H_{eq} R_{SG} T_D}} \quad \text{(III-10)}$$

(III-10) shows the parameters impacting the grid frequency. Let’s focus on the impact of the inertia constant:

- The decrease of the inertia constant results in an increase of the damping and leads to an increase of the natural frequency.
- The increase of the natural frequency results in a faster frequency response.

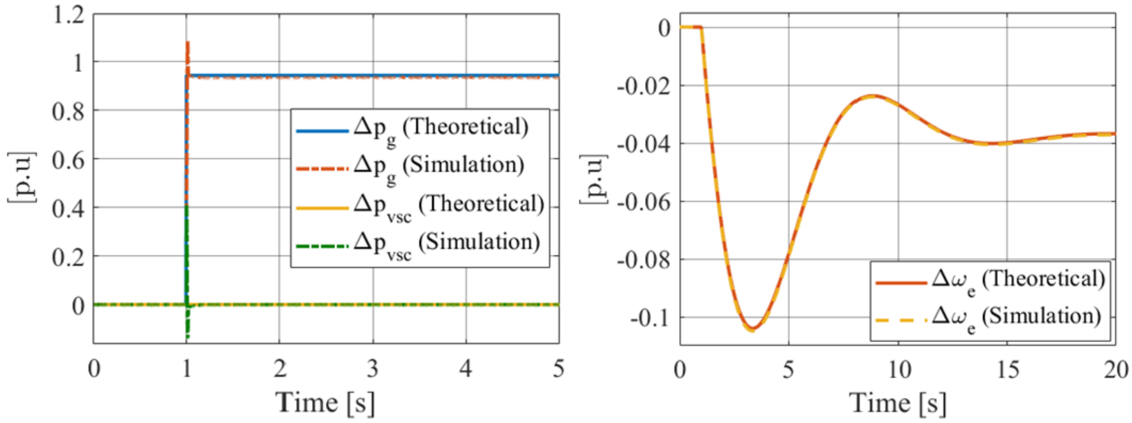

Figure III-4 - Frequency and active power dynamics with respect to the a load change

The inertia constant also has an impact on the RoCoF and frequency Nadir. The formulas of these characteristics are given by:

$$RoCoF = \lim_{t \to 0^+} \frac{df_e}{dt} = \mathcal{L}^{-1}\left(f_b \Delta\omega_e s\right) \tag{III-11}$$

$$= \frac{\Delta P_{load} f_b}{2H_{eq} S_{b2}}$$

$$Nadir = f_b + \Delta\omega_e (T_{Peak}) \tag{III-12}$$

f_e and f_b denote the grid frequency and its base value in Hz, respectively. $\mathcal{L}^{-1}$ is the inverse Laplace transform. T_{peak} is the peak time corresponding to the frequency Nadir.

$$Nadir = \frac{f_b K}{\sigma^2 + \omega_d^2}\left[z_1 + e^{-\sigma t}(z_1 \cos\left(\omega_d T_{peak}\right) - \left(\frac{z_1\sigma - \sigma^2 - \omega_d^2}{\omega_d}\right)\sin\left(\omega_d T_{peak}\right)\right] \tag{III-13}$$

with, $\omega_R = \omega_n\sqrt{1-\zeta^2}$, $\sigma = \omega_n \zeta$, $K = -\Delta P_{load} / (2H_{eq} S_{b_2})$ and $z_1 = 1/T_D$. More details are found in Appendix D.

As expected, one can remark from (III-11) and (III-12) that a decrease of the inertia leads to an increase of the frequency RoCoF and in a decrease of the frequency nadir. This affirmation is consolidated by a numerical application in Table III-2 and time-domain simulation in Figure III-5.

Table III-2 Characteristics of the frequency dynamics with high and low grid inertia constant

H_{eq} = **5 s**		H_{eq} = **0.5 s**	
RoCoF [Hz/s]	Nadir	RoCoF [Hz/s]	Nadir
5	44.8 Hz	50	41.38 Hz

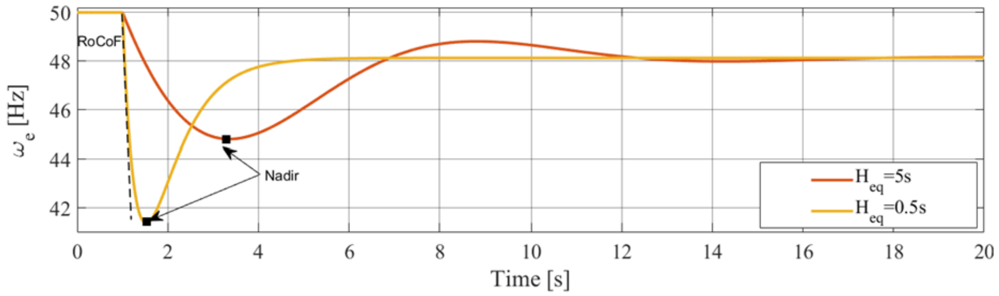

Figure III-5 - Frequency dynamics with two grid inertia constants

III.3.2 Effect of the outer droop control on the system dynamics

The droop control is introduced in the VSC control. Its equation is given by,

$$(\omega^* - \omega_m)\frac{1}{R} = p^* \tag{III-14}$$

In small-signal
$$-\Delta\omega_m \frac{1}{R} = \Delta p^* \tag{III-15}$$

As highlighted by (III-15), an expression of $\Delta\omega_m$ with respect to the other parameters is required.
The active power flow between the VSC/Load and the grid/Load are given by:

$$\Delta p_{vsc} = K_c(\Delta\delta_m - \Delta\delta_g) = K_c\frac{(\Delta\omega_m - \Delta\omega_g)}{s}\omega_b \tag{III-16}$$

$$\Delta p_g = K_g(\Delta\delta_e - \Delta\delta_g) = K_g\frac{(\Delta\omega_e - \Delta\omega_g)}{s}\omega_b \tag{III-17}$$

where $K_c = V_m V_g / X_c$, $K_g = V_e V_g / X_g$ and $\Delta\omega_m = \Delta\omega_e + \left(\frac{\Delta p_{vsc}}{K_c} + \frac{\Delta p_g}{K_g}\right)\frac{s}{\omega_b}$.

Merging (III-2), (III-15) (III-16) and (III-17), the overall system can be represented by the block diagram in Figure III-6.

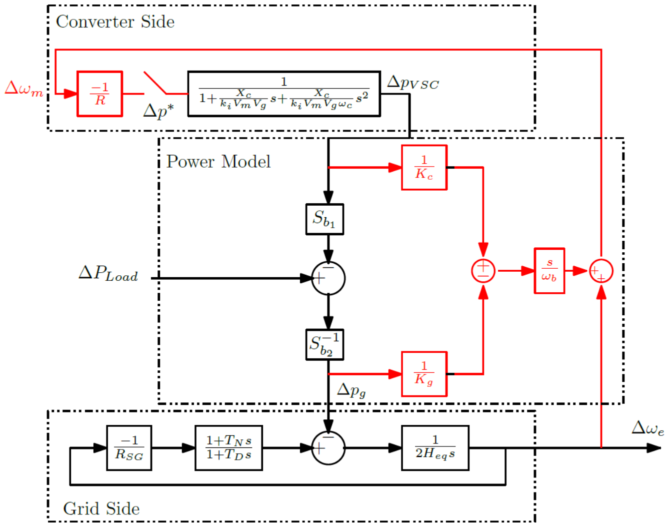

Figure III-6 - Block diagram representation of the overall system

From Figure III-6, a coupling between the VSC and the AC grid models can be noticed. It is induced by the outer droop control. To demonstrate theoretically, the impact of the droop control on the frequency dynamics, the 4th order model in Figure III-6 can be simplified by assuming that the active power dynamics are neglected ($\Delta p^{*} = \Delta p_{vsc}$) and all system frequencies are equal (i.e., $\Delta\omega_e = \Delta\omega_g = \Delta\omega_m$). These assumptions allow finding the dominant response of the frequency. Based on that, the overall system can be represented by the simplified block diagram depicted in Figure III-7.

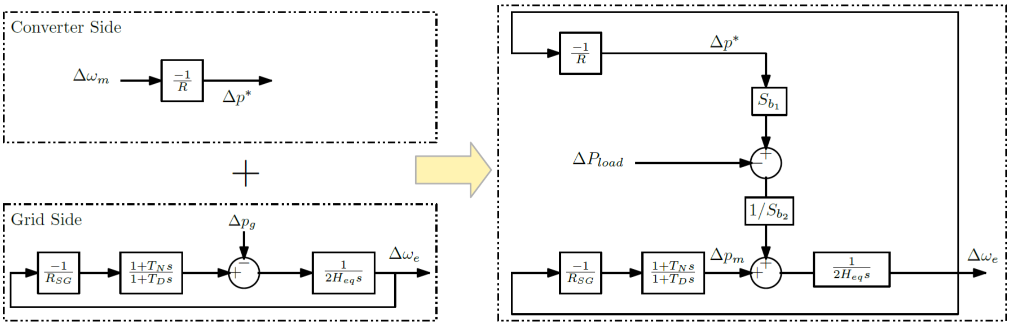

Figure III-7 - The simplified representation of the grid frequency dynamics

From Figure III-7, the transfer function of the grid frequency with respect to the load change is deduced:

$$\Delta\omega_e = \frac{-\dfrac{RR_{SG}\left(1+T_D s\right)}{R_{SG}S_{b1}+RS_{b2}}}{1+\dfrac{\left(RS_{b2}T_N+R_{SG}S_{b1}T_D+2H_{eq}RR_{SG}S_{b2}\right)}{R_{SG}S_{b1}+RSb_2}s+\dfrac{\left(2H_{eq}T_D RR_{SG}S_{b2}\right)}{R_{SG}S_{b1}+RSb_2}s^2}\Delta P_{load} \tag{III-18}$$

The damping and the natural frequency of (18) are given by:

$$\zeta = \frac{1}{2}\frac{RS_{b2}T_N+R_{SG}S_{b1}T_D+2H_{eq}RR_{SG}S_{b2}}{\sqrt{2H_{eq}T_D RR_{SG}S_{b2}}\cdot\sqrt{R_{SG}S_{b1}+RSb_2}}, \qquad \omega_n = \sqrt{\frac{R_{SG}S_{b1}+RS_{b2}}{2H_{eq}T_D RR_{SG}S_{b2}}} \tag{III-19}$$

(III-19) proves that the outer droop control increases the system damping and makes the frequency response faster. To validate the model in (III-18), time-domain simulations are performed in Figure III-8.

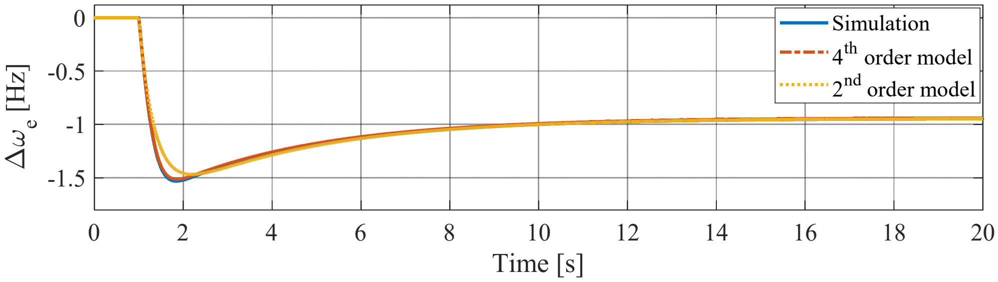

Figure III-8 - Validation of the simplified model

The results demonstrate the accuracy of the 4th order model in all frequency range, while a small mismatch between the simulated model and the 2nd order model is observed in the transient. Generally, the simplified model is still effective at this level.

Every simplified model has limitations. Actually, Figure III-9 and Figure III-10 assess the validity of the developed model (III-18) based on two values of the RoCoF. For each case, a combination of the inertia constant and PR is taken since both factors are responsible for the RoCoF change as proved in (III-11).

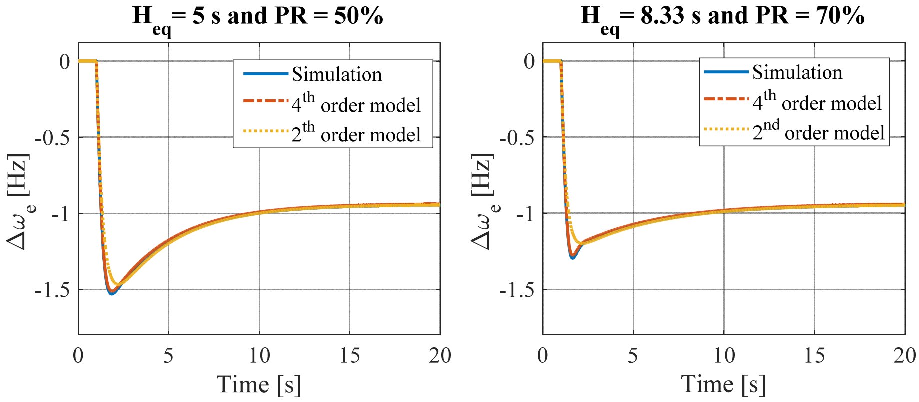

Figure III-9 - RoCoF = 5 Hz/s

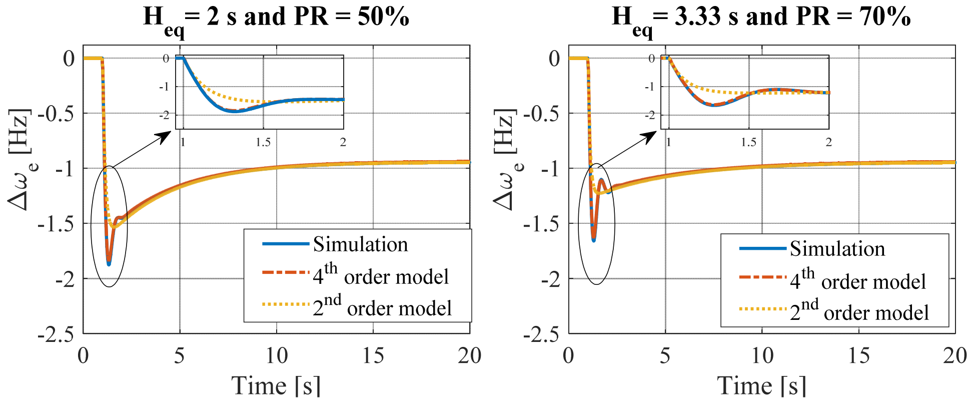

Figure III-10 - RoCoF = 12.5 Hz/s

The results confirm once again, the validity of the 4th order model for both RoCoF values, while, the 2nd order model preserves the dominant slow response, but, it may hide the fast transients (RoCoF>5 Hz/s), which may lead to wrong results, especially for the frequency Nadir.

III.3.3 Active power transient during a load change

In this section, two phenomena are studied:

- The impact of the power ratio (PR) on the requested VSC active power during a power unbalance.
- The impact of the SCR on the first active power transient following a load change disturbance.

III.3.3.1 Influence of the power ratio

Let's go back to power system basics:

- With synchronous generators, the inertia is necessary to compensate the power imbalance during the transient, since the mechanical power p_m is very slow because of the dynamics of the turbines (i.e., modeled in this thesis by a lead-lag), valves etc.

- With the Strategy A-based VSC, no inertia effect can be provided, but, the frequency can be measured in the control and used to generate a power reference p^* instantaneously, which results in a fast frequency support. This point presents one of the major differences between SGs and VSCs.

Due to very large dynamics difference between both AC sources, a large power unbalance may be induced during the transient. The following simulations (Figure III-11) highlight this phenomenon.

It is considered in this section that $P_{load} = 400$ MW is initially connected, then, ΔP_{load} of 500 MW is connected.

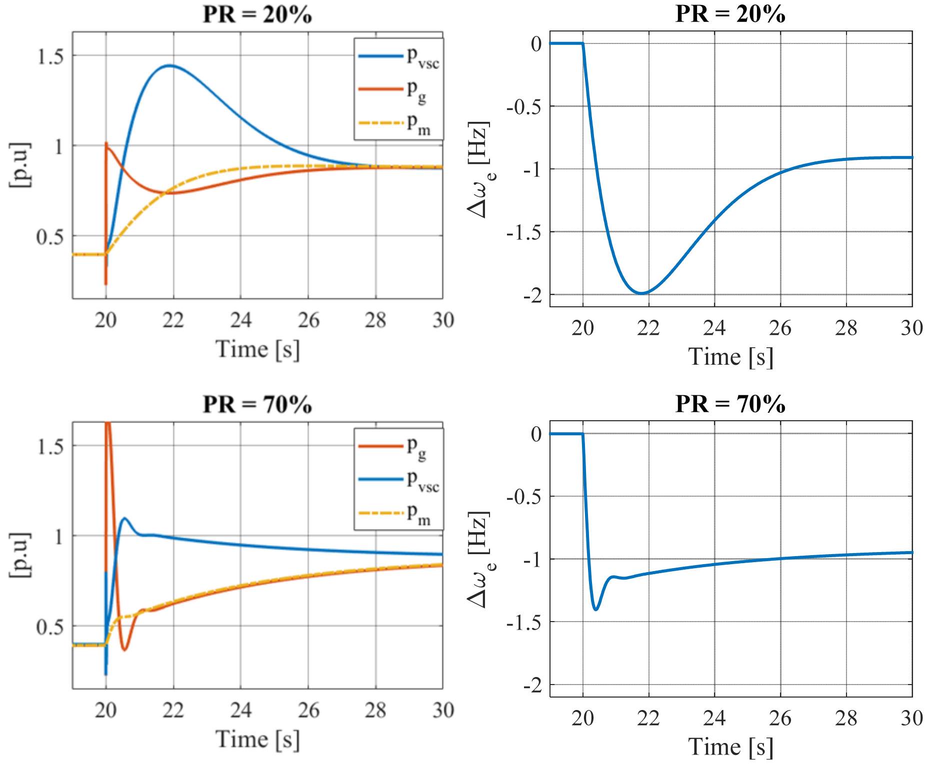

Figure III-11 - Active power transient for different values of *PR*

Figure III-11 illustrates precious results:

- In case of PR = 20%, $H_{eq} = 5$ s, the RoCoF is small <5 Hz/s, which results in a slow grid frequency response. The active power setpoint of the VSC $\left(-\Delta p^* S_{b1} / R\right)$ is negatively proportional to the frequency. The low frequency nadir results in high VSC active power overshoot. It reaches 1.48 p.u for the chosen simulation parameters. This amount of the power can never be provided by the VSC since it exceeds its rated capability.
- In case of PR = 70%, $H_{eq} = 5$ s, the RoCoF is significantly increased >10 Hz/s. This yields a quite fast frequency response, and therefore, it results in fast active

power compensation by the VSC. In this case, the VSC is not exposed to dangers. However, the frequency dynamics may not be acceptable.

To avoid the overpower issues, a power reference saturation is compulsory (Figure III-12).

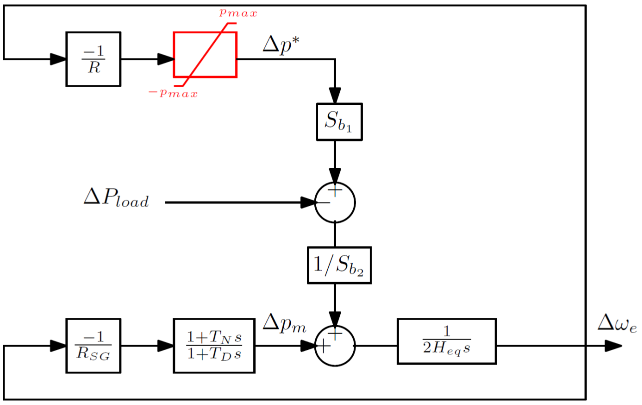

Figure III-12 - Active power reference saturation

The 1st case is taken as an example. The results in the following figure show that since the active power is limited, the frequency Nadir becomes lower.

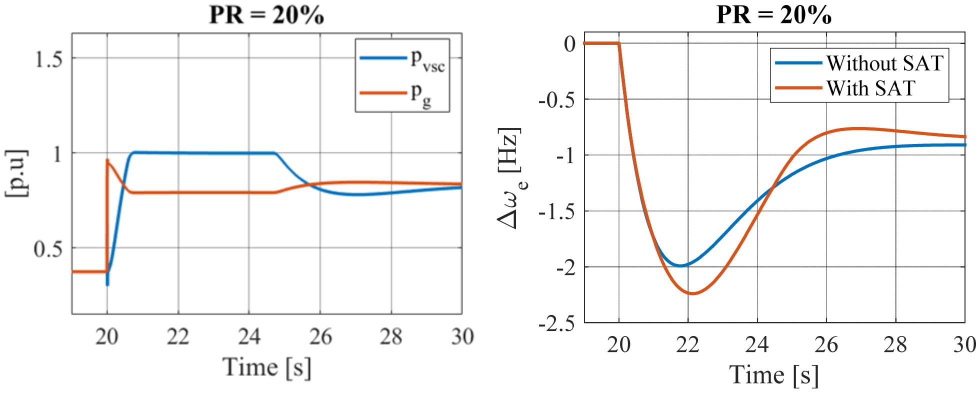

Figure III-13 - Impact of the power reference saturation on the active power and frequency

III.3.3.2 Influence of the short circuit ratio on the active power transient

In this subsection, the grid impedance is defined from the SCR. The aim is to highlight the impact of the equivalent grid impedance (lines + output filters of different sources) on the active power transient of the VSC after a few milliseconds following the load change disturbance. This behavior is the key element to characterize the voltage source behavior of the grid-forming VSC.

To highlight this phenomenon, two types of control and two values of SCR are chosen:

- SCR = 20 with and without VSC droop control
- SCR = 2 with and without VSC droop control

The results are illustrated in Figure III-14. In Figure III-14.a for instance, the overall behavior for the power is similar. However, looking into details, during the first milliseconds after a load change, both sources react as voltage sources behind their respective output impedances .i.e., in case of a large SCR (SCR = 20), since $X_g \ll X_c$, the active power provided by the equivalent AC grid is much larger than for the VSC. This power in the first transient does not depend on the control since it is exactly similar with or without droop control. In case of small SCR (SCR =2), the VSC provides more active power than the AC grid in the first millisecond.

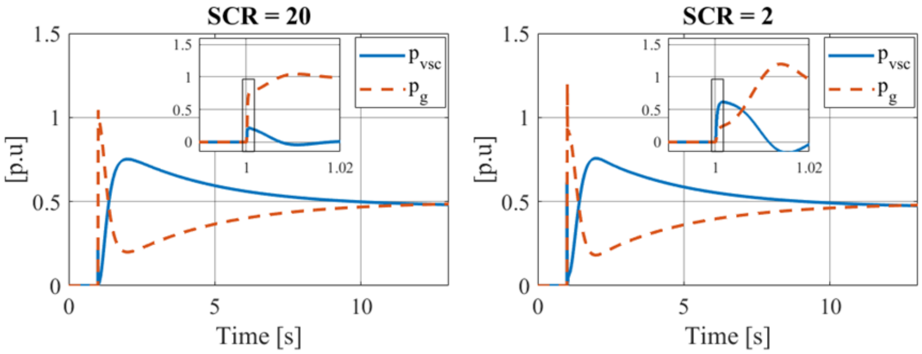

(a) With power sharing

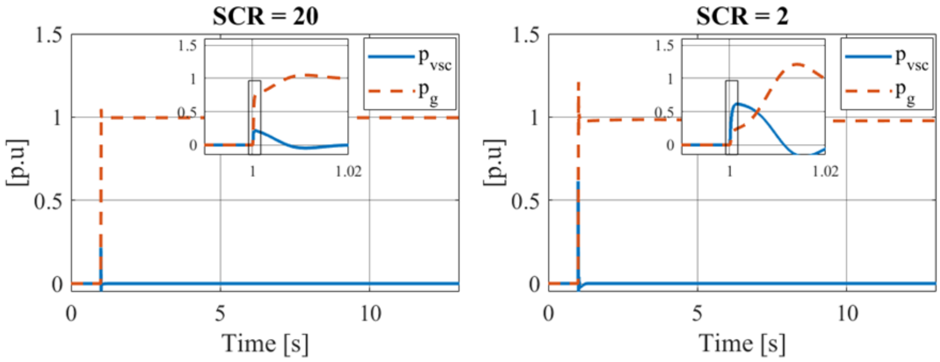

(b) Without power sharing

Figure III-14 - Active power transient with different SCRs

III.3.4 Summary

The following conclusions are drawn from this section:

- The Strategy A-based VSC is a robust power injector.
- It maintains a stable system operation, even with high PR.

Actually, large RoCoF and low frequency nadir may lead to unnecessary activation of system protections, which can lead to load shedding. Hence, power converters which emulate an inertial effect are requested. Therefore, the next section proposes some control modifications involving the VSC in the frequency support.

III.4 Strategy B for grid-forming control: Inertial and Frequency support

III.4.1 Control structure

The first control strategy derived in chapter II and in the beginning of this chapter is directly deduced from the expression of the active power linked to the angle δ_m. From the same expression, it is possible to deduce several control variants. Some of them worsen the accuracy of the active power control, but, at the same time, bring new functionalities. A first variant is shown in Figure III-15. It allows the power converter to ensure an inertial effect, and consequently, supporting the AC grid.

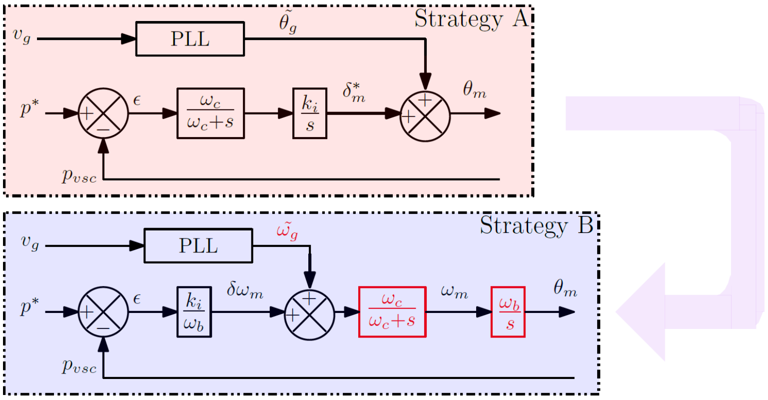

Figure III-15 - Power controller with inertial effect

Contrary to the previous control, the estimated frequency is used instead of the estimated angle. In steady state, since $\omega_m = \tilde{\omega}_g$, the active power p_{vsc} tracks its reference p^* in steady state. However, the dynamic behavior based on this control is fundamentally different. The transfer function derived from Figure III-15 is written:

$$\frac{\omega_b}{k_i\omega_c}\frac{d\omega_m}{dt} = p^* - p_{vsc} - \frac{\omega_b}{k_i}(\omega_m - \tilde{\omega}_g) \qquad \text{(III-20)}$$

In case of a grid frequency variation, ω_m is not modified instantaneously, which results in a kind of inertial effect. It is possible to present the control in another way (see (III-21)). This formulation is often referred in the literature as a virtual synchronous machine concept [58].

$$2H\frac{d\omega_m}{dt} = p^* - p_{vsc} - \frac{\omega_b}{k_i}(\omega_m - \tilde{\omega}_g) \qquad \text{(III-21)}$$

By identification,

$$H = \frac{\omega_b}{2\omega_c k_i} \qquad \frac{k_i}{\omega_b} = k_d \qquad \text{(III-22)}$$

This analogy shows the ability of the “Strategy B” to allow the inertial effect, thanks to the low-pass filter cut-off frequency ω_c and the power controller gain k_i.

Since “Strategy B” embeds an inertial effect, some new questions arise:

- What is the impact of the inertial effect on the system dynamics, and especially on the active power response?
- Since the inertia is adjustable thanks to two parameters (ω_c, k_i), what is the influence of the choice on this couple of parameters on the system dynamics?
- Does Strategy B remain robust to the topological change and grid impedance variations similarly to “Strategy A”?

These questions are treated in the next subsections.

III.4.2 Dynamics of the active power

To focus only on the active power control, the fixed-frequency system in Figure III-16 already described in chapter II is used in this section.

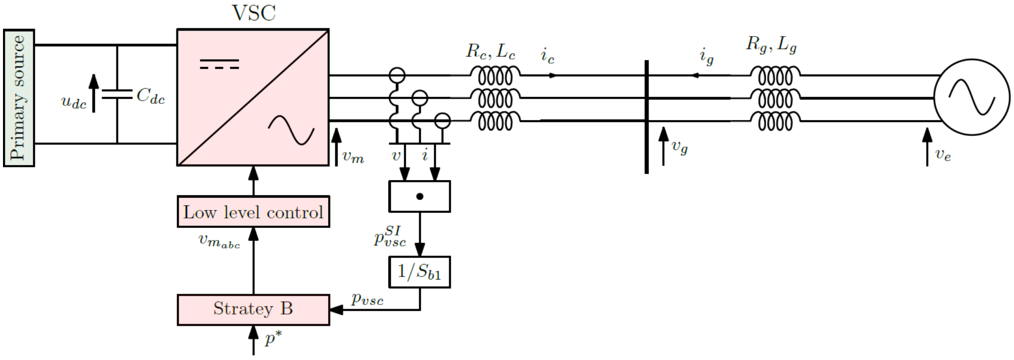

Figure III-16 - VSC connected to a fixed-frequency AC system

Simple formulas describing the active power dynamics are developed in this section. They allow a better understanding of the system behavior.

III.4.2.1 Small-signal modeling

In this subsection, a simplified modeling of the converter driven with “Strategy B” is proposed in order to have an analytical formula for the dominant poles and help in understanding the system behavior. A quasi-static model for the grid-connected VSC is used as drawn in Figure III-17.

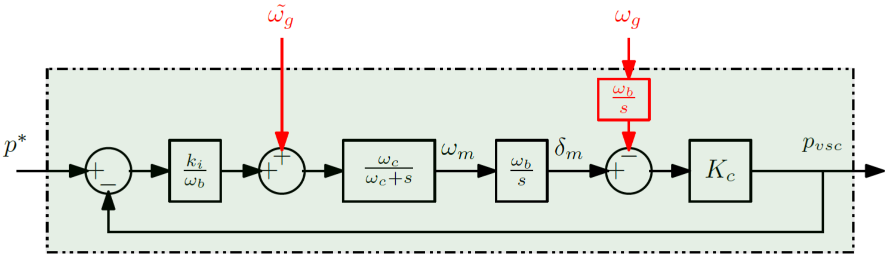

Figure III-17 - Quasi-static active power regulation

Based on Figure III-17, the differential equation of “Strategy B” can be written as,

$$\delta_m = \left[\left(p^* - p_{vsc} \right) \frac{k_i}{\omega_b} + \tilde{\omega}_g \right] \left(\frac{\omega_c}{\omega_c + s} \right) \frac{\omega_b}{s} \tag{III-23}$$

For the small signal stability analysis, the equation becomes:

$$\Delta\delta_m = \left[\left(\Delta p^* - \Delta p_{vsc} \right) \frac{k_i}{\omega_b} + \Delta\tilde{\omega}_g \right] \left(\frac{\omega_c}{\omega_c + s} \right) \frac{\omega_b}{s} \tag{III-24}$$

The active power flow between the VSC and the AC grid is expressed as,

$$\Delta p_{vsc} = K_C \left(\Delta\delta_m - \Delta\delta_g \right) \tag{III-25}$$

Merging (III-24) in (III-25) results in,

$$\Delta p_{vsc} = \left[\left(\left(\Delta p^* - \Delta p_{vsc} \right) \frac{k_i}{\omega_b} + \Delta \tilde{\omega}_g \right) \left(\frac{\omega_c}{\omega_c + s} \right) \frac{\omega_b}{s} - \frac{\Delta \omega_g \omega_b}{s} \right] K_c \tag{III-26}$$

Then Δp_{vsc} can be expressed with respect to Δp^*, $\Delta \tilde{\omega}_g$ and $\Delta \omega_g$:

$$\Delta p_{vsc} = \frac{1}{1 + \frac{1}{k_i K_C} s + \frac{1}{k_i K_C \omega_c} s^2} \Delta p^* + \frac{\frac{\omega_b}{k_i}}{1 + \frac{1}{k_i K_C} s + \frac{1}{k_i K_C \omega_c} s^2} \Delta \tilde{\omega}_g - \frac{\frac{\omega_b}{k_i} (1 + \frac{s}{\omega_c})}{1 + \frac{1}{k_i K_C} s + \frac{1}{k_i K_C \omega_c} s^2} \Delta \omega_g \tag{III-27}$$

Considering a large time-scale decoupling between the frequency estimation and the active power regulation, the grid frequency and the estimated one are assumed to be equal: $\Delta \tilde{\omega}_g = \Delta \omega_g$, which yields,

$$\Delta p_{vsc} = \frac{1}{1 + \frac{1}{k_i K_C} s + \frac{1}{k_i K_C \omega_c} s^2} \Delta p^* - \frac{\frac{\omega_b}{k_i \omega_c} s}{1 + \frac{1}{k_i K_C} s + \frac{1}{k_i K_C \omega_c} s^2} \Delta \omega_g \tag{III-28}$$

To simplify this expression, the variation of the grid frequency $\Delta \omega_g$ can be expressed with respect to Δp_{vsc}. Since the losses are neglected, the power flowing from v_m to v_g is the same as the power flowing from v_g to v_e. A similar relation as in (III-25) can be derived by using $\Delta \delta_g$ and $\Delta \delta_e$.

$$\Delta p_{vsc} = K_g \left(\Delta \delta_g - \Delta \delta_e \right) \tag{III-29}$$

Using $\Delta \omega_g$ and $\Delta \omega_e$ results in:

$$\Delta p_{vsc} = K_g \frac{\left(\Delta \omega_g - \Delta \omega_e \right)}{s} \omega_b \tag{III-30}$$

Since the grid frequency is constant, a relation between $\Delta \omega_g$ and Δp_{vsc} can be derived:

$$\Delta \omega_g = \frac{s \Delta p_{vsc}}{\omega_b} \left(\frac{1}{K_g} \right) \tag{III-31}$$

Finally, by replacing $\Delta \omega_g$ in (III-28) by (III-31), a 2nd order model is obtained,

$$\Delta p_{vsc} = \frac{1}{1 + \frac{X_c}{k_i V_m V_e} s + \frac{X_c + X_g}{k_i V_m V_e \omega_c} s^2} \Delta p^* \tag{III-32}$$

The damping and the natural frequency of the dominant modes are expressed as:

$$\zeta = \frac{X_c}{2} \sqrt{\frac{\omega_c}{k_i (X_c + X_g) V_m V_e}}, \quad \omega_n = \sqrt{\frac{k_i V_m V_e \omega_c}{X_c + X_g}} \tag{III-33}$$

Contrary to “Strategy A”, where the active power dynamics do not depend on the grid impedance, the system dynamics based on “Strategy B” are influenced by the grid impedance. Hence, the grid stiffness has an impact on the system stability and dynamics.

To illustrate the accuracy of the developed simplified small-signal model, this latter is compared to the full dynamic linear model and the non-linear model illustrated in Figure III-16. The full dynamic linearized model given by (III-34) is mainly used for robustness analysis. It is expressed as:

$$\Delta x = A\,\Delta x + B\,\Delta u \tag{III-34}$$

$$\Delta x = \begin{bmatrix} \underbrace{\Delta i_{cd}\ \Delta i_{cq}\ \Delta i_{gd}\ \Delta i_{gd}}_{Grid\ current}\ \underbrace{\Delta v_{gd}\ \Delta v_{gq}}_{PCC\ voltage}\ \ \underbrace{\Delta \zeta_{TVR_d}\ \Delta \zeta_{TVR_q}}_{TVR}\ \ \underbrace{\Delta \delta_m\ \Delta \omega_m}_{Strategy\ B}\ \ \underbrace{\Delta \zeta_{PLL}\ \Delta \delta_{PLL}}_{PLL} \end{bmatrix}$$

$$\Delta u = [v_{e_d}\ v_{e_q}\ p^*\ v_{m_d}\ v_{m_q}]$$

The control matrices A and B are calculated in Appendix E.
The results of the comparison are shown in Figure III-18. The parameters used for the simulation are chosen arbitrarily to validate the proposed model. They are indicated in the label of Figure III-18. Different steps on the active power reference are applied:

- t=3 s, a step of p^* 0.2 p.u is applied.
- t=6 s, a step of p^* = -0.4 p.u is applied.
- t=10 s, a step of p^* 0.2 p.u is applied.

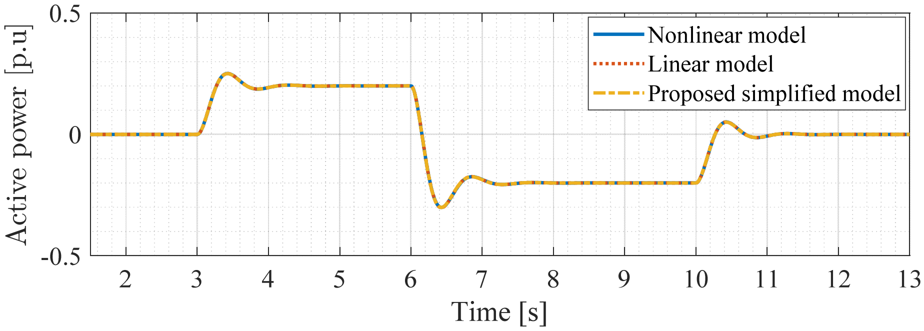

Figure III-18 - Comparison between the simulated model, the linear model and the simplified model. Simulation parameters: k_i = 1.5 p.u, ω_c = 31.4 rad/s and SCR = 3

The obtained results show that all models behave in a similar manner, and therefore, the proposed simplified model is confirmed. In the next subsection, this model is used to analyze the active power dynamics for different control and system parameters.

III.4.2.2 Impact of the couple k_i and ω_c on the active power dynamics

Due to (III-20), the choice of the inertia constant H_{VSC} imposes a link between ω_c and k_i. Both parameters are degrees of freedom. This subsection analyses the influence of the choice of ω_c and k_i on the damping and the response time of the system for the following inertia constant H_{VSC}=5s. The couple $k_i - \omega_c$ that ensures this inertia constant is drawn in Figure III-19.

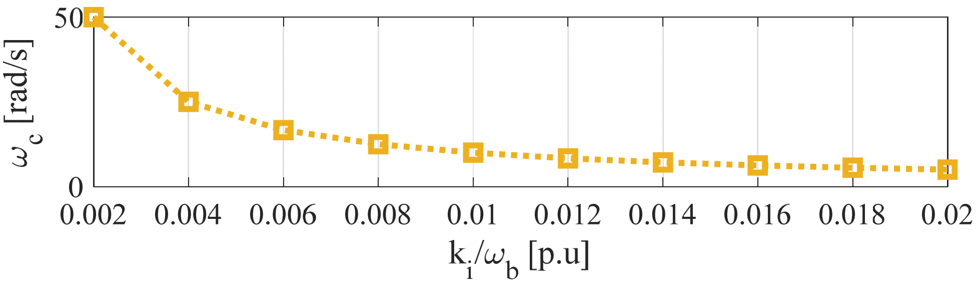

Figure III-19 - The couple $k_i - \omega_c$ that ensures $H_{VSC} = 5$s

Based on (III-32), Figure III-20 shows the evolution of the damping and response time of the active power with respect to the couple $k_i - \omega_c$ for H_{VSC} =5s and SCR = 20.

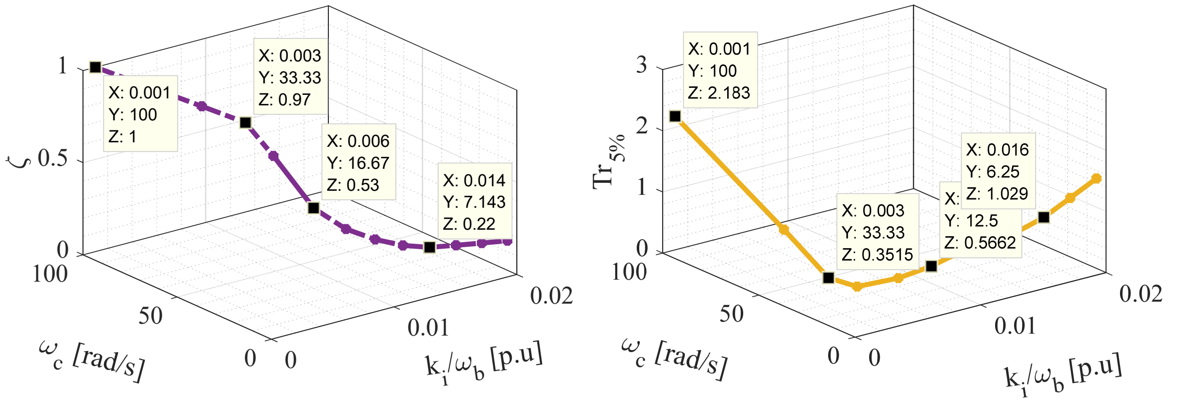

Figure III-20 - Impact of the couple $k_i - \omega_c$ on the active power damping and response time

k_i is inversely proportional to the cut-off frequency ω_c for a given inertia constant H_{VSC}. One can remark from Figure III-20 that a smaller value of k_i results in a well damped but slower response. It induces also, a higher value for ω_c. However, ω_c must be chosen in such a way:

- To filter the grid frequency and avoid the introduction of unwanted noises in the calculation of the modulated frequency ω_m.
- To ensure an acceptable active power damping.

A fast active power response with high damping and good output converter frequency quality cannot be achieved at once, since ω_c and k_i have a contradictory effect on the active power. Based on Figure III-20, a trade-off between both objectives could be achieved through the following set of parameters ω_c = 33 rad/s and k_i / ω_b = 0.003 p.u. To illustrate the obtained results, time-domain simulations are given in Figure III-21. A comparison between active power dynamics based on the chosen values (blue curve) and another couple of values (yellow curve) is performed.

The chosen couple $k_i - \omega_c$ results in a well-damped system. The response time $T_{5\%}^{R}$ is about 360 ms. These dynamic performances are verified under the assumption of a stiff AC grid. In the following subsection, the impact of the SCR on the active power behavior and system stability is studied.

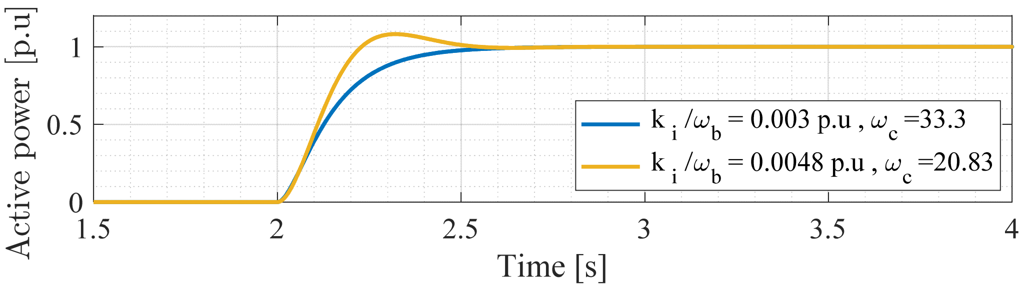

Figure III-21 - Active power and frequency dynamics based on new set of parameters (SCR = 20)

III.4.2.3 Control stability and robustness against AC grid stiffness

As explained in the previous section, the dynamics of the active power depends on the grid impedance. In this subsection, the robustness and the stability of the system under different SCRs are assessed. Figure III-22 shows the pole evolution for different SCRs (from SCR = 3, until SCR = 1.2). It is recalled that SCR = 1.2 is the minimum value that allows the system to operate at the full power range while both AC voltages are set at their nominal values $V_m = V_e = 1$ p.u.

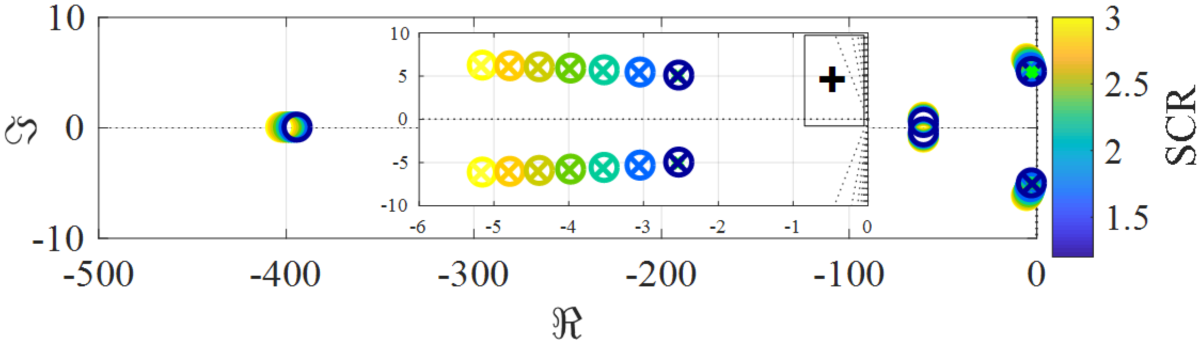

Figure III-22 - Eigenvalues evolution with respect to the SCR. '*O*' refers to the full dynamic model, '*X*' refers to the developed simplified model

The conclusions drawn from this figure are twofold. Firstly, it confirms the good accuracy of the poles calculated from (III-32) since they are superimposed with the dominant poles of the more detailed model. Secondly, as expected from (III-33), the damping is decreasing with the increase of the SCR. However, even if "Strategy B" is more sensitive to the grid impedance variations than "Strategy A", the obtained results show that the damping is still acceptable in all the range of variation for SCR (e.g., for a value of SCR = 1.2 ζ=0.447 $T_{5\%}^{R}$ = 960 ms).

The validity of the linear analysis is supported with time-domain simulations in Figure III-21, where, the linear and the nonlinear models are compared under weak and very weak grid conditions.

The active power is first set to its rated value, then, at t=5 s, a power step of p^* = -1 p.u is applied.

The results confirm the good accuracy of the simplified model compared to the nonlinear model even if some slight differences can be noticed between the simplified model and the nonlinear model under very low SCR.

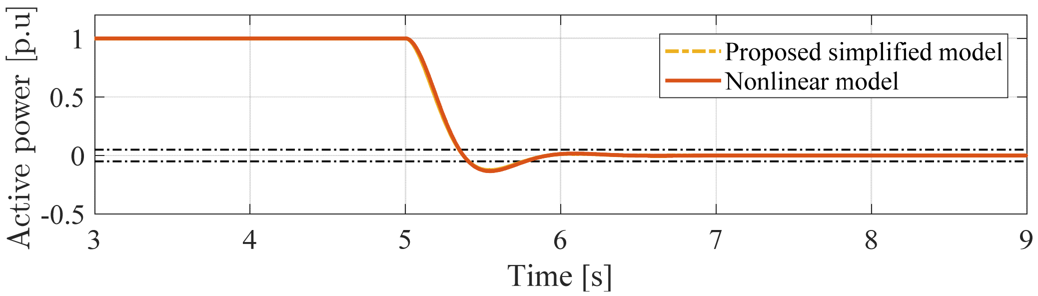

(a) SCR = 2

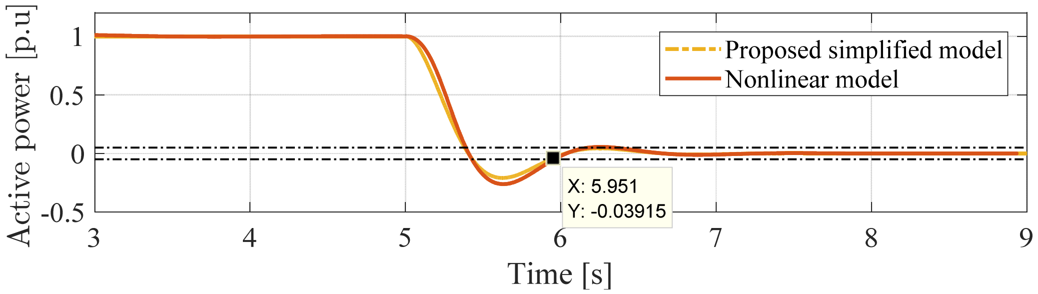

(b) SCR = 1.2

Figure III-23 - Active power dynamics under different SCR values

III.4.3 Strategy B: Dynamic analysis of the variable-frequency system

In this section, the behavior of the grid-forming converter driven with “Strategy B” in case of a variable-frequency grid is studied. The grid case in Figure III-1 is used. In “Strategy A”, the expression of the active power only depends on internal parameters of the converter. This is not the case anymore with “Strategy B”. Indeed, with the fixed frequency grid configuration (i.e., $\Delta\omega_e$=0), the active power dynamics were impacted only by the grid impedance as proved by (III-32). However, with the variable-frequency grid configuration, $\Delta\omega_e$ is not null anymore and it may have a large impact on the system dynamics.

III.4.3.1 Active power and grid frequency dynamics

To analyze the active power dynamics, the equation (III-28) is still effective. In (III-28), $\Delta\omega_g$ has to be expressed with respect to the converter and the AC grid parameters. Based on that, two models are proposed:
1st simplified model:

$$\Delta\omega_g = \frac{S_{b_1}}{S_{b_2}}\frac{(\Delta p_{vsc} - \Delta P_{load})s}{K_g\omega_b} + \Delta\omega_e \tag{III-35}$$

By putting (III-35) in (III-28), the following expression is obtained:

$$\Delta p_{vsc} = \frac{1}{1+\frac{1}{k_iK_C}s+\frac{1}{k_iK_C\omega_c}s^2}\Delta p^* - \frac{\frac{\omega_b}{k_i\omega_c}s}{1+\frac{1}{k_iK_C}s+\frac{1}{k_iK_C\omega_c}s^2}\Delta\omega_e - \frac{\frac{S_{b_1}}{S_{b2}}\frac{1}{k_i\omega_cK_g}s}{1+\frac{1}{k_iK_C}s+\frac{1}{k_iK_C\omega_c}s^2}(\Delta p_{vsc} - \Delta P_{load}) \tag{III-36}$$

From (III-4), $\Delta\omega_e$ can be written as,

$$\Delta\omega_e = \frac{S_{b_1}}{S_{b2}} \frac{R_{SG}\left(1+T_D s\right)}{\left(1+\left(T_N+2H_{eq}R_{SG}\right)s+2H_{eq}R_{SG}T_D s^2\right)}(\Delta p_{vsc} \text{ - } \Delta P_{load}) \qquad \text{(III-37)}$$

By replacing $\Delta\omega_e$ in (III-36) by (III-37), the transfer functions of the active power with respect to the setpoint Δp^* and ΔP_{load} are obtained:

$$\Delta p_{vsc} = \frac{1+\left(T_N+2H_{eq}R_{SG}\right)s+2H_{eq}R_{SG}T_D s^2}{1+as+bs^2+cs^3+ds^4}\Delta p^* + \frac{1}{S_{b2}}\frac{\dfrac{R_{SG}\omega_b\left(1+T_D s\right)s}{k_i\omega_c}}{1+as+bs^2+cs^3+ds^4}\Delta P_{load} \qquad \text{(III-38)}$$

with,

$$a = \frac{1}{k_i K_c} + T_N + 2H_{eq}R_{SG} + \frac{\omega_b S_{b1} R_{SG}}{k_i \omega_c S_{b2}}$$

$$b = \frac{1}{k_i\omega_c}\left(\frac{1}{K_c}+\frac{S_{b1}}{S_{b2}K_g}\right) + \frac{T_N+2H_{eq}R_{SG}}{K_c k_i} + \frac{\omega_b S_{b1} R_{SG} T_D}{k_i\omega_c S_{b2}} + 2H_{eq}R_{SG}T_D$$

$$c = \frac{T_N+2H_{eq}R_{SG}}{k_i\omega_c}\left(\frac{1}{K_c}+\frac{S_{b1}}{S_{b2}K_g}\right) + \frac{2H_{eq}R_{SG}T_D}{k_i K_c}$$

$$d = \frac{2H_{eq}R_{SG}T_D}{k_i\omega_c}\left(\frac{1}{K_c}+\frac{S_{b1}}{S_{b2}K_g}\right)$$

The obtained transfer function is a 4th order.

2nd simplified model:
Many simplifications can be derived by assuming that all frequencies are equal:

$$\Delta\omega_g = \Delta\omega_e = \Delta\omega_m \qquad \text{(III-39)}$$

The validity of this assumption has been proved for "Strategy A".
Let's recall the differential equation of the Strategy B-based VSC:

$$\Delta p^* \text{ - } \Delta p_{vsc} = \frac{\omega_b}{\omega_c k_i} s\Delta\omega_m + \underbrace{\frac{\omega_b}{k_i}(\Delta\omega_m \text{ - } \Delta\tilde{\omega}_g)}_{Damping} \qquad \text{(III-40)}$$

Since it is assumed that $\Delta\omega_g \sim \Delta\tilde{\omega}_g$ and $\Delta\omega_m = \Delta\omega_g$, the damping term in (III-40) is neglected, which yields:

$$\Delta p^* \text{ - } \Delta p_{vsc} = \frac{\omega_b}{\omega_c k_i} s\Delta\omega_e \qquad \text{(III-41)}$$

By putting Δp_{vsc} from (III-37) in (III-41), the grid frequency dynamics with respect to the setpoint Δp^* and ΔP_{load}:

$$\Delta\omega_e = \frac{S_{b1}}{S_{b2}} \frac{R_{SG}(1+T_D s)}{1+\left(T_N + 2R_{SG}\left(H_{eq} + H_{VSC}\frac{S_{b1}}{S_{b2}}\right)\right)s + \left(2R_{SG}T_D\left(H_{eq} + H_{VSC}\frac{S_{b1}}{S_{b2}}\right)\right)s^2} (\Delta p^* - \frac{1}{S_{b1}}\Delta P_{load}) \qquad \text{(III-42)}$$

with $H_{vsc} = \omega_b / (2k_i\omega_c)$.

By replacing $\Delta\omega_g$ in (III-28) by $\Delta\omega_e$ in (III-42), the following transfer function is deduced:

$$\Delta p_{vsc} = \frac{1+\left(T_N + 2H_{eq}R_{SG}\right)s + 2H_{eq}R_{SG}T_D s^2 \Delta p^* \quad + \quad 2H_{VSC}\frac{R_{SG}\left(1+T_D s\right)s}{S_{b2}}\Delta P_{load}}{\underbrace{\left(1+\left(T_N + 2R_{SG}\left(H_{eq} + H_{VSC}\frac{S_{b1}}{S_{b2}}\right)\right)s + \left(2R_{SG}T_D\left(H_{eq} + H_{VSC}\frac{S_{b1}}{S_{b2}}\right)\right)s^2\right)}_{T_1}\underbrace{\left(1+\frac{1}{k_i K_C}s + \frac{1}{k_i K_C \omega_c}s^2\right)}_{T_2}} \qquad \text{(III-43)}$$

(III-43) is a product of two 2nd order transfer functions.
In Table III-3, the eigenvalues λ_i of the 1st and the 2nd models are compared.

Table III-3 Eigenvalues and zeros of the 1st and 2nd models

1st simplified model		2nd simplified model	
λ_{1-2}	$-0.188 \pm 0.416i$	λ_{1-2}	$-0.188 \pm 0.416i$
λ_{3-4}	$-8.42 \pm 11.9i$	λ_3	-8.69
		λ_4	-22.7

The table confirms that the dominant eigenvalues of both models are exactly the same. These latter are linked to T_1 in (III-43). Their damping and the natural frequency are expressed as:

$$\zeta = \frac{1}{2}\frac{T_N + 2R_{SG}\left(H_{eq} + H_{VSC}\frac{S_{b1}}{S_{b2}}\right)}{\sqrt{2R_{SG}T_D\left(H_{eq} + H_{VSC}\frac{S_{b1}}{S_{b2}}\right)}}, \qquad \omega_n = \sqrt{\frac{1}{2R_{SG}T_D\left(H_{eq} + H_{VSC}\frac{S_{b1}}{S_{b2}}\right)}} \qquad \text{(III-44)}$$

To prove the validity of these theoretical approaches, time-domain simulations are performed in Figure III-24, where, active powers step of $p^* = 0.5$ p.u is applied.
The results show the high accuracy of the 1st model comparing to the nonlinear model in Figure III-1 (denoted by “simulation model” in the figures). As expected, a small difference is noticed in the first hundreds of milliseconds for the 2nd model. Globally, the 2nd model is of high interest since it allows determining analytically the dominant response of the active power and the parameters that affect it.
The frequency change resulting from the active power change is illustrated in Figure III-25. The three models of the frequency behave in quite similar manner, which confirms the effectiveness of the models. Since the response of the 2nd order and the 4th order models is quite the same, the dominant modes of the frequency are preserved. This can be confirmed on the Bode diagram (see Figure III-26), where it can be noticed that the 2nd model is more effective when the system is operating bellow 2 rad/s. Therefore, the 2nd order model is enough to analyze the frequency behavior in this case.

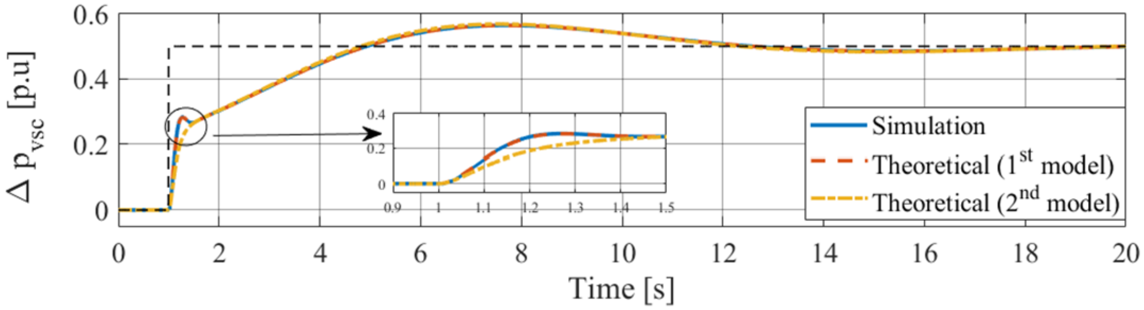

Figure III-24 - Active power dynamics with respect to the active power setpoint change.

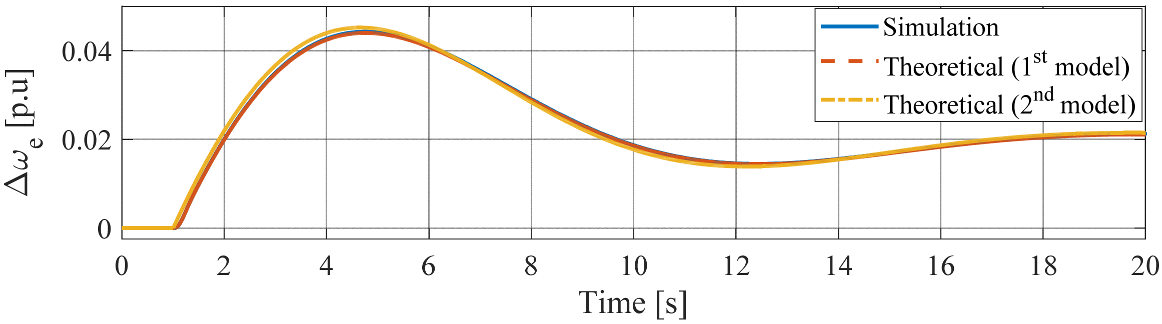

Figure III-25 - Frequency dynamics with respect to the p^* setpoint change

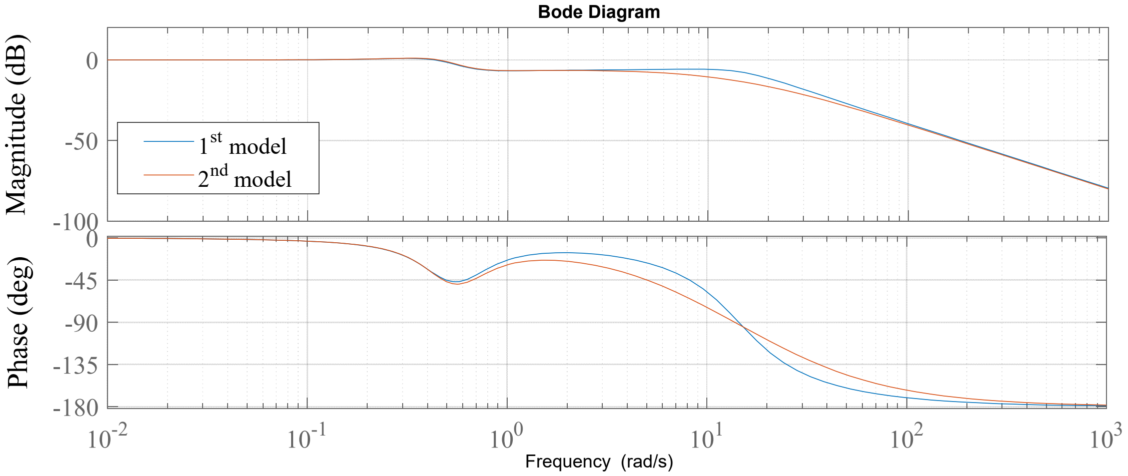

Figure III-26 - Bode diagram of the developed models

With “Strategy A”, the grid frequency dynamics are completely decoupled from the VSC control dynamics, while, with “Strategy B”, the grid frequency dynamics are modified by the red term H_{VSC} shown in Figure III-27 (This figure is a graphical representation of (III-42)).

The equation drawn from the block diagram in Figure III-27 can be written as:

$$2\left(H_{eq}+H_{VSC}\frac{S_{b1}}{S_{b_2}}\right)\Delta\omega_e s=\Delta p_m+\frac{S_{b_1}}{S_{b2}}\Delta p^* - \frac{1}{S_{b_2}}\Delta P_{load} \tag{III-45}$$

This equation is mathematically similar to the swing equation of the aggregated SGs (see Appendix F). This means, power converters based on “Strategy B” can be mathematically seen as real SG.

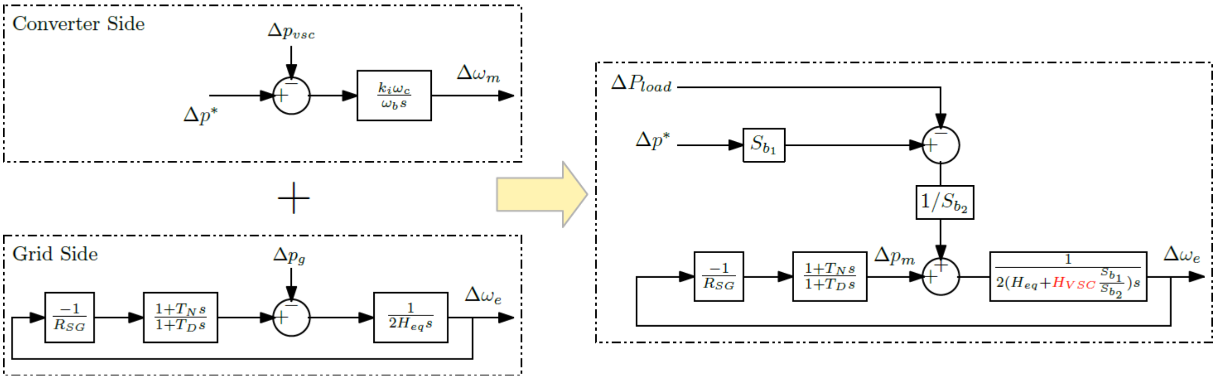

Figure III-27 - Block diagram to describe the grid frequency dynamics

In case of a load change disturbance $\Delta P_{load} = 500$ MW, the inertial support from the Strategy B-based grid-forming VSC is manifested in a strong increase of the active power in the transient. In this case, the amount of the active power requested depends on the dynamics of the mechanical source ΔP_m and on the system inertia constant. The active power requested and the frequency dynamics during the disturbance are calculated theoretically in (III-42) and (III-43). These models are validated through time-domain simulation in Figure III-28.

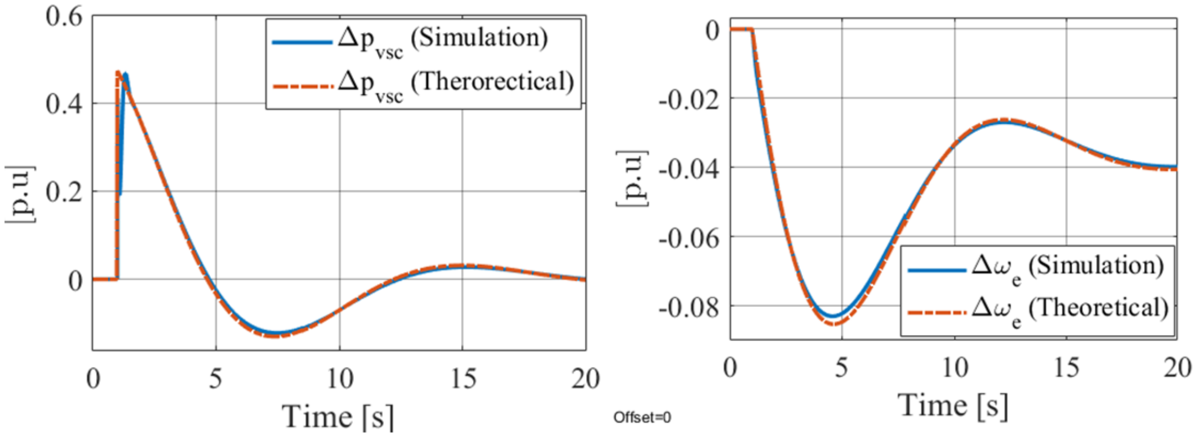

Figure III-28 - Theoretical model validation of a system subjected to a load change.

As for "Strategy A", the increase of the inertia constant decreases the damping of the frequency and slows down its variation by decreasing the natural frequency. Table III-4 demonstrates the positive side effect of H_{VSC} on the RoCoF and the frequency Nadir.

Table III-4 Characteristics of the frequency dynamics with high and low inertia constant

H_{VSC} = 5 s		**H_{VSC} = 0.5 s**	
RoCoF [Hz/s]	Nadir	RoCoF [Hz/s]	Nadir
2.5	45.7 Hz	4.54	44.9 Hz

If the outer droop control is enabled, the overall system can be presented by the simplified block diagram depicted in Figure III-29. The impact of the droop control on the system dynamics is the same for "Strategy A" and "Strategy B". Actually, the outer droop control acts rapidly on the power reference of the VSC, which results in a fast frequency support. This results in the improved frequency nadir.

Because of the fast frequency support linked to the droop control, the inertia impacts the RoCoF, whereas, it has a small effect on the frequency nadir. This statement is demonstrated through the comparative approach in Table III-5.

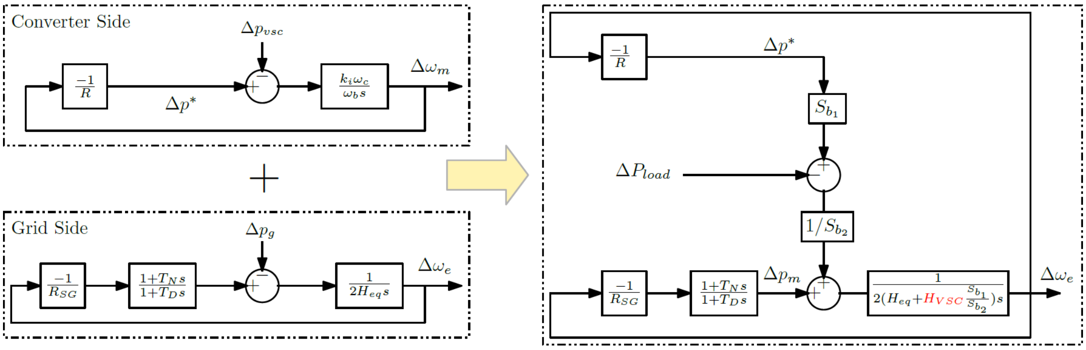

Figure III-29 - Block diagram to describe the grid frequency dynamics in response to a load change

Table III-5 Characteristics of the frequency dynamics with and without droop control

	With droop control			Without droop control		
	D [%]	*RoCoF*	*Nadir*	D [%]	*RoCoF*	*Nadir*
$H_{VSC} = 5s$	47.70	2.5 Hz/s	48.61 Hz	125.95	2.5 Hz/s	45.7 Hz
$H_{VSC} = 0.5s$	54.62	4.54 Hz/s	48.54 Hz	170.31	4.54 Hz/s	44.9 Hz

To illustrate the results in Table III-5, time-domain simulations are gathered in Figure III-30

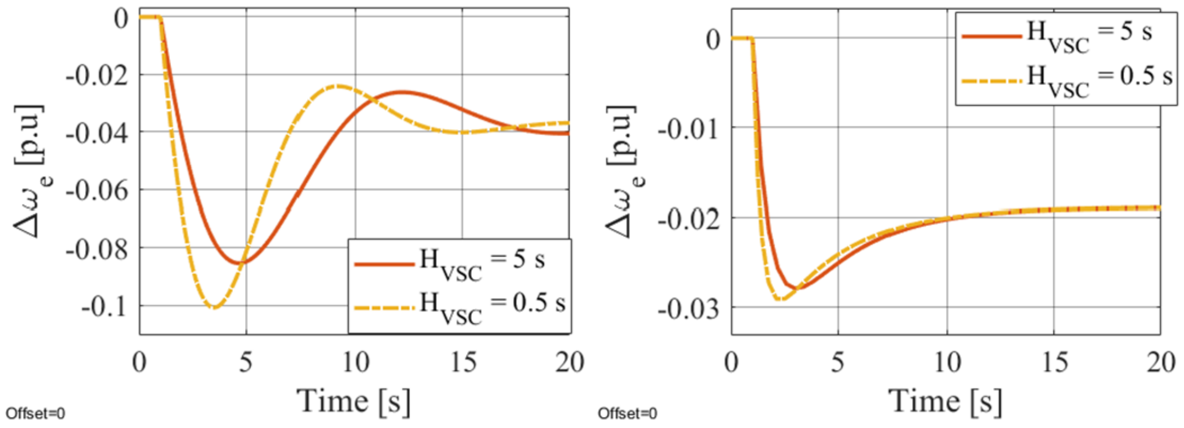

(a) Without droop control

(b) With droop control

Figure III-30 - Active power requested to compensate the power unbalance during the transient

About the active power transient during the disturbances, the same conclusions drawn in section III.3.3 are still valid for “Strategy B”.

III.5 Droop control without dedicated PLL “Strategy C”: Frequency support and robustness analysis

In most of the grid-forming applications, no PLL is used [20], [46], [73], [85], [106], [123], [126]. The “Strategy B” can be simplified by replacing the PLL by a constant value for the frequency.

III.5.1 Control structure

The changes made in the power controller based on "Strategy B" are shown in Figure III-31.

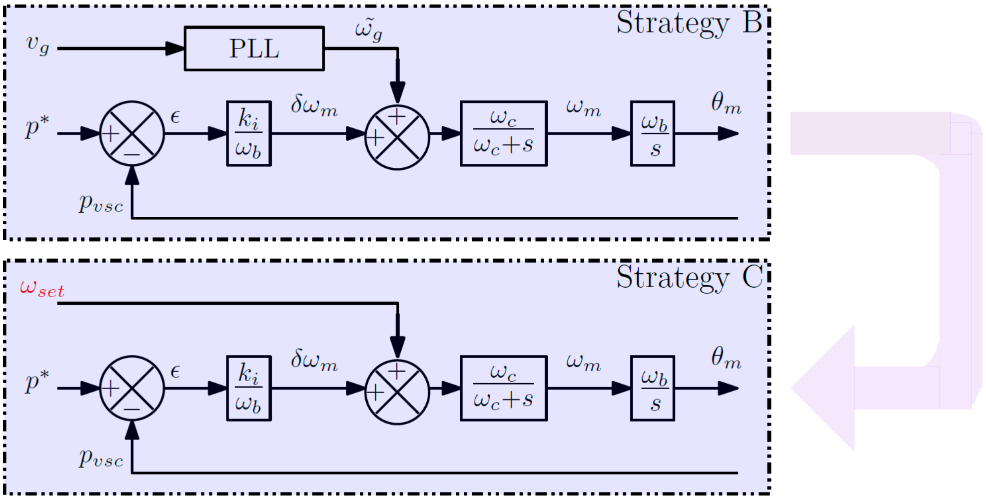

Figure III-31 - Control structure of "Strategy C"

Based on Figure III-31, the differential equation obtained from "Strategy C" with respect to the output frequency ω_m is written as follows,

$$\frac{\omega_b}{k_i\omega_c}\frac{d\omega_m}{dt} = p^* - p_{vsc} - \frac{\omega_b}{k_i}(\omega_m - \omega_{set}) \tag{III-46}$$

Compared to "Strategy B", "Strategy C" is emulating the inertial effect in a similar way.

The grid-frequency estimation for "Strategy B" aims to guarantee an active power tracking in the steady state. Since no grid frequency estimation is used for "Strategy C", new questions arise:

- What is the impact of the ω_{set} on the static and dynamic behavior of the system?
- Is the tuning of k_i and ω_c still effective?
- Does "Strategy C" remain robust to the topological change and to the grid impedance variations?

These questions are treated in the following sections. As for "Strategy B", the connection to a fixed-frequency grid is first analyzed. The study of the variable-frequency grid is much faster than previously since most of the considerations already given for "Strategy B" can be extended to "Strategy C" as it will be shown.

III.5.2 Stability, dynamics and robustness analysis

As for "Strategy B", a simple approach is proposed for the dynamic analysis.

Once again, a quasi-static model is derived and validated through a comparison with the nonlinear system illustrated in Figure III-32. The goal is to highlight the dominant poles and to ease the analysis of the system.

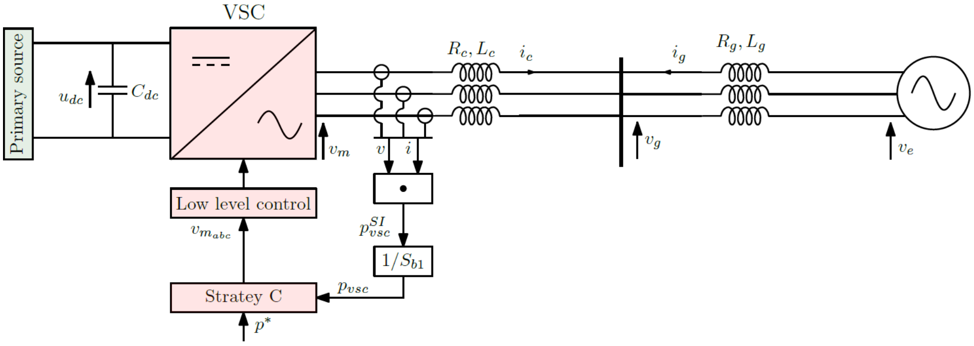

Figure III-32 - Simplified VSC connected to an AC system

III.5.2.1 Dynamic analysis of the active power exchange

III.5.2.1.1 Simplified dynamic analysis

The system in Figure III-32 can be presented by the simplified block diagram in Figure III-33.

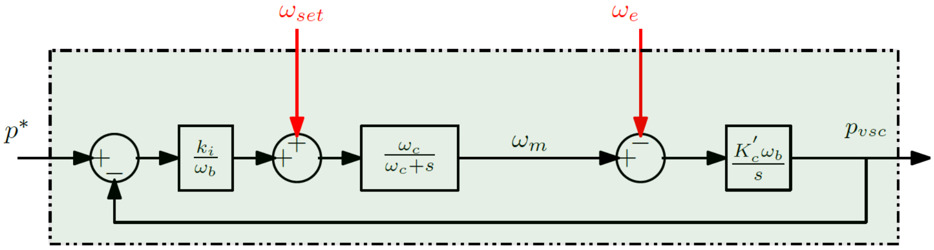

Figure III-33 - Quasi-static active power regulation

Based on Figure III-33, the differential equation of “Strategy C” can be written as,

$$\delta_m = \left[\left(p^* - p_{vsc}\right)\frac{k_i}{\omega_b} + \Delta\omega_{set}\right]\frac{\omega_c}{\omega_c + s}\frac{\omega_b}{s} \tag{III-47}$$

In small-signal

$$\Delta\delta_m = \left[\left(\Delta p^* - \Delta p_{vsc}\right)\frac{k_i}{\omega_b} + \Delta\omega_{set}\right]\frac{\omega_c}{\omega_c + s}\frac{\omega_b}{s} \tag{III-48}$$

The active power flow between the VSC and the AC grid is expressed as,

$$\Delta p_{vsc} = K_c^{'}\left(\Delta\delta_m - \Delta\delta_e\right) \tag{III-49}$$

with $K_c^{'} = V_m V_e / (X_c + X_g)$.

Putting (III-49) in (III-48) yields a determination of the closed-loop transfer function:

$$\Delta p_{vsc} = \frac{1}{1 + \frac{1}{k_i K_c{'}}s + \frac{1}{k_i K_c{'}\omega_c}s^2}\Delta p^* - \frac{\frac{\omega_b}{k_i}(1 + \frac{s}{\omega_c})}{1 + \frac{1}{k_i K_c{'}}s + \frac{1}{k_i K_c{'}\omega_c}s^2}(\Delta\omega_{set} - \Delta\omega_e) \tag{III-50}$$

The steady state error ε of the transfer function in (III-50) is expressed as follow:

$$\varepsilon = \lim_{s\to 0} s\left[\Delta p^* - \Delta p_{ac}\right] = -\frac{\omega_b}{k_i}\left(\Delta\omega_{set} - \Delta\omega_e\right) \tag{III-51}$$

One can notice from (III-51) that:

- In steady state, if the grid frequency changes, the active power will be adjusted with respect to the following equation:

$$\Delta p^{*} - \Delta p_{vsc} = \frac{\omega_b}{k_i}\left(\Delta\omega_{set} - \Delta\omega_e\right) \tag{III-52}$$

(III-52) is equivalent to the expression of the primary frequency control (droop control). However, as the frequency is deduced from the power mismatch, this function is also called “*Inverse droop control*” [127], [128]. Therefore, the feed-back gain k_i / ω_b becomes a droop gain. It has an influence on the load sharing between different sources. It cannot be tunable in the same way as with “Strategy B”. From (III-46) and (III-52), it can be concluded that “Strategy C” is a hybrid control which plays the role of a primary frequency control and inertial effect emulator.

The characteristic polynomial function of the system derived from (III-50) is given by:

$$F(s) = 1 + \frac{1}{k_i K_c'} s + \frac{1}{k_i K_c'} s^2 \tag{III-53}$$

The damping ratio ζ and the natural frequency ω_n are:

$$\zeta = \frac{1}{2}\sqrt{\frac{\omega_c}{k_i K_c'}}, \qquad \omega_n = \sqrt{k_i K_c' \omega_c} \tag{III-54}$$

As it can be noticed in (III-54), the grid impedance has an influence on the dominant poles. As explained previously, k_i coefficient is linked with the load sharing capability so it has to be chosen with respect to external considerations. ω_c is the only degree of freedom in the control. High values of ω_c ensures acceptable active power dynamic and negligible inertial effect, whereas, low values of ω_c allows emulating the inertial effect, but it leads to a very poor system damping. Consequently, it is not possible to achieve both objectives only using this degree of freedom.

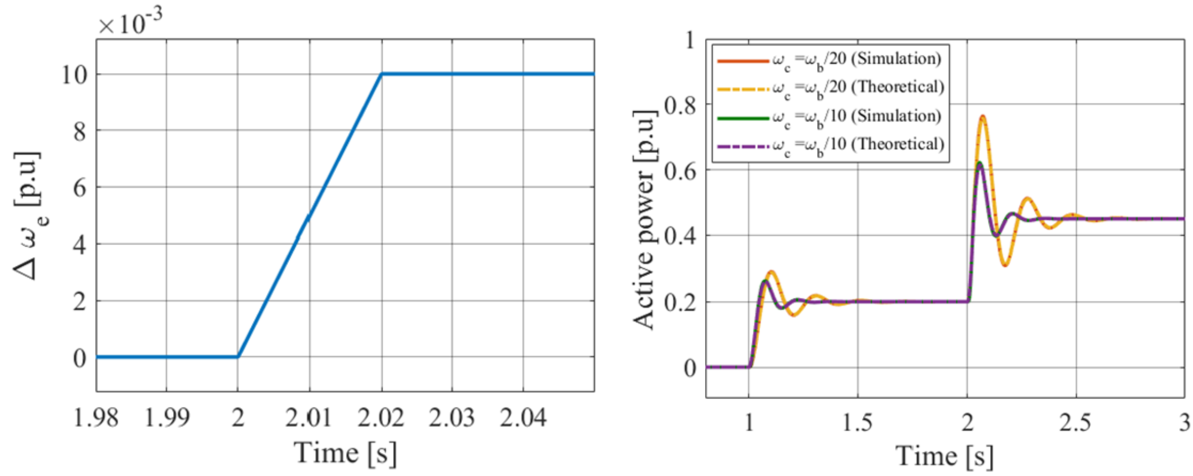

Figure III-34 - Validation of the simplified model

The accuracy of the simplified developed model in (III-50) and the correctness of the theoretical information above are validated through the time-domain simulations shown in Figure III-34. The following test case is performed:

- t=1 s, a power step of $p^* = 0.2$ p.u is applied.
- t=2 s, a frequency ramp of $\Delta\omega_e = 0.01$ p.u with a slope of 0.5 is applied.

The simulation emphasizes that the active power depends on its reference p^* and also on the grid frequency.

III.5.2.2 Stabilization of grid-forming VSC based on “Strategy C” in case of large inertia constant

Since the gain k_i cannot be modified to adjust the dynamic of the power loop, a derivative action is used to stabilize the system. A pure derivative action is infeasible. Thus, a lead-lag compensator can be used for the same purpose.

The expression of the lead-lag compensator is given,

$$C(s) = \frac{1+T_1 s}{1+T_2 s} \qquad (T_1 > T_2) \tag{III-55}$$

Two possible positions of the lead-lag controller are illustrated in Figure III-35.

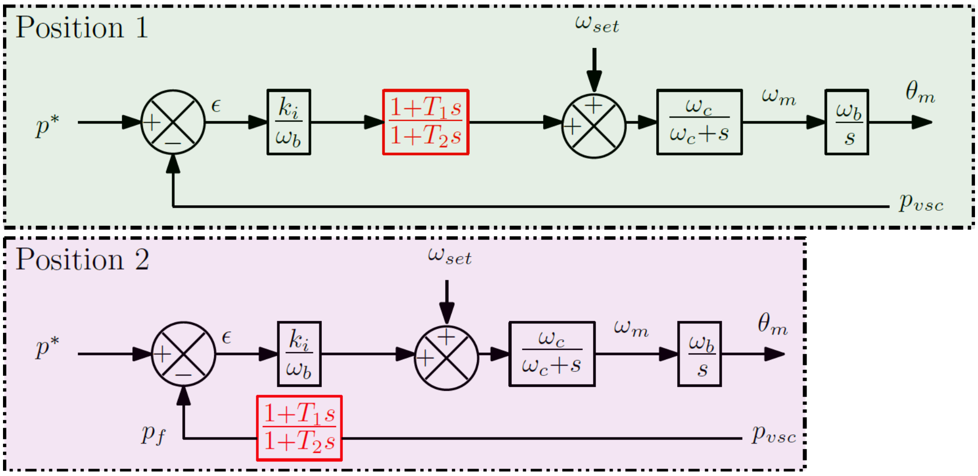

Figure III-35 - Controller positions

The transfer functions p_{vsc} / p^* for both controllers’ positions are expressed as,

$$\frac{p_{vsc}}{p^*} = \frac{1+T_1 s}{1+\left(\frac{1+k_i T_1 K_c'}{k_i \omega_c K_c'}\right)s+\left(\frac{1+T_2\omega_c}{k_i \omega_c K_c'}\right)s^2+\frac{T_2}{k_i \omega_c K_c'}s^3} \tag{III-56}$$

$$\frac{p_{vsc}}{p^*} = \frac{1+T_2 s}{1+\left(\frac{1+k_i T_1 K_c'}{k_i K_c'}\right)s+\left(\frac{1+T_2\omega_c}{k_i \omega_c K_c'}\right)s^2+\frac{T_2}{k_i \omega_c K_c'}s^3} \tag{III-57}$$

where (III-56) is linked to the controller in position 1 and (III-57) refers to the controller in position 2.

From both transfer functions, the system has three dominant modes (3rd order system). The difference between them lies in the zeros of the transfer function. Since $T_2 < T_1$, the impact of the zero is lower when the controller is in the position 2. Therefore, the dynamic performances of the active power are better. In the following, the lead-lag controller is located in position 2.

To ensure a good operation of the system based on the proposed improvements, the following constraints have to be considered:

- T_1 should be smaller that ω_c^{-1}. The goal is to avoid the impact of the derivative action on the frequency, and also, to avoid the compensation between the numerator of the controller and the denominator of the low-pass filter.
- T_1 / T_2 is between 5 and 10. This interval guarantees the feasibility of the control.

In Figure III-36, parametric sensitivities of the lead-lag controller with respect to the damping of the system are performed. The aim is to improve the system dynamics based on the chosen inertia constant e.g., H =5 s (i.e., $\frac{k_i}{\omega_b}$ = 4% and ω_c = 2.5 rad/s). ζ =0.7 is obtained for $\lambda_{1\text{-}2}$ with T_2 = 0.022 s and T_1 = 0.121 s. These values respect the constraints imposed above (Figure III-36). However, the chosen values make $\lambda_3 = \text{-}14.5$ dominant against $\lambda_{1\text{-}2} = \text{-}16.76 \pm 14.6i$ in the present condition (SCR = 20). Thus the active power dynamics in low frequencies depend mainly on λ_3.

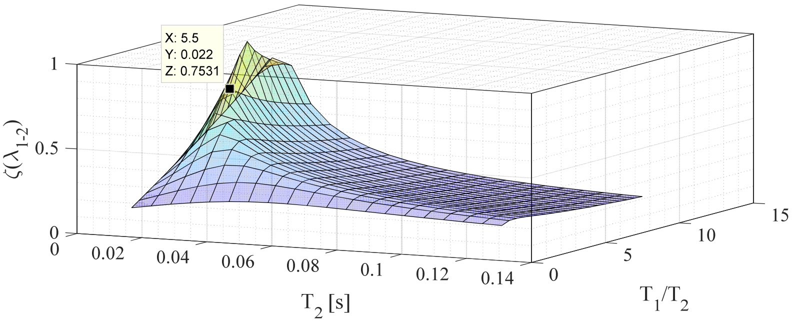

Figure III-36 - Damping evolution of active power oscillatory modes in respect with the controller parameters

The improvements brought by the proposed controller are well demonstrated through the time-domain simulations carried-out in Figure III-37. These improvements are considered in the rest of this thesis.

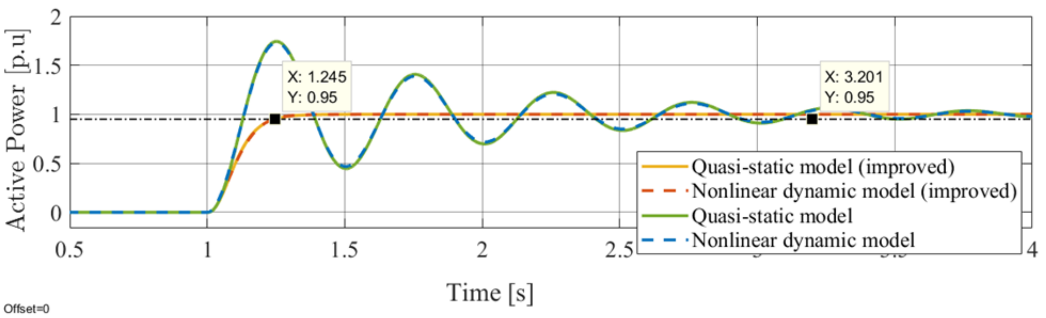

Figure III-37 - Improvement of the active power dynamic behavior with H_{VSC}=5s. SCR = 20

III.5.2.3 Control stability and robustness against AC grid stiffness

Similarly to “Strategy A” and “Strategy B”, the robustness and stability of “Strategy C” has to be addressed.

Based on the linear model in (III-57), the evolution of the eigenvalues with respect to the SCR is illustrated in the pole map shown in Figure III-38.

As expected from the simplified model, the obtained results show that the active power dynamics are impacted by the grid impedance change. Indeed, the decrease of the SCR leads to a decrease of the real part of λ_3, whereas, λ_{1-2} are moving towards the origin. Consequently, $\lambda_{1-2} = -3.02 \pm 5.03i$ (SCR = 1.2) become the dominant modes that impose the active power response in low frequencies.

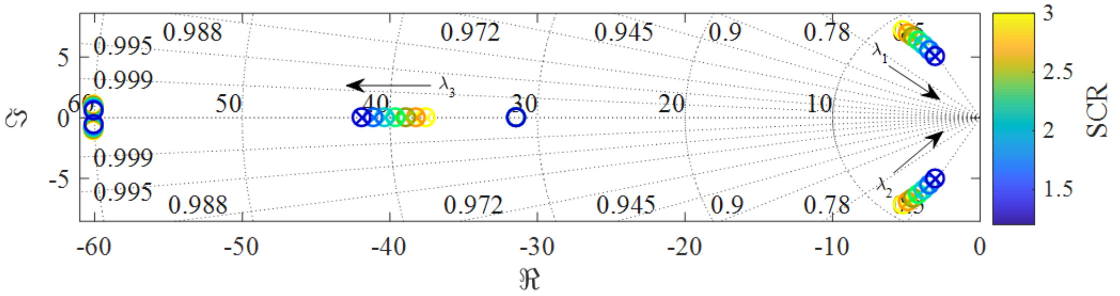

Figure III-38 - Dominant eigenvalues evolution with respect to the AC grid stiffness, ‘*O*’ refers to the full linear dynamic model, ‘*X*’ refers to the developed simplified model

Time-domain simulations in Figure III-39 aim to support the linear analysis above.

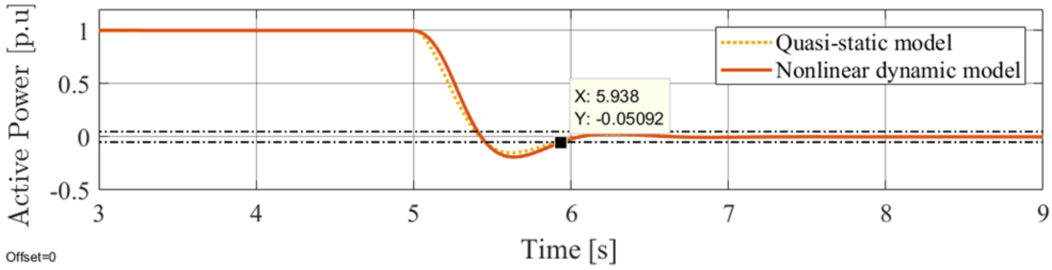

Figure III-39 - Active power dynamics under SCR = 1.2. The operating point is set to 1 p.u

Firstly, the active power is driven to its rated value, then, at t=5 s, a power step of p^* = -1 p.u is applied to the system. One can remark that the nonlinear system is stable. Moreover, in spite of the small difference noticed between the linear and the nonlinear models, the dynamic trends are still effective, where the response time of the nonlinear model is closer to the theoretical one $T_{5\%}^{R}$ = 938 ms. It can be concluded that the stability is guaranteed on a very wide range of SCR. However, the time response for the active power is widely modified.

III.5.3 Frequency support of the grid-forming VSC based on Strategy C

As already mentioned, “Strategy C” combines two features i.e., primary frequency control and inertial effect. The overall system in Figure III-1 based on Strategy C can be represented by the simplified block diagram in Figure III-40. The droop gain in this case is ω_b / k_i instead of $1/R$. Assuming that $\Delta p_{vsc} = \Delta p_f$, the simplified block diagram of “Strategy C” and the one of “Strategy B” are the same. This assumption hold true since the dynamics of the lead-lag compensator are faster than the frequency dynamics.

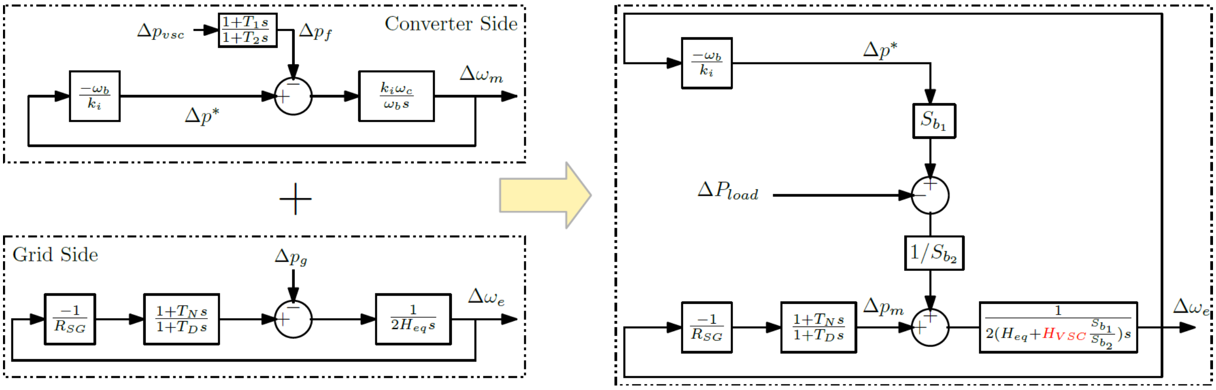

Figure III-40 - Block diagram to describe the grid frequency dynamics in response to a load change

The resemblance between “Strategy B” and “Strategy C” in terms of frequency dynamics is demonstrated in Figure III-41. From the obtained results, it can be said that the conclusions drawn for “Strategy B” with a droop control are valid for “Strategy C”.

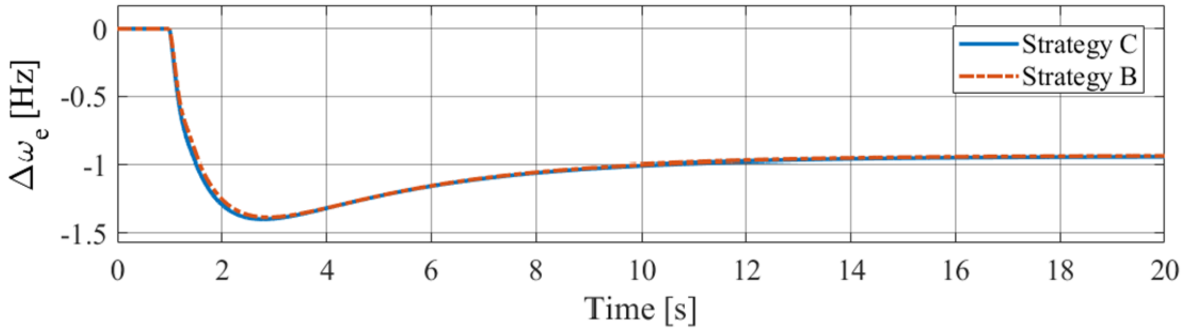

Figure III-41 - Comparison between “Strategy B” and “Strategy C” in terms of a grid supporting

III.6 Association of two power electronic converters

In this section, the considerations made with the equivalent voltage source are extended to the association of 2 power converters. The aim is to show the stable operation of small interconnected system based on different control laws.

The grid case used in this section is illustrated in Figure III-42. It consists of two converters with the same rated power (1000 MW) driven by grid-following or grid-forming control laws. The converters are connected to a P_{load} via PI distributed lines. The line parameters are listed in the following table.

Table III-6 Distributed line parameters

Symbol	Value
R_{line}	0.03 Ω/km
X_{line}	0.3 Ω/km

A load change of 700 MW is applied to the system while considering the following modes:

1- Converter 1 is driven by “Strategy B”; Converter 2 is driven by “Strategy B”. The length of the lines is the same (100km).
2- Converter 1 is driven by “Strategy B”; Converter 2 is driven by “Strategy B”. Line 1 length is 100km and the line 2 length is 10km.
3- Converter 1 is driven by “Strategy C”; Converter 2 is driven by “Strategy A”. The length of the lines is the same (100km).
4- Converter 1 is driven by “Strategy C”; Converter 2 is driven by “Strategy A”. Line 1 length is 100km and the line 2 length is 10km.
5- Converter 1 is driven by “Strategy C”; Converter 2 is driven by “Grid-following”. The length of the lines is the same (100km).
6- Converter 1 is driven by “Grid-following”; Converter 2 is driven by “Strategy C”. Line 1 length is 100km and the line 2 length is 10km.

In all cases a droop control is enabled for both VSCs. The results are given in Figure III-43.

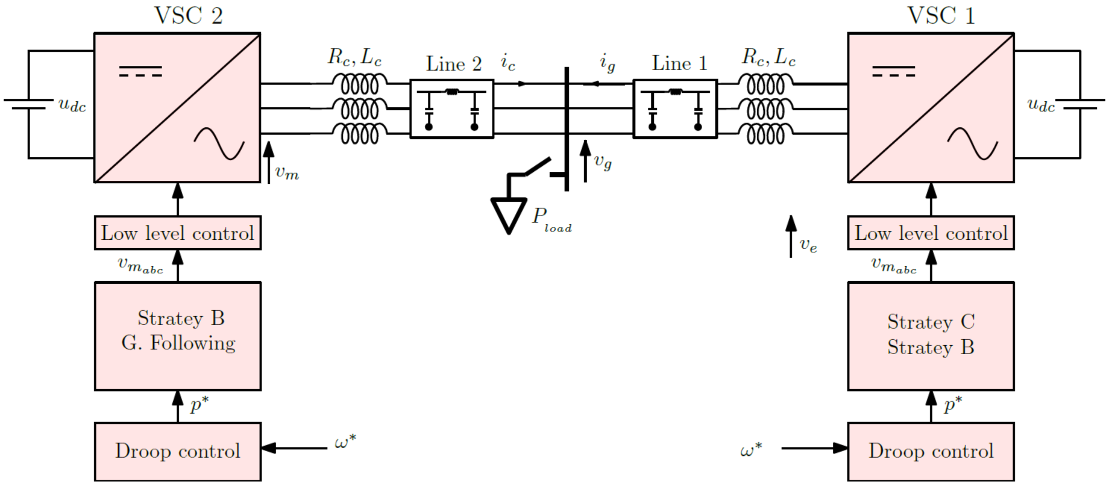

Figure III-42 - Interconnection of two VSCs based on different control strategies

From the simulations, the following conclusions are drawn:

- The system is stable in all the proposed case studies.
- Following a load change, it can be clearly noticed from Figure III-43.1, Figure III-43.2, Figure III-43.3 and Figure III-43.4 that power converters react naturally to the power demand according to their output impedances. Indeed, when the electrical distance is the same between VSC1 and VSC2, the power is equally distributed between them. Otherwise, the converter electrically close to the load provides more power.
- In Figure III-43.5 and Figure III-43.6, the transient behavior of power converters is fundamentally different regardless the length of lines towards the load i.e.; power converter 2 takes all the load despite being farther from the load than the converter 1, which confirms that power converter 2 behaves as a voltage source, and power converter 1 behaves as a current source.

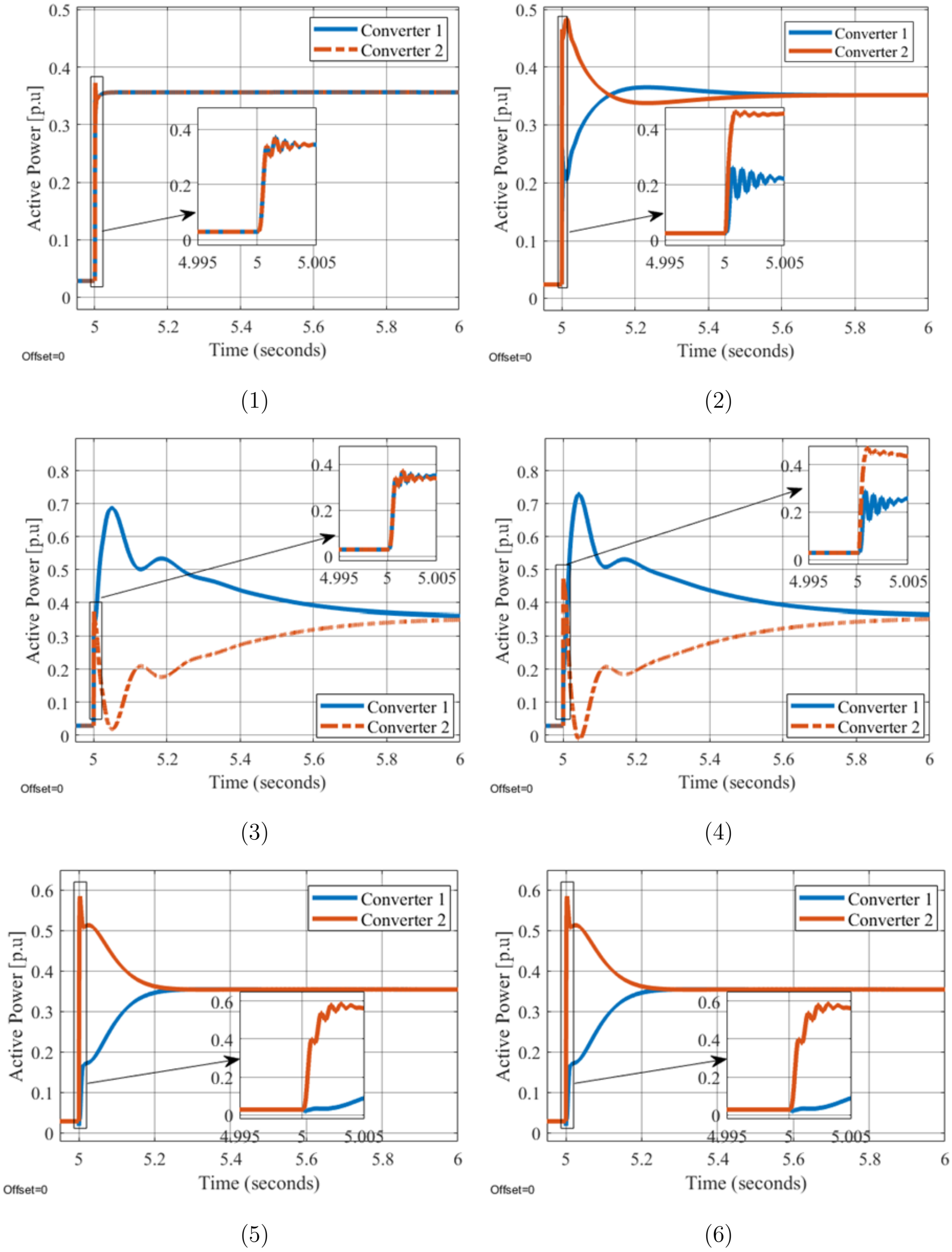

(1) (2)

(3) (4)

(5) (6)

Figure III-43 - Transient behavior of power converters following a load change. (1) Test case 1, (2) Test case 2, (3) Test case 3, (4) Test case 4, (5) Test case 5, (6) Test case 6

The preceding sections were mainly interested in the frequency and active power aspects. The next section deals with the reactive and AC voltage management.

III.7 AC voltage and reactive power management

In this section, AC voltage and reactive power management are briefly discussed. Indeed, the permanent primary voltage regulation for synchronous machine at the local level can be compared to the inner voltage regulation for a power converter. This regulation stage aims to set an instantaneous AC voltage behind the transformer impedance. An intermediate stage of the voltage setpoint management through the reactive droop control can be added to regulate locally the reactive power sharing between different units. This regulation stage may react along the same time scale as the primary voltage control (from milliseconds to seconds):

$$V_m^* = V_{mset} + n_q \left(Q^* - Q_{ac} \left(\frac{1}{1+T_Q s} \right) \right) \tag{III-58}$$

where, $V_{m_{set}}$, Q_{set}, n_q, Q_{ac} and T_Q are the initial voltage setpoint, the reactive power setpoint, the reactive droop gain, the measured reactive power, and the reactive power loop time constant, respectively. Note that the low-pass filter aims to eliminate the reactive power noises from the voltage regulation loop.

The reactive droop gain should be designed so as to respect the AC voltage requirement (+5%, -10%). It is usually designed using the following formula:

$$n_q = \frac{V_{m_{\max}} - V_{m_{\min}}}{Q_{\max} - Q_{\min}} \tag{III-59}$$

The maximum and the minimum reactive power exchanged during normal operation are around ±30% of the rated power. Note that these values determine the maximum value of the droop gain n_q that should not be exceeded, otherwise the voltage drop or rise with respect to the reactive power exchange will be important. Moreover, an important voltage rise leads to a physical saturation of the power converter ($m \le 2V_{\max} / U_{dc}$). Nevertheless, the droop gain can be set to lower values $n_q < 0.25$. In this thesis, the reactive droop gain is set to zero. However, its dynamics are including in all models for future work. Referring to the literature, some improvements for the reactive power droop have been proposed [129], [130]. However, they are more suitable for well-known system architectures such as those of Microgrids and UPS, than those of large power transmission systems.

A higher level of the AC voltage regulation can be also considered: in this case, the AC voltage setpoint change is handled by system operators, and it is done at the scale of some seconds to minutes [71]. In a future power system based on PE, the high level AC voltage management may keep the same principle as today.

III.8 Conclusion

In this chapter, three control strategies are presented and studied. Their contribution to the AC grid support and their stability in several conditions were investigated. The main differences between them are listed in Table III-7.

Table III-7 Functionalities and performances of control strategies

	Active power tracking	**Frequency support**	**Active power saturation**	**Inertial effect**	**Robustness**
Strategy A	++	++	++	-	++
Strategy B	++	++	++	++	+
Strategy C	-	++	-	++	+

From the synthetic Table III-7, some additional precisions are mentioned:

- **VSC based on Strategy A** is able to operate as an active power injector (i.e., active power reference tracking in the steady state). It is robust to the grid topological change. The dynamic behavior of the system based on this strategy is stable and respects the imposed dynamic specifications. It can contribute to the primary frequency support similarly to grid-following converters. However, it cannot be used to provide the inertial support. As a result, the dominance of power converters based on "Strategy A" does not comply with the current frequency requirements.

"Strategy A" can be equipped with a power reference saturation to avoid the converter providing more power than its rated value.

- **VSC based on Strategy B** is able to operate as an active power injector. It is more sensitive to the topological changes of the grid. The active power dynamics based on this strategy are not of the ultimate priority, since it is designed to allow an inertial support, therefore, the active power dynamics depend on the inertia constant. Similarly to "Strategy A", "Strategy B" contributes to the primary frequency support.

This control strategy is also equipped with saturation on the power reference to avoid the converter exceeding its rated power.

- **VSC based on Strategy C** is a hybrid control embedding an inertial effect and a "compulsory" load sharing features. However, "Strategy C" cannot operate as an active power injector and it is sensitive to the topological changes of the grid. "Strategy" C cannot be equipped with saturation on the active power reference. This is one of its major drawbacks.

A theoretical approach has been developed in chapter II and chapter III, allowing a model order reduction, i.e., in grid-connected mode, both "Strategy A and B" can simply be represented by 2nd order systems and "Strategy C" with a 2nd or a 3rd order system. These simplified models are of high accuracy, and allow understanding the dynamic behavior of the active power and frequency.

IV. Inner control of the 2-Level VSC and MMC-VSC in power transmission systems

IV.1 Introduction

In the previous chapter, the grid-forming concept has been explained by using a simplified VSC model. The ideal voltage source does not exist in real life and this chapter aims to link the theoretical approach with real life implementations.
Two different types of converters are studied in this chapter:

- **2-Level VSC technology:** It is always connected to the AC system through an LCL filter when it is controlled as a voltage source. The input LC filter is used to pass the fundamental frequency and attenuate the rest of undesired high order harmonics e.g. Pulse width modulation (PWM) switching effect, which appears in the current and voltage profiles. The presence of the LCL filter requires a voltage control feedback across the filter capacitor. The aim is to guarantee AC voltage stiffness and also to avoid exciting the system resonances when the converter operates in a grid-connected mode. Indeed, the stability of the voltage control is a challenging task in power transmission systems as the 2-Level VSC can be connected to the AC system with no information about the rest of the grid. The main questions to answer are: Do the dynamics of the inner loops (i.e., current and voltage) influence the overall system dynamics studied in the previous chapters? Does the limited bandwidth of the inner control influence the overall stability of the system? These questions are addressed in this chapter.
  Modular Multilevel converter (VSC-MMC): For high power application (e.g. HVDC application), an MMC is used. An input LC filter is not needed due to the high quality of generated output voltage waveform. Therefore, no AC voltage control is needed. However, The VSC-MMCs contain internal capacitors in each submodule, which require some internal loops to control the energy. The main question to answer for the MMC is about a potential interaction between the grid-forming control and the closed-loop energy control which are used in the MMC control.

This chapter is organized as follows;

- Recall on the cascaded control structure and the conventional tuning method of the controllers.
- Propose a method for controllers tuning to ensure more stability and damping especially in grid-connected mode.
- Propose a direct AC voltage control.
- Analyze the decoupling between inner and outer control loops.
- Apply the concept of grid-forming to the VSC-MMC.

IV.2 Grid-forming control for the 2-level voltage source converters with LC filter

IV.2.1 System modeling

Let’s consider the 2-Level voltage source converter interfacing the DC to the AC sides as depicted in Figure IV-1. An LC filter has been added to mitigate the harmonics generated by the converter. The design of the LC filter has to be done while respecting the following criteria:

- Attenuation of PWM harmonics.
- Limitation of the size of the filter.

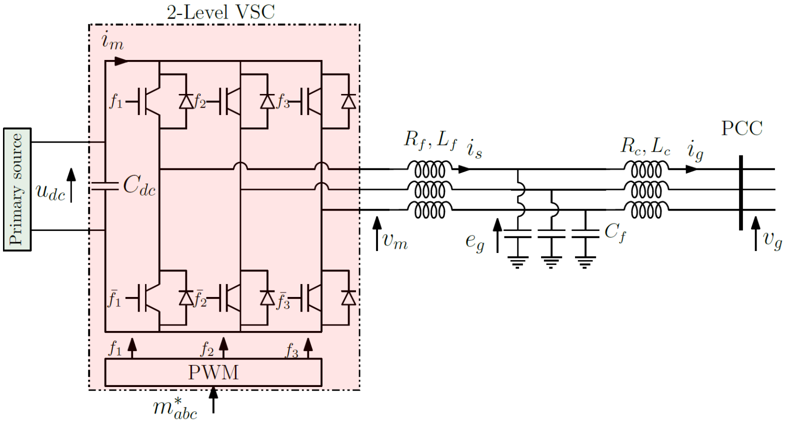

Figure IV-1 - 2-Level voltage source converter connected to the AC system through an LCL filter

The LC filter design method is well explained in many references [131]–[134]. In this thesis, the filter design synthesis in [20] is adopted. The system and output filter parameters are listed in the following table:

Table IV-1 System and control parameters

Symbol	Value	Symbol	Value
P_n	1 GW	$f_{s\omega}$	5 kHz
$\cos\phi$	0.95	u_{dc}	640 kV
E_g (ph-ph)	320 kV	C_f	0.066 p.u
L_f	0.15 p.u	R_f	0.005 p.u
L_c	0.15 p.u	R_c	0.005 p.u

The VSC modelling has already been explained in chapter II, only the modelling of the LCL is detailed in the following lines. In (abc) frame, the LCL filter dynamics are expressed by the following equations,

$$\frac{d}{dt} i_{s_{ab}} = \frac{\omega_b}{L_f}\left(v_{m_{ab}} - e_{g_{ab}} - R_f i_{s_{ab}}\right) \qquad \text{(IV-1)}$$

$$\frac{d}{dt} e_{g_{ab}} = \frac{\omega_b}{C_f}\left(i_{s_{ab}} - i_{g_{ab}}\right) \qquad \text{(IV-2)}$$

$$\frac{d}{dt} i_{g_{ab}} = \frac{\omega_b}{L_c}\left(e_{g_{ab}} - v_{g_{ab}} - R_c i_{g_{ab}}\right) \qquad \text{(IV-3)}$$

Considering a perfect DC side and a balanced AC system ($i_c = -i_a - i_b$ and $v_c = -v_a - v_b$), the overall system contains 6 independent state variables $x = [i_{s_a}\ i_{s_b}\ e_{g_a}\ e_{g_b}\ i_{g_a}\ i_{g_b}]$, 2 control inputs $u = [v_{m_a}\ v_{m_b}]$ and 2 disturbance inputs $h = [v_{g_a}\ v_{g_b}]$.

(IV-1), (IV-2) and (IV-3) can also be represented in d-q frame as following:

$$\frac{L_f}{\omega_b}\frac{d}{dt} i_{s_{dq}} = v_{m_{dq}} - e_{g_{dq}} - R_f i_{s_{dq}} \pm L_f \omega_0 i_{s_{dq}} \tag{IV-4}$$

$$\frac{C_f}{\omega_b}\frac{d}{dt} e_{g_{dq}} = i_{s_{abc}} - i_{g_{abc}} \pm C_f \omega_0 e_{g_{dq}} \tag{IV-5}$$

$$\frac{L_c}{\omega_b}\frac{d}{dt} i_{g_{dq}} = e_{g_{dq}} - v_{g_{dq}} - R_c i_{s_{dq}} \pm L_c \omega_0 i_{g_{dq}} \tag{IV-6}$$

Equations (IV-1 & IV-3) depend explicitly on the time. The solution of these equations in steady state is time-variant. Therefore, the control of the electrical variables requires resonant controllers or multi-resonant control [135]. The system model in *d-q* frame is more favorable for control purpose, since the use of a simple PI control achieves acceptable performances.

IV.2.2 AC voltage control

Two different types of control algorithms are proposed. The first control is based on a conventional cascaded control structure. The second control strategy is based on a direct AC voltage generation. It relies on the physical operation of a voltage source converter, where no current and voltage loops based on PI controllers are required.

IV.2.2.1 Cascaded controller structure

The cascaded control structure is recalled in Figure IV-2.

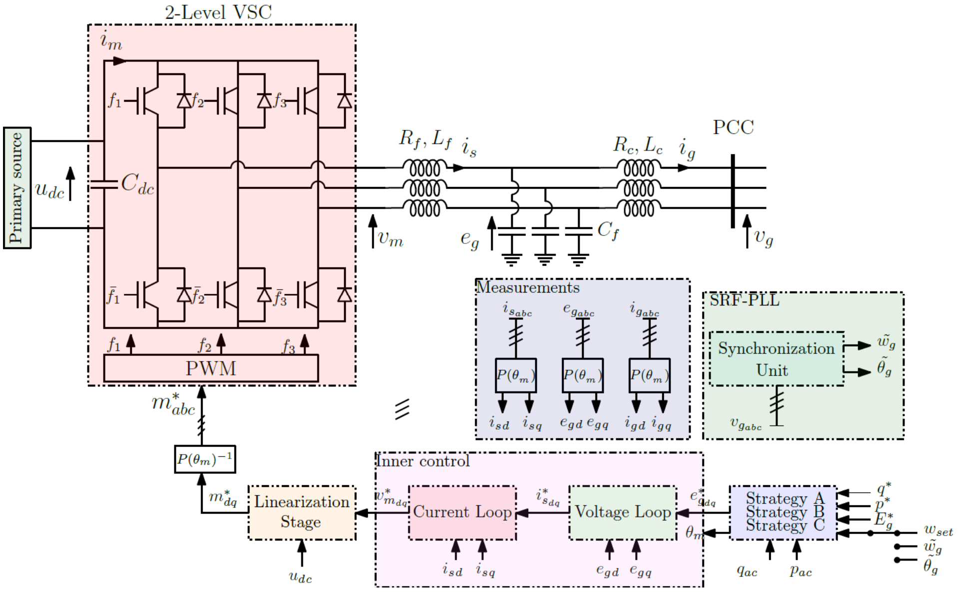

Figure IV-2 - Cascaded inner control structure

This topology has been employed in many applications such as UPS and Micro-grids [34], [36], [104], [130], [130]. The converter is protected from overcurrent by the implementation of the current control loop. However, because of the limited bandwidth of the VSCs in power transmission systems, the cascaded control structure may suffer from instability issues with the conventional controller tuning method in grid-connected mode.

Some solutions have been proposed in the literature [73], [75], [136]. However, AC voltage dynamics are still very slow and poorly damped. Hence, in the next subsections, these issues are discussed and some reliable solutions proposed.

Based on the model inversion principle, the cascaded control structure is obtained (see Figure IV-3). The coupling terms $L_f \omega_0 i_{s_{dq}}$, $C_f \omega_0 e_{g_{dq}}$ and disturbances $e_{g_{dq}}, i_{g_{dq}}$ are compensated in order to support the PI controllers and to achieve the desired dynamics. The frequencies in power and control sides are assumed to be equal to ω_0. This assumption holds true since the converter frequency variations are supposed to be negligible i.e., 4%. Moreover, this assumption is very useful for small-signal stability analysis.

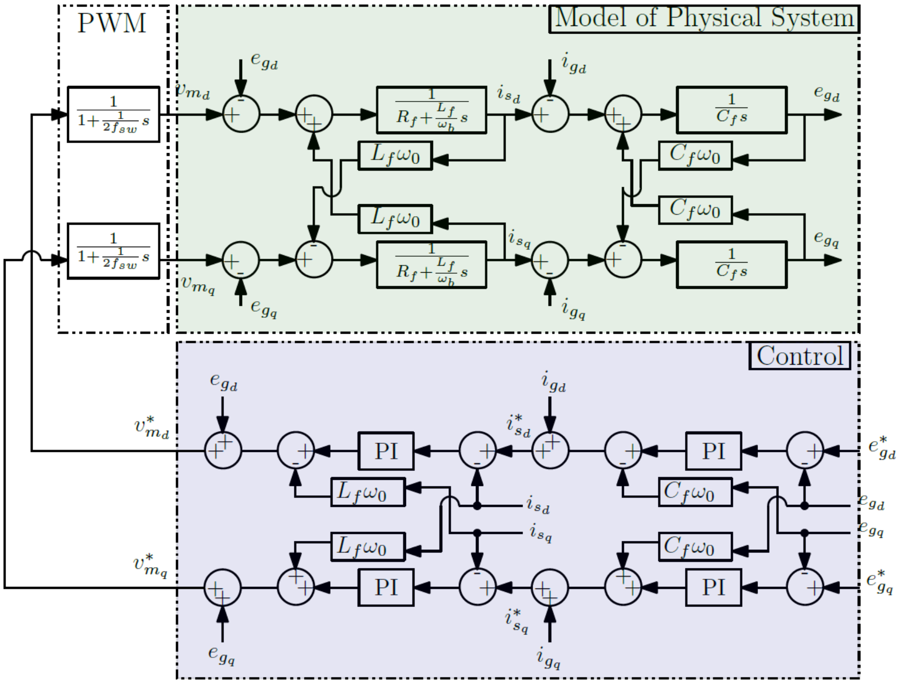

Figure IV-3 - Inner control of 2-Level voltage source converter

IV.2.2.1.1 Conventional current and voltage controllers design

The tuning of the current controllers has already been discussed in II.3.2. It is the same for grid-forming and grid-following. Therefore, the focus in this section is on the AC voltage loop.

The response time of the AC voltage loop is assumed to be slower than the current loop and the approximated PWM transfer function, which leads to the following simple representation shown in Figure IV-4.

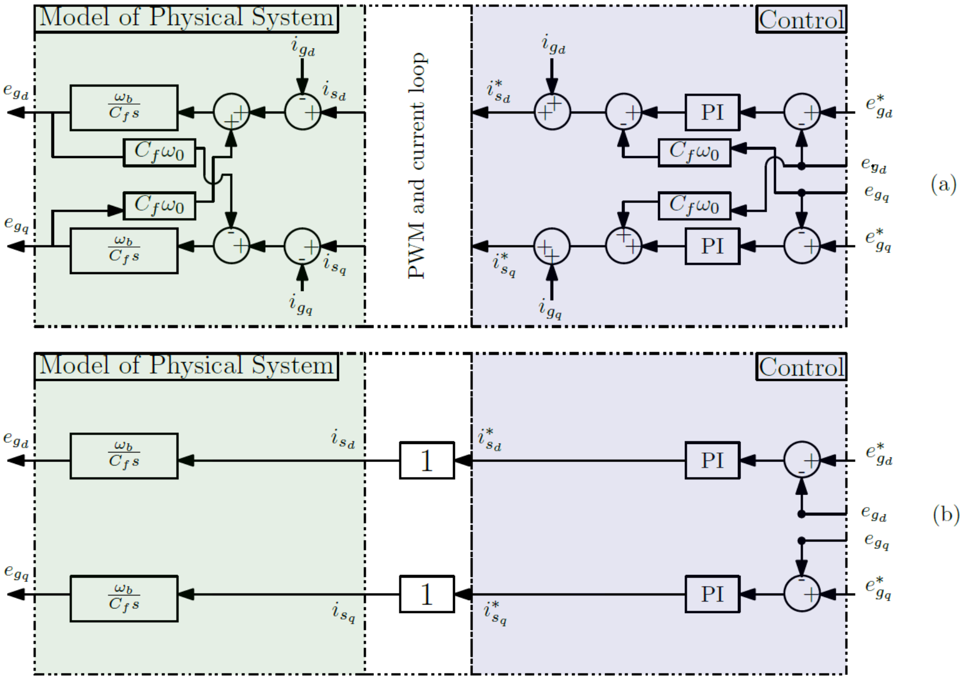

Figure IV-4 - (a) Output AC voltage control and the C_f circuit modeling (b) simplified modeling of the voltage loop

From Figure IV-4, a 2nd order transfer functions of the AC voltage loops for both *d-q* axes are expressed in (IV-7).

$$\frac{e_{g_{dq}}}{e^*_{g_{dq}}} = \frac{1+\frac{k_{pv}}{k_{iv}}s}{1+\frac{k_{pv}}{k_{iv}}s+\frac{C_f}{\omega_b}s^2} \tag{IV-7}$$

k_{pv} and k_{iv} are the controller proportional and the integrator gains, respectively.

To avoid interaction with the current loop, the following condition has to be respected,

$$T^R_{5\%_v} \geq 10 T^R_{5\%_c} \tag{IV-8}$$

Following the imposed specifications, the controller gains are deduced. In the following, the response time of the voltage loop $T^R_{5\%_v}$ and its damping ζ_v are set to 50 ms and 0.7, respectively.

To assess the validity of the conventional controllers design, time-domain simulations and “Eigenvalues analysis” are performed in the next subsection.

IV.2.2.1.2 Limitations of the conventional controllers design

Based on the controller parameters calculated and listed in Table IV-2, the system is simulated to deal with two extreme grid configurations (see Figure IV-5) .i.e., Standalone mode (at no load) (K_s opened), and grid-connected mode (K_s closed).

A +5% voltage magnitude step on e^*_{gd} is applied to the system in both topologies in order to check its dynamic behavior. The results are gathered in Figure IV-6, where the three primary control strategies developed in the previous sections are implemented.

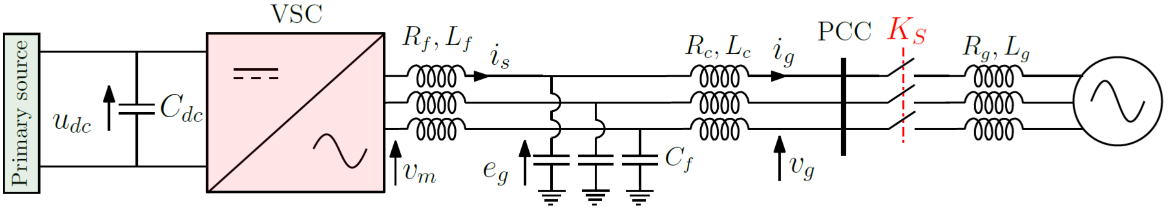

Figure IV-5 - 2-Level voltage source converter operating in various grid topologies

Table IV-2 System and control parameters

Symbol	Value	Symbol	Value
P_b	1 GW	$f_{s\omega}$	5 kHz
$\cos\phi$	0.95	u_{dc}	640 kV
f_b	50 Hz	V_b	320 kV
L_f	0.15 p.u	R_f	0.005 p.u
L_c	0.15 p.u	R_c	0.005 p.u
C_f	0.066 p.u	k_{pv}	0.017 p.u
k_{iv}	0.75 p.u	k_{pc}	0.4 p.u
k_{ic}	171.88 p.u	SCR	20

Starting with the results from Figure IV-6.a, at no load, the AC voltage dynamics are globally respected resulting in stable behavior of the system. Indeed, since the tuning was carried out in standalone mode, these results were expected. The grid-connected mode simulated in Figure IV-6.b shows an unstable system operation for all primary control strategies. Hence, a new design of the control has to be achieved for the grid-connected mode. But first, the instability origin should be highlighted, and then, a solution is proposed in the following lines to stabilize the system.

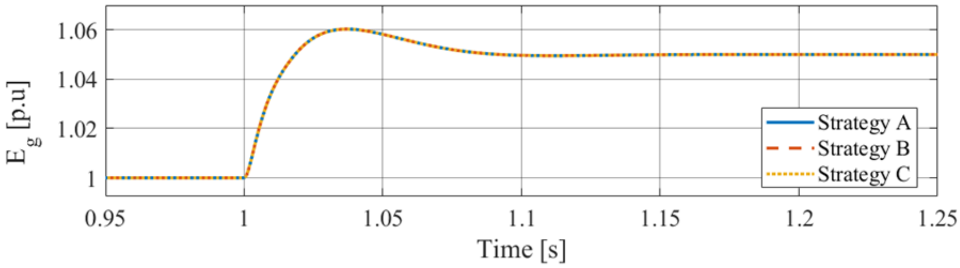

(a) Standalone mode

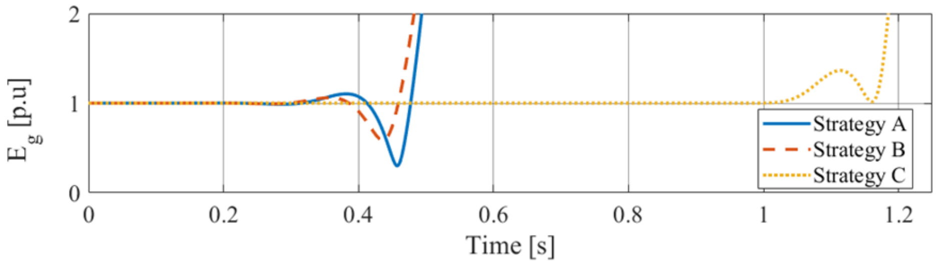

(b) Grid-connected mode

Figure IV-6 - Dynamics of AC voltage

As explained in the introduction of this chapter, the limited bandwidth of 2-Level VSCs can result in slow dynamics [73], [78], [81], restrained stability regions and interactions between control loops that can lead to unstable system in a grid-connected mode [81]. In such conditions, AC voltage controllers tuning has to be reconsidered. In the literature, some solutions have been proposed in order to improve the dynamics of the AC voltage e.g., Sliding mode control for inner current loop and a mixed H_2 / H_∞ for AC voltage loop [78]. This control technique aims to design a robust controller in order to achieve high performances; however, this technique is complex and requires very high computation burden. In [73], authors propose an algorithm which deduces the cascaded PI controller gains based on eigenvalues location. This method improves the system stability. However, the AC voltage response time is still very large ($T^R_{5\%_v} > 3s$), the system is poorly damped and presents a strong transient coupling between the AC voltage and the active power. Moreover, because of the control loops interaction, it is not possible to achieve the desired performances. Another conventional solution in [75], [136] aims to neglect the feed-forward compensation terms $e_{g_{dq}}$ from the current control loop. This solution keeps a system stable in different grid topologies. However, the voltage dynamics remain very slow ($T^R_{5\%_v} > 2s$) and poorly damped.

For classical voltage regulation, these dynamics could be considered as acceptable. Nevertheless, we will see further that a fast dynamic voltage loop may be very useful for restoring the normal operation after a faulty condition.

IV.2.2.1.3 Origin of the instability

To analyze the previously described problem, a state space model of the grid-connected system is derived. In the first step, only Strategy C is used for the outer loop. Then, the proposed solution is tested with all outer control strategies.

The dynamic model of the grid-connected 2-Level converter depicted in Figure IV-5 combined with the cascaded control in Figure IV-3 is linearized around an operating point using small-signal tool.

$$\left[\dot{\Delta x}\right] = [A]_{(x_0,u_0)}[\Delta x] + [B]_{(x_0,u_0)}[\Delta u] \tag{IV-9}$$

$$\Delta x = \left[\underbrace{\Delta e_{g_q}\ \Delta e_{g_d}\ \Delta i_{s_d}\ \Delta i_{s_q}\ \Delta i_{g_d}\ \Delta i_{g_q}}_{LCL\ filter}\ \underbrace{\Delta\delta_m\ \Delta\omega_m\ \Delta p_f\ \Delta\delta e_g}_{Outer\ Control}\ \underbrace{\Delta C_{v_d}\ \Delta C_{v_q}\ \Delta C_{c_d}\ \Delta C_{c_q}}_{Inner\ Controllers}\ \underbrace{\Delta\zeta_{TVR_d}\ \Delta\zeta_{TVR_q}}_{TVR}\right]^T.$$

$$\Delta u = \left[\Delta E_g^*\ \Delta V_e\ \Delta p^*\right]^T$$

The linear state space model of the system is given in Appendix G.

Based on the system eigenvalues listed in Table IV-3, the instability is linked to $\lambda_{5\text{-}6}$ located on the right half plane (RHP).

To define the link between the unstable modes $\lambda_{5\text{-}6}$ and system state variables, the participation factors P_{Factor} are used. They determine the degree of participation of each state variable on the eigenvalues. The participation factors for $\lambda_{5\text{-}6}$ are shown in

Figure IV-7. (Note that the participation factors are normalized with respect to the highest value).

Table IV-3 System eigenvalues

λ_{1-2}=-16.6±8.23i	λ_{10-11}=-56.152± 1.2007i
λ_{3-4}=-417.67± 2475.1i	λ_{12}=-31.418
λ_{5-6}=27.084± 34.959i	λ_{13-14}=-21.902± 21.215i
λ_{7-8}=-10.019± 34.673i	λ_{15-16}=-16.031±2.5151i
λ_{9}=-57.932	

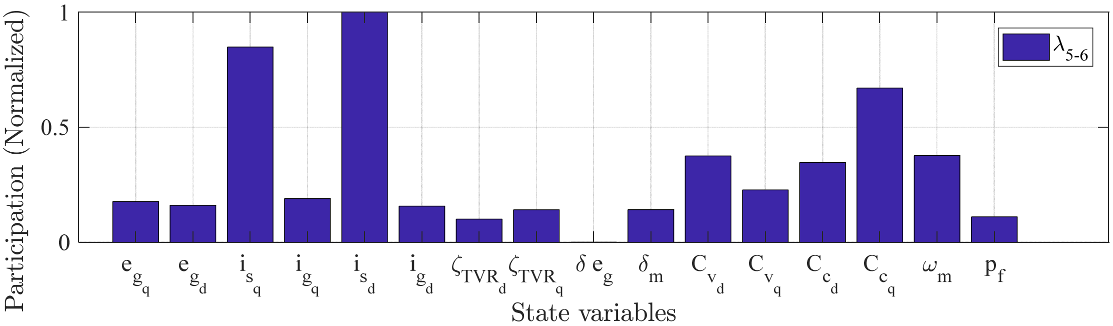

Figure IV-7 - Participation of state variables on $\lambda_{5\text{-}6}$

It can be noticed from participation factors that the unstable modes are linked to all state variables; however, their link with the output current dynamics $i_{s_{dq}}$ and the current controllers is very important.

To assess the impact of the current loop dynamics on $\lambda_{5\text{-}6}$, the current loop response time $T^{R}_{5\%_C}$ is decreased as depicted in Figure IV-8.

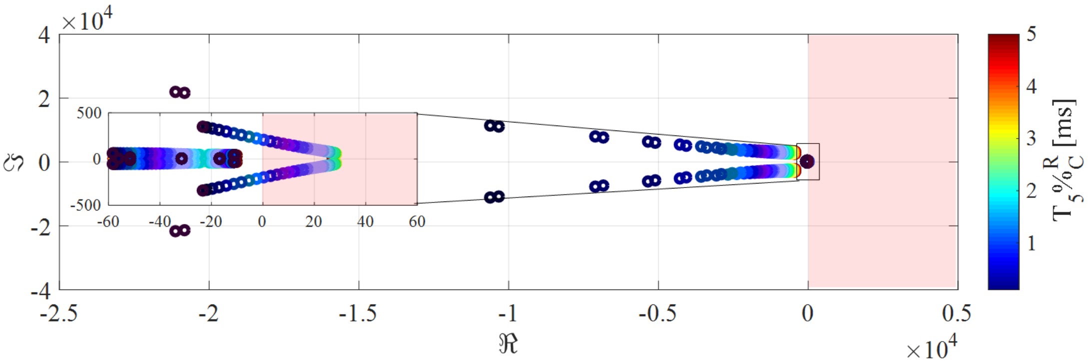

Figure IV-8 - Impact of current loop dynamics

Following the results obtained in the figure above, the unstable eigenvalues move toward the LHP when the current loop response time decreases. Faster current loop results in more decoupling with the voltage control loops. The reason why the system becomes more stable.

The limit of stability is obtained for $T^{R}_{5\%_C} \leq 900\,\mu s$.This is not a realistic response time for such converters. Moreover, even with these parameters, the poles $\lambda_{5\text{-}6}$ would still be poorly damped ($\zeta = 0.0106$). Therefore, it can be concluded that the conventional controllers tuning is not effective in such conditions.

IV.2.2.1.4 New way to design the controller

Another way of designing the controller parameters is now proposed. The idea is to assess the controller gains that give the best system poles placement calculated for the 16th order system in grid-connected mode. As the proposed method is applied offline, there is no need for complex optimization methods. It means that once the parameters are defined, they are not changed whatever the grid topology is.
The determination of the controller parameters is done following three steps as illustrated in Figure IV-9:

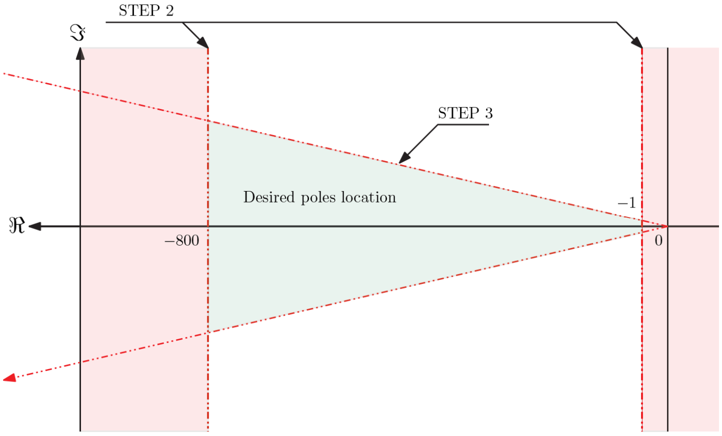

Figure IV-9 - Proposed method for controllers tuning

Step 1: The eigenvalues are calculated for a wide range of the controller gains (e.g., [0 100]).
Step 2: Two constraints are imposed on the system poles:

$$\Re\lambda_i(A) \leq -1 \tag{IV-10}$$

$$\Re\lambda_i(A) \geq \omega_0 \tag{IV-11}$$

where $\omega_0 > -2 f_{s\omega}$.
The choice of ω_0 =-800 rad/s is linked to the limited bandwidth of power converters.

When the poles respect these two constraints, the set of the 4 parameters k_{pc}, k_{ic}, k_{pv} and k_{iv} is stored.
Step 3: From the stored controller gains, the damping ratio is calculated for different poles for all the solutions. For each solution, the smaller damping is isolated ($\zeta_{i_{\min}}$). All the ($\zeta_{i_{\min}}$) are compared. Finally, the solution which is chosen is the one which gives the maximum damping for all ($\zeta_{i_{\min}}$). This guarantees the optimal dynamic behavior among all possible solutions with the chosen set of four controller parameters.
Following these steps, the controller parameters in Table IV-4 are obtained.

Table IV-4 Controller gains

$\mathbf{k_{pc}} = 0.73$ p.u	$\mathbf{k_{ic}} = 1.19$ p.u
$\mathbf{k_{pv}} = 0.52$ p.u	$\mathbf{k_{iv}} = 1.16$ p.u

The two main parameters that have a significant impact on pole placement are especially the current controller integral gain k_{ic} and voltage controller proportional gain k_{pv}.

Using these new parameters, the location of the system poles is illustrated in the pole map bellow.

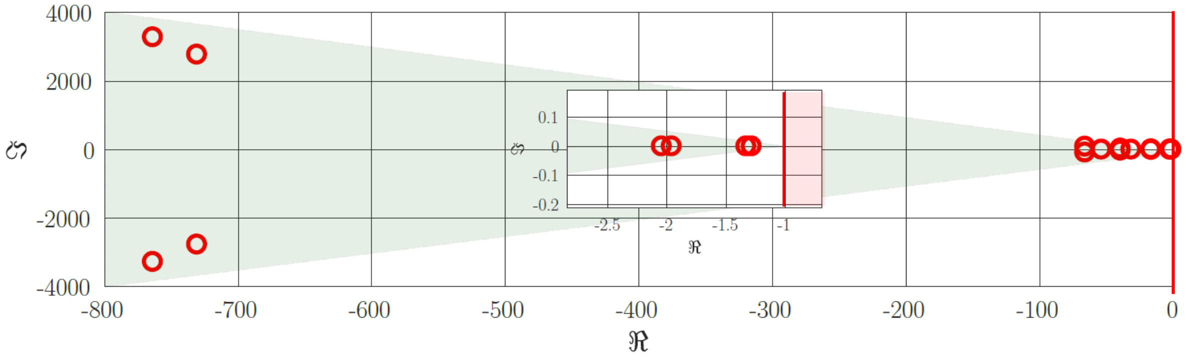

Figure IV-10 - Poles location based on the conventional method and the proposed one

Two major remarks are drawn from the pole map:

1- The system is stable based on the proposed method.
2- The overall system damping is improved.

To show the effectiveness of the new controller parameters, time-domain simulations are gathered in Figure IV-11. The same grid cases performed previously in Figure IV-6 are simulated.

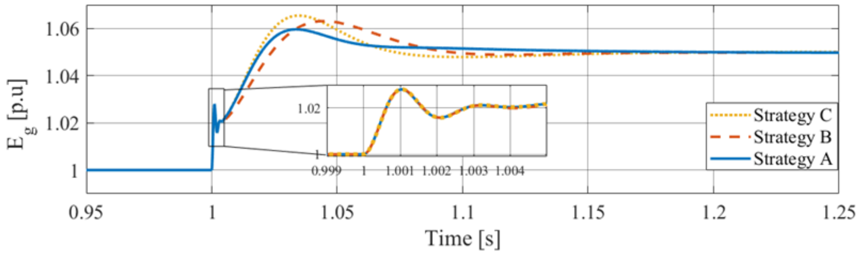

(a) Grid-connected mode

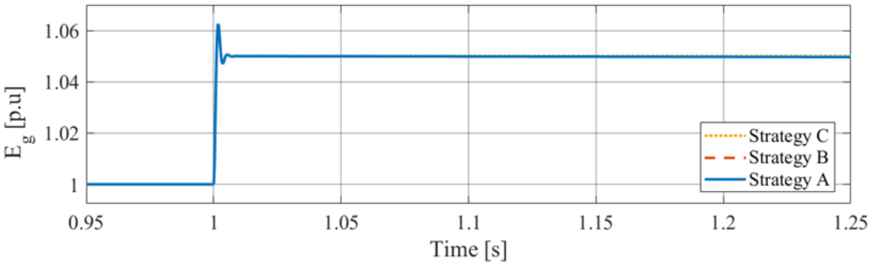

(b) Standalone mode

Figure IV-11 - AC voltage dynamics based on the new controllers gains

- In grid-connected mode, the AC voltage achieves its reference within 70 ms. It has a double dynamic response. The faster dynamic noticed in the first 5 ms oscillates around 475 Hz. This frequency corresponds to the eigenvalues $\lambda_{3\text{-}4} = \text{-}731 \pm 2.78e3i$. The slower response oscillates around 17 Hz. It corresponds to the eigenvalues $\lambda_{5\text{-}6} = \text{-}66.35 \pm 85.4i$. This behavior is from interactions between eigenvalues and their dependency on common state variables, precisely between AC voltages and AC currents. These interactions are unavoidable with the cascaded control structure.

  Depending on the primary control, the AC voltage transient is slightly different.
- In standalone mode, the AC voltage dynamics are faster, where the AC voltage reaches its reference within 5 ms.

Globally, the system is stable in both grid cases and based on the three primary control strategies. At no load and in standalone mode, the AC voltage dynamics are faster, where the AC voltage achieves its reference within 5 ms.

The next section proposes an alternative direct AC voltage control structure that rests on the physical potential of the VSC, where no complicated controllers design is required.

IV.2.2.2 Direct AC voltage Control

In this subsection, another solution for the inner control is proposed: a direct AC voltage control which is an open-loop control structure. Employing the system model in (IV-4), (IV-5) and (IV-6), the modulated AC voltage reference V_m^* is generated from the voltage setpoint E_g^* and the inversion of the quasi-stationary model of the filter R_f, L_f (Compensation impedance). The inversed quasi-stationary model of the filter R_f, L_f allows reaching $E_g^* = E_g$ as proved by the equations (IV-12 & IV-14):

$$v_{m_d}^* = e_{g_d}^* + R_f i_{s_d} - L_f \omega_m i_{s_q} \tag{IV-12}$$

$$v_{m_q}^* = e_{g_q}^* + R_f i_{s_q} + L_f \omega_m i_{s_d} \tag{IV-13}$$

By putting IV-12 & IV-13 in IV-4, in steady state, the approximated PWM transfer function and the current derivatives are neglected, which yields,

$$e_{g_d} \approx e_{g_d}^* \quad , \quad e_{g_q} \approx e_{g_q}^* \tag{IV-14}$$

An illustration of the control structure is given in Figure IV-12.

To avoid particular resonances linked to the LCL filter an active damping control has to be implemented.

$$v_{m_d}^* = R_f i_{s_d} \text{-} L_f \omega_m i_{s_q} + e_{g_d}^* - \underbrace{R_{LCL_D}(i_{s_d} \text{-} i_{gd})}_{e_{g_d}^{*\prime}} \tag{IV-15}$$

$$v_{mq}^{*} = R_f i_{s_q} + L_f \omega_m i_{s_d} + e_{g_q}^{*} - \underbrace{R_{LCL_D}(i_{s_q} - i_{gq})}_{e_{gq}^{*}} \qquad \text{(IV-16)}$$

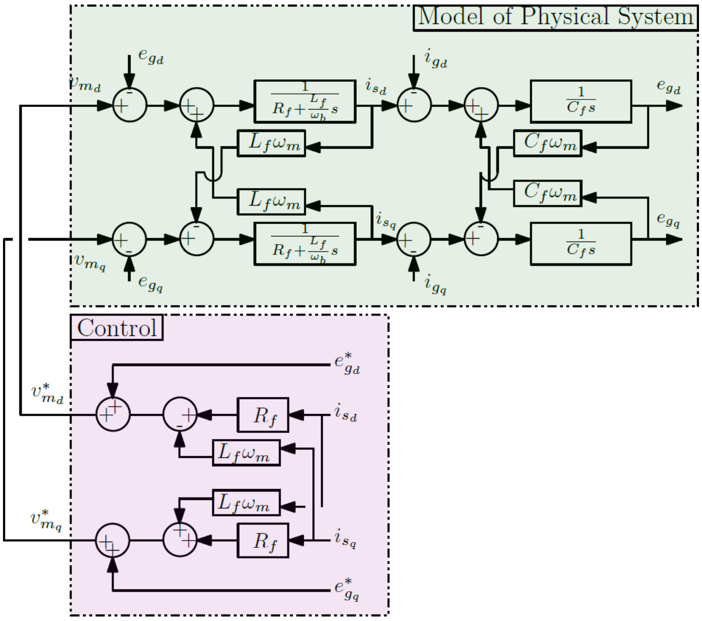

Figure IV-12 - Quasi-stationary control for AC voltage drop across the filter L_f

The active damping control in (IV-15 & IV-16) reacts as a physical resistor in series with the filter capacitor C_f (Figure IV-13).

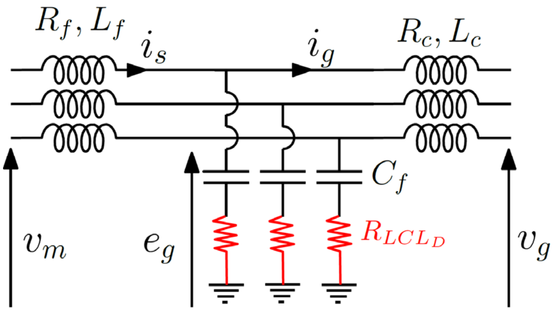

Figure IV-13 - Active damping for LCL filter

The tuning of R_{LCL_D} is done through eigenvalues location.

The dynamic model of the grid-connected 2-Level converter depicted in Figure IV-5 combined with the direct AC voltage control is linearized around an operating point using small-signal tool,

$$\left[\dot{\Delta x}\right] = [A]_{(x_0,u_0)}[\Delta x] + [B]_{(x_0,u_0)}[\Delta u] \qquad \text{(IV-17)}$$

$$\Delta x = \left[\underbrace{\Delta e_{g_q}\ \Delta e_{g_d}\ \Delta i_{s_d}\ \Delta i_{s_q}\ \Delta i_{g_d}\ \Delta i_{g_q}}_{LCL\ Filter}\ \underbrace{\Delta\delta_m\ \Delta\omega_m\ \Delta p_f\ \Delta\delta e_g}_{Outer\ Control}\ \underbrace{\Delta\zeta_{TVR_d}\ \Delta\zeta_{TVR_q}}_{TVR} \right]^T$$

$$\Delta u = \left[\Delta E_g^{*}\ \Delta V_e\ \Delta p^{*}\right]^T$$

The linear state space model of the system is given in Appendix H. To check the impact of the active damping control on the poles location, R_{LCL_D} is varied from 0 to 1 p.u as shown in Figure IV-14.

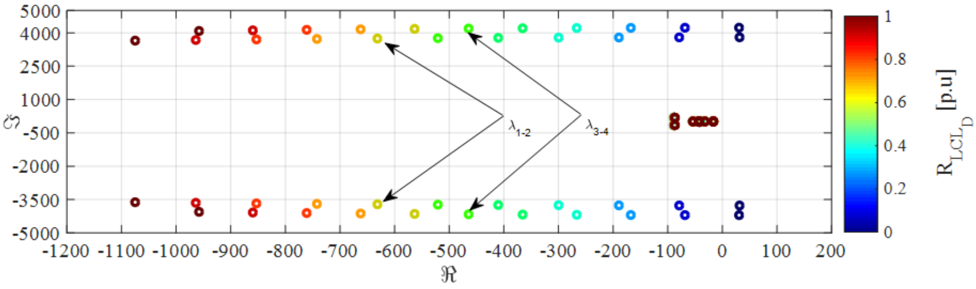

Figure IV-14 - Tuning of the Active damping resistor

The system becomes stable for $R_{LCL_D} > 0.1$ p.u.

In the rest of this work, R_{LCL_D} is set to 0.7 p.u in order to improve modes damping ($\lambda_{1\text{-}2}$ and $\lambda_{3\text{-}4}$). The set of values for R_{LCL_D} limits the fastest modes ($\lambda_{1\text{-}2}$ and $\lambda_{3\text{-}4}$) to $\Re = -800$ rad/s as in the previous study.

The additional active damping shows its effectiveness in improving the system stability and damping. However, it may induce an important AC voltage drop with respect to the power exchange. Therefore, a high-pass filter is added so that the damping resistor only reacts to transients.

$$v^*_{m_d} = R_f i_{s_d} - L_f \omega_m i_{s_q} + e^*_{g_d} - \underbrace{R_{LCL_D}(i_{s_d} - i_{gd})\frac{s}{s+\omega_R}}_{e^*_{gd}} \tag{IV-18}$$

$$v^*_{mq} = R_f i_{s_q} + L_f \omega_m i_{s_d} + e^*_{g_q} - \underbrace{R_{LCL_D}(i_{s_q} - i_{gq})\frac{s}{s+\omega_R}}_{e^*_{gq}} \tag{IV-19}$$

ω_R is the cut-off frequency of the high-pass filter. It is set to 100 Hz.

The overall control structure is depicted in Figure IV-15.

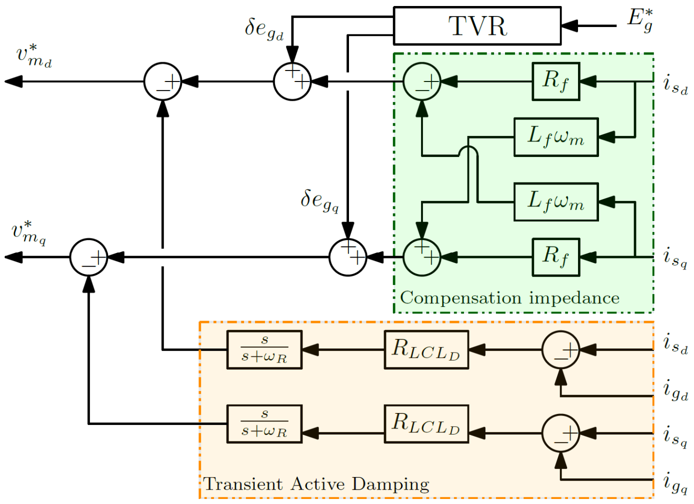

Figure IV-15 - Direct AC voltage control

The system eigenvalues are listed in Table IV-5.

Table IV-5 System eigenvalues

$\lambda_{1\text{-}2}$=-656.9± 4334.4i	λ_{9}=-16.051 + 0i
$\lambda_{3\text{-}4}$=-735.89± 3883.7i	$\lambda_{10\text{-}11}$=-23.279± 12.50i
$\lambda_{5\text{-}6}$=-98.424± 144.46i	λ_{12}=-31.408 + 0i
$\lambda_{7\text{-}8}$=-42.97± 23.171i	$\lambda_{13\text{-}14}$=-9.91± 0.43287i

To illustrate the dynamic behavior of the system based on the proposed control strategy, an active power setpoint change of $p^* = 1$ p.u is applied to the system at *t*=1 s, where the three outer control strategies are simulated. The results are gathered in Figure IV-16.

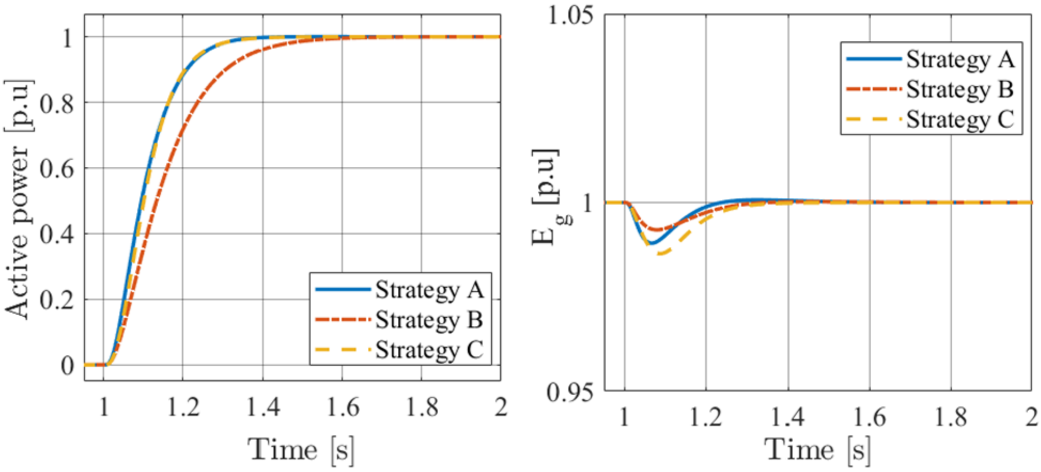

Figure IV-16 - Active power setpoint change and its impact on the AC voltage

One can remark from the results that the system is stable based on the proposed inner control structure. Moreover, the AC voltage recovers its reference in steady state without error.

Another inner control strategy based on Linear Quadratic Regulation (LQR) has also been proposed in the context of this thesis. More details can be found in [80], [137].

IV.2.3 Impact of the inner loop on the outer control loops

When the studies focus on the active power exchange, inertial effect and the transient stability analysis, the dynamics of the LC filter and its inner control are often neglected for simplicity purposes as it has been done in chapter II and III. This assumption considers a sufficient time decoupling between control loops i.e.; the voltage and current loops are faster than the outer loops. The validity of this assumption is discussed in this section.

The decoupling function between the voltage regulation loops and the primary control is necessary in order to maintain the same performances reached in the previous sections. Moreover, the aim is to show that the simplified models without inner voltage control loops and LC filter are good enough for large system analysis [138].

IV.2.3.1 Cascaded control structure

In the simplified model, e_g is assimilated to v_m and the voltage and current loops are not implemented. Considering the outer loop based on “Strategy C”, the simplified model is 3rd order system (see (III-57)):

$$\frac{p_{ac}}{p^*}=\frac{1+T_2 s}{1+\left(\frac{\omega_c+k_i T_1 \omega_c T_{p\delta}(0)}{k_i \omega_c T_{p\delta}(0)}\right)s+\left(\frac{1+T_2\omega_c}{k_i\omega_c T_{p\delta}(0)}\right)s^2+\frac{T_2}{k_i\omega_c T_{p\delta}(0)}s^3} \tag{IV-20}$$

In the following, the indices “S” and “F” denote the simplified model and the full model respectively.

To check the accuracy and the validity of the reduced models compared to the full dynamic model, a pole map with the 3rd and 16th order models is presented in Figure IV-17.

It is recalled from chapter III that $\lambda_1^S = \text{-}14.49 \pm 0i$ is the dominant pole that imposes the active power dynamics.

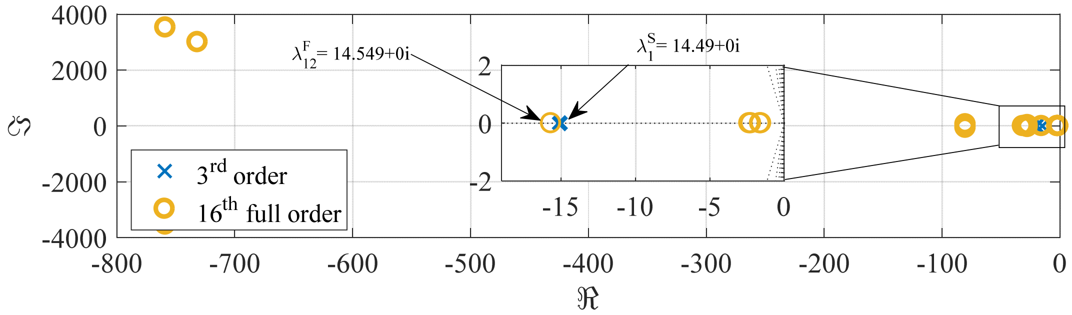

Figure IV-17 - Impact of the model reduction on the dominant mode location

One can remark from the pole map above that the $\Re$ and $\Im$ part of λ_1^S are approximatively equal to those of λ_{12}^F. For the simplified model, it is clear that λ_1^S is linked to the state variables $\Delta\omega_m$, Δp_f and $\Delta\delta_m$ that impose the active power dynamics. However, it is not certain that λ_{12}^F is also linked to the same state variables. The answer to this question requests establishing a link between the state variables and the eigenvalues. Hence, the participation factors tool is used for this aim.

The results from Table IV-6 show that $\Delta\omega_m$, Δp_f and $\Delta\delta_m$ are mostly participating in λ_{12}^F. However, they are also participating in λ_{13}^F, λ_{14}^F, λ_{15}^F and λ_{16}^F. Although the participation rate of $\Delta\omega_m$, Δp_f and $\Delta\delta_m$ in these latter is negligible. It creates a small coupling between them and λ_{12}^F, which results in the error between λ_{12}^F and λ_1^S.

Since $\Delta\omega_m$, Δp_f and $\Delta\delta_m$ are mostly participating in λ_{12}^F comparing to the rest of eigenvalues, this means that the active power dynamics are mainly linked to λ_{12}^F. Therefore, it can be concluded that the full order model and the simplified model behave similarly.

Table IV-6 PARTICIPATION FACTORS (NORMALIZED)

Dominant modes State variables	$\boldsymbol{\lambda}^{\mathbf{F}}_{\mathbf{12}}$	$\boldsymbol{\lambda}^{\mathbf{F}}_{\mathbf{13}}$	$\boldsymbol{\lambda}^{\mathbf{F}}_{\mathbf{14}}$	$\boldsymbol{\lambda}^{\mathbf{F}}_{\mathbf{15}}$	$\boldsymbol{\lambda}^{\mathbf{F}}_{\mathbf{16}}$
$\Delta\delta_m$	0.4	0	0	0	0
Δp_f	1	0.06	0.06	0.02	0.02
$\Delta\omega_m$	0.5	0	0	0	0

To demonstrate the validity of this analysis, the simplified and the full dynamic model are compared through time-domain simulations. The results are gathered in Figure IV-18.

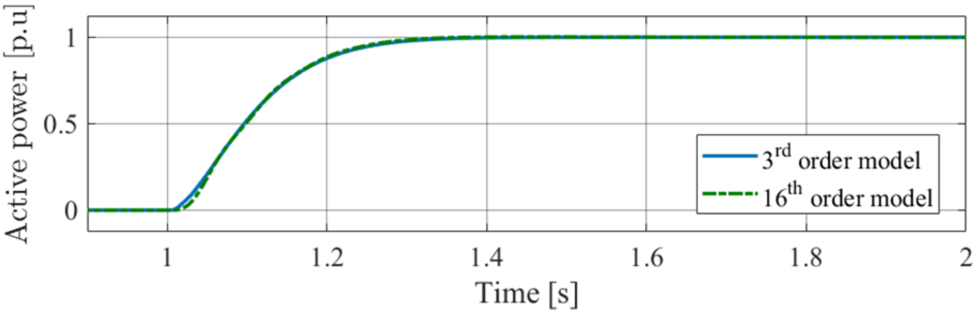

Figure IV-18 - Inner and outer loop decoupling based on Strategy C

The result shows that the error between the simplified model and the full dynamic model could be neglected. Consequently, it can be initially concluded that the decoupling between inner and outer control loops is guaranteed. Moreover, the simplified model will be enough for the quasi-static analysis.

Similarly to "Strategy C", the decoupling between the inner control loops and "Strategy A and B" is checked. It is recalled that the system based on "Strategy A and B" is a 17th order, with:

$$\Delta x = \left[\underbrace{\Delta e_{g_q}\ \Delta e_{g_d}\ \Delta i_{s_d}\ \Delta i_{s_q}\ \Delta i_{g_d}\ \Delta i_{g_q}}_{LCL\ filter}\ \underbrace{\Delta\delta_m\ \Delta\omega_m\ \Delta\delta e_g}_{Outer\ Control}\ \underbrace{\Delta\tilde{\delta}_g\ \Delta\zeta_{PLL}}_{PLL}\ \underbrace{\Delta C_{v_d}\ \Delta C_{v_q}\ \Delta C_{c_d}\ \Delta C_{c_q}}_{Inner\ Controller}\ \underbrace{\Delta\zeta_{TVR_d}\ \Delta\zeta_{TVR_q}}_{TVR} \right]^T$$

The simplified models based on both control strategies are second order systems,

Strategy A:
$$\frac{p_{ac}}{p^*} = \frac{1}{1+\dfrac{X_c}{k_i V_m V_e}s+\dfrac{X_c}{k_i V_m V_e \omega_c}s^2} \tag{IV-21}$$

Strategy B:
$$\frac{p_{ac}}{p^*} = \frac{1}{1+\dfrac{X_c}{k_i V_m V_e}s+\dfrac{X_c+X_g}{k_i V_m V_e \omega_c}s^2} \tag{IV-22}$$

The results shown in Figure IV-19 demonstrate the decoupling between the inner loops and the outer control loops based on Strategy A and B, respectively, where, dominant modes of the simplified models are close to the ones from the full dynamic models.

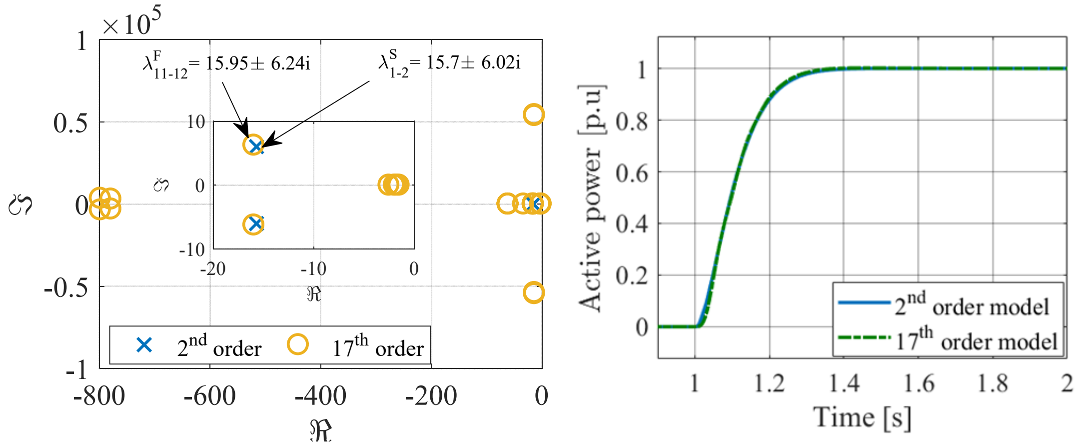

(a) Strategy A

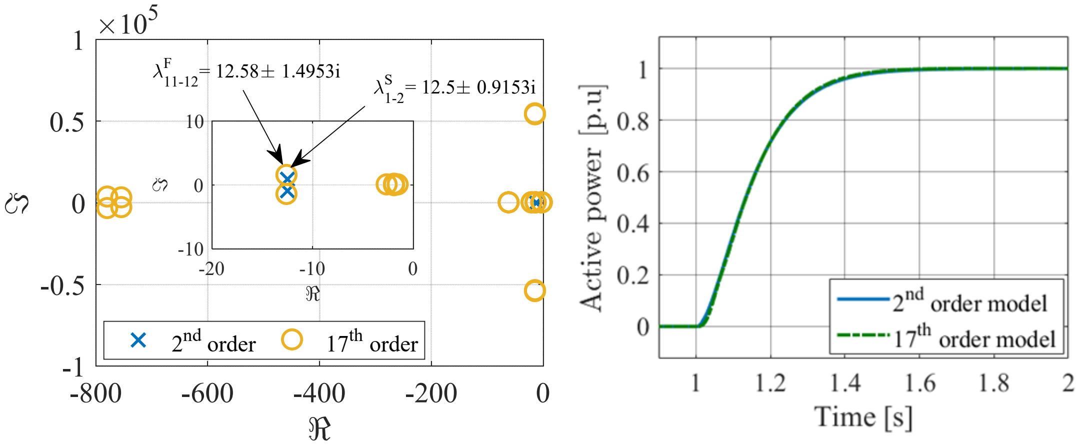

(b) Strategy B

Figure IV-19 - Inner and outer loop decoupling based on cascaded control structure

These results lead to interesting conclusions:

- The simplified model (reduced order system) used in the previous sections is sufficient to analyze large systems without embedding all system dynamics.
- All the results obtained previously without inner control and LC filter are still valid.

In the next subsection, the same analysis is performed for the direct AC voltage control.

IV.2.3.2 Direct AC voltage control structure

The system orders based on the direct AC voltage control are:

- 15th full order system (Strategy A and B).
- 14th full order system (Strategy C).

Similar to the previous section, a comparison between the full and the reduced models is assessed through time-domain simulation. The results are presented in Figure IV-20.

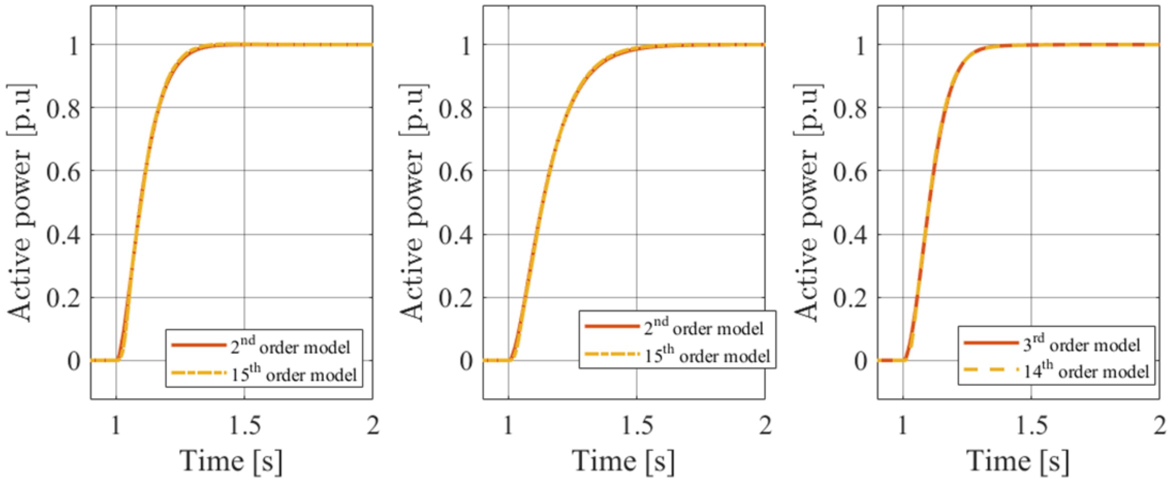

(a) Strategy A (b) Strategy B (c) Strategy C

Figure IV-20 - Inner and outer loop decoupling based on Direct AC voltage control

Once again, the results demonstrate the decoupling between the inner loops and the outer control loops, where, the active power dynamics remain nearly the same. These results lead to same conclusions drawn for the cascaded control structure.

In case of MMC, the output LC filter is not required. The application of the grid-forming control to the MMC is addressed in the following section.

IV.3 Grid-forming control for Modular multilevel converters (MMC-VSC)

The Modular Multilevel Converter is a technology able to achieve high voltage and power levels. The topology of a three-phase MMC is constituted by the series connection of *N* sub-modules (SMs) with independent capacitors *C* to build one arm of the converter as indicated by Figure IV-21. For HVDC application, *N* can be of several hundreds. The sub-modules in each arm are connected to a filter inductor (L_{arm}, R_{arm}) whose aim is to limit the derivative of current in case of a DC short-circuit. Two identical arms are connected, one to the upper and the other to lower DC-side, respectively, to form one leg for each phase *i=[a,b,c]*. Thanks to its modularity, the converter allows generating a sinusoid output AC voltage. The absence of the LC filter leads to cost saving compared to the conventional 2-Level converter.

Given the large number of sub-modules (SMs), it is necessary to find a model in order to design the different high level controllers (current, energy). This model has been developed for several years, it is called Arm Averaged Model (AAM) as depicted in Figure IV-21 for the lower arm of phase. Based on AAM representation, each arm is modelled as a controllable voltage source with a modulation ratio m (m is defined as the ratio of the active sub-modules number divided by the total number of sub-modules) and an equivalent voltage $v_{c_{UL_{tot}}}$ across the equivalent capacitor C_{tot}.

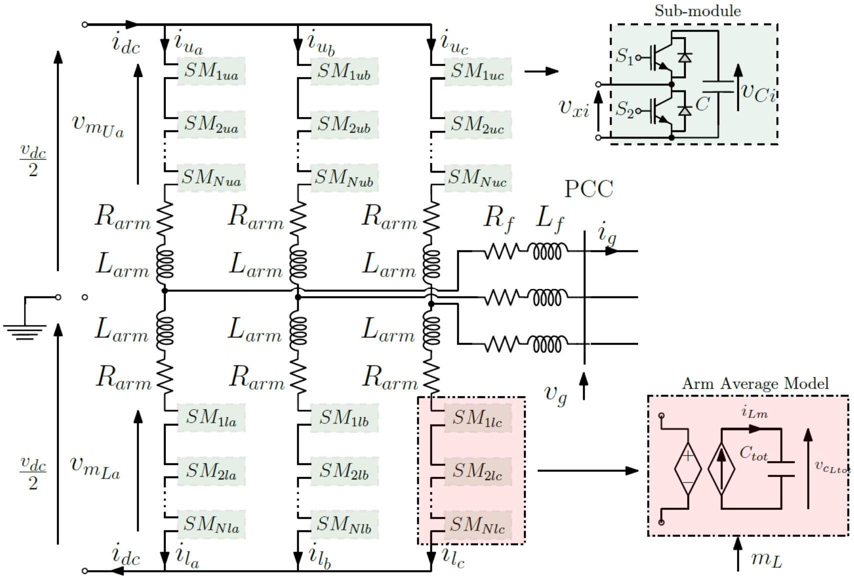

Figure IV-21 - Modular Multilevel converter (MMC)

The modulated voltages $v_{m_{UL_i}}$ and currents $i_{m_{UL_i}}$ of each arm are respectively expressed as follow:

$$v_{m_{U_i}} = m_{U_i} v_{c_{i_U tot}} \ , \qquad v_{m_{L_i}} = m_{L_i} v_{c_{i_L tot}} \tag{IV-23}$$

$$i_{m_{U_i}} = m_{U_i} i_{U_i} \ , \qquad i_{m_{L_i}} = m_{L_i} i_{L_i} \tag{IV-24}$$

where i_{U_i} and i_{L_i} are the currents of the upper and the lower arms.

The currents and voltages of the equivalent capacitor are related by the following expressions,

$$C_{tot}\frac{d}{dt} v_{c_{U_i tot}} = i_{m_{U_i}} \ , \qquad C_{tot}\frac{d}{dt} v_{c_{L_i tot}} = i_{m_{L_i}} \tag{IV-25}$$

IV.3.1 AC and DC sides modeling of MMC

According to Kirchhoff's law, two equations are obtained from the inner loop of the MMC allowing a first modeling,

$$\frac{v_{dc}}{2} - v_{m_{U_i}} - L_{arm}\frac{d}{dt} i_{U_i} - R_{arm} i_{U_i} = v_{g_i} + L_c \frac{d}{dt} i_{g_i} + R_c i_{g_i} \tag{IV-26}$$

$$-\frac{v_{dc}}{2} + v_{m_{L_i}} + L_{arm}\frac{d}{dt} i_{L_i} + R_{arm} i_{L_i} = v_{g_i} + L_c \frac{d}{dt} i_{g_i} + R_c i_{g_i} \tag{IV-27}$$

The addition of equations (IV-26) and (IV-27) leads to the AC side model,

$$v_{m_{L_i}} - v_{m_{U_i}} + L_{arm}\frac{d}{dt}\left(i_{L_i} - i_{U_i}\right) + R_{arm}(i_{L_i} - i_{U_i}) = 2(v_{g_i} + L_c \frac{d}{dt} i_{g_i} + R_c i_{g_i}) \tag{IV-28}$$

Considering the variable change as in [139],

$$v_{v_i} = \frac{1}{2}(v_{m_{L_i}} - v_{m_{U_i}}) \ , \qquad v_{diff_i} = \frac{1}{2}(v_{m_{L_i}} + v_{m_{U_i}}) \ , \qquad i_{diff_i} = \frac{1}{2}(i_{L_i} + i_{U_i}) \tag{IV-29}$$

where i_{diff_i}, v_{v_i} and v_{diff_i} are the common-mode currents of the MMC, the modulated voltage driving the AC grid currents and the modulated voltage driving the common-mode currents, respectively.

Putting (IV-29) into (IV-28) yields:

$$v_{v_i} - v_{g_i} = L_{eq}^{ac}\frac{d}{dt}i_{g_i} + R_{eq}^{ac}i_{g_i} \tag{IV-30}$$

with $L_{eq}^{ac} = \left(\frac{1}{2}L_{arm} + L_c\right)$ and $R_{eq}^{ac} = \left(\frac{1}{2}R_{arm} + R_c\right)$.

With the subtraction of (IV-26) and (IV-27), the three-phase common-mode current dynamics can be obtained,

$$\frac{v_{dc}}{2}(1,1,1)^T - v_{diff_{abc}} = L_{arm}\frac{d}{dt}i_{diff_{abc}} + R_{arm}i_{diff_{abc}} \tag{IV-31}$$

Based on (IV-25), (IV-30) and (IV-31), the system contains 11 state variables: 2 independent grid currents, 3 common-mode currents and 6 voltages across equivalent capacitors. The obtained equations are represented in the block diagram bellow,

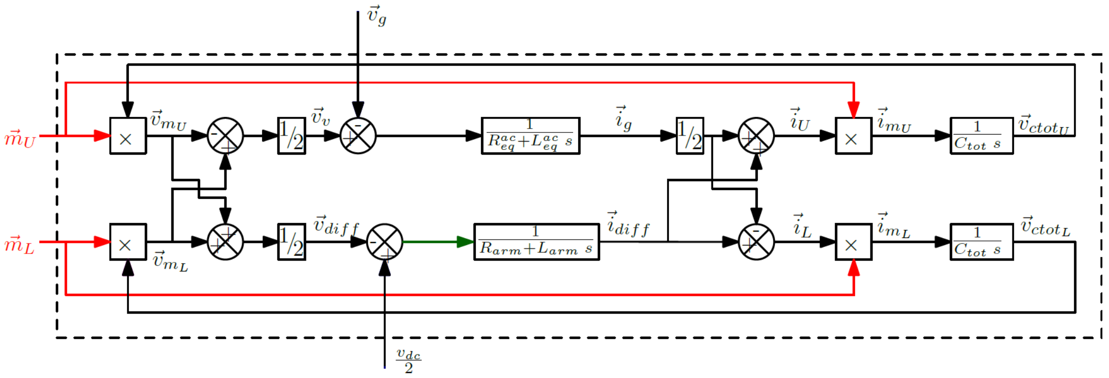

Figure IV-22 - Modular Multilevel converter representation in (abc) frame

The objectives of the control law are:

1- Controlling the common mode currents $i_{diff_{abc}}$ [140]–[142] to suppress the internal circulating current, and thereby, avoiding unwanted oscillations on the DC side.

2- Controlling the exchange of energy between arms and phases to guarantee an equipartition of the internal energy of the MMC [143].

3- Controlling the modulated voltage v_{v_i} driving the AC-grid currents to guarantee a power exchange between AC and DC sides.

The two first objectives have been widely discussed in the literature and they have been achieved through different control strategies so-called Circulating Current Suppression Controller (CCSC) [140], [141], Energy-based control and improved CCSC with DC energy management [141], [143], [144]. All these control strategies have been applied for MMCs operating as current sources. However, little work has been focused on the VSC-MMC controlled as a voltage source [145]–[147].

In [145], the authors want to mimic the electrical behavior of the synchronous machine (SM). The proposed control structure requires many control loops to ensure an AC voltage regulation (i.e., AC voltage loop, virtual SM stator emulator, AC current loop and synchronization unit). However, in addition to the energy management loops and common-mode currents control, the proposed structure in [145] makes the control very complex, and therefore, the setting of its controllers becomes a real challenge. In this thesis, one of our goals is to simplify as much as possible the control laws while looking for high dynamic performances. It is recalled that contrary to the 2-Level VSCs, MMCs are able to generate a nearly perfect modulated voltage waveform if the number of sub-modules is high (e.g.; 400 SM). Hence, the MMC can simply be controlled according to its physical voltage source nature without a need for additional regulation loops for the AC voltage control. In other words, the outer control strategy can be used to provide directly, the AC voltage $v_{v_i}^*$ references [148]. In this thesis, the energy-based control strategy has been adopted for energy management and common mode currents control.

IV.3.2 AC voltage-controlled MMC

The idea of the Energy-based control consists of achieving a high-level of controllability by implementing two additional control loops for the energy management. These loops aim to control the sum "W^{Σ}" and the difference "W^{Δ}" of the energy between arms [149]. The sum of the energy provides the DC component of the common mode currents that ensures a power balance between AC and DC sides, whereas the energy difference control loops aim to provide the AC components of the common mode currents, which allows suppressing unwanted frequencies on the DC side and reduces internal losses of the MMC. The controllers of the energy are depicted in (b) "$\Delta\sum$" Figure IV-23.

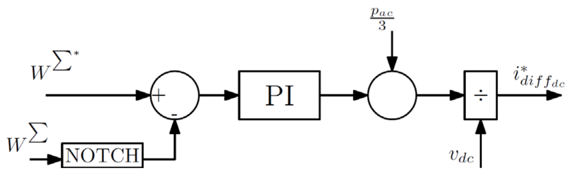

(a) "∑"

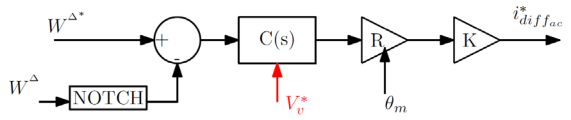

(b) "Δ∑"

Figure IV-23 - Energy control

where,
$$R = \begin{bmatrix} \cos(\theta_m) & 0 & 0 \\ 0 & \cos\left(\theta_m - \frac{2\pi}{3}\right) & 0 \\ 0 & 0 & \cos\left(\theta_m + \frac{2\pi}{3}\right) \end{bmatrix}, K = \begin{bmatrix} 1 & -\frac{1}{2} & \frac{1}{2} \\ -\frac{1}{2} & 1 & -\frac{1}{2} \\ -\frac{1}{2} & -\frac{1}{2} & 1 \end{bmatrix} \quad \text{(IV-32)}$$

For controlling the energy sum for each phase W_i^{Σ}, three independent PI controllers are used. The W_i^{Σ} is obtained from a second-order notch filter tuned at $-2\omega_g$. The references for the energy sum $W_{abc}^{\Sigma *}$ of each phase are set to the same value. The energy sum loop provides the DC component of the common-mode currents $i_{diff_{dc_i}}$.

The energy difference control for each phase W_i^{Δ} requires three independent PI controllers. The W_i^{Δ} is obtained from a second-order notch filter tuned at ω_g. The references of the energy difference $W_{abc}^{\Delta *}$ of each phase are set to zero. The output of the energy difference loop is the AC component of the common mode currents $i_{diff_{ac_i}}$.

For the energy difference control, constant amplitude of the AC voltage V_g is usually used, while in this thesis, the reference modulated voltage amplitude V_v^* will be used instead of V_g (see Figure IV-23).

The sum of the AC and DC current components generated by the energy control loops are used as references for controlling the common-mode currents. These are controlled through three independent PI controllers. More details on the energy management of the MMC and it operation principle can be found in [143].

Once the energy-based control is implemented, the modulated voltage V_v^* can be provided directly from primary control strategies, which leads to the general scheme of the AC voltage-controlled MMC as shown in Figure IV-24.

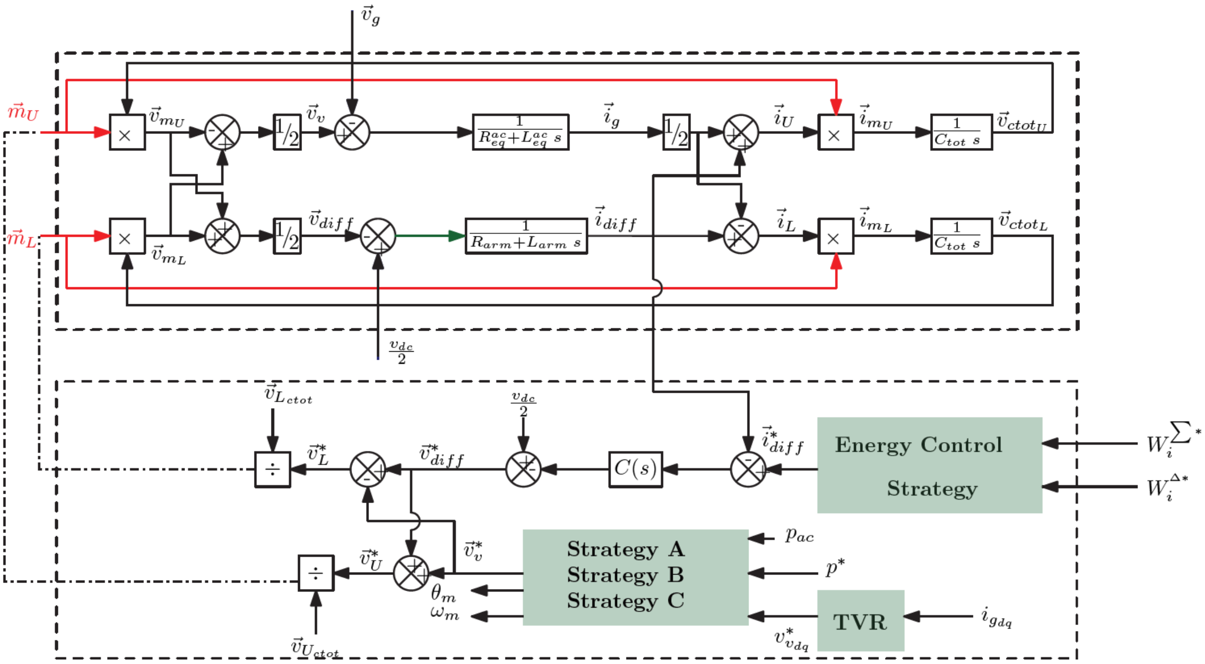

Figure IV-24 - AC voltage-controlled MMC

The three control algorithms proposed in chapter II and III can be implemented with the MMC. The inductance to take into account is the so-called L_{eq}^{ac}. The active power controller gain k_i in "Strategy A" should be adapted in order to ensure a given response time of the power loop $T_{5\%}^R$ =300 ms:

$$k_i = \frac{3L_{eq}^{ac}\omega_g}{T_{5\%}^{R}} \quad \text{(IV-33)}$$

The proposed MMC control strategy is analyzed through time-domain simulations, which are gathered in Figure IV-26, where two test cases are performed based on the example from Figure IV-25. System and control parameters are listed in Table IV-7.

Table IV-7 System and control parameters

Symbol	Value	Symbol	Value
P_b	1 GW	SCR	20
$\cos\phi$	1	v_{dc}	640 kV
f_b	50 Hz	V_b	320 kV
L_f	0.15 p.u	R_f	0.005 p.u
L_{arm}	0.18 p.u	R_{arm}	0.005 p.u
C	0.0138 F	SM	400
C_{arm}	C/SM	$T^R_{5\%_{diff}}$	5 ms
$T^R_{5\%_{W^\Delta}}$	200 ms	$T^R_{5\%_{W^\Sigma}}$	100 ms
$W^{\Sigma*}_{abc}$	1 p.u	$W^{\Delta*}_{abc}$	0 p.u

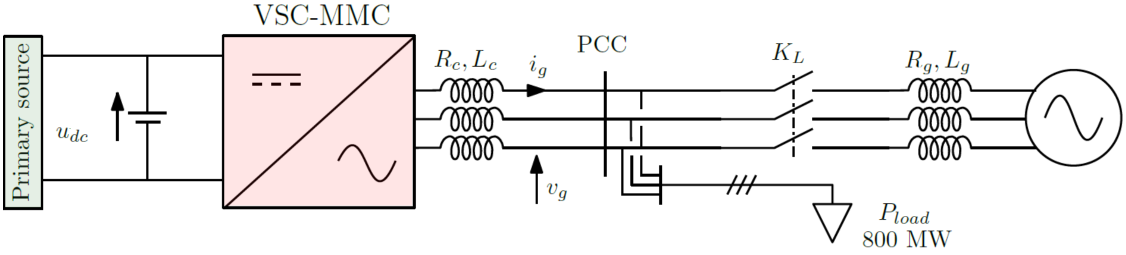

Figure IV-25 - Operation of the MMC in two extreme grid topologies

- The MMC is operating in grid-connected mode (K_L= ON), at t=2 s, active power step of $p^* = 0.5$ p.u is applied.
- At $t = 4$ s, the system moves from grid-connected mode to islanded mode.

The variables shown are the active power p_{ac}, the output VSC frequency ω_m, the energy sum W_{abc}^{Σ} and the energy difference W_{abc}^{Δ}, respectively.

The results for all primary control strategies show a stable system operation. In the grid-connected mode, the active power achieves its reference, while respecting the dynamic behavior of each control strategy. Once the AC grid is disconnected at t=4s, the power converter supplies the load autonomously; consequently, the frequency deviates from its nominal value ω_g = 50 Hz because of the droop frequency loop. The energy sum and difference are well controlled around their references. Moreover, they recover stably to their references with acceptable transient behavior e.g. energy overshoot of 5% during the islanding situation. The energy overshoot has to be considered in the sizing of sub-module capacitors in order to avoid damaging the system.

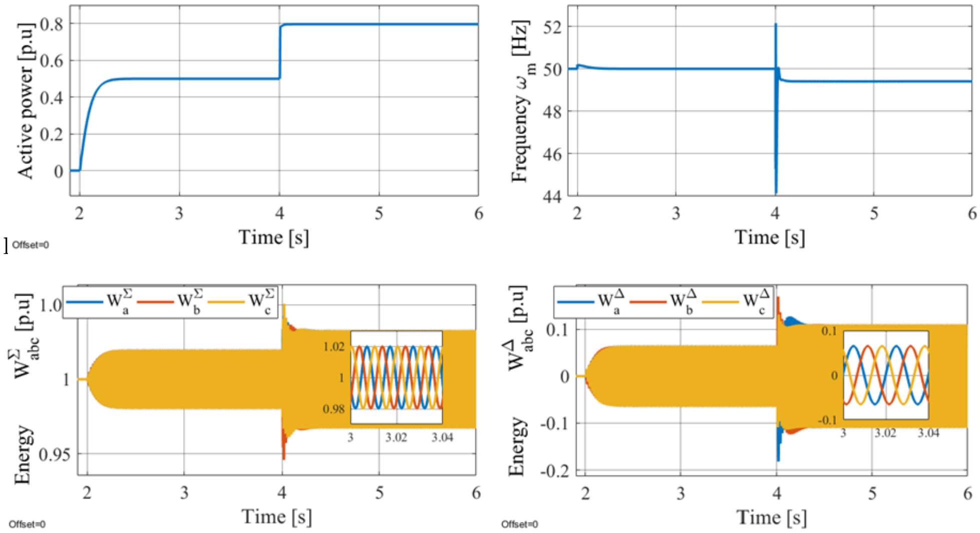

(a) Strategy A

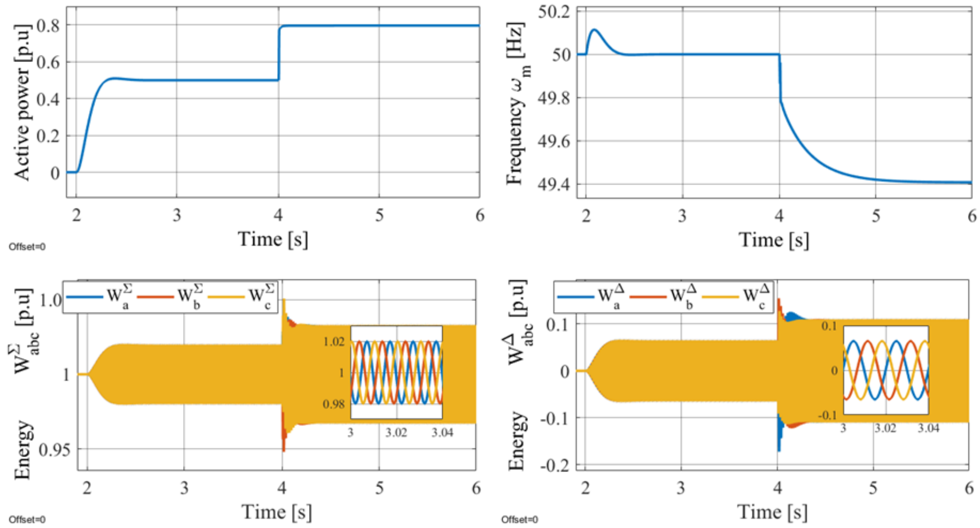

(b) Strategy B

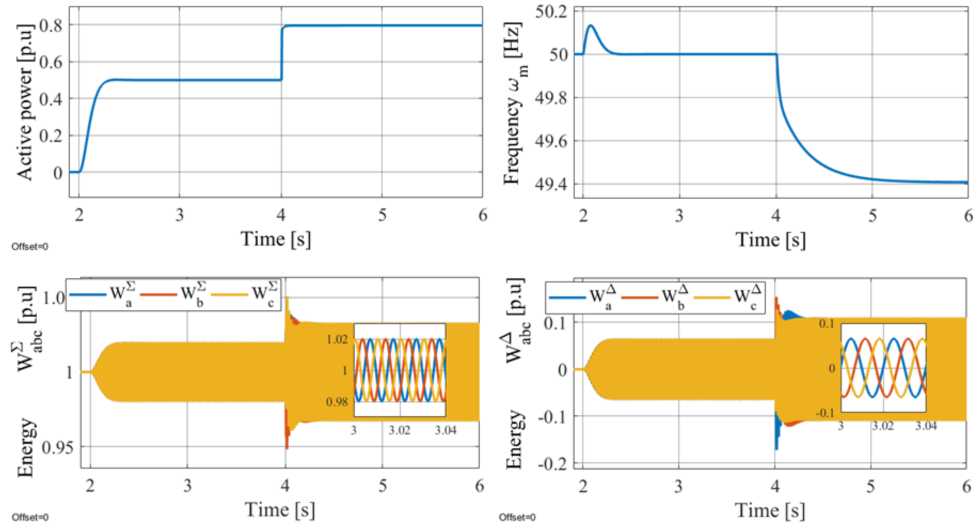

(c) Strategy C

Figure IV-26 - Dynamic performances of the MMC in both grid-connected and autonomous modes

IV.4 Conclusion

In this chapter, two different control strategies for AC voltage regulation have been adopted for the 2-Level voltage source converter:

- Cascaded control structure with new controllers design.
- Direct AC voltage control.

Both control structures have shown their effectiveness in ensuring a stable system operation and acceptable dynamic behavior in different grid cases i.e.; in both standalone mode and grid-connected mode. The difference between the proposed methods is not their performances, but their flexibility to achieve the desired dynamics i.e., because of the modes interactions caused by the current loop in cascaded control structure, it is difficult to tune the controller gains in a classical way. Indeed, all the dynamics have to be considered to improve the overall system dynamics and guarantee a stable behavior. While, based on the direct AC voltage control, no current control loop is required, only transient active damping is used to avoid the resonance frequency of the LCL filter. This allows the converter operating according to its physical voltage source behavior. Furthermore, it allows more flexibility for the control design and less interactions between modes.

Far from the 2-Level VSC, the MMC-based grid-forming control has also been studied in this chapter. As no output LC filter is required, the MMC simply behaves as a controllable voltage source with a perfect output AC voltage sinewave. In addition to the AC voltage management, a high level energy regulation is required to maintain the submodule capacitors of the MMC around their nominal values. The results obtained in this chapter did not reveal any particular interaction between the energy management loop and active power control loop.

The great advantage of the cascaded structure is the ability to switch from voltage mode control to the current mode control in order to protect the system against overcurrent, whereas, with the direct AC voltage control based on 2-Level VSC and VSC-MMC, the system requires other methods to protect equipment; this question will discussed further in the next chapter.

V. Current limitation and transient stability

Two fundamental strategies have been proposed for grid-forming converters in order to limit the current during transients. The first is the Current Saturation Algorithm (CSA), which has been implemented in different ways [82], [88], [89], [93]. Despite that the current saturation limits the current during a transient, the AC voltage controllers will not be able to keep the AC voltage aligned with the grid voltage if no adequate synchronization unit is utilized (i.e.; PLL-based synchronization usually used for current-controlled VSCs). Hence, the system may become unstable during the post-fault phase [84].

The second solution is based on Virtual Impedance (VI) [84]–[87], [94] that has been adopted to emulate the effect of a physical impedance when the current exceeds its nominal value. These methods have shown their effectiveness to limit the current transients in case of tripping lines [87] and heavy load connection [84] while keeping the same nature of the power source i.e.; voltage source. Moreover, they ensure more transient stability in comparison to the current saturation [84] in such events. These concepts have been used especially for 2-Level converters based on cascaded control structure. Consequently, their implementation depends mainly on the AC voltage controller dynamics, and therefore, important transient overshoots may occur during the first fault moments before limiting the current. Such behavior is worth analyzing. Contrary to the VSC based on the inner cascaded control, the direct AC voltage control does not have voltage and current regulation loops. Thus, it has no restrictions on the output current. This major question will be dealt with in this chapter by considering a threshold current loop that only reacts when the current exceeds its maximum allowable value.

Once the fault is cleared, the post-fault synchronization is of highest importance. Indeed, an unstable behavior when the overcurrent protection is disabled would lead to an unavoidable trip from the main grid for safety purposes [18]. However, in future power systems, all different power sources have to cope with various events and guarantee the stability. In this context, the transient stability of the system is defined as the ability of the power converter to stably recover its equilibrium point after fault clearing. The choice of the current limiting algorithm has a large influence on the transient stability. In [92], [95], the transient instability phenomenon using the CSA while keeping the droop control (Strategy C) has been studied. To avoid this instability issue, some papers proposed to switch from voltage control based on the droop control to current control based on a phase-locked loop [22], [98]. These methods require a complex algorithm for fault detection and triggering conditions. Moreover, as specified by [22], fault recovery could only be achieved after a considerable retuning of the voltage controller and the power controller in order to avoid AC voltage collapse. In [84], the authors showed through time-domain simulations, the ability of the VI to ensure a better transient stability than the CSA in case of a heavy load connection. However, this result has not been theoretically investigated.

In this chapter, the focus is initially on the current limitation and the post-fault synchronization of a grid-forming converter based on “Strategy C”, where no grid information is required for synchronization. Then, the developed approach will be applied to “Strategy A” and “Strategy B”. In this context, this chapter aims to:

- Compare the CSA and VI in terms of current dynamics.
- Study the impact of the CSA and the VI on the transient stability of the system.
- Propose a hybrid current limiting control (HCLC) to ensure an accurate current limitation thanks to the CSA and a better transient stability thanks to the VI.
- Propose an adaptive droop control gain to increase the critical clearing time and to limit the angle variation during a fault, and thereby, to enhance the system dynamics and its transient stability after fault clearing.

The analysis is mainly focused on a grid-forming control with a negligible inertial effect, which allows to develop some simplified analytical expressions and to give some general considerations in terms of transient stability analysis. Since the inertial effect can be modified by the control, it is also interesting to study the case when it is not negligible. Simplified approaches are not possible anymore. However, thanks to the simulation results, it is still possible to use the same methodology to evaluate the transient stability and enhance the critical clearing time.

V.1 Algorithms for current limitation

V.1.1 Current saturation algorithm

As explained previously, the first solution to limit the current is to apply saturation on the current reference. In case of a cascaded control structure, the current loop already exists. It is then possible to limit the current reference with no major modification in the control. In case of a direct voltage control, this current loop does not exist, hence it is needed to create a kind of an artificial current loop in order to be able to saturate the current reference.

V.1.1.1 Cascaded control structure

A way to limit the current in the converter is to apply saturation on the current references. One solution is the d-axis priority-based CSA [95]. This strategy is described as,

$$\begin{cases} |\, i^*_{s_{dS}} | = \min(I_{\max SAT}, |\, i^*_{s_d} |) \\ |\, i^*_{s_{qS}} | = \min(\sqrt{I^2_{\max_{SAT}} - {i^*_{s_{dS}}}^2}, |\, i^*_{s_q} |) \end{cases} \tag{V-1}$$

A second possibility is to limit the current magnitude I_s^* without giving a priority to the direct current $i_{s_d}^*$ or to the quadratic one $i_{s_q}^*$. This strategy is described as,

$$\begin{cases} i_{s_{dqS}}^* = i_{s_{dq}}^* & if \quad \sqrt{i_{s_d}^2 + i_{s_q}^2} < I_{max_{SAT}} \\ i_{s_{dS}}^* = I_{max_{SAT}} \cos\left[\arctan 2\left(\dfrac{i_{s_q}^*}{i_{s_d}^*}\right)\right] & if \quad \sqrt{i_{s_d}^2 + i_{s_q}^2} \geq I_{max_{SAT}} \\ i_{s_{qS}}^* = I_{max_{SAT}} \sin\left[\arctan 2\left(\dfrac{i_{s_q}^*}{i_{s_d}^*}\right)\right] & if \quad \sqrt{i_{s_d}^2 + i_{s_q}^2} \geq I_{max_{SAT}} \end{cases} \tag{V-2}$$

$I_{\max SAT}$ denotes the maximum allowable current magnitude of the converter, whereas $i_{s_{dqS}}^*$ denote the saturated *d-q* currents.

During the current limitation, the voltage controller integrator may diverge. To avoid this issue, an anti-windup feedback is used during the saturated mode. The gain k_{iv} of the controllers is set to zero as illustrated in Figure V-1.

The overall control of a 2-level VSC based on the cascaded control loops and the CSA is depicted in Figure V-2.

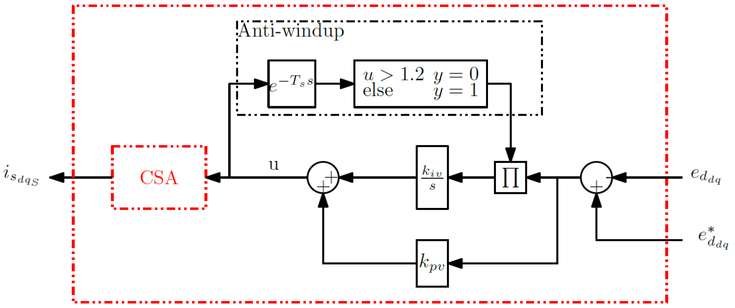

Figure V-1 - CSA and AC voltage PI controller with anti-windup

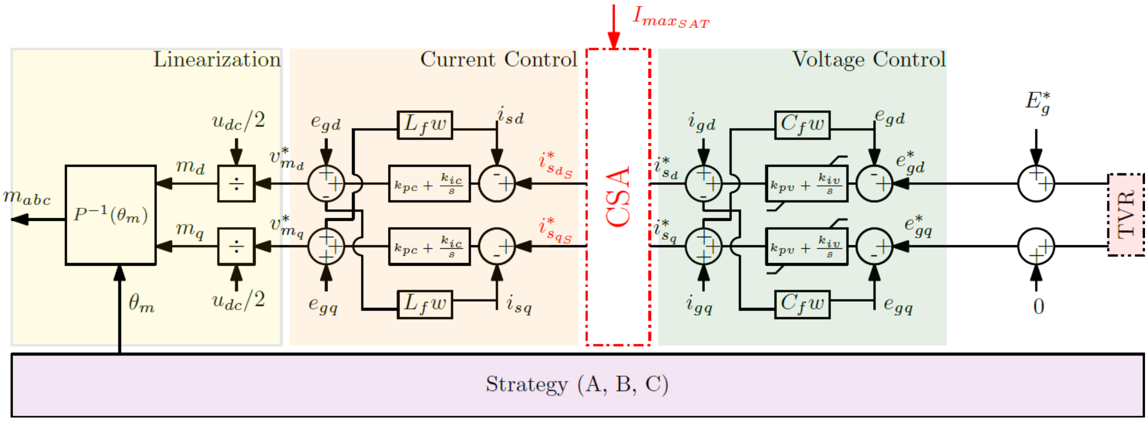

Figure V-2 - Grid-forming 2-Level VSC based on cascaded control structure and CSA

V.1.1.2 Direct AC voltage control structure

As explained previously, the CSA cannot be directly implemented for the 2-Level VSC and MMC based on the direct AC voltage control structure since it does not use any current loop. Therefore, the idea of this subsection is to add a fictitious current loop named “Threshold Current Control (TCC)”, which allows saturating the current reference only when it exceeds its maximum allowable magnitude. Therefore, all the performances achieved by the control in normal operation mode remain effective. This idea has been initiated in [22]. In this thesis, more details on its design are given.

V.1.1.2.1 Threshold current control principle

The aim of the grid-forming control is to define a set of voltage references $v^*_{m_{dq_i}}$. The idea is to generate *d-q* current references from these voltage setpoints, then implement a current control loop to generate a new set of references for the modulated voltages ($v^*_{m_{dq_o}}$). In normal operation, the two sets of voltage references have to be equal ($v^*_{m_{dq_i}} = v^*_{m_{dq_i}}$) to avoid modifying the overall behavior of the system. In case of overcurrent, a limitation can be applied on the generated current references.

Let’s recall the conventional *d-q* current control formulation:

$$v^*_{m_{dq_o}} = \left(i^*_{s_{dqS}} - i_{s_{dq}}\right)C(s) \pm L_f\omega_m i_{s_{dq}} + e_{g_{dq}} \tag{V-3}$$

C(s) is the current controller.

The trick of the threshold current control consists in reversing (V-3):

$$i^*_{s_{dq}} = \left(v^*_{m_{dq_i}} \mp L_f\omega_m i_{s_{dq}} - e_{g_{dq}}\right)C(s)^{-1} + i_{s_{dq}} \tag{V-4}$$

By paying attention to the red and green terms, important conclusions can be drawn:

- If $i^*_{s_{dq}} = i^*_{s_{dqS}}$, then, (V-3) and (V-4) are compensated and their effect is canceled, $v^*_{m_{dq_i}} = v^*_{m_{dq_o}}$.
- If $i^*_{s_{dq}} \neq i^*_{s_{dqS}}$, consequently, the current control loop in (V-3) is activated and the converter moves to a current regulation mode, where $v^*_{m_{dq_o}}$ are calculated to achieve the desired current references $i^*_{s_{dqS}}$.

This idea is well illustrated in Figure V-3.

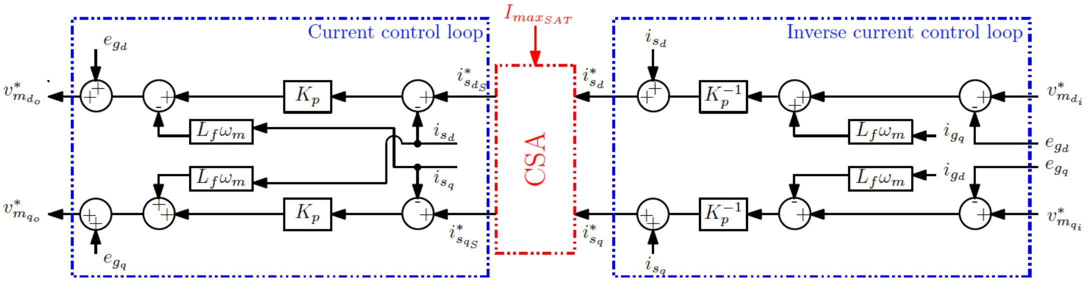

Figure V-3 - Threshold current loop

Actually, if the CSA is implemented, $i^*_{s_{dq}}$ is equal to $i^*_{s_{dqS}}$ if the current is lower than the maximum allowable current $I_{\max_{SAT}}$. Otherwise, the current is saturated to protect the converter against overcurrent, and thus, the converter moves from a voltage source to a current source. To achieve a perfect compensation between (V-3) and (V-4) in the unsaturated mode, the choice of C(s) is very important. Actually, it is compulsory that the controller has to be a proportional one, C(s) = K$_P$ in order to be able to easily invert the control.

V.1.1.2.2 Threshold current controller design

Assuming that the current saturation mode is enabled, the threshold current loop is activated (i.e., the VSC is controlled as a current injector) and the resistive part is neglected, the closed-loop transfer function of the current loop is expressed as,

$$\frac{i_{s_{dq}}}{i^*_{s_{dqS}}} = \frac{1}{1+\tau_{des}s} \tag{V-5}$$

With $\tau_{des} = L_f / (\omega_b K_p)$ for 2-level VSC and $\tau_{des} = L^{ac}_{eq} / (\omega_b K_p)$ for the MMC-VSC.

The current loop controllers are set to K_P = 0.45 p.u for 2-level VSC and K_P =2.05 p.u for VSC-MMC. The chosen gains ensure acceptable dynamics and small currents steady state error.

The overall control of a 2-level VSC and VSC-MMC based on the direct AC voltage control and the CSA are depicted in Figure V-4.

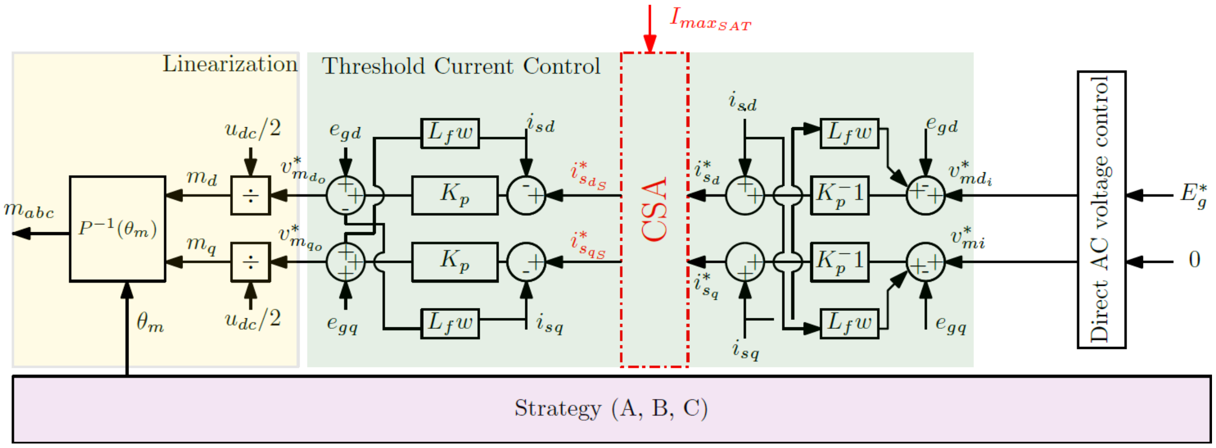

(a) 2-level VSC

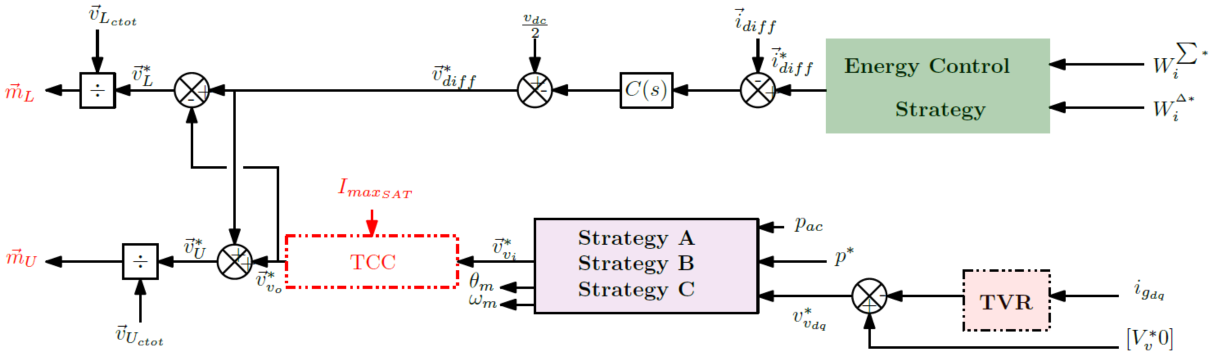

(b) VSC-MMC

Figure V-4 - Grid-forming VSC based on direct AC voltage control and CSA

V.1.2 Virtual impedance

A second solution to limit the current is the virtual impedance strategy [84].

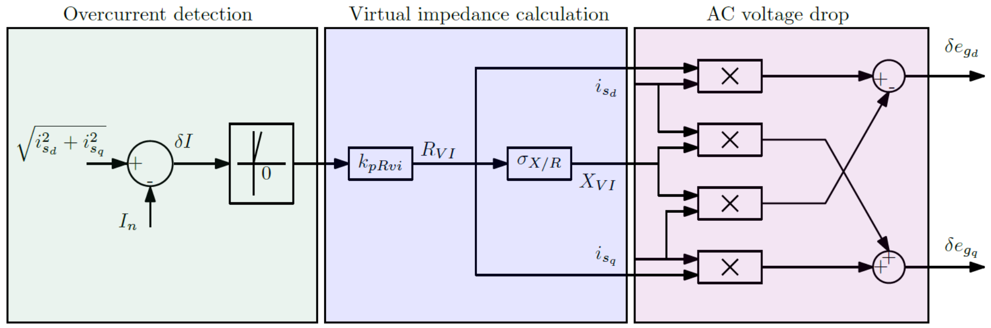

Figure V-5 - Virtual impedance principle

As illustrated in Figure V-5, the VI operation principle is divided into three main phases:

- Overcurrent detection and activation (i.e., activation only when the current exceeds its nominal value $I_n = 1$ p.u).
- Virtual impedance calculation.
- AC voltage drop calculation.

The expressions of X_{VI}, and R_{VI} are given in (V-6) and (V-7).

$$X_{VI} = \begin{cases} k_{p_{R_{VI}}} \sigma_{X/R} \delta I & if\ \delta I > 0 \\ 0 & if\ \delta I \leq 0 \end{cases} \qquad \text{(V-6)}$$

$$R_{VI} = X_{VI} / \sigma_{X/R} \qquad \text{(V-7)}$$

Where $\delta I = I_s - I_n$. $k_{p_{R_{VI}}}$ and $\sigma_{X/R}$ are defined respectively as the virtual impedance proportional gain and the virtual impedance ratio.

The parameter $k_{p_{R_{VI}}}$ is tuned to limit the current magnitude to a suitable level $I_{\max_{VI}}$ during overcurrent in steady state, while $\sigma_{X/R}$ ensures good system dynamics during the overcurrent and keeps a higher X/R ratio. The tuning method of these parameters is explained in [20], [84].

When the virtual impedance is activated, the new modulated AC voltage references are given by (V-8 & V-10):

Cascaded control $$e^*_{g_d} = e^{*'}_{g_d} - \delta e_{g_d} \quad , \quad e^*_{g_q} = e^{*'}_{g_q} - \delta e_{g_q} \qquad \text{(V-8)}$$

Direct control $$v^*_{m_{di}} = v^{*'}_{m_{di}} - \delta e_{g_d} \quad , \quad v^*_{m_{qi}} = v^{*'}_{m_{qi}} - \delta e_{g_q} \qquad \text{(V-9)}$$

Direct control MMC $$v^*_{v_{di}} = v^{*'}_{v_{di}} - \delta e_{g_d} \quad , \quad v^*_{v_{qi}} = v^{*'}_{v_{qi}} - \delta e_{g_q} \qquad \text{(V-10)}$$

where, $$\delta e_{g_d} = R_{VI} i_{s_d} - X_{VI} i_{s_q} \qquad \text{(V-11)}$$

$$\delta e_{g_q} = R_{VI} i_{s_q} + X_{VI} i_{s_d} \qquad \text{(V-12)}$$

The implementation of the VI on the 2-level VSC and VSC-MMC is depicted in Figure V-6 and Figure V-7, respectively.

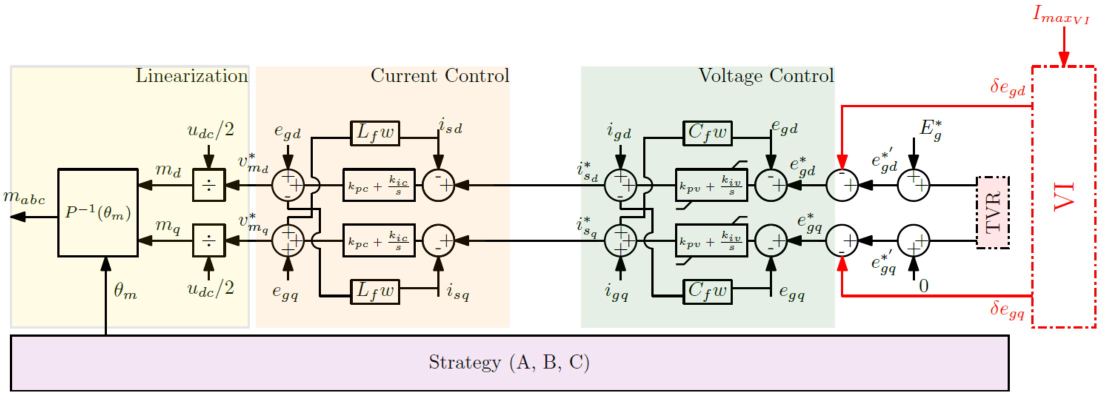

(a) Cascaded control structure

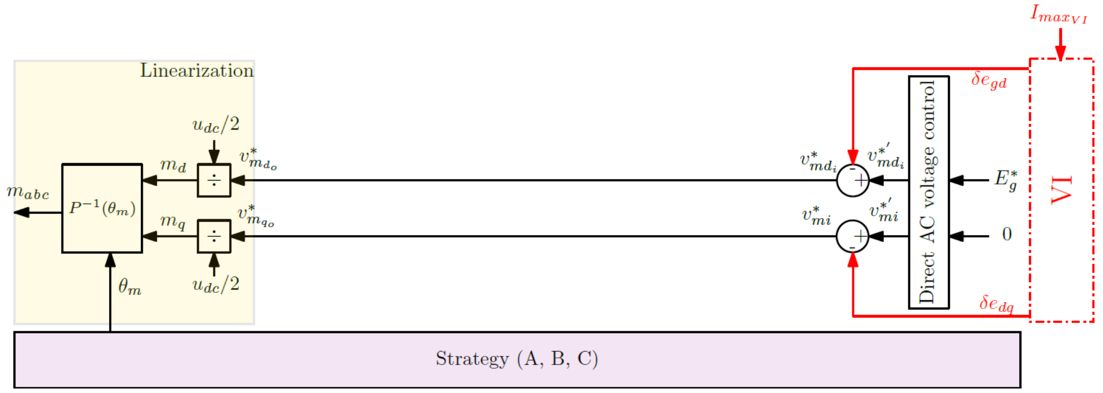

(b) Dierect control structure

Figure V-6 Grid-forming 2-Level VSC based on VI

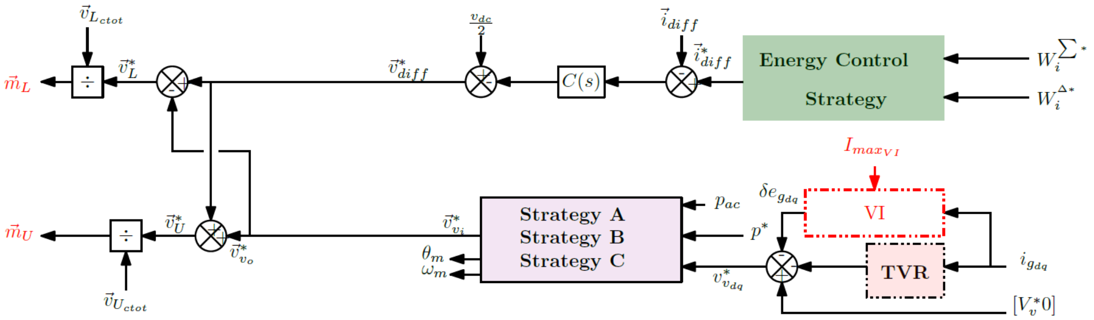

Figure V-7 - Grid-forming 2-Level VSC and MMC-VSC based on VI

V.2 Validation and dynamic comparison between CSA and VI

At t = 1s, a symmetrical three-phase bolted fault is applied to the system at the PCC. System and control parameters are listed in Table V-1.

Table V-1 System and control parameters

Symbol	Value	Symbol	Value
$I_{max_{SAT}}$	1.2 p.u	SCR	10
$I_{max_{VI}}$	1.2 p.u	$kp_{R_{VI}}$(MMC)	0.8478 p.u.
$\sigma_{X/R}$	5	$kp_{R_{VI}}$(VSC)	0.6716 p.u.

The operating point is $p^* = 0.9$ p.u. The electrical variable simulated is the VSC output current magnitude I_s. Simulation results are gathered in Figure V-8.

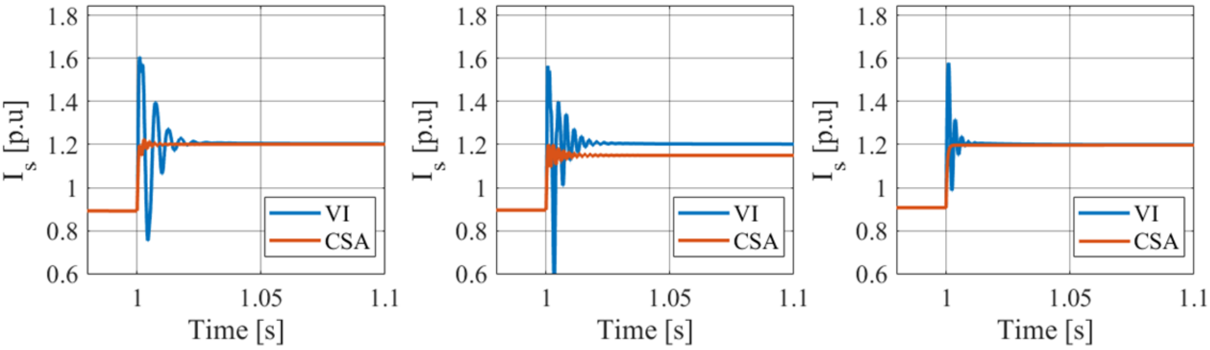

(a) 2-level VSC "cascaded control" (b) 2-level VSC "direct control" (c) MMC-VSC direct control

Figure V-8 - System dynamics during a symmetrical three-phase fault

One can observe from the results that the VI limits the current to the specified value ($I_{max_{VI}}$=1.2 p.u) after a repetitive current transient. This could be dangerous since it reaches higher current peaks during the first 20 ms (I_s = 1.6 p.u).

Compared to the VI, the CSA shows its effectiveness to ensure with more accuracy a current limitation throughout the fault duration. This is due to its direct action on the current. From these results, a first conclusion is drawn: CSA is more efficient than VI for current limitation.

V.3 Post-fault synchronization of a grid-forming converter based on "Strategy C"

Once the fault is cleared (i.e., three-phase bolted fault), the power converter has to be able to resynchronize to the AC grid only using local measurements. The aim of this section is to compare the transient stability of the system in case of a bolted fault with VI and CSA. For the sake of simplicity, it is assumed that: The $L_f C_f$ filter and the inner control are ignored and the inertial effect is neglected (see Figure V-9).

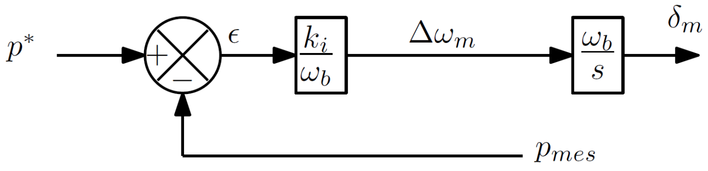

Figure V-9 - Strategy C without inertial effect

To check the conclusion drawn from this first analysis, some simulations are proposed with the full system dynamics and with inertial effect.

V.3.1 Transient stability analysis without current limitation algorithms

A simplified quasi-static model in Figure V-10 is derived from the previous assumptions. In this first approach, the current limiting algorithms are not introduced. The simplified model gathers actual electrical variables I_g,V_e and the AC voltage V_m.

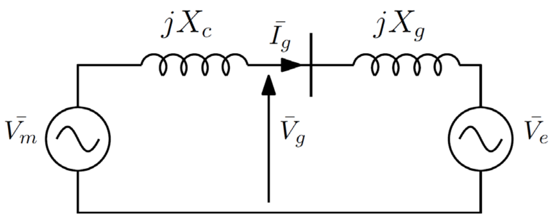

Figure V-10 - Simplified quasi-static grid-forming model in unsaturated mode

In quasi-static operation, it is possible to calculate the active power with the classical formula:

$$p_{mes} = P_{\max} \sin(\delta_m) \tag{V-13}$$

with,

$$P_{\max} = \frac{V_m V_g}{X_c + X_g} \tag{V-14}$$

Based on the simplified model, Figure V-11 depicts the synchronization process of the grid-forming converter subject to a three-phase bolted fault.

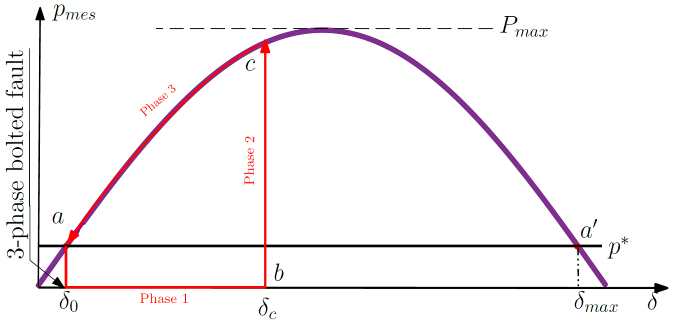

Figure V-11 - $p_{mes}(\delta_m)$ diagram of a droop control based VSC without inertial effect

For a given p^*, there are two equilibrium points (a) and (a') where the power p_{mes} is equal to its reference p^*. However, only the equilibrium point (a) is stable in small-signal analysis [150]. The initial angle δ_0 is given by,

$$\delta_0 = \arcsin\left(\frac{p^*}{P_{\max}}\right) \tag{V-15}$$

The maximum angle $\delta_{\max}$ of the operating point a' is expressed as,

$$\delta_{\max} = \pi - \delta_0 \tag{V-16}$$

In normal operation $\omega_m = \omega_e$. When the fault occurs, p_{mes} drops to zero resulting in an instantaneous frequency deviation.

$$\omega_m = k_i p^* / \omega_b + \omega_{set} \tag{V-17}$$

Considering that $p^* \geq 0$, ω_m will be higher than ω_m during the fault (Hyper-synchronism), which results in a positive angle deviation (phase 1). When the fault is cleared, the voltage is supposed to recover instantaneously. The consequence is a straight vertical line from the operating point (b) to (c) (phase 2). During this phase

$\delta_m = \delta_c$ (δ_c is named the clearing angle). At the end of phase 2, p_{mes} is higher than p^* leading to $\omega_m < \omega_e$ (Hypo-synchronism). It results in a decrease of the angle from (c) to the equilibrium point (a) (phase 3), where $\omega_m = \omega_e$ and $p_{mes} = p^*$.

The system recovers the equilibrium point (a) after fault clearance if δ_m does not exceed $\delta_{\max}$ [92].

V.3.2 Transient stability analysis of a VSC based on virtual impedance

The effect of the virtual impedance is introduced to embed the current limitation in this analysis. Therefore, Figure V-10 is modified when the current exceeds its rated current I_n (Figure V-12).

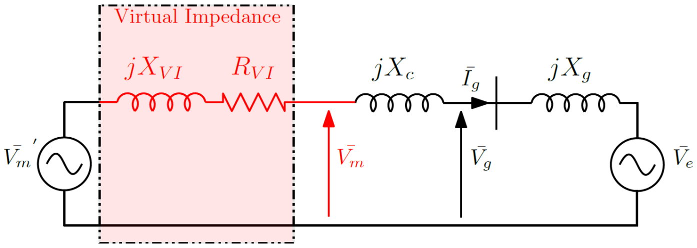

Figure V-12 - Simplified quasi-static grid-forming model including the VI

From Figure V-12, the new expression of the delivered active power including the virtual impedance is expressed as follow:

$$p_{mes} = \frac{V_m^{'} V_e}{\sqrt{(X_T^2 + R_T^2)}} \sin\left(\arctan\left(\frac{R_T}{X_T}\right) + \delta_m\right) - \frac{V_e^2 R_T}{X_T^2 + R_T^2} \tag{V-18}$$

with $X_T = X_c + X_g + X_{VI_{\max}}$ and $R_T = R_c + R_g + R_{VI_{\max}}$.

$X_{VI_{\max}}$ and $R_{VI_{\max}}$ are the virtual inductance and resistance defined from the current limit $I_{\max_{VI}}$. Note that $R_{VI\max}$ could be neglected since $X_{VI} \gg R_{VI}$. However, it is considered to have more accurate theoretical results.

The maximum active power, including the virtual impedance is given by:

$$P_{\max 2} = \frac{V_m^{'} V_e}{\sqrt{(X_T^2 + R_T^2)}} + \frac{V_e^2 R_T}{X_T^2 + R_T^2} \tag{V-19}$$

Several curves $p_{mes}(\delta_m)$ can be drawn in Figure V-13 for different values of the virtual impedance comprised between $Z_{VI} = Z_{VI\max}$ $(I_s = I_{\max})$ and $Z_{VI} = 0$ $(I_s \leq I_n)$. The sequence of operations is now modified:

- Phase 1 is similar with or without virtual impedance.
- Phase 2, the fault is cleared. As a consequence, the operating point moves first to (c), which is now located on the new curve p_{mes} in (V-18).
- Phase 3, the operating point moves from (c) to (d). In this phase, Z_{VI} progressively decreases until Z_{VI} is equal to zero (i.e., the operating point is equal to (d)).

- Phase 4, the virtual impedance is disabled and the operating point moves from (d) to the equilibrium point (a).

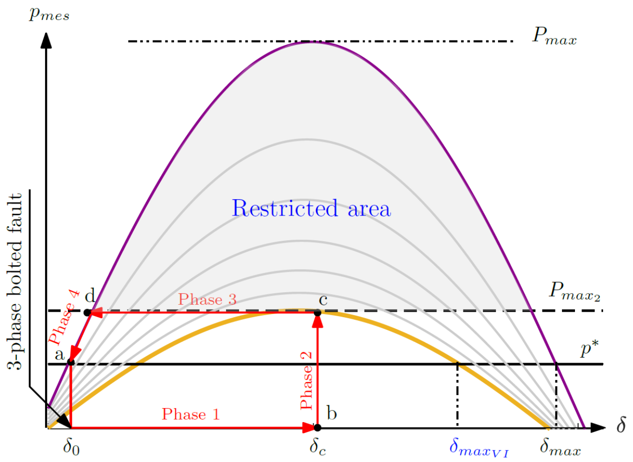

Figure V-13 - $p_{mes}(\delta_m)$ diagram of a droop control based-VSC and VI

The activation of the virtual impedance results in a decrease of $P_{\max}$ to $P_{\max 2}$ since the total impedance increases. As a consequence, the system remains stable if the fault is cleared before $\delta_{\max VI}$ expressed in (V-20).

$$\delta_{\max VI} = \pi - \arctan\left(\frac{R_T}{X_T}\right) - \arccos\left(\frac{p^*(X_T^2 + R_T^2) + V_e^2 R_T}{V_m^{'} V_e \sqrt{(X_T^2 + R_T^2)}}\right) \tag{V-20}$$

Based on (V-20), a stability limit δ_{cc} (the critical clearing angle) is defined,

$$\delta_{cc} = \delta_{\max VI} \tag{V-21}$$

V.3.3 Transient stability analysis of a VSC based on current saturation algorithm

The transient stability is now analyzed in case of a Current Saturation Algorithm considering the CSA solution where the current is aligned with the d-axis. The expression of the delivered active power when the current exceeds its maximum allowable magnitude $I_{\max_{SAT}}$ is expressed as follow:

$$p_{mes} = P_{\max 3} \cos(\delta_m) \tag{V-22}$$

where,
$$P_{\max_3} = I_{\max_{SAT}} V_e \tag{V-23}$$

Figure V-14 depicts the evolution of the grid-forming converter angle in the current saturated mode. The sequence of operation is now:
- Phase 1 is similar with or without the current saturation algorithm.
- Phase 2, the fault is cleared. As a consequence, the operating point moves first to (c), which is now located in the new curve $p_{mes} = P_{\max_3} \cos(\delta_m)$.
- Phase 3, the operating point moves from (c) to (d). At this particular operating point, the saturated curve crosses the unsaturated one. Indeed, when the operating

point reaches (d), the modulated AC voltage recovers its nominal value, and then, it is possible to recover a normal voltage control mode, which leads to a natural switch from the saturated mode to the unsaturated mode.

- Phase 4, the system moves from (d) to its equilibrium point (a).

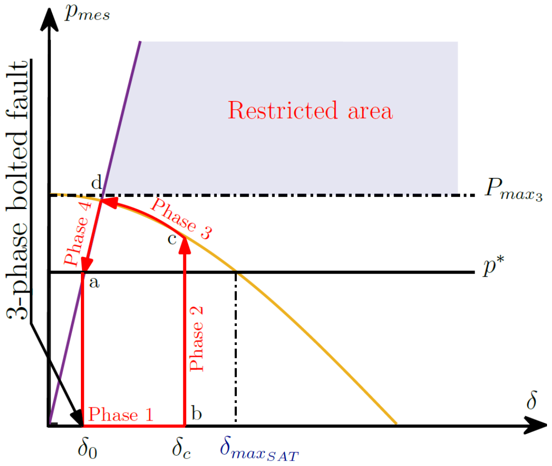

Figure V-14 - $p_{mes}(\delta_m)$ diagram of a “Strategy C” based VSC and current saturation algorithm

The activation of the CSA results in a decrease of $P_{\max}$ to $P_{\max 3}$. Therefore, the system remains stable if the fault is cleared before $\delta_{\max SAT}$ expressed in (V-24).

$$\delta_{\max SAT} = \arccos\left(\frac{p^*}{P_{\max_3}}\right) \tag{V-24}$$

Based on (V-24), a new stability limit is defined,

$$\delta_{cc} = \delta_{\max SAT} \tag{V-25}$$

The first ascertainment from the analysis shows that the critical clearing angle of the system based on VI is higher than the one of CSA, which confirms the effectiveness of the VI to ensure a higher transient stability against CSA. This conclusion could also be confirmed through the calculation of the critical clearing time for both methods.

V.3.4 Critical clearing time calculation

Thanks to the previous analysis and considerations, it is now possible to calculate the critical clearing time t_c, which is the maximum fault duration that guaranteeing the stability of the system. It is determined based on the critical clearing angle.

Since p_{mes} is equal to zero during the fault, the evolution of the angle in time domain is given by the following equation,

$$\delta(t) = k_i p^* t + \delta_0 \tag{V-26}$$

The critical clearing time is obtained when δ reaches δ_{cc}, which is equal to $\delta_{\max_{VI}}$ when using the VI and $\delta_{\max_{SAT}}$ when using the CSA as explained in the previous subsection. It yields:

$$t_{c_{VI}} = \frac{[\delta_{\max VI} - \delta_0]}{m_p \omega_b p^*} \tag{V-27}$$

$$t_{c_{SAT}} = \frac{[\delta_{\max SAT} - \delta_0]}{m_p \omega_b p^*} \tag{V-28}$$

To have more general trends, a comparison between the critical clearing times $t_{c_{VI}}$ (red curve) and $t_{c_{SAT}}$ (yellow) has been performed in Figure V-15 for large range of operating points.

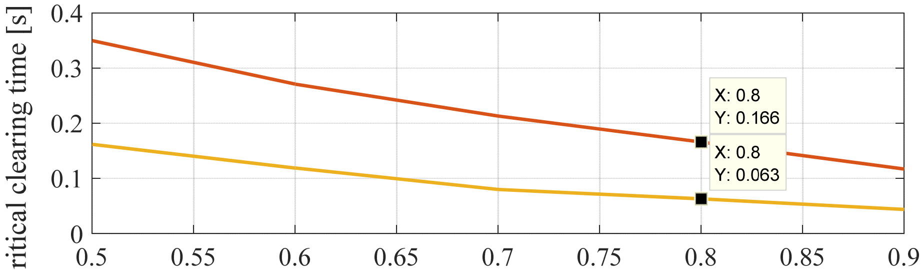

Figure V-15 - Comparison between critical clearing time for VI and CSA

As claimed in [84] and proved in this thesis, the virtual impedance ensures a transient stability of the system for a larger fault duration compared to the current saturation algorithm (e.g., for p^* = 0.8 p.u, the maximum fault duration based on VI is $t_{c_{VI}}$ = 165 ms, whereas, the maximum fault duration based on CSA is $t_{c_{SAT}}$ = 63.7 ms).

V.3.5 Validation through time-domain simulations

In this section, the theoretical and simplified approach developed previously is verified through time-domain simulations. In Figure V-16 and Figure V-17, dynamic $p_{mes}(\delta_m)$ curves (red and green curves) are drawn for both VI and CSA, respectively.

In Figure V-16 two test cases are performed:

- The fault duration is equal to $t_{c_{VI}}$ = 165 ms (Figure V-16.a).
- The fault duration is higher than $t_{c_{VI}}$ = 175 ms (Figure V-16.b).

The first ascertainment from the obtained results confirms the effectiveness of the theoretical approach, where the system stably recovers its equilibrium point when $t_{fault} \leq t_{c_{VI}}$ (Figure V-16.a), whereas, the system loses the synchronism when $t_{fault} > t_{cVI}$ (Figure V-16.b).

In Figure V-17, two test cases are performed for the CSA:

- The fault duration is equal to the $t_{c_{SAT}}$ = 63.7 ms (Figure V-17.a).
- The fault duration is higher than $t_{c_{SAT}}$ = 74 ms (Figure V-17.b).

Based on the angle evolution, it can be noticed that the system recovers stably its equilibrium point when $t_{fault} \leq t_{c_{SAT}}$ (Figure V-17.a), whereas, the system loses the synchronism when $t_{fault} > t_{cSAT}$ (Figure V-17.b).

Some differences can be observed between the theoretical $p_{mes}(\delta_m)$ curves and the dynamic ones. Nevertheless, the general trend of the evolution is confirmed.

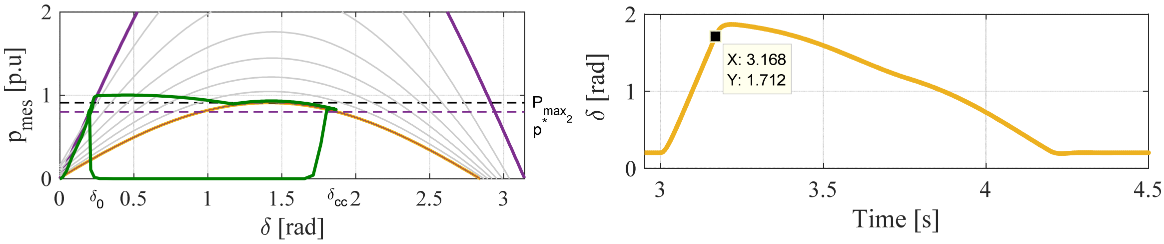

(a) Fault duration 165ms

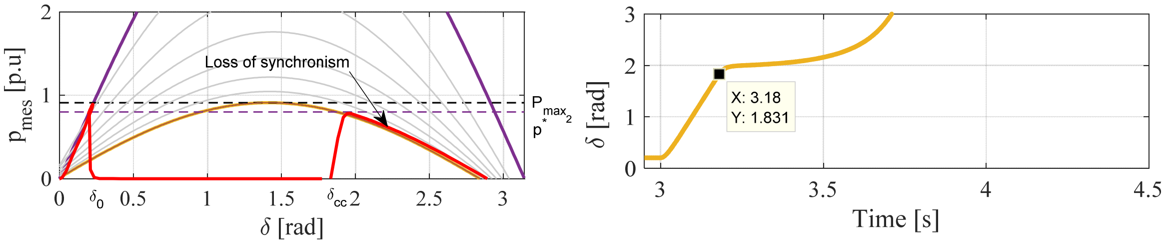

(b) Fault duration 175ms

Figure V-16 - Dynamic $p_{mes}(\delta_m)$ curve of the VSC based on droop control and VI

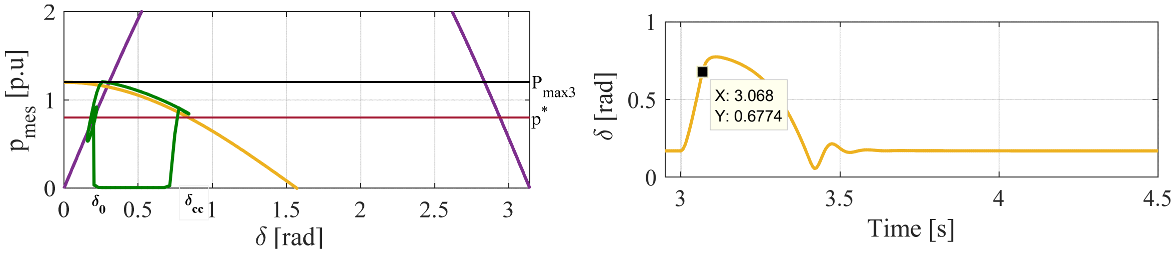

(a) Fault duration 65ms

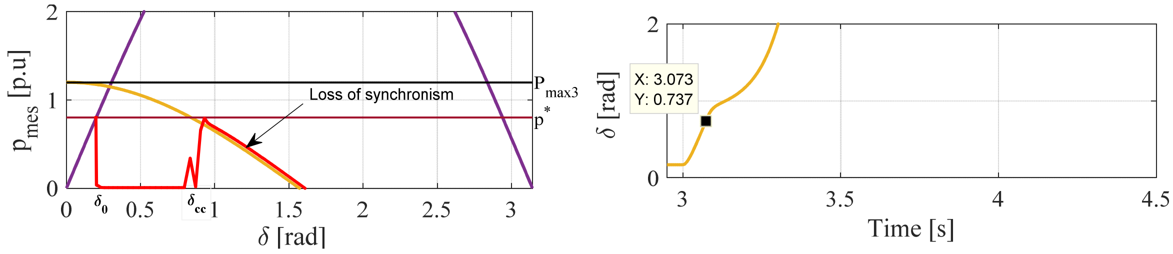

(b) Fault duration 75ms

Figure V-17 - Dynamic $p_{mes}(\delta_m)$ curve of the VSC based on droop control and CSA

V.3.1 Qualitative transient stability analysis of a VSC based on “Strategy C” and VI when taking into account the inertial effect

When the inertial effect is considered, the two first phases in Figure V-18 are unchanged compared to the system with a negligible inertial effect (Figure V-11). However, a new phase has to be introduced as shown in Figure V-18. When the fault is cleared, ω_m starts to decrease from the value calculated in (V-17) following the low-pass filter time constant. As long as $\omega_m > \omega_e$, the angle keeps increasing till $\omega_m = \omega_e$

(phase 3). Once this condition is fulfilled, the angle reaches its maximum value denoted by $\delta_c^{'}$. Then, since p_{mes} is still higher than p^*, the frequency keeps decreasing, which results in a decrease of the angle, and hence, a movement of the operating point from (c') to the equilibrium point (a) (phase 4). Once again, at the equilibrium point, $\omega_m = \omega_e$ and $p_{mes} = p^*$.

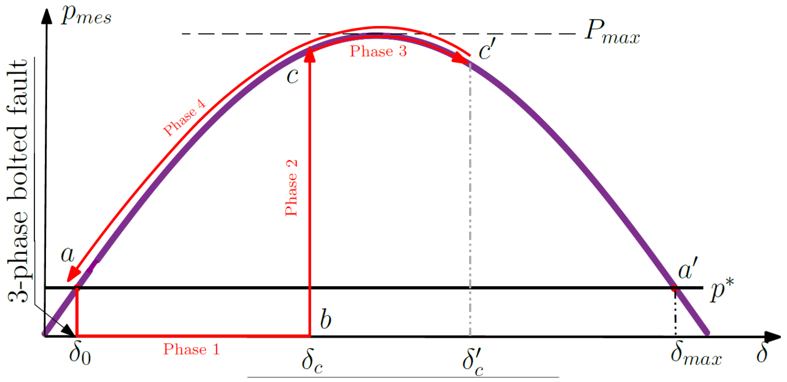

Figure V-18 - $p_{mes}(\delta_m)$ diagram of "Strategy C" based VSC with inertial effect (without current limitation)

When the inertial effect is considered, the stability limit is reached when $\delta_c^{'} = \delta_{\max}$. Hence, it can be concluded that the critical clearing angle δ_{cc} is strictly lower than $\delta_{\max}$. When the virtual impedance algorithm is embedded, the $p_{mes}(\delta_m)$ curve in Figure V-18 is modified as shown in Figure V-19. As previously explained, when the inertial effect is considered, the angle keeps diverging till (c') after the fault clearing, before recovering to the equilibrium point (a). In this condition, a new stability limit is defined,

$$\delta'_c = \delta_{\max VI} \tag{V-29}$$

Then $\delta_{cc} < \delta_{\max_{VI}}$.

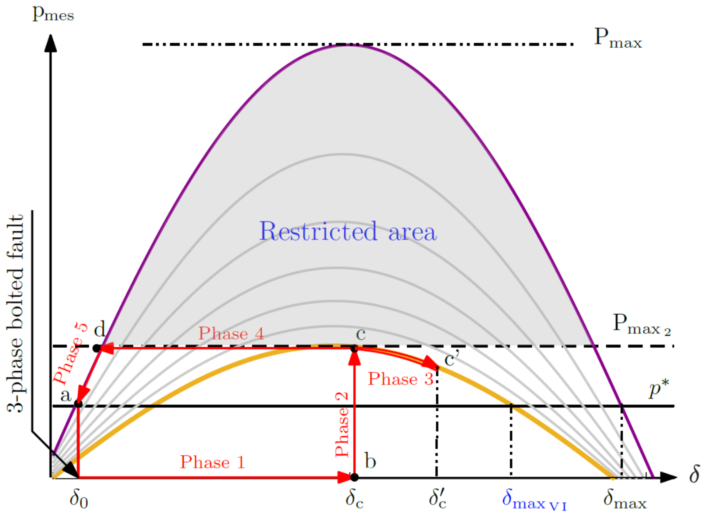

Figure V-19 - $p_{mes}(\delta_m)$ diagram of "Strategy C" based VSC and VI with inertial effect

In Figure V-20, time-domain simulations of $p_{mes}(\delta_m)$ is performed with an inertial effect of H_{VSC} = 5s (yellow curve). The operating point is p^* = 0.5 p.u.

Compared to the illustrative curve in Figure V-19, it can be noticed from the yellow dynamic $p_{mes}(\delta_m)$ curve in Figure V-20 that the general trend of the evolution is confirmed, where the phases described previously are clearly depicted.

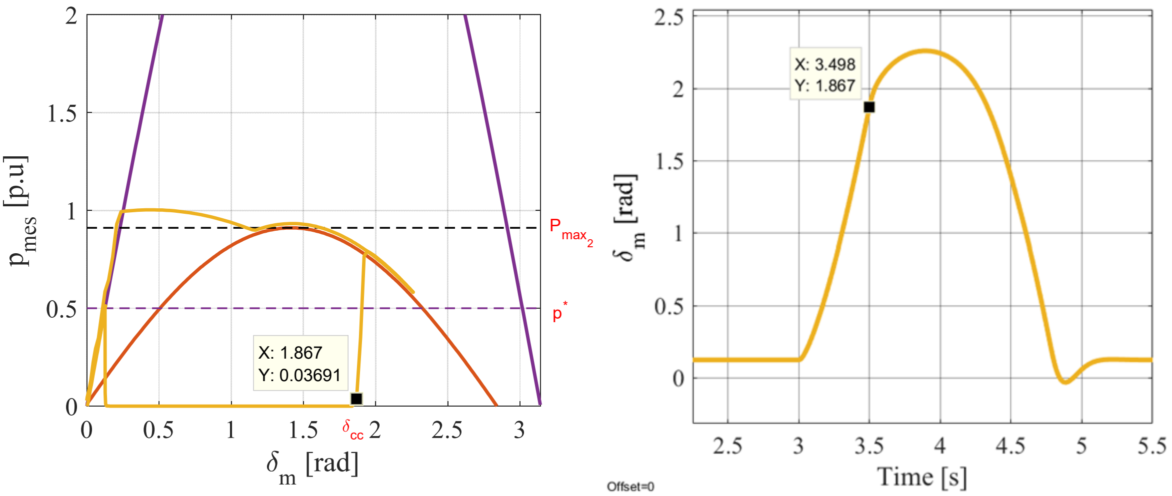

Figure V-20 - Dynamic $p_{mes}(\delta_m)$ curves obtained from time-domain simulations with H=5s

It can be noticed that the inertial effect has a positive impact on the critical clearing time. Actually, for the same operating point $p^* = 0.5$ p.u, $t_c = 350$ ms with $H_{VSC} \sim 0$ s and $t_c = 498$ ms with $H_{VSC} = 5$ s. This positive side effect of the inertia on the transient stability is well-known in the conventional power system [150].

V.3.2 Summary

Based on the analysis and results obtained from the previous sections, a comparison between the developed algorithms for current limitation is given in Table V-2.

Table V-2 Comparison between different algorithms for current limitation

Algorithm	Current limitation	Transient stability
CSA	+	-
VI	-	+

V.4 Hybrid current limitation algorithm (HCLC)

It is recalled from the previous sections that:

- CSA is better than VI in terms of current limitation.
- VI is better than CSA in terms of transient stability.

The idea in this section consists in hybridizing both control strategies in order to combine both advantages of each method [151].

In this section, the proposed control is applied to the 2-Level VSC based on cascaded control structure. The same approach can be adopted for 2-Level VSC and MMC based on direct AC voltage control as it will be illustrated through different test cases in section V.6.

To avoid the simultaneous operation of the virtual impedance and the current saturation algorithms, the maximum allowable current for the CSA should be higher than the current limitation for the VI e.g., $I_{\max_{SAT}}$ = 1.25 p.u and $I_{\max_{VI}}$ = 1.2 p.u are set as the maximum allowable current for the CSA and VI, respectively.

- When a fault occurs, the virtual impedance is activated as long as $I_s > 1$ p.u.
- If the current exceeds $I_{\max_{SAT}}$, the current saturation is enabled.
- The virtual impedance decreases the AC voltage reference to keep $I_s = I_{max_{VI}}$. As soon as $i^*_{s_{dqS}} = i^*_{s_{dq}}$, the CSA is disabled naturally without any supplementary conditions, and hence, the current limitation is guaranteed by the virtual impedance for the rest of the fault duration.

To demonstrate the operation of the proposed HCLC, a three phase fault is applied considering two fault durations:

- t_f = 65 ms (It corresponds to $t_{c_{CSA}}$ for p^* =0.8 p.u)
- t_f = 100 ms (This fault duration is higher than $t_{c_{CSA}}$ for p^* =0.8 p.u)

The following conclusions are drawn from Figure V-21 and Figure V-22:

- The HCLC limits the current transient during the first 10ms to $I_{\max SAT}$ thanks to CSA, and then, the VI guarantees the current limitation to $I_{\max VI}$ for the rest of the fault duration.
- When the fault duration $t_f \leq t_{cSAT}$, all algorithms allow a stable recovery to the equilibrium point. Whereas, when the fault duration $t_f > t_{cSAT}$, the system based on the CSA loses the synchronism, while both HCLC and VI guarantee the stability of the system.

Based on these conclusions, a new comparison between the developed algorithms for current limitation is given in Table V-3.

Table V-3 Comparison between different algorithms for current limitation

Algorithm	Current limitation	Transient stability
CSA	+	-
VI	-	+
HCLC	+	+

Despite that, the transient stability based on VI and HCLC is better than CSA, the risk of instability remains high if the fault duration is longer than the critical clearing time defined previously. Since all the dynamics of this kind of system are defined by the control, it is possible to adjust the control during the fault in order to improve the transient stability. The HCLC is adopted for the rest of this thesis.

V.5 Variable droop gain for transient stability enhancement

Focusing on a system with negligible inertia, (V-26) and (V-27) highlights the large impact of the droop gain k_i and the active power setpoint p^* on the angle evolution, and therefore, on the critical clearing time: by decreasing k_i or p^* during the fault, the critical clearing time increases and the angle evolution decreases as well. Therefore, the system remains stable for a longer fault duration and recovers its equilibrium point faster after fault clearing [152].

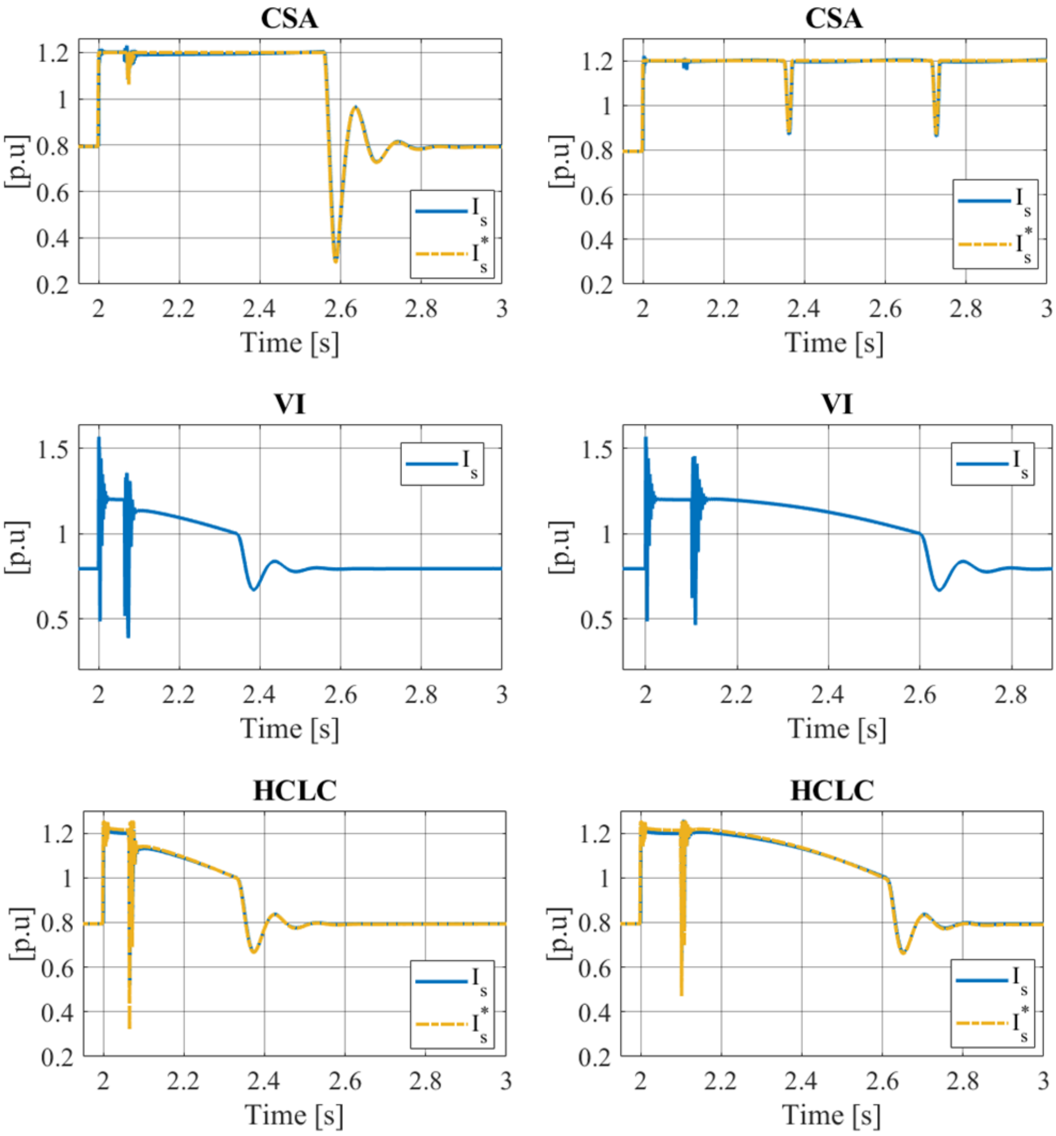

(a) Fault duration of 65ms

(b) Fault duration of 100ms

Figure V-21 - Comparison between CSA, VI and HCLC

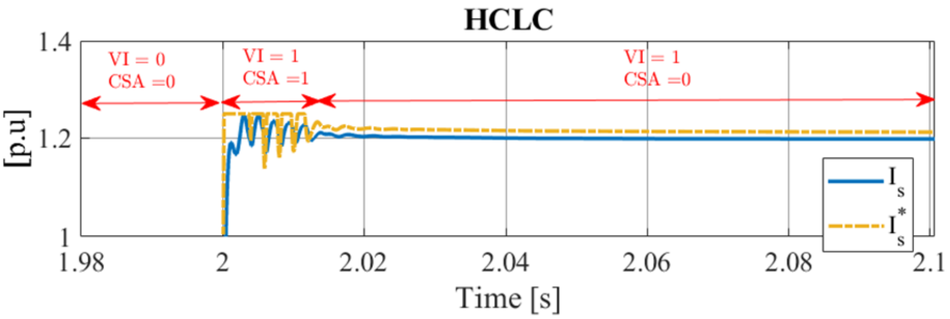

Figure V-22 - Operation sequences of the HCLC

Focusing on the parameter k_i, a question arises about the way to manage the evolution of k_i. Two different solutions are proposed in this section. To increase the critical clearing time, k_i must be decreased. The 1st solution proposes to decrease k_i with respect to the current magnitude. The 2nd solution proposes to decrease k_i with respect to the AC voltage magnitude resulting from the virtual impedance. At the end of this section, the effect of k_i is illustrated when the inertial effect is not negligible.

V.5.1 1st solution: Adaptive droop gain with respect to the current magnitude

A criterion to adjust k_i with respect to the current seems to be more intuitive. The aim of this section consists in showing the advantages and drawbacks of using this solution. k_i is defined by (V-30). α can take two pre-defined values in (V-31). If the output current exceeds its rated value, k_i is equal to one-tenth of its nominal value. Once the fault is cleared and the current returns to a safe value, the droop gain recovers its initial value k_{i0}.

$$k_i = \alpha k_{i0} \tag{V-30}$$

$$\alpha = \begin{cases} 1, & I_s \le 1\, p.u \\ 0.1, & I_s > 1\, p.u \end{cases} \tag{V-31}$$

Figure V-23 illustrates the system behavior using the 1st solution. For a given operating point p^* = 0.9 p.u, a 400 ms fault is applied on the system. Contrary to “Strategy C” with a fixed droop gain, the variable droop gain ensures a stable operation even if the fault duration is much longer than the critical clearing time computed in the previous section.

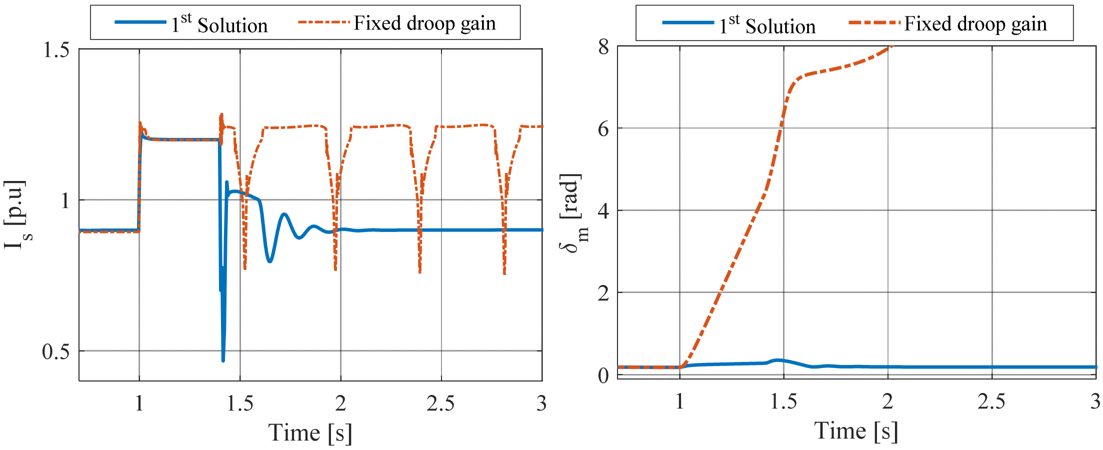

Figure V-23 - Transient stability with and without variable droop control

Decreasing k_i may have a second positive side effect. In Figure V-24, the system behavior for a 75 ms fault duration based on the “Strategy C” with a fixed droop gain ($k_i = k_{i0}$) and the 1st solution ($k_i = \alpha k_{i0}$) is analyzed. With a fixed droop gain, the system needs around 800 ms to re-stabilize, whereas with the variable droop gain, the recovery time is around 300ms. Actually, when the droop gain decreases during the fault, the angle variation is limited as demonstrated by (V-26), which explains the faster steady state recovery.

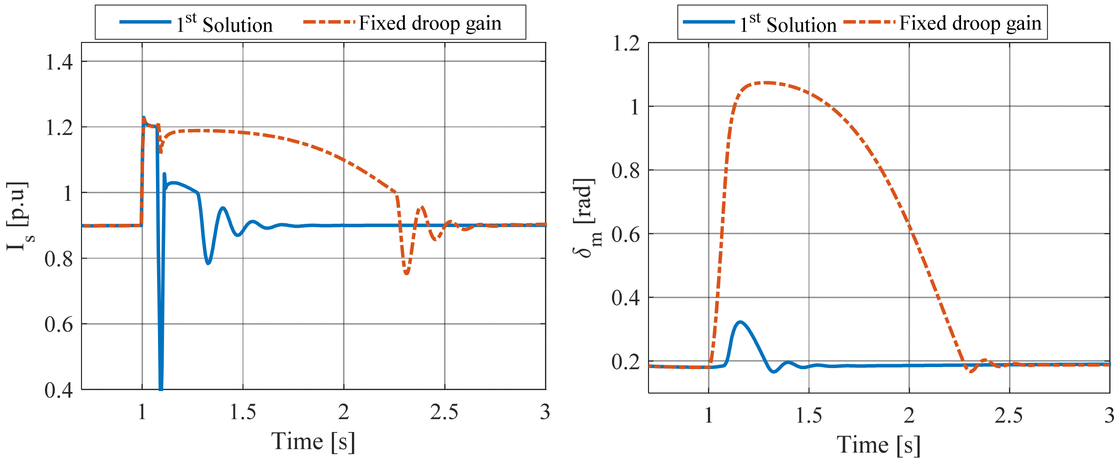

Figure V-24 - Comparison of the system dynamics for 75ms fault duration with constant and variable droop gain.

Nevertheless, the 1st solution may have a negative side effect if the overcurrent occurrence is due to a phase shift. In Figure V-25, a 30° phase shift is applied on the grid voltage (in power transmission systems, the phase shifts are especially linked to the lines tripping). As soon as the phase shift occurs, the current increase is limited by the HCLC. However, the current remains higher than 1 p.u for a long duration, and thus, the droop gain k_i remains frozen in $k_i = \alpha k_{i0}$, which completely modifies the system dynamics as proved in chapter III. Therefore, the resynchronization time is much longer than with the fixed droop gain.

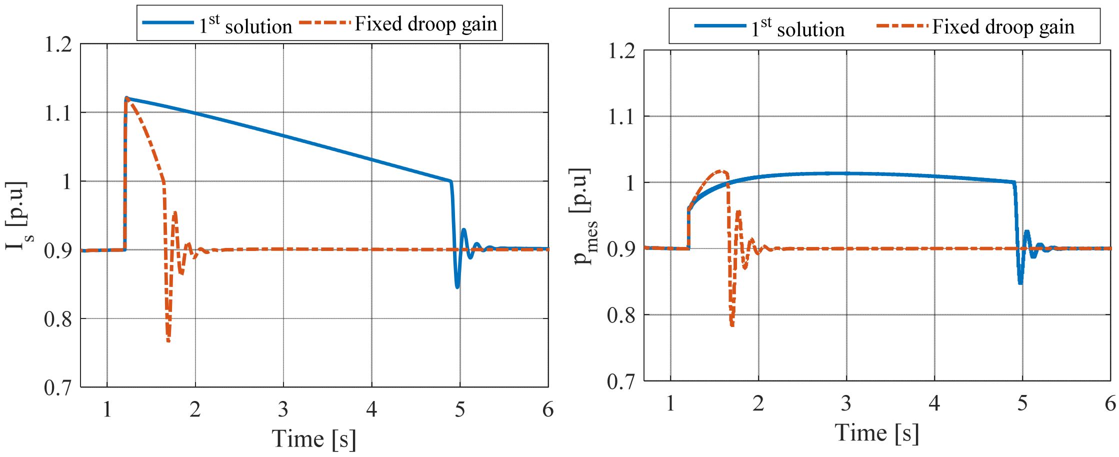

Figure V-25 - Impact of the 1st solution on the system dynamics during a phase shift

V.5.2 2nd Solution: Adaptive droop gain with respect to the AC voltage amplitude

The AC voltage can be considered as a good indicator of the fault nature. In case of a short circuit, the voltage is decreasing and the droop gain equally has to be decreased.

In case of a phase shift, the voltage amplitude remains approximately constant and the droop gain does not need to be modified. A solution could be to adjust the droop gain value with respect to the AC voltage level. However, it may lead to unwanted noises and fast transient variations in normal conditions. Therefore, a proposed solution consists of using the AC voltage reference instead of the measured value. The adaptive droop gain is expressed as follows:

$$k_i = \left(\sqrt{e_{gd}^{*2} + e_{gq}^{*2}} \right)^n k_{i0} \tag{V-32}$$

(V-32) shows that the droop gain can be slightly modified in case of AC voltage reference change. To avoid this effect, (V-33) is introduced. Hence, the droop gain is modified only when the current limitation algorithm is activated.

$$k_i = \left(\sqrt{\left(1 - \delta e_{g_d}\right)^2 + \delta e_{g_q}^2} \right)^n k_{i0} \tag{V-33}$$

The parameter $n \geq 1$ aims to control the decrease of the droop gain, and thereby, increasing the critical clearing time to the desired value. During the fault, the droop gain is modified. It is possible to calculate the new droop gain in order to evaluate the new critical clearing time. During a three phase bolted fault at PCC level, the droop gain is equal to $k_i = \left(Z_c I_{\max_{VI}} \right)^n k_{i_0}$ (e.g., n = 1 yields t_c = 950 ms and if n = 2, t_c = 5 s). These values ensure a large stability margin compared to what is required by the present grid code [18].

Such a small value of k_i cannot be maintained in normal operation, because it would induce a large active power variation during frequency fluctuations.

Time-domain simulations are performed with 400ms fault duration (Figure V-26.a) and a 30° phase shift (Figure V-26.b). A comparison is achieved between the first and the second solution based on variable droop control with n = 1.

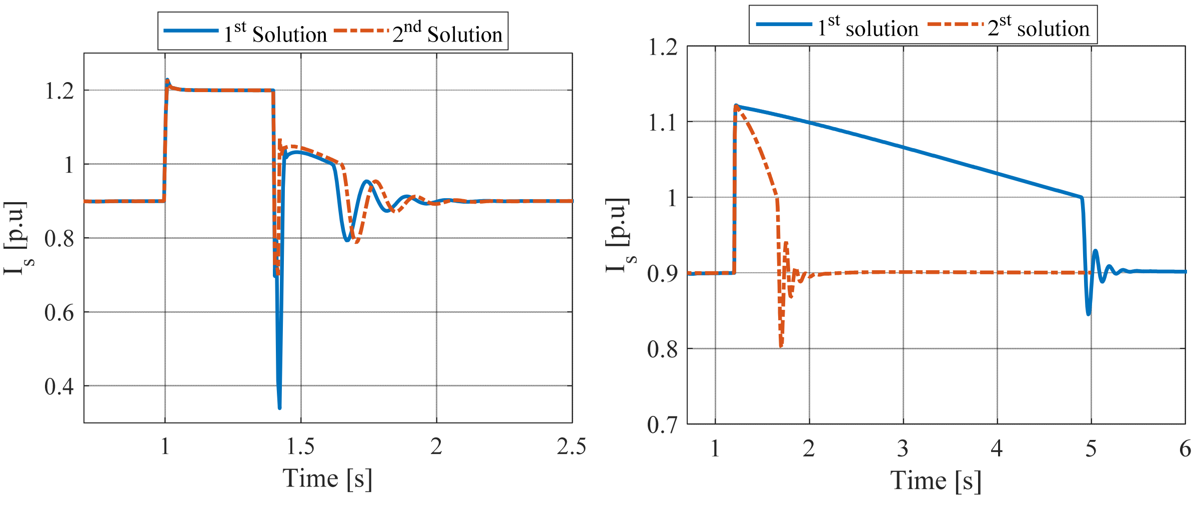

(a) Three phase fault

(b) 30° phase shift

Figure V-26 - Dynamic comparison between the 1st and 2nd solution based on variable droop control

The results show similar behavior with both solutions for a three-phase bolted fault. While, in the case of a phase shift, the second solution reveals a much better dynamic behavior. Indeed, since the voltage magnitude is nearly constant during a phase shift, the droop gain is not modified and the system dynamics have not changed considerably. Therefore, it is possible to conclude that the 2nd solution is more generic since it copes with various overcurrent situations.

In the following simulations, the same test cases in Figure V-26 are performed, where the proposed solution is applied to the system with an inertial effect of $H = 5$s. Simulation results are gathered in Figure V-27.

The system based on the “Strategy C” with fixed droop control and $H = 5$s remains stable if the fault duration is $t_c \leq 230$ ms for $p^* = 0.9$ p.u. In this context, the simulation results draw interesting results: with or without inertia effect, the proposed solution shows its effectiveness to ensure a stable operation for longer fault duration.

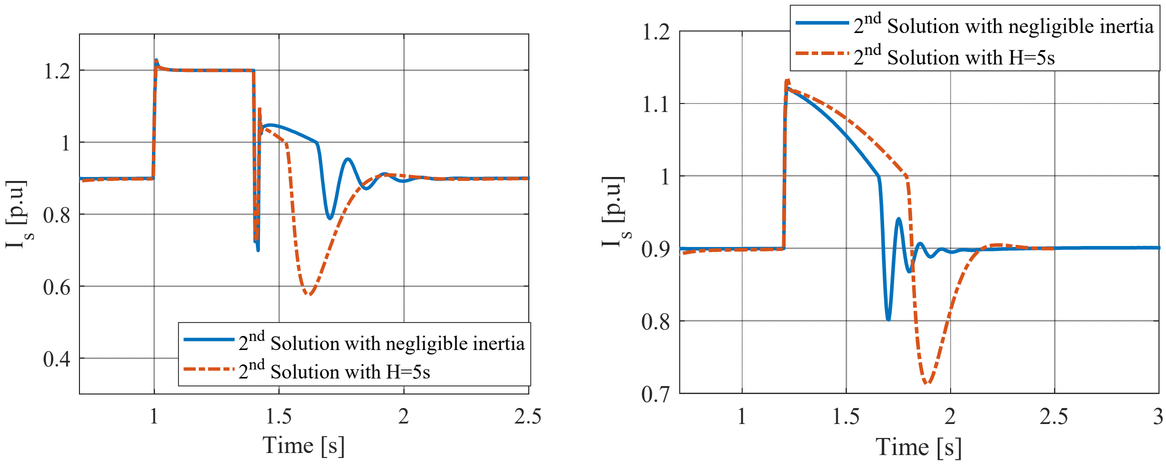

(a) Three phase fault (b) 30° phase shift

Figure V-27 - Impact of the 2nd solution on the high inertia system subjected to a three phase bolted fault

The post-fault synchronization issue of power converters based on “Strategy C” has been addressed and solved in this section. In the following section, an application of the proposed control on “Strategy A” and “Strategy B” is illustrated.

V.5.1 Application of the adaptive gain on “Strategy A” and “Strategy B”

The post-fault synchronization remains an issue for “Strategies A and B”. Indeed, during a three phase bolted fault, the PLL is disturbed since the grid voltage drops to zero, this may lead to a PLL angle deviation.

To deal with this issue, the solution proposed in this section can also be applied for “Strategy A and B” with an additional multiplication of $\Delta\tilde{\omega}_g$ and $\Delta\tilde{\delta}_g$ by $\sqrt{\left(1-\delta e_{g_d}\right)^2+\delta e_{g_q}^2}$ (see Figure V-28).

The effectiveness of the adaptive gain is illustrated through time-domain simulation in Figure V-29, where a 400ms three-phase fault and phase shift of 30° are performed, respectively.

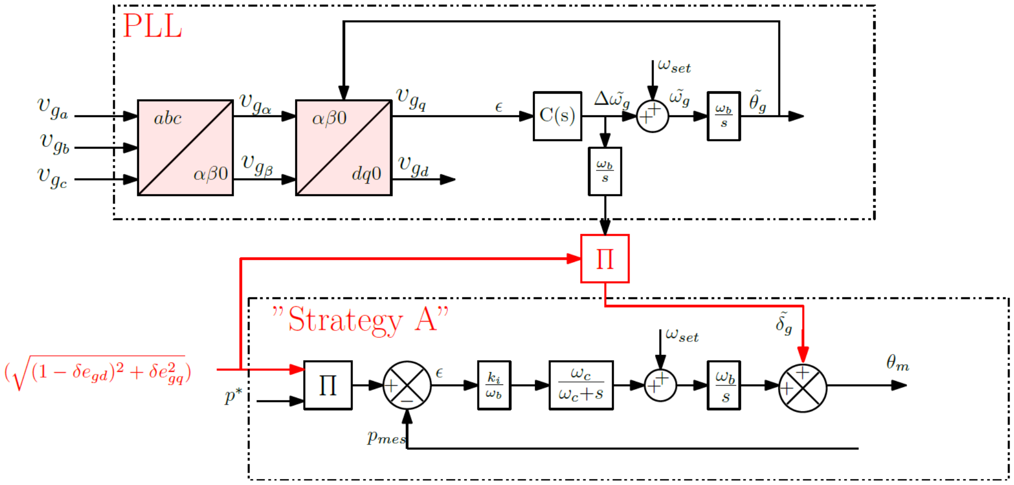

(a) Strategy A

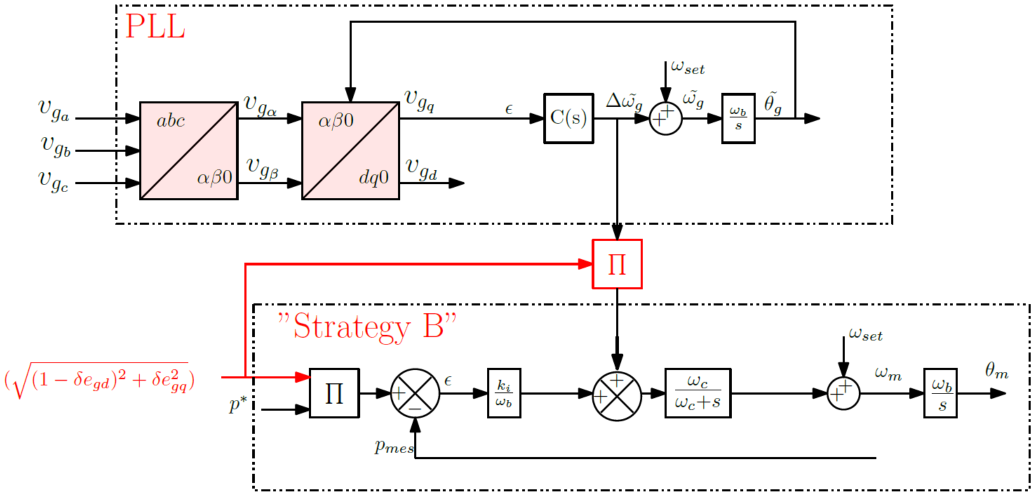

(a) Strategy B

Figure V-28 - Implementation of the post-fault algorithm for "Strategy A" and "Strategy B"

One can remark that the system stably recovers its equilibrium point after disturbances. However, the post-fault dynamics are not the same since the control structure and the tuning of the controllers are not the same.

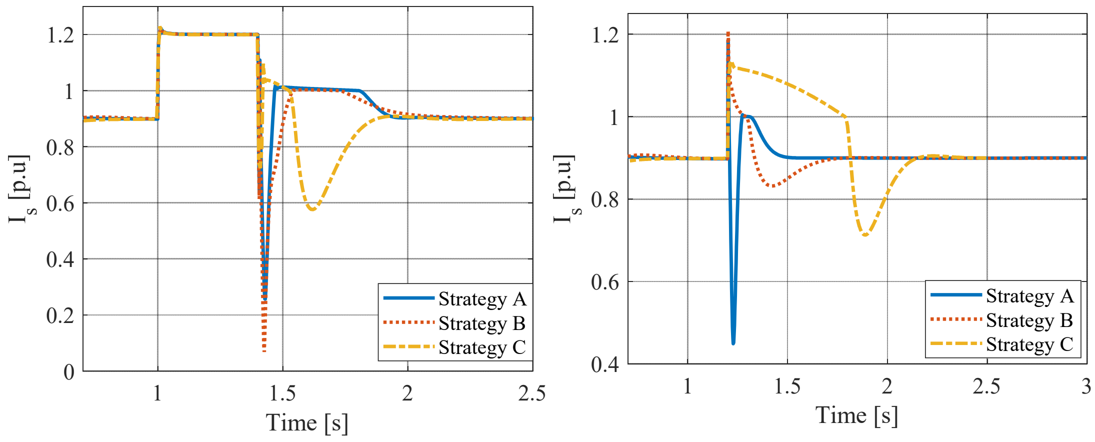

Figure V-29 - Dynamic comparison between outer control strategies based on 2nd solution in case of a three-phase fault and phase-shift

V.6 Test cases

V.6.1 Grid case 1: Single converter subjected to a three-phase fault followed by a line tripping

In this section, the response of a single power converter to a three-phase short circuit fault followed by a line tripping is investigated using the case study depicted in Figure V-30.

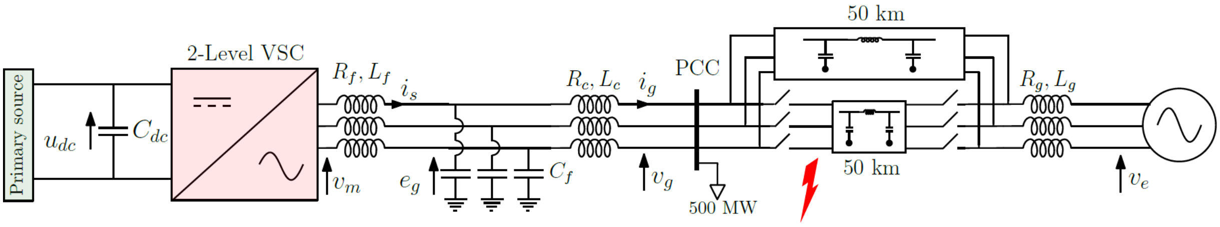

(a) 2-Level VSC

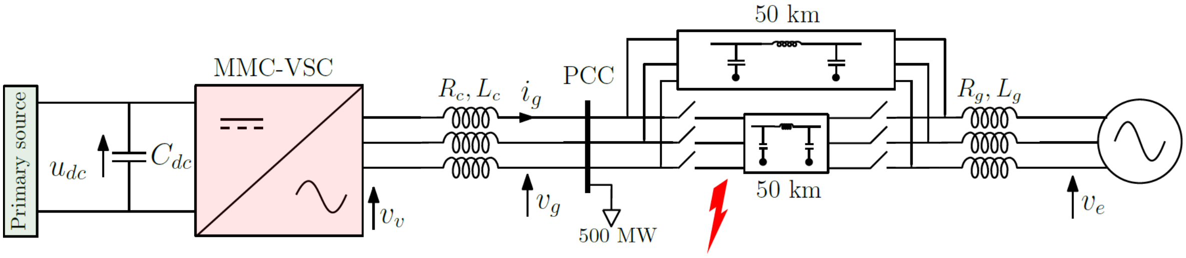

(b) VSC-MMC

Figure V-30 - Single bus case study used to check the stability and the ability to withstand large transients after a short circuit fault followed by a line tripping. Fault occurred t = 1.5 s. After 400 ms both 25 km lines are disconnected.

Both 2-Level VSC and VSC-MMC topologies are studied, where the converters are connected to a resistive $P_{load} = 500$ MW and to the AC system through parallel distributed PI lines.

A switching model is used for the power converters. For 2-level converters, the switching frequency is equal to 5 kHz. For MMC, the switches are controlled through a low-level control, so-called “Sorting algorithm”. More details on MMC low-level control are found in [153], [154].

A three-phase short circuit fault occurs at the departure of the 50 km line and cleared by tripping this line at 400 ms. The purpose of this case study is used to check the system behavior based on different algorithms for current limitation and synchronization.

For each of the simulation results, the three outer control strategies are compared. The parameters of the distributed line are $R_{line} = \frac{X_{line}}{10}$=0.03 Ω/km and C_{line} =9.74e-9 F/km.

Figure V-31 shows the AC variables of the 2-Level converter and its internal frequency based on cascaded control and direct AC voltage control structures, while Figure V-32 shows the same signals for MMC-VSC topology.

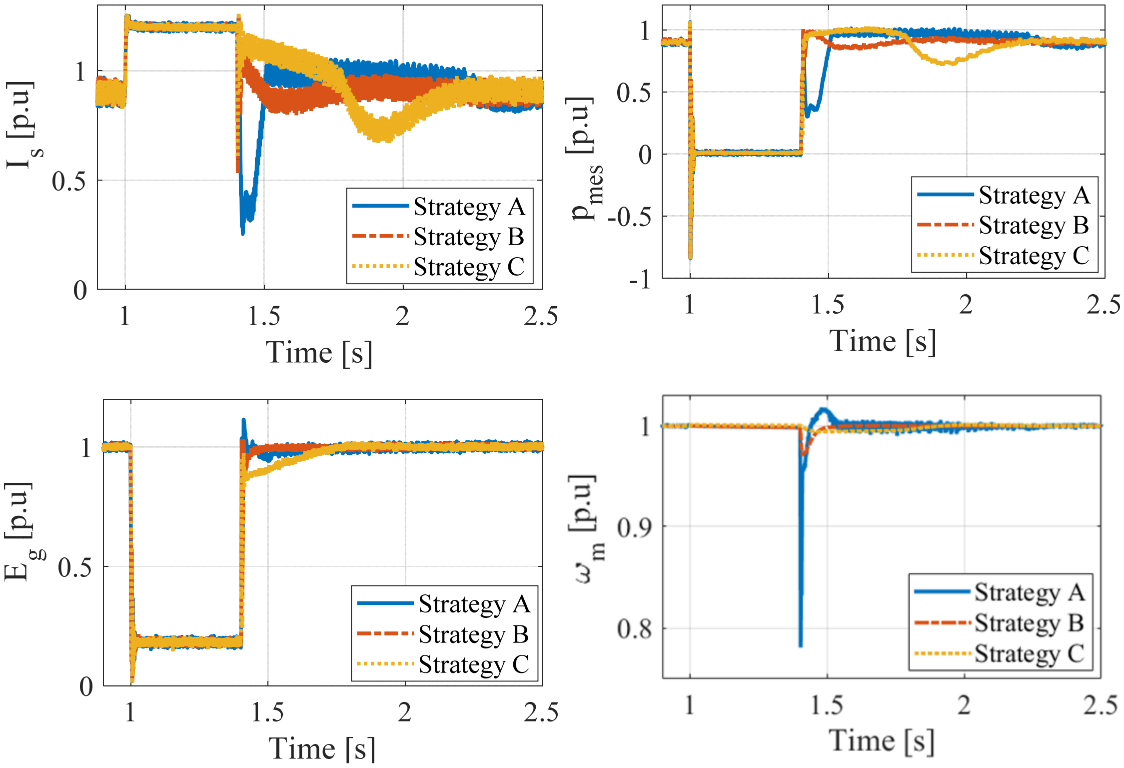

(a) Cascaded control structure

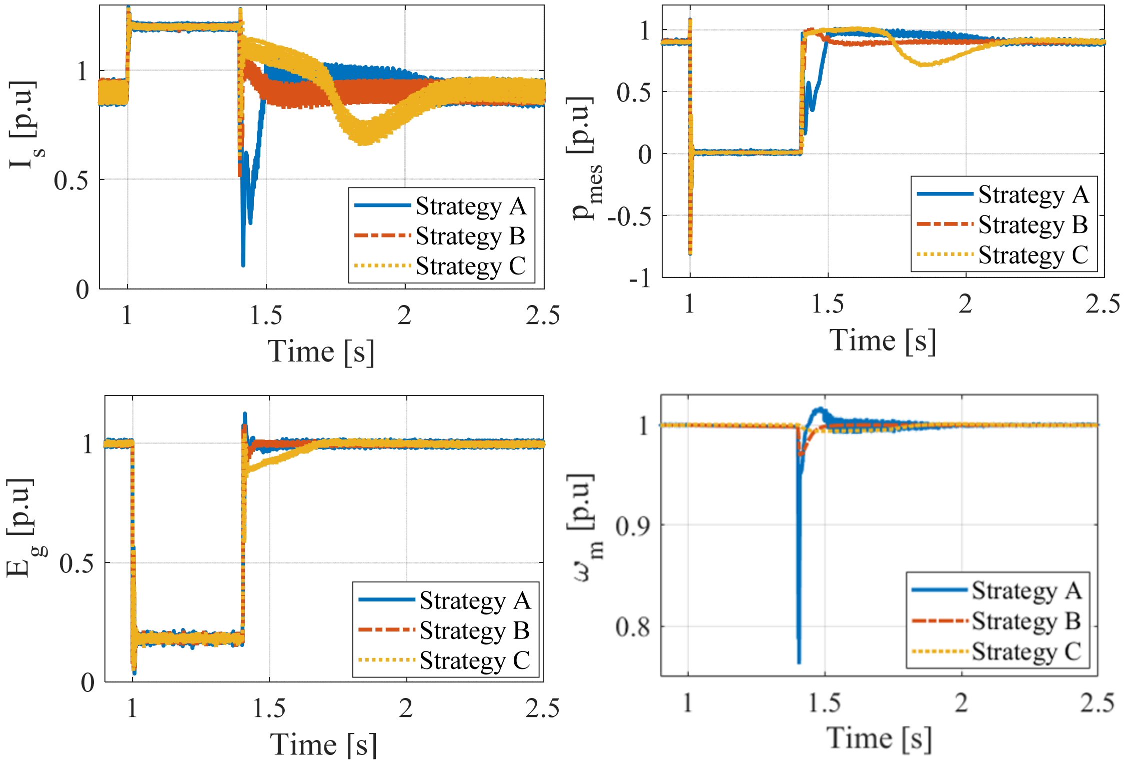

(b) Direct AC voltage control

Figure V-31 - AC signals and converter frequency of a single 2-Level converter during a three phase short-circuit and subsequent line opening.

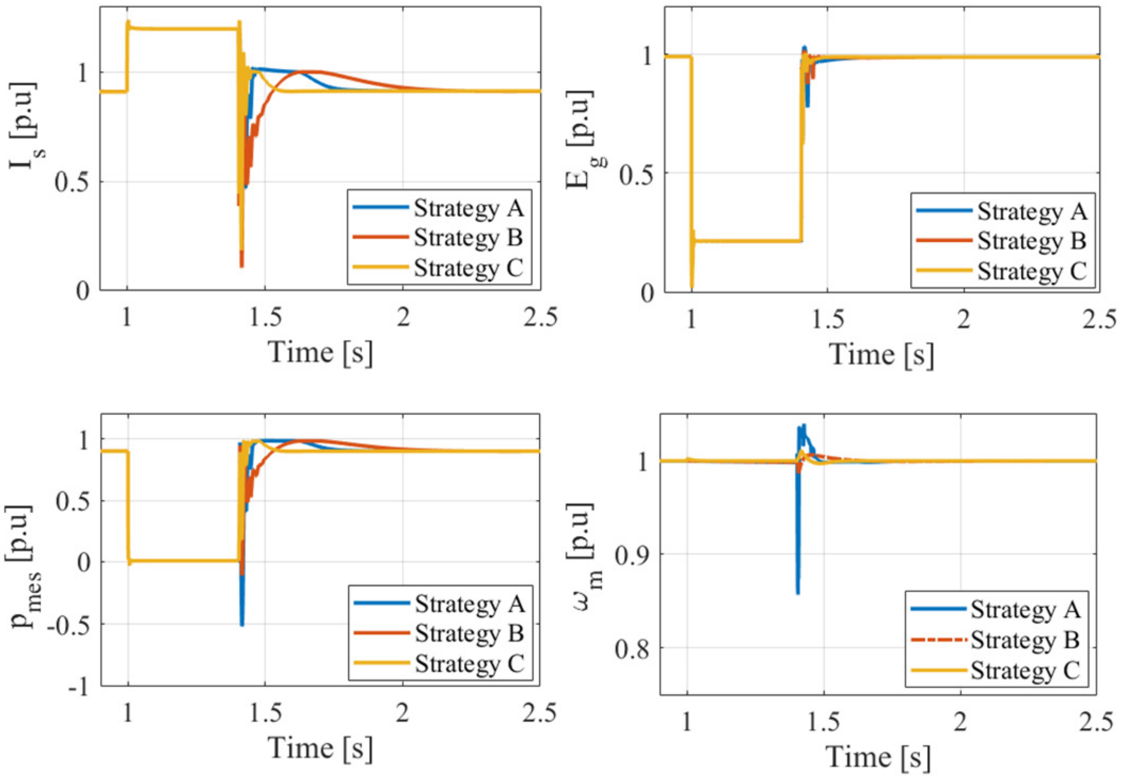

Figure V-32 - AC signals and converter frequency of a single MMC during a three phase short-circuit and subsequent line opening.

V.6.2 Grid case 2: Interoperability of power converters based on different control structures and their response to grid events

In previous subsections, the expected behavior and performances of the controllers have been validated using single-converter test case. However, in the future power system, AC voltage-controlled converters of different ratings will be interconnected via transmission grids with diverse topologies. To study the behavior and performance of the controllers in such a scenario, the simple but representative meshed grid of 320 kV overhead lines, a resistive load P_{load}=1000 MW and three nodes shown in Figure V-33 are used.

The rated power of each converter is indicated under their respective icons in Figure V-33. All the converters are based on the 2-Level topology.

VSCs 1, 2 and 3 are controlled through ‘Strategy A, C and B’, respectively. VSCs 1 and 3 are based on the cascaded control structure, whereas converter 2 is based on the direct AC voltage control.

At t =1.5 s, a three phase bolted fault is applied in the middle of the parallel 100 km lines between the first and the second converter. Then, a line is opened after 400 ms in order to clear the fault (Figure V-34).

Firstly, it should be noticed that the power system formed by the three converters operates in a stable manner for both inner control strategies. Moreover, it is stably recovered after a fault clearing, where the converters converge to the same frequency in less than 100 ms after event. Once again, contrary to “Strategy B and C” where the generated frequency is filtered to emulate the inertial effect, the maximum frequency deviation and RoCoF of the converter based on ‘Strategy A’ is high. Secondly, the different ratings and electrical distance of converters from the events lead to different individual responses. The AC voltage drops for VSC 2 and VSC 3 are more important since they are closer to the fault location. Thus, the current increase for these converters is more significant. During the fault, all the converters keep their output current magnitude around 1.2 p.u as expected.

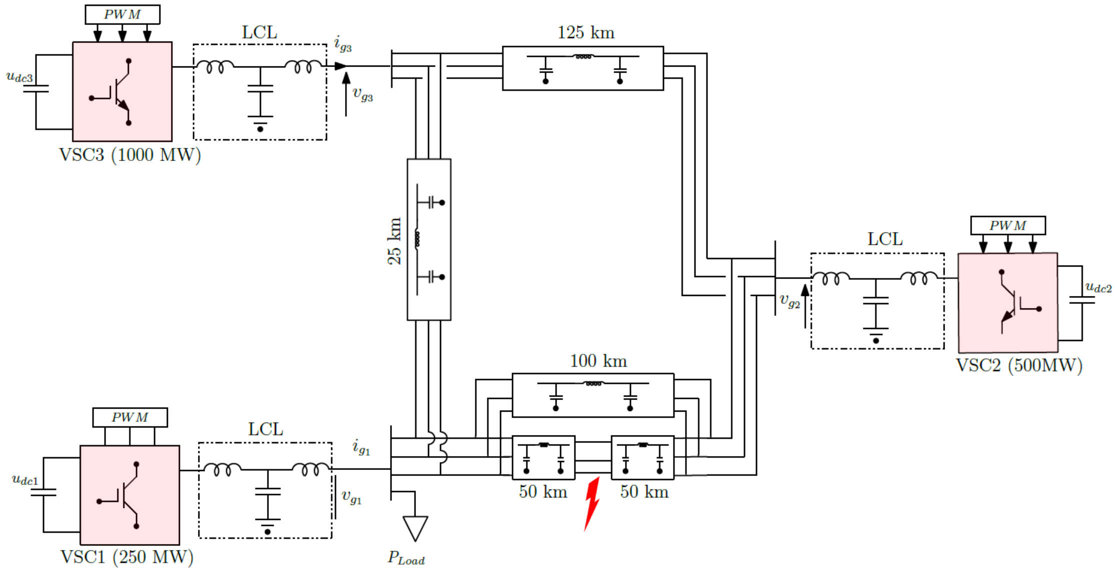

Figure V-33 - Three bus test case to study the compatibility of different controls and robustness of the system following grid events such as short-circuit, disconnecting a line, loss of unit and brutal connection of converters

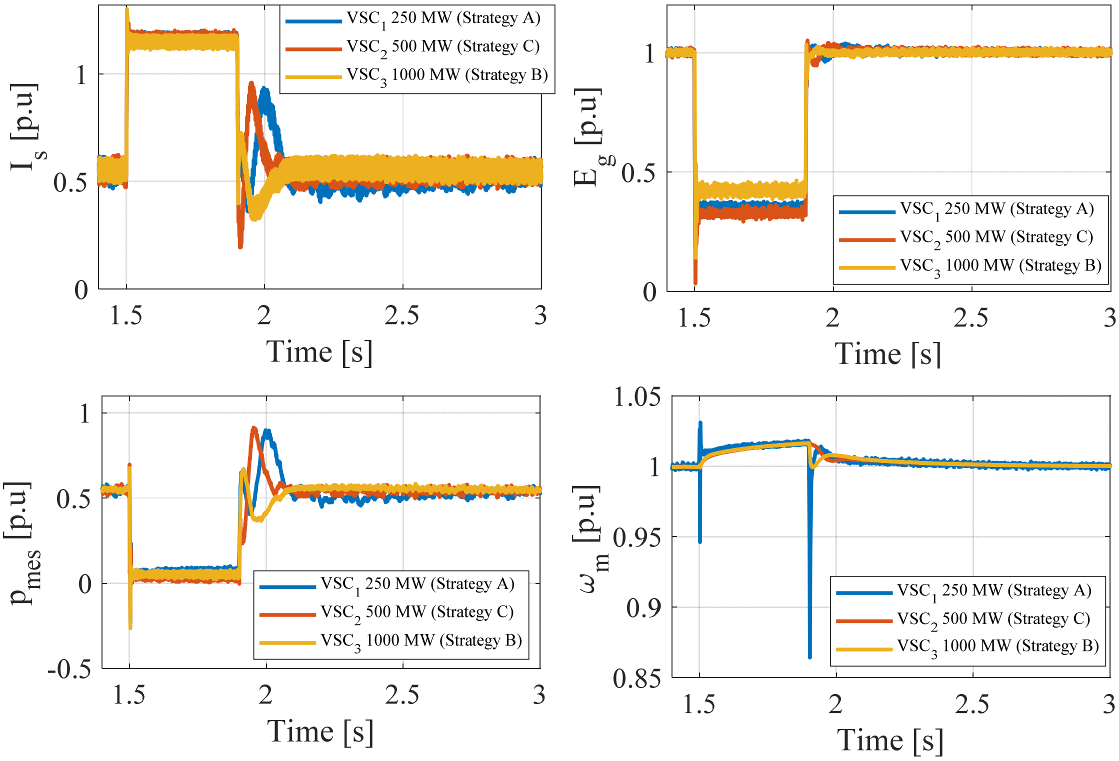

Figure V-34 - AC signals and converter frequency of a multi-converter grid topology during a three phase short-circuit and subsequent line opening.

V.7 Conclusion

In this chapter, the current limitation and post-fault synchronization of grid-forming converters are discussed when the system is subjected to large disturbances. In this context, a hybrid current limitation control (HCLC) is developed based on a combination of virtual impedance and current saturation algorithms. Depending on the inner control structure and the topology of the converter, the HCLC can be directly used if a cascaded control structure is adopted, while an additional threshold current loop has to be added in order to generate current references if a direct AC voltage control structure is used.

After fault clearing, the synchronization of the power converter has to be ensured in order to avoid converters tripping. Hence, by neglecting the inertia effect, a simple critical clearing time analytical formula is derived based on VI or HCLC and CSA. It shows the effectiveness of the VI and HCLC in ensuring a higher transient stability than CSA and also brings out the main influent parameters on the transient stability.

A method to improve the critical clearing time and the dynamic behavior has been proposed. Comparisons with simulation show that the proposed simplified model is relevant for the estimation of the critical clearing time and understanding the general behavior during the resynchronization period. Even if the inertial effect has been neglected in this analysis, the general trends will remain effective with inertial effect as proved through time-domain simulations.

To show the system operation in different situations, two grid cases with single and multi-converter topologies have been proposed to assess the stability of the overall system including the proposed algorithms. The obtained results based on the proposed grid cases are satisfactory.

VI. Experimental Validation of the Grid-Forming Converters

VI.1 Introduction

To show the effectiveness of the work developed in this thesis, an experimental validation of the different control algorithms is presented in this chapter. The aim is to:

- Present the demonstrator on a reduced scale which will serve as a validation support for the different works.
- Explain clearly the different steps for control implementation.
- Explain the principle of the Power Hardware In the Loop (PHIL), which will mainly serve to emulate the AC grid and allow checking the interoperability of different control strategies.

In this chapter, three main types of experimentations are presented, where the small-scale power converter is connected to:

- An ideal voltage source (Grid-connected) or a resistive load (standalone mode).
- A three bus system with different rated power and different control strategies.
- The Irish power system based on mixed power sources (simplified SG model and grid-forming converters).

VI.2 Mock-up description

A description of the overall system is depicted in Figure VI-1 and Figure VI-2. This mock-up is composed of the following components:

- An open 2-level VSC (designed by **Cinergia**) with its internal LCL filter
- A dSPACE 1005 Board.
- A Linear resistive load (4 kW).
- A Real-Time Simulator (RTS) manufactured by Opal-RT and used to emulate a power system.
- A linear power amplifier manufactured by **Spherea** to interconnect the RTS with the VSCs.
- A SCADA system called **PcVue,** manufactured by **Arc Informatique** to monitor the VSC and the main components simulated in the RTS.
- A homemade fault generator controlled by a **Crouzet Millennium PLC**.

VI.2.1 General description

The small-scale experimental bench is illustrated in Figure VI-1.

The 2-level VSC contains an internal LCL filter, measurement board and physical protections against overheating, overvoltage and overcurrent. The converter is controlled by a dSPACE 1005 board (2) and supplied by an ideal DC voltage source (4). It is connected to a high bandwidth AC amplifier (5) through an isolation power transformer (3), which is monitored through the RT-Simulator and SCADA system. The RTS is simulating various types of AC grid.

The nominal ratings of the 2-level VSC are listed below:

- Rated power: 7.5kVA,
- Nominal DC voltage: 800V
- Nominal AC voltage: 400V ph-ph.

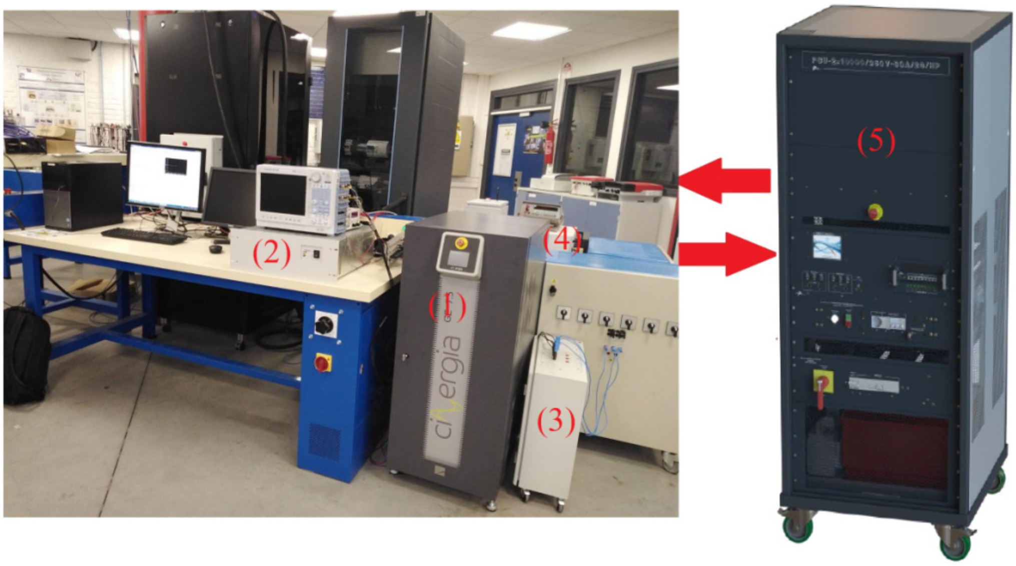

Figure VI-1 - Small-scale experimental bench

The LCL filter has been designed following the per-unit values chosen in chapter IV [20]:

$$L_{f_{pu}} = 0.15 \text{ p.u}, \quad C_{f_{pu}} = 0.066 \text{ p.u}, \quad L_{c_{pu}} = 0.15 \text{ p.u}$$

Using the base values of the small-scale converter: Sb = 7.5k VA, U_b = 400 V, the base impedance value is determined: $Z_b = 21.3\Omega$.

For the LCL mock-up parameters, it results in:

$$L_f = 10.91mH, \; C_f = 9.19\mu F, \; L_c = 10.91mH$$

Regarding the control hardware, it has been implemented using the ds1005 rapid control prototyping environment. The internal structure is illustrated in Figure VI-3. This environment is a modular system built around a central computing unit based on a 1GHz PowerPC processor.

An adaptation board has been developed from the specifications of L2EP (Figure VI-4.a). It is used to connect the control board (Figure VI-4.b) to the CINERGIA converter (e.g., sending/receiving measurement and control signals).

The controller algorithm is generated from MATLAB/Simulink and several I/Os boards are used to make the measurements and control the VSCs:

- A DS4003 to control the different contactors
- A DS4004 to control the power electronic switches
- A DS2003 to measure some physical values (AC grid voltages)

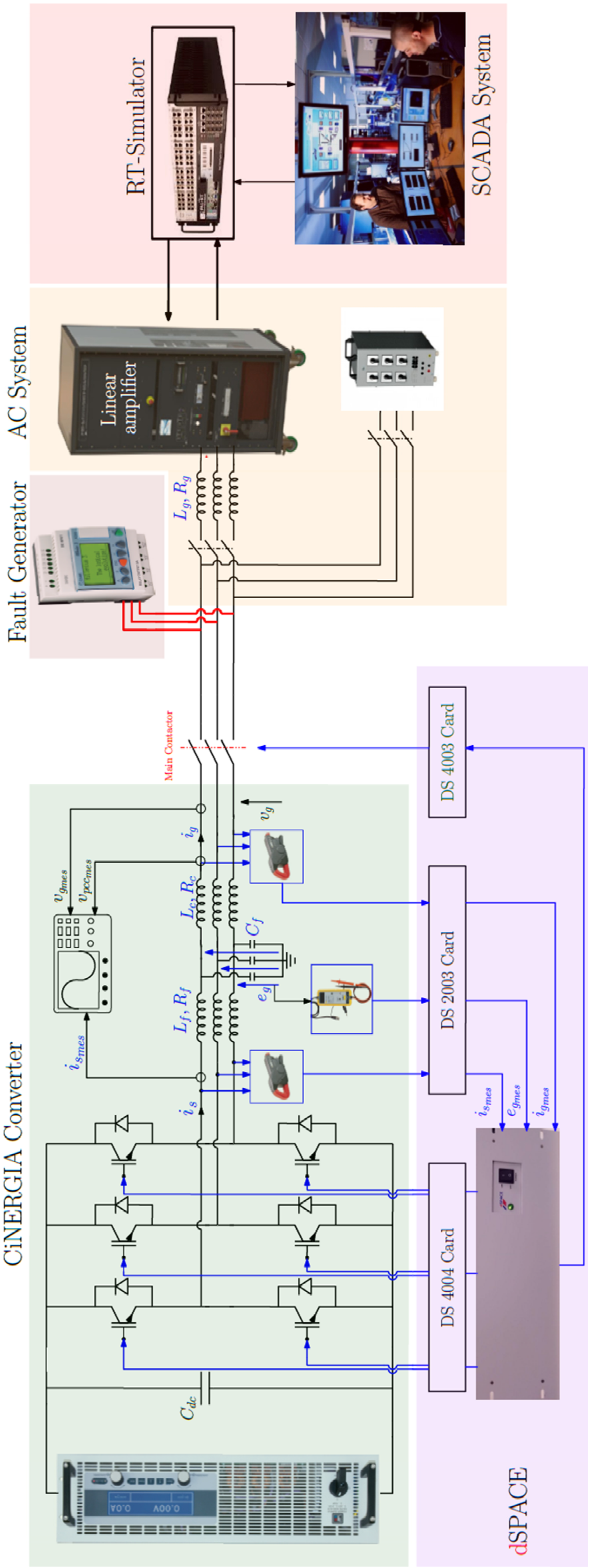

Figure VI-2 - Functional scheme of small-scale VSC connected to AC system [155]

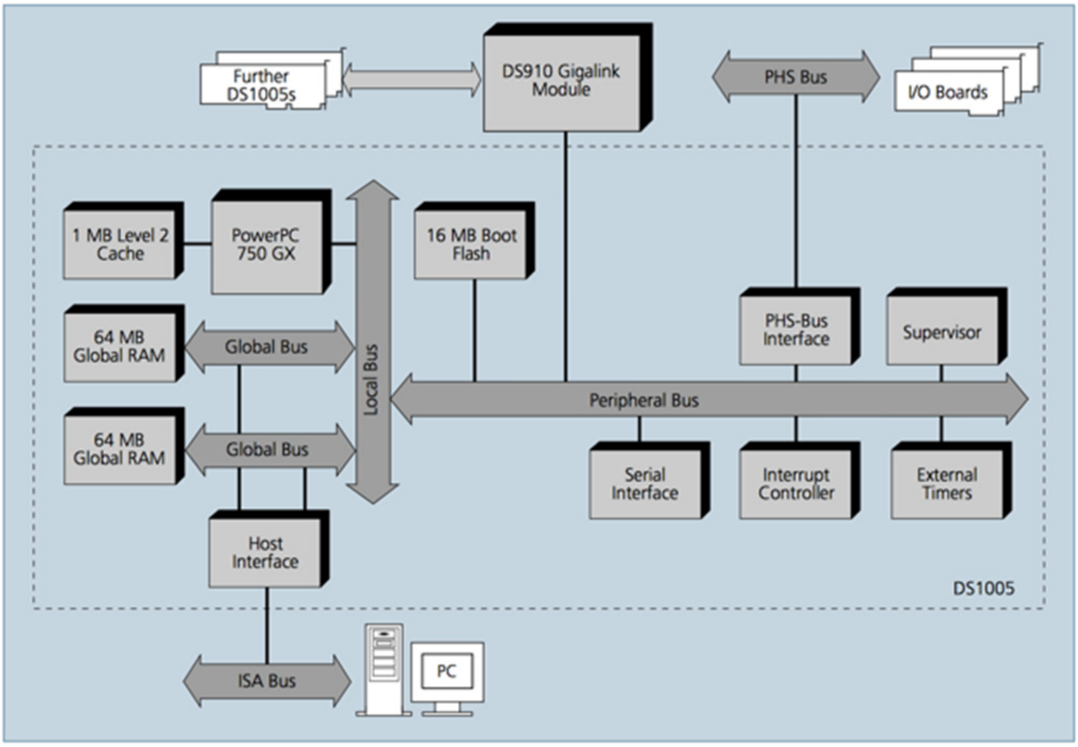

Figure VI-3 - dS1005 internal architecture

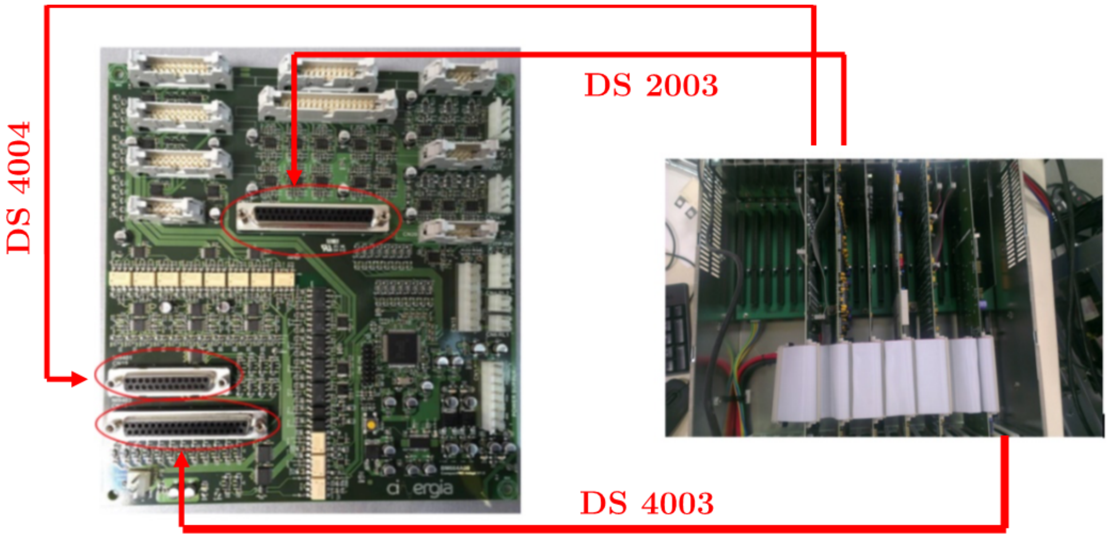

(a) (b)

Figure VI-4 - Connection between (a) CiNERGIA adaptation board and (b) dSPACE boards

VI.2.2 Fault generator

The fault generator is described by the electrical scheme in Figure VI-5.
This fault generator mainly consists of a couple set of three-phase 10 **Ω** power resistors, which may be coupled in parallel in order to decrease the total resistance, and thereby, increase the current during the fault. Opening and closing of the switches and the main circuit breaker are controlled through a ***Crouzet millennium 3 PLC***.

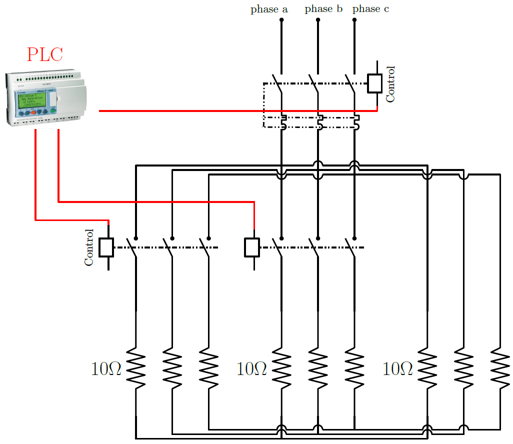

Figure VI-5 - Fault generator

VI.2.3 Real-Time Simulator and PHIL application

An RT-LAB simulator is used to simulate the dynamic behavior of several power systems. 3 models are implemented:

- An ideal voltage source for a standalone test,
- A three-node test case as presented in chapter V.
- The Irish power system.

All the models are designed in Matlab/Simulink R2017a and then compiled for a Real Time Simulation. The PHIL principle is used to interconnect the physical parts with the real-time simulated part, as illustrated in Figure VI-6 for the Irish power system test. The inputs/outputs available in the RTS are used to interconnect the linear amplifier and the RTS.

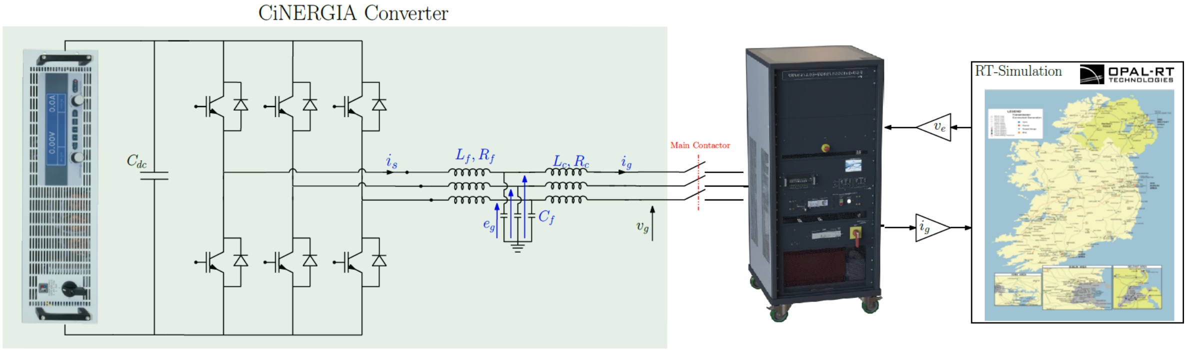

Figure VI-6 - PHIL application – Irish power system example

The main characteristics of the 2 simulated power systems are summed up in Table VI-1. Some computations are parallelized in the internal CPU cores of the RTS. The total used CPU cores are equal to the subsystem number.

Table VI-1 Real Time simulation characteristics

	Three nodes test case	Irish power system
Computation Time Step	20 μs	45 μs
Number of subsystems (i.e number of used CPU cores)	3	5

N.B: all the models have been designed to balance computation between each CPU cores in the RTS. This is a complex manual process. In addition, these models are initialized by a Load Flow algorithm to guarantee a smooth starting point.

VI.2.3.1 Three-node test case description

This test corresponds to the real-time implementation of the test case proposed in chapter V. A description of the overall system is presented in Figure VI-7. The model is constituted of:

- 3 Subsystems called ***SM_Migrate***, ***SS_M*** and ***SS_control*** which are executed in Real Time.
- 1 Subsystem called ***SC_user_interface*** which is used as a user interface and as a gateway for the SCADA system.
- 2 Subline systems used to parallelize computations.

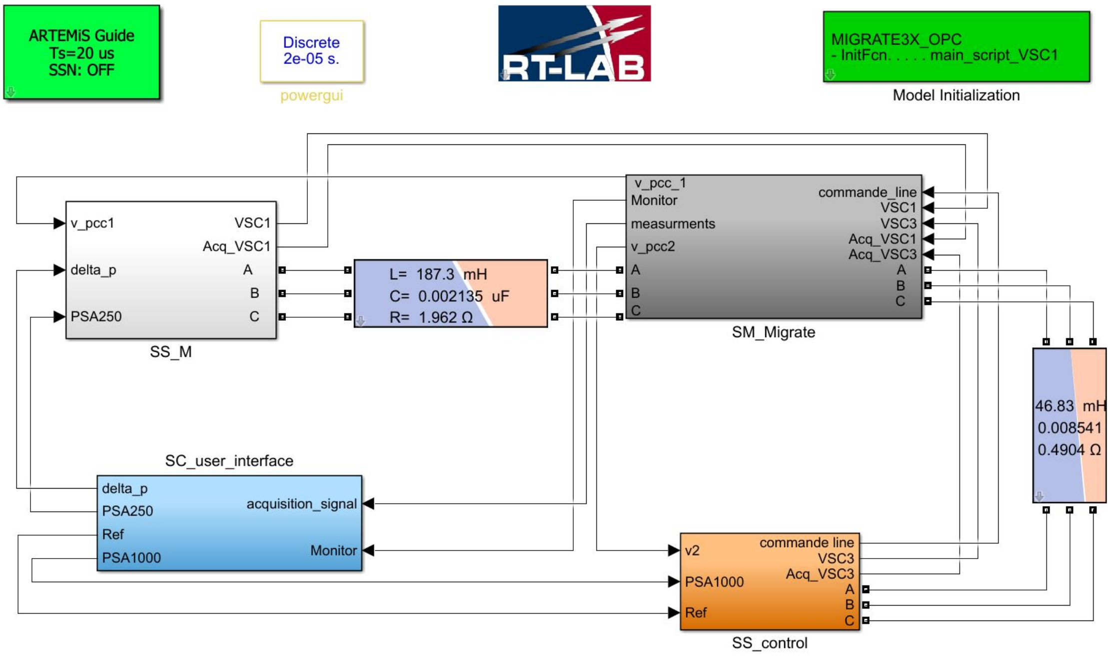

Figure VI-7 - Structure of the RT Lab model

The Subsystem ***SM_MIGRATE*** corresponds to the grid part and includes the following components:

- Loads
- Lines with distributed parameters
- Short-circuit fault generator
- Interface with Real VSC
- Data acquisition

The other subsystems:

- ***SS_M*** and ***SS_C*** contain the average VSCs models and the developed grid-forming controls.
- ***SC_user_interface*** contains the signal references set by the user.

All subsystems are depicted in Appendix I.

VI.2.3.2 Irish power system

The Irish transmission system as of year 2016 is given in Figure VI-8.

The different components used in the Irish power system model are listed in Table VI-2. This model has been designed from *EirGrid Data*. The characteristics of the Buses, lines, loads and generators have been stored in several Excel files. A Matlab script has been created to read these data and generate automatically the correct Simulink model. In addition, regarding the generators, an equivalent voltage source with inertia has been implemented. This model is presented in Figure VI-9. The inertia constant H_{eq} has been set to 5 s for all the generators and the droop gain R_{SG} to 4%.

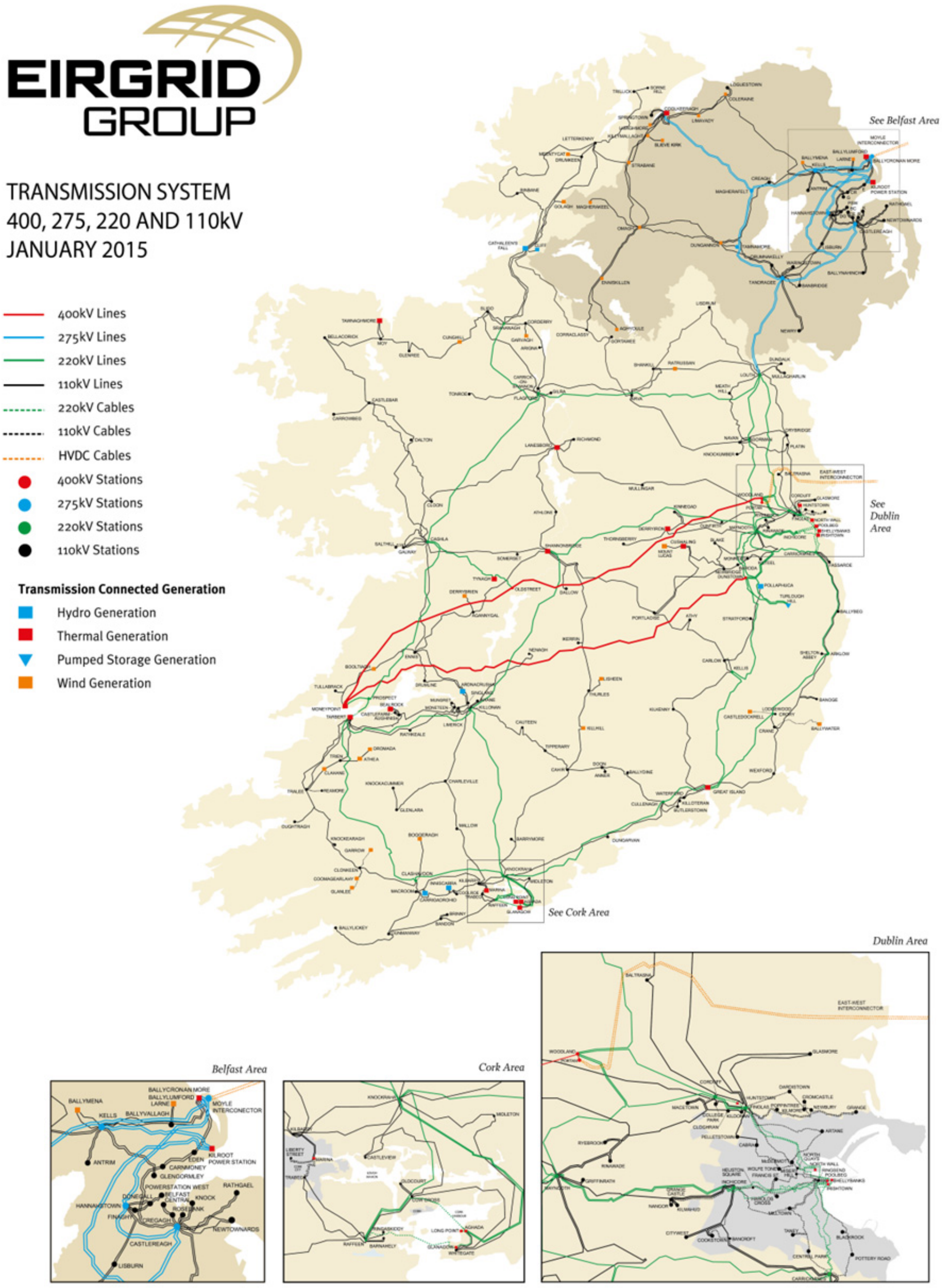

Figure VI-8 - Irish Transmission system –Year 2016 [156]

Table VI-2 Synthesis of elements of Irish grid RT-LAB model

Elements	Number
Generator	*14*
Bus	*88*
Line	*90*
Load	*47*
Shunt	*7*
Transformer	*26*
Three-phase VI Measurement	*88*
RMS Measurement	*5*
Power (P,Q) measurement	*90*
PLL Frequency Measurement (Real VSC)	*1*
Real VSC interface power amplifier	*1*
Three-Phase Breaker	*1*
Supplementary Load (reduction numerical faults)	*1*
IOs interface	*1*
Total elements	*460*

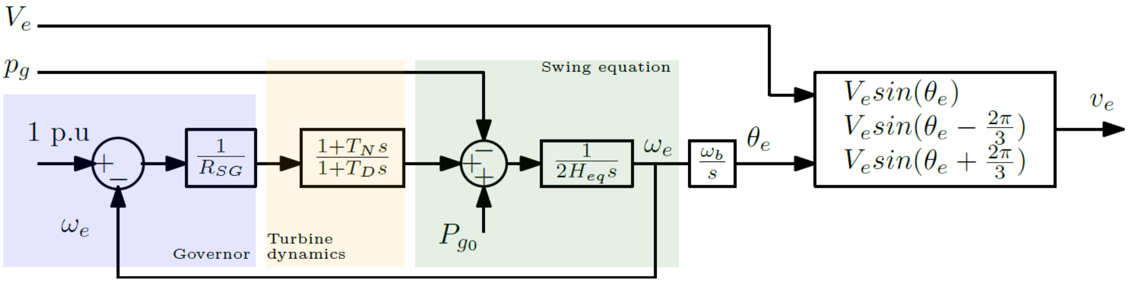

Figure VI-9 - Model of generators: voltage source with inertia

Considering that the obtained model is very large and hard to display, the overall structure has been depicted in Figure VI-10. It has been divided into 6 subsystems. As for the previous model, the subsystem SC_user_interface is used as a user interface and as a gateway for the SCADA system.

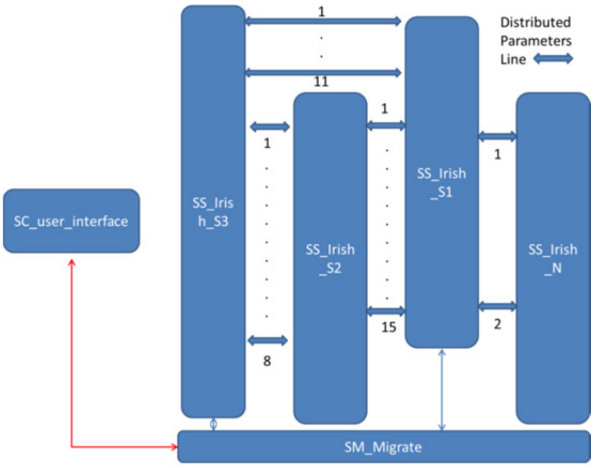

Figure VI-10 - Structure of simulation for Irish grid with 6 processors

VI.2.4 SCADA System

In order to be able to remotely control and visualize internal data from the RT simulation, a SCADA system has been used. It acts as a small Control Center, which is able to measure any data from the simulated power systems.

As presented in Figure VI-11, data and control orders are sent through an OPC communication link. A mapping between the SCADA and RTS variables allows information to be linked. As an OPC link is not a real-time communication link, the frame rate has been fixed to 100 ms, which allows the measurement of the steady-state variables such as power exchanges or the voltage levels.

The remaining ones correspond to the power parts and are simulated in real time. The connections between them used some distributed parameter lines in order to parallelize the computations. The number of connections has been included in Figure VI-10.

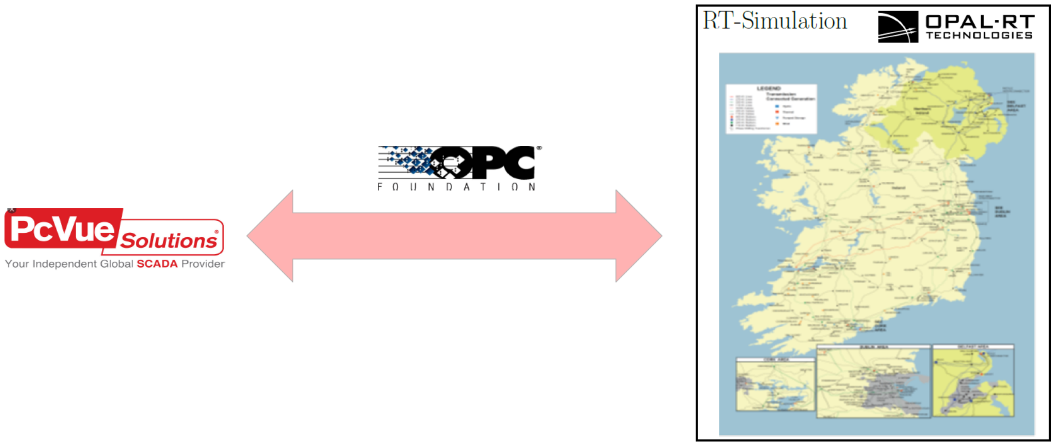

Figure VI-11 - SCADA and RTS interconnection

Then, this information can be included within different Human-Machine Interfaces illustrated in the following part. As an illustration, the HMI for the three-node case is depicted in Figure VI-12. Power, frequency and voltage levels are monitored and events (line tripping, faults) can be generated through this HMI.

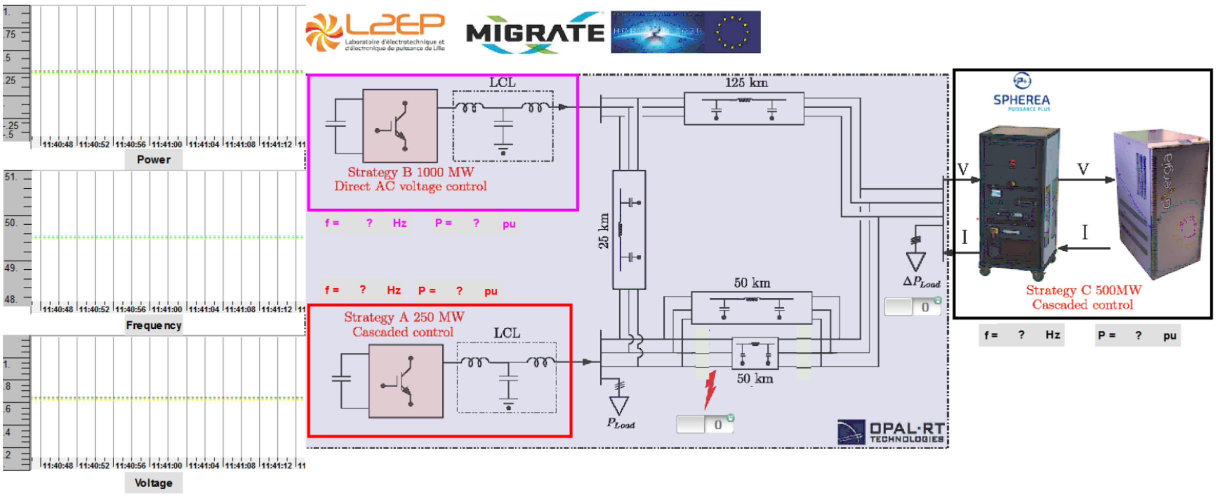

Figure VI-12 - Three node test case HMI illustrations

VI.3 Initial Synchronization of a grid-forming converter to the AC grid

A VSC control needs information about the grid angle when connecting the converter to the grid. Let's start with the outer control based on Strategy C. The synchronization process is depicted in Figure VI-13 and described with the following steps.

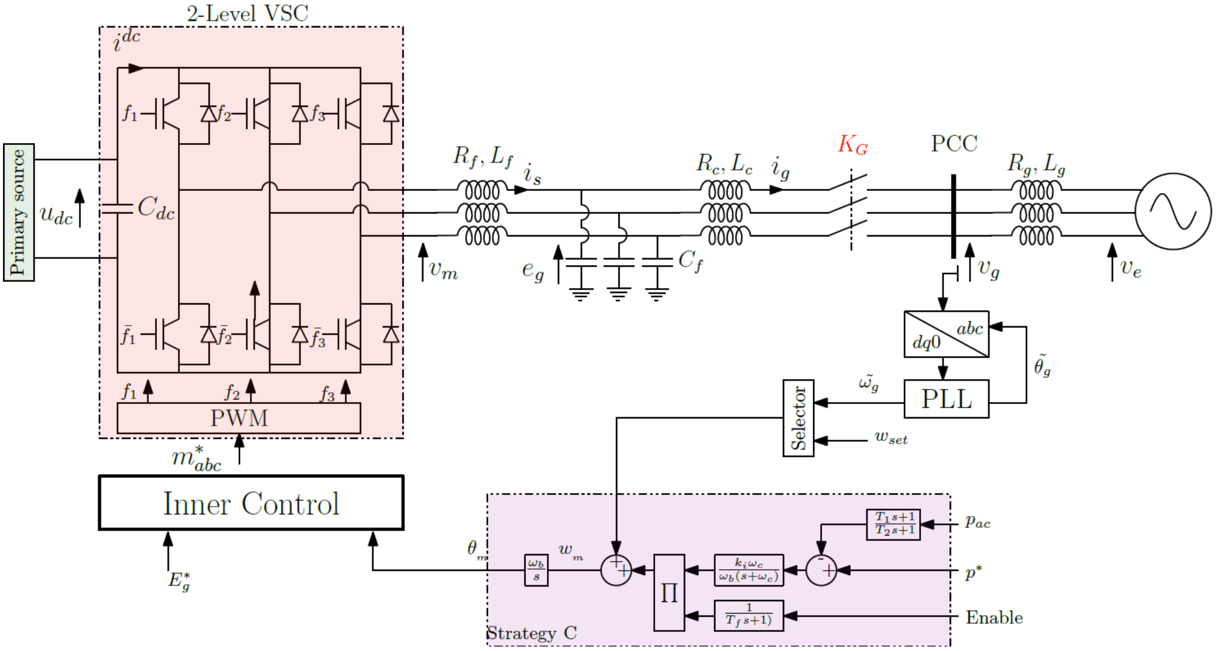

Figure VI-13 - Synchronization process of grid-forming converters

Synchronization is achieved if the following steps are respected:
K_G remains open and the outer control is disabled (Enable = 0).

Step 1:

- The PLL is activated.
- ω_{PLL} is selected for ω_m

Step 2:

- The switch K_g is closed.
- The outer control is enabled (Enable = 1).
- The PLL is disabled.
- Switch from ω_{PLL} to ω_{set} .

To smooth the introduction of power control loop, a filtered "Enable" signal is used (enable is a Boolean signal). The time constant of the low-pass filter is set to 100 ms.
Since "Strategies A and B" contain PLL, the synchronization can be easily done compared to "Strategy C":

- The switch K_G is closed.
- The outer control is enabled (Enable = 1).

Then, the power converter is synchronized to the grid.

VI.4 Experimental results

VI.4.1 Single VSC connected to AC system

The functional scheme for this experiment is presented in Figure VI-14.

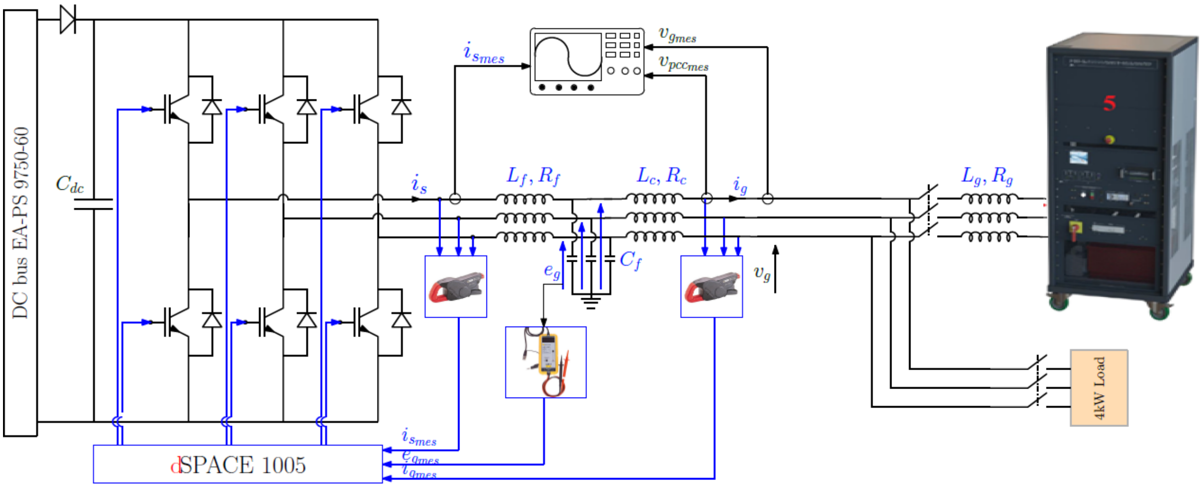

Figure VI-14 - Single converter connected to an emulated AC grid and a resistive load

Initially, the resistive load is disconnected. The power converter is generating a reduced AC voltage of 300V ph-ph. The linear amplifier is used to produce a 300 V balanced phase-phase AC voltage. The system and control parameters are listed in Table VI-3.

Table VI-3 System and control parameters

Symbol	Value	Symbol	Value
P_n	5 kW	k_i/ω_b	0.04 pu
$\mathrm{Cos}\phi$	0.9	k_{ic}	1.19 pu
f_n	50 Hz	$f_{s\omega}$	10 kHz
U_{ac}	300 V ph-ph	L_g	10.9 mH
U_{dc}	600 V	ω_c	2 rad/s
$L_f = L_c$	10.9 mH.	$I_{max_{SAT}}$	1.25 pu
C_f	9.19 uF.	I_n	1 pu
k_{pc}	0.73 p.u.	k_{pv}	0.52 pu
$\sigma_{X/R}$	5	k_{iv}	1.16 pu
$kp_{R_{VI}}$	0.6716 p.u.	T_1	0.121 ms
T_2	0.022 ms	$I_{max_{VI}}$	1.2 pu

For this configuration, four test cases have been realized. For all test cases, the three outer controls are tested:

Test in grid-connected mode:

- Power exchange with the AC grid based on all outer control strategies.
- 100% voltage sag.
- 40° Phase shift.

Test in islanded mode:

- Three-phase fault.

The electrical quantities displayed in the experiment are respectively:

- The grid voltage v_g in (abc).
- The grid current i_g in (abc).
- The VSC output current I_s.
- The active power p_{ac}.

VI.4.1.1 Active power management

At $t=t_0$, $p^*=$ 0.1 p.u, then, a 0.5 p.u power step is applied on p^*. Figure VI-15, Figure VI-16, and Figure VI-17 show the system dynamics for Strategies, respectively. The response time of each control is around the theoretical values calculated in the previous chapters ($T_R^{Strategy\ A} \approx T_R^{Strategy\ C} \approx =$ 250 ms and $T_R^{Strategy\ B} \approx$ 400 ms). A difference between the simulation and the experimentation can be simply explained by the fact that the X/R ratio in a small-scale converter is small, which impacts the dynamic performances of the system. Moreover, an additional transformer is used to isolate the converter in case of a failure. This transformer increases the total output impedance, which also results in the slight modification on the system dynamics.

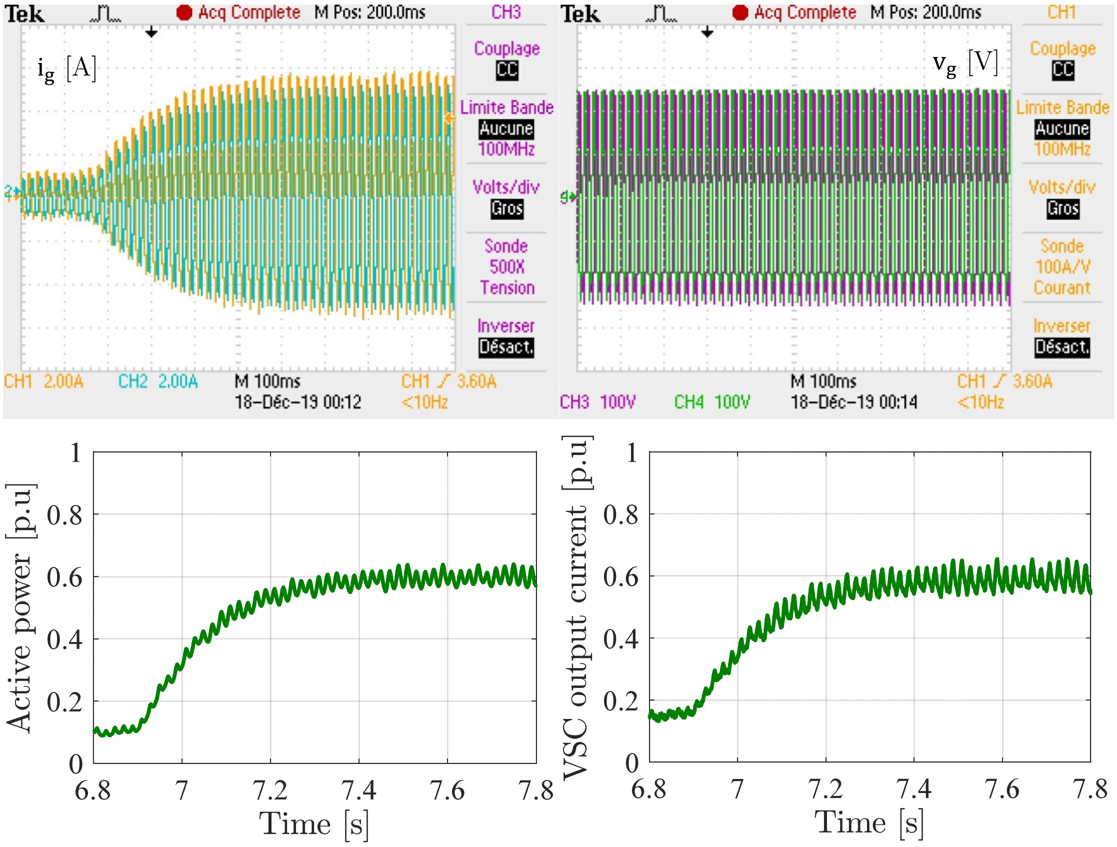

Figure VI-15 - Strategy A

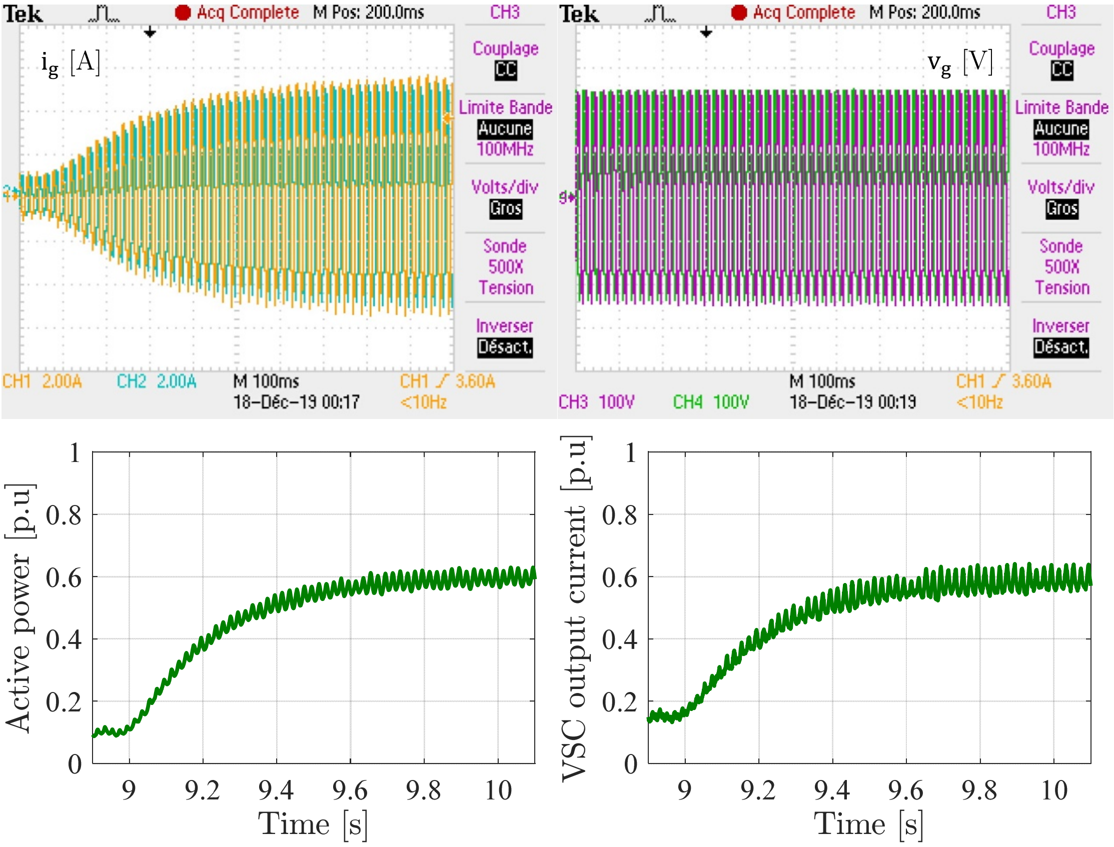

Figure VI-16 - Strategy B

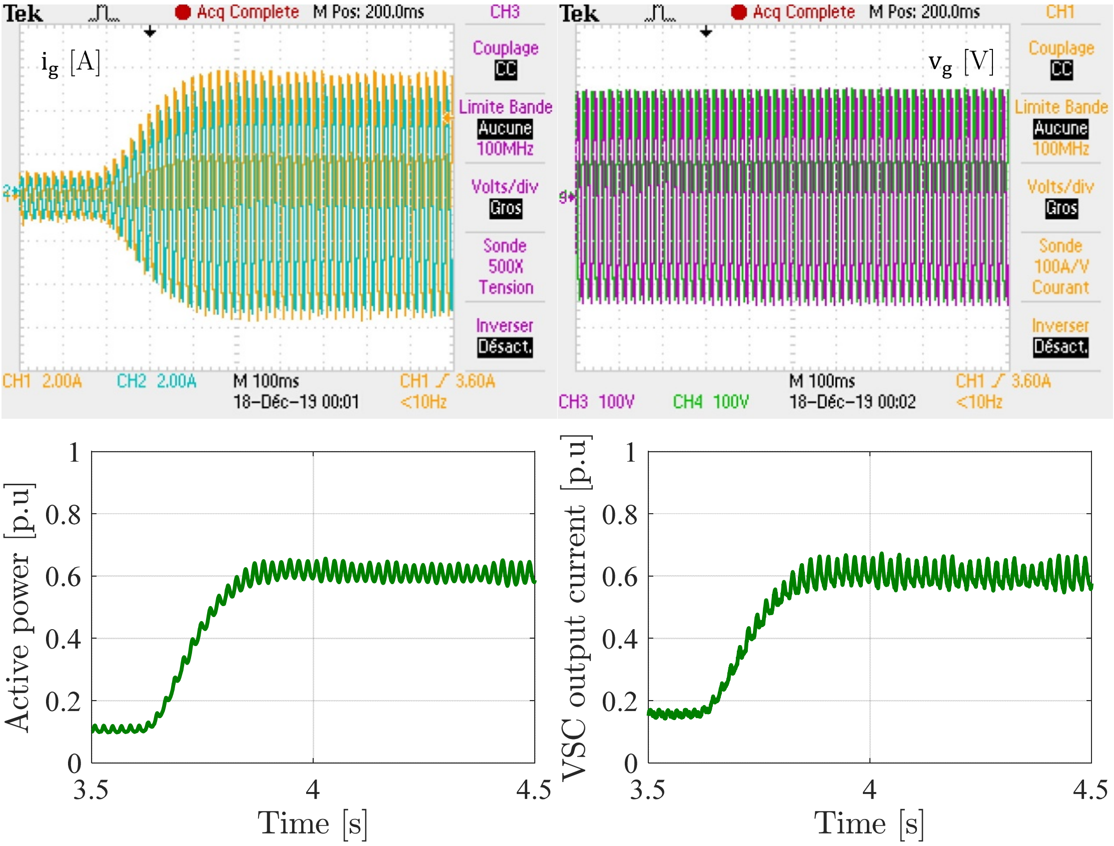

Figure VI-17 - Strategy C

VI.4.1.2 100% grid voltage sag

Initially, $p^* = 0.6$ p.u. Subsequently, a 400 ms voltage sag is applied as shown in Figure VI-18, Figure VI-19 and Figure VI-20. When the fault occurs, the AC voltage drop induces an increase in the VSC output current, which is limited to its maximum allowable current magnitude, 1.2 p.u. Once the fault is cleared, the system stably recovers its equilibrium point.

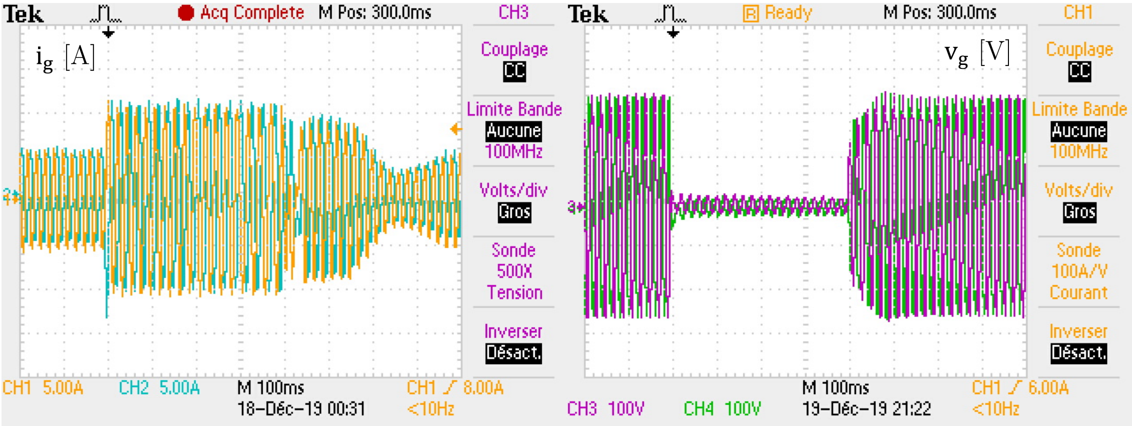

Figure VI-18 - Strategy A

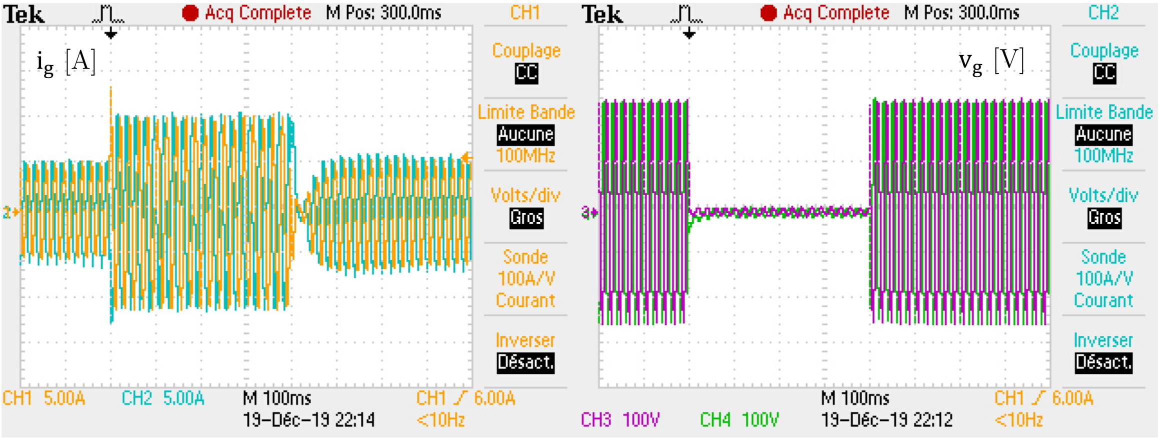

Figure VI-19 - Strategy B

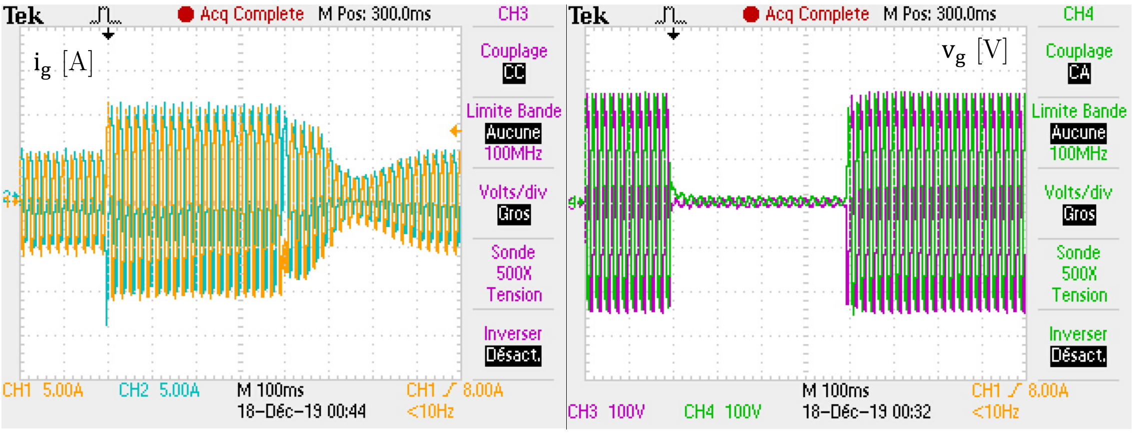

Figure VI-20 - Strategy C

VI.4.1.3 Phase shift

In this subsection, the power reference is first set to $p^* = 0.6$ p.u and a phase-shift of 40° is then applied, as illustrated in Figure VI-21, Figure VI-22 and Figure VI-23. The current rises to its maximum allowable value, then, the system recovers its equilibrium point depending on the dynamics of each controller. Since Strategy A uses the grid angle information. Its behavior under a phase shift is fundamentally different from Strategy B and C (i.e., it recovers it equilibrium point rapidly).

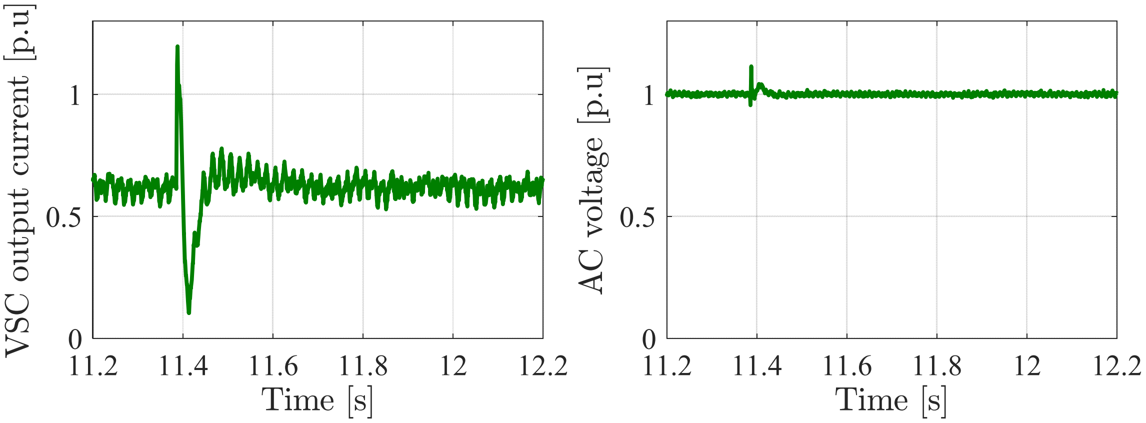

Figure VI-21 - Strategy A

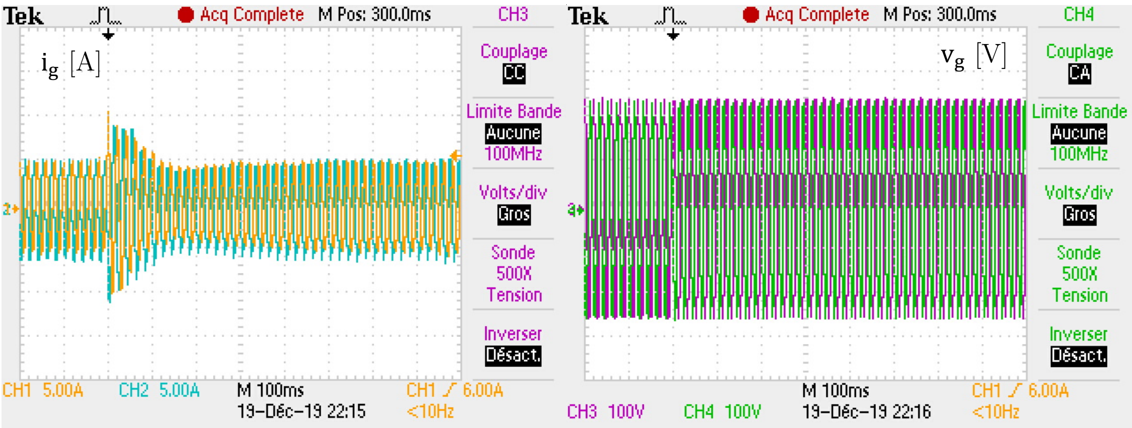

Figure VI-22 - Strategy B

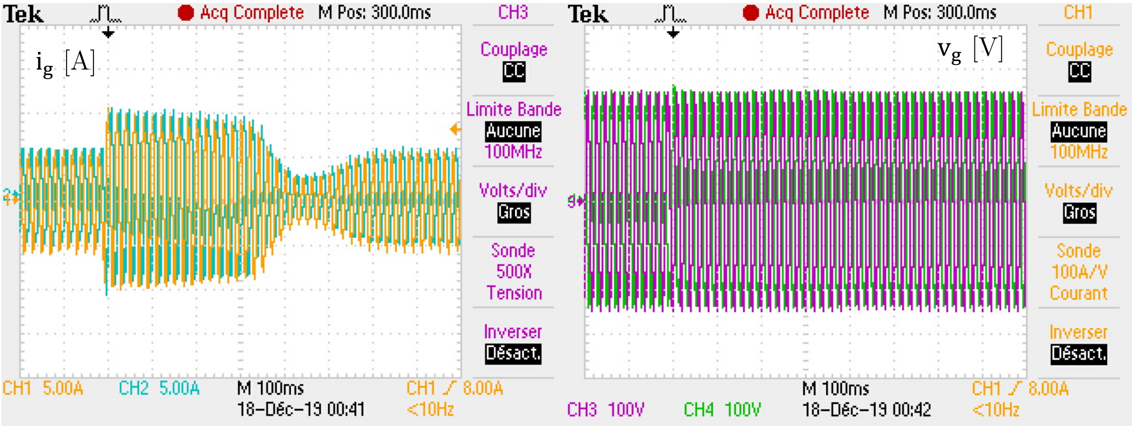

Figure VI-23 - Strategy C

VI.4.1.4 Three-phase fault in islanding condition

In this subsection, the system is operating in a standalone mode. A 0.4 p.u P_{load} is first connected to the system as illustrated in Figure VI-1, then, a 400 ms three-phase fault is applied using the fault generator as shown in Figure VI-4. (Note that the fault duration is not precise because of the mechanical reaction of the breaker). The results are presented in Figure VI-24 and they are the same for all outer controls.

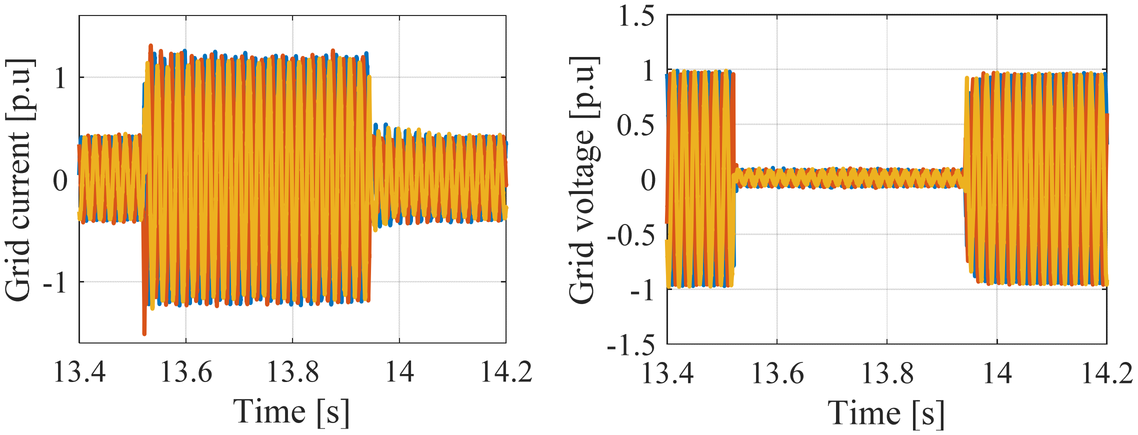

Figure VI-24 - Three-phase short circuit in islanding mode

When the fault occurs, the AC voltage drop induces an increase in the VSC output current I_g , which is limited to the allowable current magnitude, 1.2 p.u. Once the fault is cleared the system rapidly recovers its equilibrium point.

VI.4.2 Three-bus system: controllers interoperability

In the previous subsections, the expected behavior and the performances of a grid-forming-based VSC on each outer control strategy was validated using an ideal voltage source test case. However, in the future power system, grid-forming converters of different power ratings and employing different control strategies will be interconnected through transmission grids with diverse topologies. In order to study the behavior and the performances of the controllers in such a scenario, the simple, but representative meshed grid of 320 kV overhead distributed lines, resistive loads, and three nodes is used. It is shown in Figure VI-25.

The distributed lines and the two power converters based on “Strategy B with direct AC voltage control (VSC2)” and “Strategy A with cascaded control (VSC1)” are simulated in real-time. They are virtually connected to the physical power converter through the linear amplifier, which is controlled based on “Strategy C with cascaded control (VSC3)”.

Adaptive gains for the physical currents and voltages have been added to the real-time simulation such that the physical 5 kW, 300V converters are seen as a 500 MW, 320 kV converter.

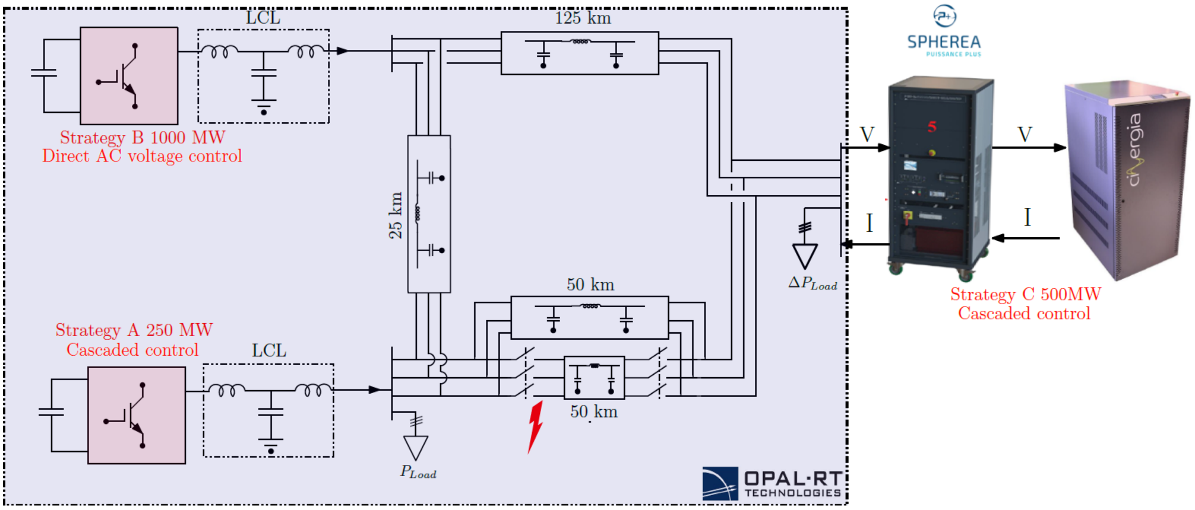

Figure VI-25 - Three-bus system

For this configuration, three test cases are performed:

- Heavy load connection and disconnection.
- Power exchange between power converters.
- Three-phase bolted fault at the middle of the 50km line followed by a line tripping.

VI.4.2.1 Load change

Initially, the system supplies a 281 MW of P_{load}. Then, a 450 MW load change is applied and removed after 3 s.

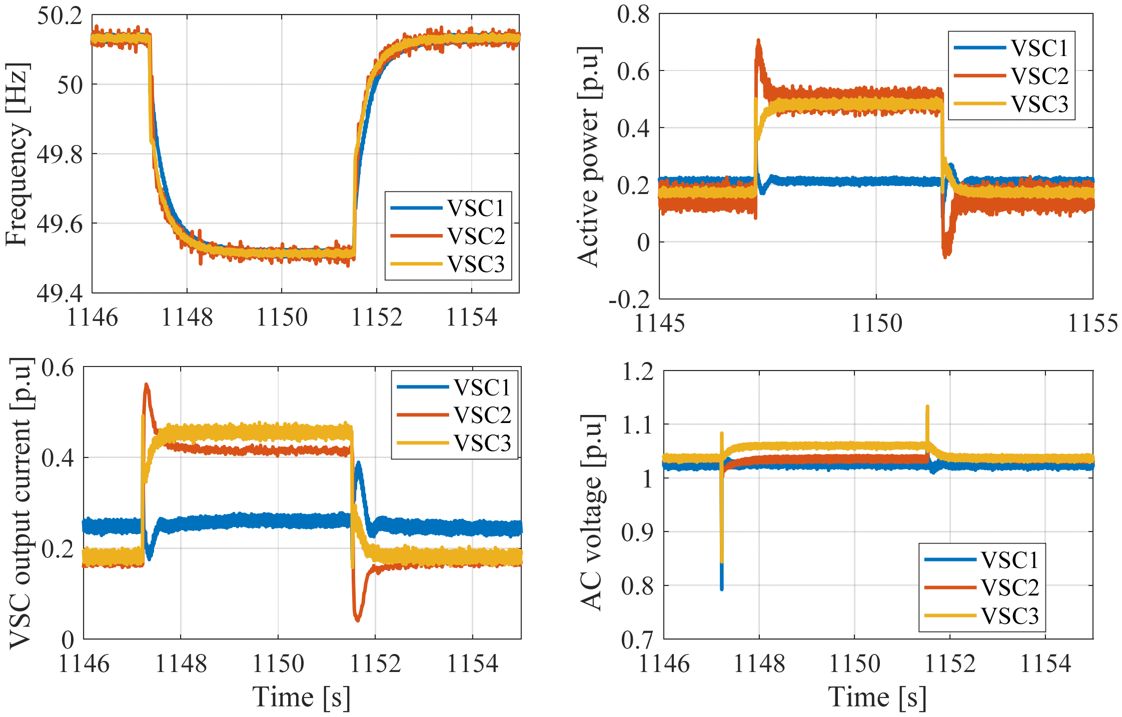

Figure VI-26 - Load change

As shown in Figure VI-26, a load change leads to a voltage transient reflected on all VSCs. The AC voltage drop and rise during the load connection and disconnection mainly depends on the distance between the VSCs and the load. Since the primary frequency control of VSC1 is disabled, it does not contribute to the power sharing.

VI.4.2.2 Active power change on VSC1

The active power of VSC1 is initially set to $p^* = 0.2$ p.u. Then, active power steps of $\Delta p^* = 0.3$ p.u and $\Delta p^* = -0.3$ p.u are applied to VSC1. The results are gathered in Figure VI-27. Since the VSC1 is operating as a power injector (no droop control is implemented), its active power tracks the reference p^* following the specified dynamics. The noises appeared on the frequency of the real converter are due to the AC voltage measurement used for the frequency estimation.

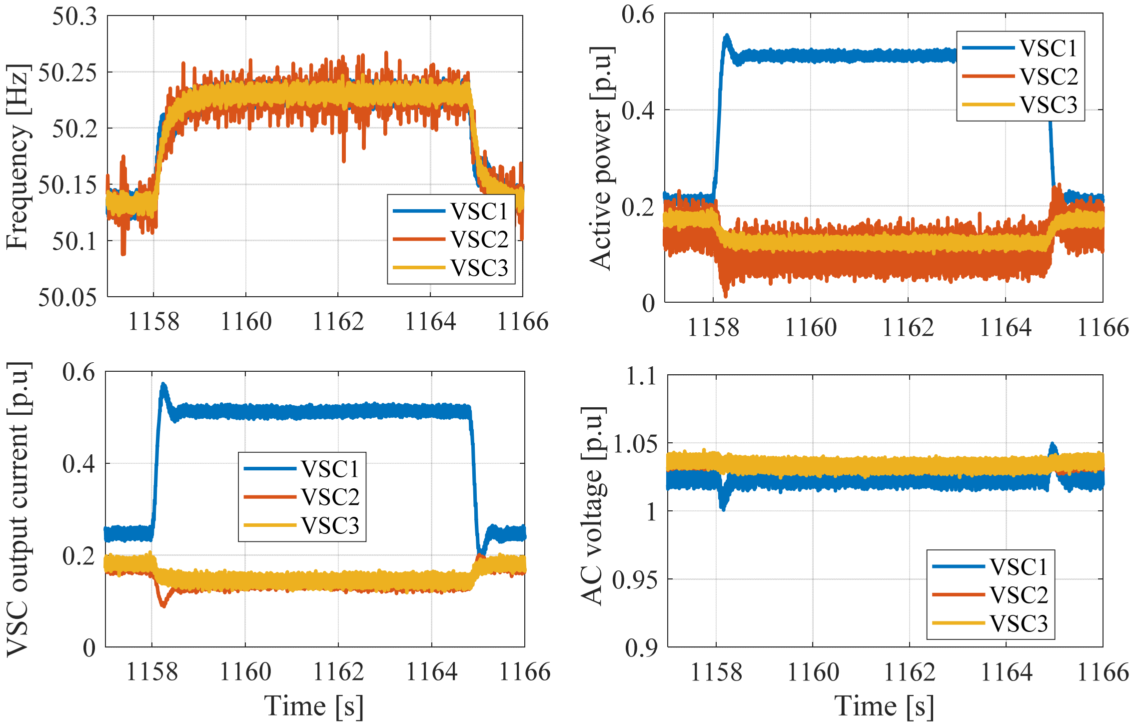

Figure VI-27 - Active power change on VSC 1

VI.4.2.3 Three-phase bolted fault

At $t = t_1$, a 400 ms, symmetrical three-phase short circuit occurred at the departure of the 50 km line. Subsequently, it is cleared by tripping the lines using the switches. In this test case, a P_{load}=731 MW is assumed to be connected initially and converter participates in the primary frequency support.

As shown in Figure VI-28, the output current of each converter increases and reaches its maximum allowable current 1.2 p.u when a fault occurs. Once the fault is cleared, the system quickly recovers its operating point within 100 ms.

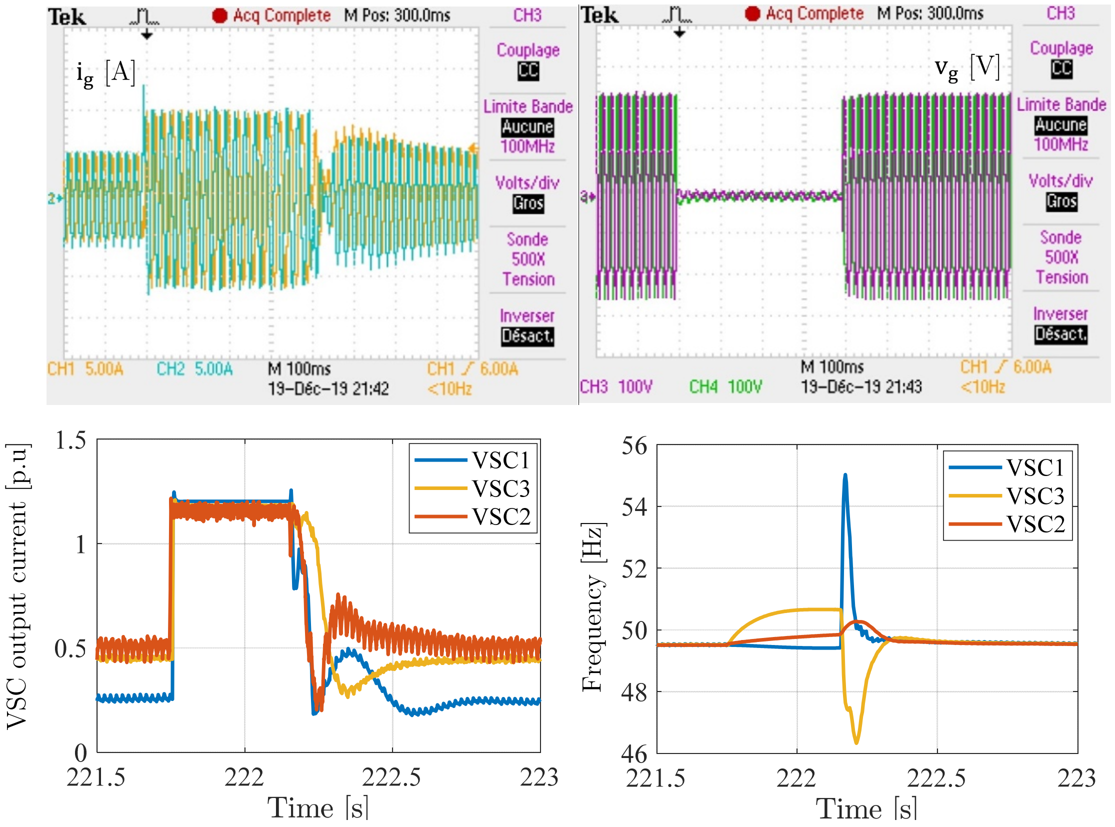

Figure VI-28 - Three-phase fault followed by a tripping line

VI.4.3 Irish power system: interaction with simplified model of Synchronous machines

In this proposed test case, a generator has been substituted by a grid-forming converter. It is shown for this specific test case *(and only for this specific test case)* that the Irish power system remains stable, even if an equivalent synchronous generator is tripped. A screenshot of the SCADA HMI is presented in Figure VI-29.

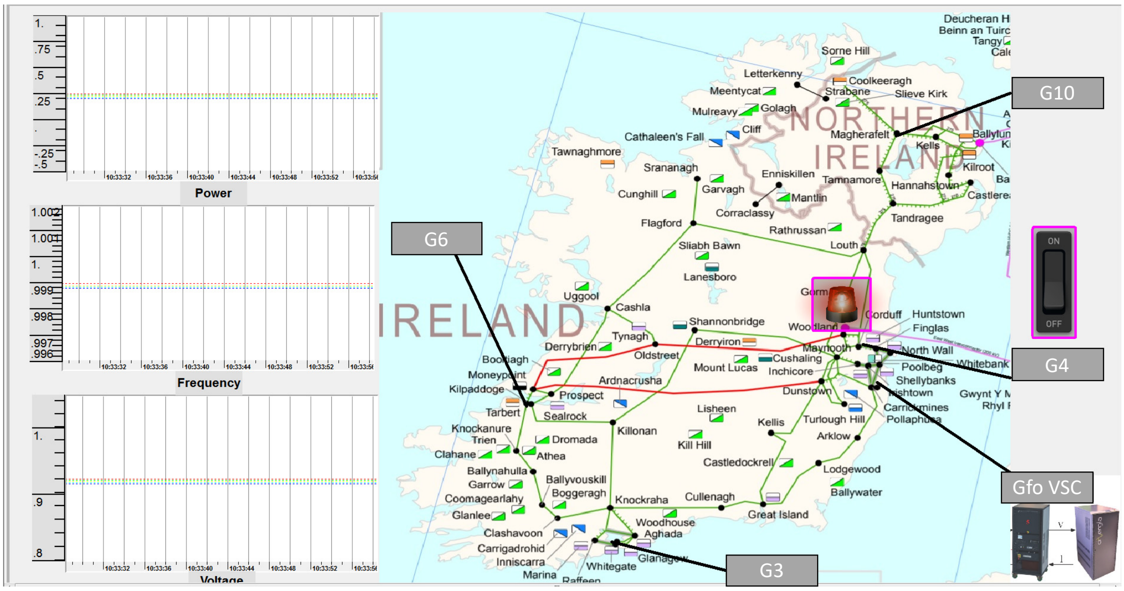

Figure VI-29 - SCADA HMI

In this grid configuration, all the generators are substituted by an inertial equivalent source, as illustrated in Figure VI-9. At first, the physical converter is synchronized to the AC system, where it is participating in the power sharing with the other units. Then, the loss of the generator G4 occurred.

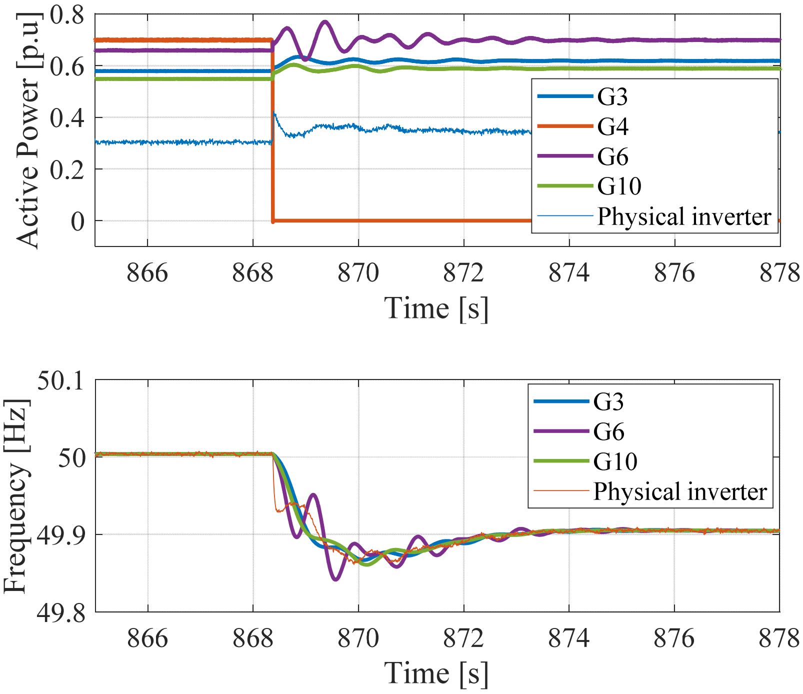

Figure VI-30 - Dynamic behavior of the power system during a loss of the generator G4

The results in Figure VI-30 show that the loss of the unit G4 leads to a frequency decrease and a new power distribution between the other units. After the disturbance, all generators recover in a stable manner to new equilibrium point.

VI.5 Conclusion

The previous chapters focused on the introduction of theoretical aspects and simulation-based validation. This chapter presents experimental validation of the proposed concepts.

These experimental validations have been based on an original small-scale test bench using physical hardware and Real-Time Simulation principles. The behavior of power converters in different power system topologies has been simulated with a real-time simulator. Then, a power amplifier has been used to interconnect equipment based on the PHIL principle.

The grid-forming control implementation has been described in section VI.3. In the following, three experiments have been realized:

1- Experimentation on a perfect voltage source, in order to test the proposed local controllers
2- Experimentation on the three-node grid case.
3- Experimentation on the Irish Power System to show interaction with synchronous machines

It has been shown that:

- The proposed local controllers are operating in a stable manner.
- The proposed current limiting algorithm can protect the converter in the case of a three-phase fault or phase-shift.
- Different kinds of local controllers can be interconnected together.
- A grid-forming converter can be integrated in an actual power system containing classical synchronous machines.

VII. General conclusion & Perspectives

General conclusion

High penetration of new means of electrical generation triggers more PE devices being incorporated into the bulk power system. It modifies the foundation of today's power system operation and control. In the case of a 100% PE power system, some grid-connected converters should act as AC voltage sources behind an impedance. These converters require different control laws in order to respond to the system needs, and allowing a stable operation during large disturbances. This thesis focuses on the grid-forming control principle used for power electronic converters connected to a transmission system. It comes back to the basics of this control in order to explain the origin of the power control with a voltage source.

Since the main function of a power source is to inject active power into the grid, monitoring the grid states is a compulsory task. In other words, synchronization to the grid is required. This task is fundamentally different according to the nature of the power source (i.e., current or voltage source). In the case where the converter operates as a voltage source, self-synchronization is achieved thanks to a power control loop similarly to a synchronous machine. Contrary to the ideas considering the grid-forming as a PLL-less control, an estimate of the grid angle and frequency through a PLL is not mandatory for the control but it can be considered. The PLL has always been seen as a main source of instability, which TSOs seek to avoid at all cost. However, the PLL does not have the same objectives for grid-following as for grid-forming. The PLL for grid-forming control is not intended to guarantee the synchronization, but to reject the grid disturbances (Strategy A) or to decouple the power and the frequency control features (Strategy B). This is one of the main ideas this thesis aims to convey.

Unlike grid-following control where a fast PLL dynamics reduce the stability margin of the system, a fast PLL ($T_R^{PLL} <$ 50 ms) for the grid-forming ensures more stability and better dynamic performances. This choice has another major advantage proved in chapter III: when the PLL dynamics are fast, the estimated grid-frequency can be assimilated to the real grid frequency, which allows demonstrating some similarities between "Strategy B" (VSM) and synchronous machines e.g. the same mathematical formulations used to evaluate the RoCoF and system inertia in the conventional power system are still valid for 100% PE system. Otherwise, if the PLL dynamics are slow, the inertia concept will not be true anymore and the equivalence between VSM and SM will be wrong.

The developed controls in this thesis are inspired from the present operation of the electrical grid, where, not all power sources are asked to participate to the frequency and the inertial support. Therefore, chapter II firstly proposes a robust grid-forming control that allows injecting the active power with specified dynamics, whatever the grid stiffness and topology are. It allows participating in the load sharing if needed, but does not allow inertia emulation. The design of this control takes into account, the transient coupling between active and reactive power, and includes a transient virtual resistor to damp the grid currents, and thereby, avoiding a resonance around the grid frequency. This virtual resistance should be implemented regardless the grid-forming control structure. If some power sources are asked to participate in the fast frequency support, two kinds of control are proposed in chapter III “Strategy B and C” to meet this need. Both controls allow a fast frequency support (primary frequency control and inertia emulation). However, with Strategy B, the active power setpoint tracking is still possible and the primary frequency control is an optional feature, whereas, with “Strategy C”, the primary frequency control is compulsory. This does not allow steady state active power setpoint tracking.

Depending on the power converter topology, the connection to AC system can be different. In the case of a 2-Level VSC, an LC filter is needed, which requires additional control loops. Usually a cascaded control loops structure is used to control the AC voltage across the filter capacitor, which helps avoiding a resonance of the LCL filter. Moreover, this control structure allows the generation of a current reference that serves to protect the equipment. However, because of the limited bandwidth of the power converter in high power applications, specific tuning of the cascaded controllers is of a highest importance. In this thesis, tuning based on the global pole placement is proposed to put all system eigenvalues in a given area that respects some stability and dynamic constraints. The ability of the resulting gains to guarantee a stable operation has been tested in different grid cases. Moreover, the set of parameters guarantees a good decoupling between the inner and outer power control loops as demonstrated through the participation factors in chapter IV.

A second method has been proposed based on the knowledge of the system, where, a simple quasi-stationary virtual impedance is implemented in the control to compensate the voltage drop across the output impedance. Then, a transient virtual LCL damping resistor is added to avoid instability issues linked to the resonance of the LCL filter.

Regarding the MMC topology, only an L filter is needed for the grid connection. Consequently, no need for inner control loops. The complexity of the MMC control is mainly linked to the management of its internal energy in each submodule. In this thesis, the operation of the MMC has been tested through time-domain simulations, where the behavior of the MMC is analyzed in normal and abnormal conditions. The obtained results do not reveal any major interactions between the energy control and power control loops.

The protection of power converters against faults and their post-fault synchronization is very important task. In chapter V, two well-known methods for current limitation (CSA and VI) and their impact on the transient stability have been discussed. Thanks to the comparative and the theoretical approaches proposed in this thesis, the advantages and limitations of each method are highlighted. This approach leads to fundamental conclusions: the CSA is better for current limitation, whereas, the VI is better in terms of transient stability. Based on this consideration, hybridization between both strategies is proposed to benefit from their advantage in one single control strategy called Hybrid Current Limiting Control (HCLC). Despite that the transient stability has been enhanced thanks to the HCLC, a risk of angle instability remains likely to happen if the fault duration is long. To deal with this issue, a simple algorithm to improve the transient stability has been proposed. It consists of modifying the power reference or the power controller gains during the fault to increase the critical clearing time. With Strategy B and C, an additional freezing action on the PLL is required.

The effectiveness of the developed controllers and theoretical approaches along with this thesis has been proved via different experimentations (single and multi-inverter system). These experimentations have been based on an original small-scale test bench using physical hardware and Real-Time Simulation principles. The behavior of power converters in different power system topologies has been simulated with a real-time simulator. Then, a power amplifier has been used to interconnect equipment based on the PHIL principle.

Perspectives

From this thesis, various tracks may be followed to extend the studies of grid-forming VSC:

Impact of DC bus control: In the whole thesis, the control of the DC bus has been neglected. Ongoing works by Artur Avazov and Ebrahim Rokrok at L2EP-Lille are dealing with the connection of the grid-forming converter to HVDC systems (Inertia Provision Project) and offshore wind farms.

PLL-less synchronization unit with decoupled features: Many grid-forming control strategies without PLL have been proposed, however, few controls if any among them are ensuring power control, inertial emulation and load sharing in a decoupled manner.

Impact of different types of loads: Studies on different kinds of loads such as motor loads and non-linear loads are missing. Actually, non-linear loads induce harmonics, which may impact the control performances.

Inner controllers tuning: For the cascaded control structure, more sophisticated optimization-based method can be developed to determine the optimal control gains not violating other constrains (response time of each loop for instance).

Modular Multilevel Converters: In-depth analytical studies for grid-forming MMC are missing in this work.

Transient stability: The transient stability linked with the virtual impedance assumes a bounded X_{VI}, R_{VI} to ease the studies. Non-linear approach can be developed to have more precise stability proof including the current limitation aspects. Additionally, a theoretical approach has only been developed for Strategy C and tested on Strategy B and A. Analytical stability proof based on Strategy B and A has not been developed in this thesis.
Multi-inverter transient stability analysis was not discussed in this work. In power systems dominated by power electronic devices, such analysis will be very useful to determine the boundaries and the limitations of the transient stability studies based on a single converter connected to an infinite bus.

Unbalanced fault: Current limitation in unbalanced grid conditions is a real challenge. This point will be considered in our future works.

References

[1] "TOWARDS 100% RENEWABLE ENERGY: STATUS, TRENDS AND LESSONS LEARNED." IRENA Coalition for action, 2019.

[2] B. Kroposki *et al.*, "Achieving a 100% Renewable Grid: Operating Electric Power Systems with Extremely High Levels of Variable Renewable Energy," *IEEE Power Energy Mag.*, vol. 15, no. 2, pp. 61–73, Mar. 2017, doi: 10.1109/MPE.2016.2637122.

[3] W. Zappa, M. Junginger, and M. van den Broek, "Is a 100% renewable European power system feasible by 2050?," *Appl. Energy*, vol. 233–234, pp. 1027–1050, Jan. 2019, doi: 10.1016/j.apenergy.2018.08.109.

[4] B. Singh, "Introduction to FACTS Controllers in Wind Power Farms: A Technological Review," p. 47, 2012.

[5] S. K. Chaudhary, R. Teodorescu, and P. Rodriguez, "Wind Farm Grid Integration Using VSC Based HVDC Transmission - An Overview," in *2008 IEEE Energy 2030 Conference*, Atlanta, GA, USA, Nov. 2008, pp. 1–7, doi: 10.1109/ENERGY.2008.4781061.

[6] H. Lund and B. V. Mathiesen, "Energy system analysis of 100% renewable energy systems—The case of Denmark in years 2030 and 2050," *Energy*, vol. 34, no. 5, pp. 524–531, May 2009, doi: 10.1016/j.energy.2008.04.003.

[7] B. V. Mathiesen, H. Lund, and K. Karlsson, "100% Renewable energy systems, climate mitigation and economic growth," *Appl. Energy*, vol. 88, no. 2, pp. 488–501, Feb. 2011, doi: 10.1016/j.apenergy.2010.03.001.

[8] F. Wagner, "Electricity by intermittent sources: An analysis based on the German situation 2012," *Eur. Phys. J. Plus*, vol. 129, no. 2, Feb. 2014, doi: 10.1140/epjp/i2014-14020-8.

[9] V. Krakowski, E. Assoumou, V. Mazauric, and N. Maïzi, "Feasible path toward 40–100% renewable energy shares for power supply in France by 2050: A prospective analysis," *Appl. Energy*, vol. 171, pp. 501–522, Jun. 2016, doi: 10.1016/j.apenergy.2016.03.094.

[10] M. Z. Jacobson, M. A. Delucchi, M. A. Cameron, and B. V. Mathiesen, "Matching demand with supply at low cost in 139 countries among 20 world regions with 100% intermittent wind, water, and sunlight (WWS) for all purposes," *Renew. Energy*, vol. 123, pp. 236–248, Aug. 2018, doi: 10.1016/j.renene.2018.02.009.

[11] "https://tyndp.entsoe.eu/."

[12] S. J. Finney, G. P. Adam, B. W. Williams, D. Holliday, and I. A. Gowaid, "Review of dc–dc converters for multi-terminal HVDC transmission networks," *IET Power Electron.*, vol. 9, no. 2, pp. 281–296, Feb. 2016, doi: 10.1049/iet-pel.2015.0530.

[13] R. Zeng, L. Xu, L. Yao, and B. W. Williams, “Design and Operation of a Hybrid Modular Multilevel Converter,” *IEEE Trans. Power Electron.*, vol. 30, no. 3, pp. 1137–1146, Mar. 2015, doi: 10.1109/TPEL.2014.2320822.

[14] “Phase locked loop FINAL.pdf.” Accessed: Sep. 06, 2018. [Online]. Available: https://www.nationalgrid.com/sites/default/files/documents/Phase%20locked%20loop%20FINAL.pdf.

[15] A. Ulbig, T. S. Borsche, and G. Andersson, “Impact of Low Rotational Inertia on Power System Stability and Operation,” *ArXiv13126435 Math*, Dec. 2013, Accessed: Aug. 24, 2018. [Online]. Available: http://arxiv.org/abs/1312.6435.

[16] “High Penetration of Power Electronic Interfaced Power Sources (HPoPEIPS),” ENTSO-E, Technical, Mar. 2017. [Online]. Available: https://consultations.entsoe.eu/system-development/entso-e-connection-codes-implementation-guidance-d-3.

[17] T. Pieter, H. Pierre, and C. Stijn, “Penetration of renewables and reduction of synchronous inertia in the European power system – Analysis and solutions.” Nov. 2018, [Online]. Available: https://asset-ec.eu/.

[18] “COMMISSION REGULATION (EU) 2016/ 631 - of 14 April 2016 - establishing a network code on requirements for grid connection of generators,” p. 68.

[19] A. Adib, B. Mirafzal, X. Wang, and F. Blaabjerg, “On Stability of Voltage Source Inverters in Weak Grids,” *IEEE Access*, vol. 6, pp. 4427–4439, 2018, doi: 10.1109/ACCESS.2017.2788818.

[20] G. Denis, “From grid-following to grid-forming: The new strategy to build 100 % power-electronics interfaced transmission system with enhanced transient behavior,” thesis, Ecole centrale de Lille, 2017.

[21] Y. Wang, V. Silva, and M. Lopez-Botet-Zulueta, “Impact of high penetration of variable renewable generation on frequency dynamics in the continental Europe interconnected system,” *IET Renew. Power Gener.*, vol. 10, no. 1, pp. 10–16, 2016, doi: 10.1049/iet-rpg.2015.0141.

[22] L. Zhang, L. Harnefors, and H. Nee, “Power-Synchronization Control of Grid-Connected Voltage-Source Converters,” *IEEE Trans. Power Syst.*, vol. 25, no. 2, pp. 809–820, May 2010, doi: 10.1109/TPWRS.2009.2032231.

[23] M. C. Chandorkar, D. M. Divan, and R. Adapa, “Control of parallel connected inverters in standalone AC supply systems,” *IEEE Trans. Ind. Appl.*, vol. 29, no. 1, pp. 136–143, Jan. 1993, doi: 10.1109/28.195899.

[24] K. D. Brabandere, B. Bolsens, J. V. den Keybus, A. Woyte, J. Driesen, and R. Belmans, “A Voltage and Frequency Droop Control Method for Parallel Inverters,” *IEEE Trans. Power Electron.*, vol. 22, no. 4, pp. 1107–1115, Jul. 2007, doi: 10.1109/TPEL.2007.900456.

[25] H. Nikkhajoei and R. H. Lasseter, “Distributed Generation Interface to the CERTS Microgrid,” *IEEE Trans. Power Deliv.*, vol. 24, no. 3, pp. 1598–1608, Jul. 2009, doi: 10.1109/TPWRD.2009.2021040.

[26] T. Shintai, Y. Miura, and T. Ise, “Reactive power control for load sharing with virtual synchronous generator control,” in *Proceedings of The 7th International Power Electronics and Motion Control Conference*, Harbin, China, Jun. 2012, pp. 846–853, doi: 10.1109/IPEMC.2012.6258956.

[27] W. Wu *et al.*, “A Virtual Inertia Control Strategy for DC Microgrids Analogized With Virtual Synchronous Machines,” *IEEE Trans. Ind. Electron.*, vol. 64, no. 7, pp. 6005–6016, Jul. 2017, doi: 10.1109/TIE.2016.2645898.

[28] N. Pogaku, M. Prodanovic, and T. C. Green, “Modeling, Analysis and Testing of Autonomous Operation of an Inverter-Based Microgrid,” *IEEE Trans. Power Electron.*, vol. 22, no. 2, pp. 613–625, Mar. 2007, doi: 10.1109/TPEL.2006.890003.

[29] F. Katiraei, R. Iravani, N. Hatziargyriou, and A. Dimeas, “Microgrids management,” *IEEE Power Energy Mag.*, vol. 6, no. 3, pp. 54–65, May 2008, doi: 10.1109/MPE.2008.918702.

[30] J. W. Simpson-Porco, F. Dörfler, and F. Bullo, “Synchronization and power sharing for droop-controlled inverters in islanded microgrids,” *Automatica*, vol. 49, no. 9, pp. 2603–2611, Sep. 2013, doi: 10.1016/j.automatica.2013.05.018.

[31] H. Fakham, T. Qoria, M. Legry, O. Ducarme, and F. Colas, “Development of a power hardware in the loop simulation of an islanded microgrid,” in *IECON 2019 - 45th Annual Conference of the IEEE Industrial Electronics Society*, Oct. 2019, vol. 1, pp. 6438–6443, doi: 10.1109/IECON.2019.8927122.

[32] J. M. Guerrero, J. C. Vasquez, J. Matas, M. Castilla, and L. G. de Vicuna, “Control Strategy for Flexible Microgrid Based on Parallel Line-Interactive UPS Systems,” *IEEE Trans. Ind. Electron.*, vol. 56, no. 3, pp. 726–736, Mar. 2009, doi: 10.1109/TIE.2008.2009274.

[33] J. M. Guerrero, L. G. de Vicuna, J. Matas, M. Castilla, and J. Miret, “Output impedance design of parallel-connected UPS inverters with wireless load-sharing control,” *IEEE Trans. Ind. Electron.*, vol. 52, no. 4, pp. 1126–1135, Aug. 2005, doi: 10.1109/TIE.2005.851634.

[34] Y. A. I. Mohamed and E. F. El-Saadany, “Adaptive Decentralized Droop Controller to Preserve Power Sharing Stability of Paralleled Inverters in Distributed Generation Microgrids,” *IEEE Trans. Power Electron.*, vol. 23, no. 6, pp. 2806–2816, Nov. 2008, doi: 10.1109/TPEL.2008.2005100.

[35] A. Engler and N. Soultanis, “Droop control in LV-grids,” in *2005 International Conference on Future Power Systems*, Nov. 2005, p. 6 pp. – 6, doi: 10.1109/FPS.2005.204224.

[36] Y. Li and Y. W. Li, “Power Management of Inverter Interfaced Autonomous Microgrid Based on Virtual Frequency-Voltage Frame,” *IEEE Trans. Smart Grid*, vol. 2, no. 1, pp. 30–40, Mar. 2011, doi: 10.1109/TSG.2010.2095046.

[37] J. C. Vasquez, J. M. Guerrero, M. Savaghebi, J. Eloy-Garcia, and R. Teodorescu, “Modeling, Analysis, and Design of Stationary-Reference-Frame Droop-Controlled Parallel Three-Phase Voltage Source Inverters,” *IEEE*

Trans. Ind. Electron., vol. 60, no. 4, pp. 1271–1280, Apr. 2013, doi: 10.1109/TIE.2012.2194951.

[38] J. M. Guerrero, J. C. Vásquez, and R. Teodorescu, "Hierarchical control of droop-controlled DC and AC microgrids — a general approach towards standardization," in *2009 35th Annual Conference of IEEE Industrial Electronics*, Nov. 2009, pp. 4305–4310, doi: 10.1109/IECON.2009.5414926.

[39] A. Bidram and A. Davoudi, "Hierarchical Structure of Microgrids Control System," *IEEE Trans. Smart Grid*, vol. 3, no. 4, pp. 1963–1976, Dec. 2012, doi: 10.1109/TSG.2012.2197425.

[40] J. M. Guerrero, L. Hang, and J. Uceda, "Control of Distributed Uninterruptible Power Supply Systems," *IEEE Trans. Ind. Electron.*, vol. 55, no. 8, pp. 2845–2859, Aug. 2008, doi: 10.1109/TIE.2008.924173.

[41] Il-Yop Chung, Wenxin Liu, D. A. Cartes, E. G. Collins, and Seung-Il Moon, "Control Methods of Inverter-Interfaced Distributed Generators in a Microgrid System," *IEEE Trans. Ind. Appl.*, vol. 46, no. 3, pp. 1078–1088, 2010, doi: 10.1109/TIA.2010.2044970.

[42] Y. Zhu, F. Zhuo, F. Wang, B. Liu, and Y. Zhao, "A Wireless Load Sharing Strategy for Islanded Microgrid Based on Feeder Current Sensing," *IEEE Trans. Power Electron.*, vol. 30, no. 12, pp. 6706–6719, Dec. 2015, doi: 10.1109/TPEL.2014.2386851.

[43] T.-L. Lee and P.-T. Cheng, "Design of a New Cooperative Harmonic Filtering Strategy for Distributed Generation Interface Converters in an Islanding Network," *IEEE Trans. Power Electron.*, vol. 22, no. 5, pp. 1919–1927, Sep. 2007, doi: 10.1109/TPEL.2007.904200.

[44] J. Hu, J. Zhu, D. G. Dorrell, and J. M. Guerrero, "Virtual Flux Droop Method—A New Control Strategy of Inverters in Microgrids," *IEEE Trans. Power Electron.*, vol. 29, no. 9, pp. 4704–4711, Sep. 2014, doi: 10.1109/TPEL.2013.2286159.

[45] S. D'Arco and J. A. Suul, "Equivalence of Virtual Synchronous Machines and Frequency-Droops for Converter-Based MicroGrids," *IEEE Trans. Smart Grid*, vol. 5, no. 1, pp. 394–395, Jan. 2014, doi: 10.1109/TSG.2013.2288000.

[46] T. QORIA, F. GRUSON, F. COLAS, G. Denis, T. PREVOST, and G. Xavier, "Inertia effect and load sharing capability of grid forming converters connected to a transmission grid," *The 15th IET international conference on AC and DC Power Transmission*, UK, p. 6, Jan. 2019.

[47] J. Liu, Y. Miura, and T. Ise, "Comparison of Dynamic Characteristics Between Virtual Synchronous Generator and Droop Control in Inverter-Based Distributed Generators," *IEEE Trans. Power Electron.*, vol. 31, no. 5, pp. 3600–3611, May 2016, doi: 10.1109/TPEL.2015.2465852.

[48] Bin Li and Lin Zhou, "Power Decoupling Method Based on the Diagonal Compensating Matrix for VSG-Controlled Parallel Inverters in the Microgrid," *Energies*, vol. 10, no. 12, p. 2159, Dec. 2017, doi: 10.3390/en10122159.

[49] J. Driesen and K. Visscher, “Virtual synchronous generators,” in *2008 IEEE Power and Energy Society General Meeting - Conversion and Delivery of Electrical Energy in the 21st Century*, Jul. 2008, pp. 1–3, doi: 10.1109/PES.2008.4596800.

[50] Q. Zhong and G. Weiss, “Synchronverters: Inverters That Mimic Synchronous Generators,” *IEEE Trans. Ind. Electron.*, vol. 58, no. 4, pp. 1259–1267, Apr. 2011, doi: 10.1109/TIE.2010.2048839.

[51] Q. Zhong, P. Nguyen, Z. Ma, and W. Sheng, “Self-Synchronized Synchronverters: Inverters Without a Dedicated Synchronization Unit,” *IEEE Trans. Power Electron.*, vol. 29, no. 2, pp. 617–630, Feb. 2014, doi: 10.1109/TPEL.2013.2258684.

[52] Z. Ma, Q. Zhong, and J. D. Yan, “Synchronverter-based control strategies for three-phase PWM rectifiers,” in *2012 7th IEEE Conference on Industrial Electronics and Applications (ICIEA)*, Jul. 2012, pp. 225–230, doi: 10.1109/ICIEA.2012.6360727.

[53] R. Rosso, J. Cassoli, G. Buticchi, S. Engelken, and M. Liserre, “Robust Stability Analysis of *LCL* Filter Based Synchronverter Under Different Grid Conditions,” *IEEE Trans. Power Electron.*, vol. 34, no. 6, pp. 5842–5853, Jun. 2019, doi: 10.1109/TPEL.2018.2867040.

[54] R. Rosso, S. Engelken, and M. Liserre, “Robust Stability Analysis of Synchronverters Operating in Parallel,” *IEEE Trans. Power Electron.*, vol. 34, no. 11, pp. 11309–11319, Nov. 2019, doi: 10.1109/TPEL.2019.2896707.

[55] Y. Chen, R. Hesse, D. Turschner, and H.-P. Beck, “Comparison of methods for implementing virtual synchronous machine on inverters,” *Renew. Energy Power Qual. J.*, pp. 734–739, Apr. 2012, doi: 10.24084/repqj10.453.

[56] H. Beck and R. Hesse, “Virtual synchronous machine,” in *2007 9th International Conference on Electrical Power Quality and Utilisation*, Oct. 2007, pp. 1–6, doi: 10.1109/EPQU.2007.4424220.

[57] Y. Chen, R. Hesse, D. Turschner, and H. Beck, “Improving the grid power quality using virtual synchronous machines,” in *2011 International Conference on Power Engineering, Energy and Electrical Drives*, May 2011, pp. 1–6, doi: 10.1109/PowerEng.2011.6036498.

[58] S. D’Arco, J. A. Suul, and O. B. Fosso, “A Virtual Synchronous Machine implementation for distributed control of power converters in SmartGrids,” *Electr. Power Syst. Res.*, vol. 122, pp. 180–197, May 2015, doi: 10.1016/j.epsr.2015.01.001.

[59] M. Yu *et al.*, “Use of an inertia-less Virtual Synchronous Machine within future power networks with high penetrations of converters,” in *2016 Power Systems Computation Conference (PSCC)*, Jun. 2016, pp. 1–7, doi: 10.1109/PSCC.2016.7540926.

[60] R. Hesse, D. Turschner, and H.-P. Beck, “Micro grid stabilization using the virtual synchronous machine (VISMA),” *Renew. Energy Power Qual. J.*, vol. 1, no. 07, pp. 676–681, Apr. 2009, doi: 10.24084/repqj07.472.

[61] N. Soni, S. Doolla, and M. C. Chandorkar, “Improvement of Transient Response in Microgrids Using Virtual Inertia,” *IEEE Trans. Power Deliv.*, vol. 28, no. 3, pp. 1830–1838, Jul. 2013, doi: 10.1109/TPWRD.2013.2264738.

[62] J. Zhu, C. D. Booth, G. P. Adam, A. J. Roscoe, and C. G. Bright, “Inertia Emulation Control Strategy for VSC-HVDC Transmission Systems,” *IEEE Trans. Power Syst.*, vol. 28, no. 2, pp. 1277–1287, May 2013, doi: 10.1109/TPWRS.2012.2213101.

[63] D. Groß, M. Colombino, J.-S. Brouillon, and F. Dörfler, “The effect of transmission-line dynamics on grid-forming dispatchable virtual oscillator control,” *ArXiv180208881 Math*, Feb. 2018, Accessed: Oct. 01, 2018. [Online]. Available: http://arxiv.org/abs/1802.08881.

[64] M. Ali, A. Sahoo, H. I. Nurdin, J. Ravishankar, and J. E. Fletcher, “On the Power Sharing Dynamics of Parallel-Connected Virtual Oscillator-Controlled and Droop-Controlled Inverters in an AC Microgrid,” in *IECON 2019 - 45th Annual Conference of the IEEE Industrial Electronics Society*, Lisbon, Portugal, Oct. 2019, pp. 3931–3936, doi: 10.1109/IECON.2019.8927510.

[65] Z. Shi, H. I. Nurdin, J. E. Fletcher, and J. Li, “Similarities Between Virtual Oscillator Controlled and Droop Controlled Three-Phase Inverters,” in *2018 IEEE 18th International Power Electronics and Motion Control Conference (PEMC)*, Budapest, Aug. 2018, pp. 434–439, doi: 10.1109/EPEPEMC.2018.8521928.

[66] M. Colombino, D. Groß, J.-S. Brouillon, and F. Dörfler, “Global phase and magnitude synchronization of coupled oscillators with application to the control of grid-forming power inverters,” *ArXiv171000694 Math*, Oct. 2017, Accessed: Oct. 01, 2018. [Online]. Available: http://arxiv.org/abs/1710.00694.

[67] D. Raisz, T. T. Thai, and A. Monti, “Power Control of Virtual Oscillator Controlled Inverters in Grid-Connected Mode,” *IEEE Trans. Power Electron.*, vol. 34, no. 6, pp. 5916–5926, Jun. 2019, doi: 10.1109/TPEL.2018.2868996.

[68] T. T. Thai, D. Raisz, A. Monti, F. Ponci, and A. Ahmadifar, “Voltage harmonic reduction using virtual oscillator based inverters in islanded microgrids,” in *2018 18th International Conference on Harmonics and Quality of Power (ICHQP)*, Ljubljana, May 2018, pp. 1–6, doi: 10.1109/ICHQP.2018.8378896.

[69] M. Ashabani, F. D. Freijedo, S. Golestan, and J. M. Guerrero, “Inducverters: PLL-Less Converters With Auto-Synchronization and Emulated Inertia Capability,” *IEEE Trans. Smart Grid*, vol. 7, no. 3, pp. 1660–1674, May 2016, doi: 10.1109/TSG.2015.2468600.

[70] T. Qoria, Q. Cossart, C. Li, X. Guillaud, F. Gruson, and X. Kestelyn, “Deliverable 3.2: Local control and simulation tools for large transmission systems,” p. 89.

[71] I. Erlich *et al.*, “New Control of Wind Turbines Ensuring Stable and Secure Operation Following Islanding of Wind Farms,” *IEEE Trans. Energy Convers.*, vol. 32, no. 3, pp. 1263–1271, Sep. 2017, doi: 10.1109/TEC.2017.2728703.

[72] I. Erlich *et al.*, “Overvoltage phenomena in offshore wind farms following blocking of the HVDC converter,” in *2016 IEEE Power and Energy Society General Meeting (PESGM)*, Boston, MA, USA, Jul. 2016, pp. 1–5, doi: 10.1109/PESGM.2016.7741697.

[73] S. D’Arco, J. A. Suul, and O. B. Fosso, “Automatic Tuning of Cascaded Controllers for Power Converters Using Eigenvalue Parametric Sensitivities,” *IEEE Trans. Ind. Appl.*, vol. 51, no. 2, pp. 1743–1753, Mar. 2015, doi: 10.1109/TIA.2014.2354732.

[74] T. QORIA, F. GRUSON, F. COLAS, X. GUILLAUD, M.-S. DEBRY, and T. PREVOST, “Tuning of cascaded controllers for robust grid-forming Voltage Source Converter,” p. 7.

[75] F. Salha, “Microréseaux îlotables: étude et coordination des protections des générateurs et du réseau,” p. 198.

[76] Y. W. Li and C. Kao, “An Accurate Power Control Strategy for Power-Electronics-Interfaced Distributed Generation Units Operating in a Low-Voltage Multibus Microgrid,” *IEEE Trans. Power Electron.*, vol. 24, no. 12, pp. 2977–2988, Dec. 2009, doi: 10.1109/TPEL.2009.2022828.

[77] E. A. A. Coelho, P. C. Cortizo, and P. F. D. Garcia, “Small-signal stability for parallel-connected inverters in stand-alone AC supply systems,” *IEEE Trans. Ind. Appl.*, vol. 38, no. 2, pp. 533–542, Apr. 2002, doi: 10.1109/28.993176.

[78] Z. Li, C. Zang, P. Zeng, H. Yu, S. Li, and J. Bian, “Control of a Grid-Forming Inverter Based on Sliding-Mode and Mixed $H_2/H_ınfty $ Control,” *IEEE Trans. Ind. Electron.*, vol. 64, no. 5, pp. 3862–3872, May 2017, doi: 10.1109/TIE.2016.2636798.

[79] D. Pullaguram, S. Mishra, N. Senroy, and M. Mukherjee, “Design and Tuning of Robust Fractional Order Controller for Autonomous Microgrid VSC System,” *IEEE Trans. Ind. Appl.*, vol. 54, no. 1, pp. 91–101, Jan. 2018, doi: 10.1109/TIA.2017.2758755.

[80] T. Qoria, C. Li, K. Oue, F. Gruson, F. Colas, and X. Guillaud, “Direct AC voltage control for grid-forming inverters,” *J. Power Electron.*, vol. 20, no. 1, pp. 198–211, Jan. 2020, doi: 10.1007/s43236-019-00015-4.

[81] T. Qoria, F. Gruson, F. Colas, X. Guillaud, M. Debry, and T. Prevost, “Tuning of Cascaded Controllers for Robust Grid-Forming Voltage Source Converter,” in *2018 Power Systems Computation Conference (PSCC)*, Jun. 2018, pp. 1–7, doi: 10.23919/PSCC.2018.8443018.

[82] Q.-C. Zhong and G. C. Konstantopoulos, “Current-Limiting Droop Control of Grid-Connected Inverters,” *IEEE Trans. Ind. Electron.*, vol. 64, no. 7, pp. 5963–5973, Jul. 2017, doi: 10.1109/TIE.2016.2622402.

[83] N. Bottrell and T. C. Green, “Comparison of Current-Limiting Strategies During Fault Ride-Through of Inverters to Prevent Latch-Up and Wind-Up,” *IEEE Trans. Power Electron.*, vol. 29, no. 7, pp. 3786–3797, Jul. 2014, doi: 10.1109/TPEL.2013.2279162.

[84] A. D. Paquette and D. M. Divan, “Virtual Impedance Current Limiting for Inverters in Microgrids With Synchronous Generators,” *IEEE Trans. Ind. Appl.*, vol. 51, no. 2, pp. 1630–1638, Mar. 2015, doi: 10.1109/TIA.2014.2345877.

[85] X. Lu, J. Wang, J. M. Guerrero, and D. Zhao, “Virtual-Impedance-Based Fault Current Limiters for Inverter Dominated AC Microgrids,” *IEEE Trans. Smart Grid*, vol. 9, no. 3, pp. 1599–1612, May 2018, doi: 10.1109/TSG.2016.2594811.

[86] F. Salha, F. Colas, and X. Guillaud, “Virtual resistance principle for the overcurrent protection of PWM voltage source inverter,” in *2010 IEEE PES Innovative Smart Grid Technologies Conference Europe (ISGT Europe)*, Gothenburg, Sweden, Oct. 2010, pp. 1–6, doi: 10.1109/ISGTEUROPE.2010.5638965.

[87] G. Denis, T. Prevost, M. Debry, F. Xavier, X. Guillaud, and A. Menze, “The Migrate project: the challenges of operating a transmission grid with only inverter-based generation. A grid-forming control improvement with transient current-limiting control,” *IET Renew. Power Gener.*, vol. 12, no. 5, pp. 523–529, 2018, doi: 10.1049/iet-rpg.2017.0369.

[88] I. Sadeghkhani, M. E. Hamedani Golshan, J. M. Guerrero, and A. Mehrizi-Sani, “A Current Limiting Strategy to Improve Fault Ride-Through of Inverter Interfaced Autonomous Microgrids,” *IEEE Trans. Smart Grid*, vol. 8, no. 5, pp. 2138–2148, Sep. 2017, doi: 10.1109/TSG.2016.2517201.

[89] M. G. Taul, X. Wang, P. Davari, and F. Blaabjerg, “Current Limiting Control With Enhanced Dynamics of Grid-Forming Converters During Fault Conditions,” *IEEE J. Emerg. Sel. Top. Power Electron.*, vol. 8, no. 2, pp. 1062–1073, Jun. 2020, doi: 10.1109/JESTPE.2019.2931477.

[90] X. Wang, Y. W. Li, F. Blaabjerg, and P. C. Loh, “Virtual-Impedance-Based Control for Voltage-Source and Current-Source Converters,” *IEEE Trans. Power Electron.*, vol. 30, no. 12, pp. 7019–7037, Dec. 2015, doi: 10.1109/TPEL.2014.2382565.

[91] D. M. Vilathgamuwa, P. C. Loh, and Y. Li, “Protection of Microgrids During Utility Voltage Sags,” *IEEE Trans. Ind. Electron.*, vol. 53, no. 5, pp. 1427–1436, Oct. 2006, doi: 10.1109/TIE.2006.882006.

[92] L. Huang, H. Xin, Z. Wang, L. Zhang, K. Wu, and J. Hu, “Transient Stability Analysis and Control Design of Droop-Controlled Voltage Source Converters Considering Current Limitation,” *IEEE Trans. Smart Grid*, vol. 10, no. 1, pp. 578–591, Jan. 2019, doi: 10.1109/TSG.2017.2749259.

[93] M. Yu, W. Huang, N. Tai, X. Zheng, P. Wu, and W. Chen, “Transient stability mechanism of grid-connected inverter-interfaced distributed generators using droop control strategy,” *Appl. Energy*, vol. 210, pp. 737–747, Jan. 2018, doi: 10.1016/j.apenergy.2017.08.104.

[94] T. QORIA, F. Gruson, F. COLAS, X. Kestelyn, and X. GUILLAUD, “Current Limiting Algorithms and Transient Stability Analysis of Grid-Forming VSCs,” *PSCC 2020*, p. 9, Jun. 2020.

[95] H. Xin, L. Huang, L. Zhang, Z. Wang, and J. Hu, “Synchronous Instability Mechanism of P-f Droop-Controlled Voltage Source Converter Caused by Current Saturation,” *IEEE Trans. Power Syst.*, vol. 31, no. 6, pp. 5206–5207, Nov. 2016, doi: 10.1109/TPWRS.2016.2521325.

[96] L. Huang, L. Zhang, H. Xin, Z. Wang, and D. Gan, “Current limiting leads to virtual power angle synchronous instability of droop-controlled converters,” in *2016 IEEE Power and Energy Society General Meeting (PESGM)*, Jul. 2016, pp. 1–5, doi: 10.1109/PESGM.2016.7741667.

[97] D. Pan, X. Wang, F. Liu, and R. Shi, “Transient Stability of Voltage-Source Converters With Grid-Forming Control: A Design-Oriented Study,” *IEEE J. Emerg. Sel. Top. Power Electron.*, vol. 8, no. 2, pp. 1019–1033, Jun. 2020, doi: 10.1109/JESTPE.2019.2946310.

[98] K. O. Oureilidis and C. S. Demoulias, “A Fault Clearing Method in Converter-Dominated Microgrids With Conventional Protection Means,” *IEEE Trans. Power Electron.*, vol. 31, no. 6, pp. 4628–4640, Jun. 2016, doi: 10.1109/TPEL.2015.2476702.

[99] I. Erlich, “Control Challenges in Power Systems Dominated by Converter Interfaced Generation and Transmission Technologies,” in *NEIS 2017; Conference on Sustainable Energy Supply and Energy Storage Systems*, Sep. 2017, pp. 1–8.

[100] G. Denis and T. Prevost, “MIGRATE D3.6: Requirement guidelines for operating a grid with 100% power electronic devices.,” 2019, doi: 10.13140/RG.2.2.36586.67528.

[101] “https://www.promotion-offshore.net/.” .

[102] “H2020 Migrate.” https://www.h2020-migrate.eu/ (accessed Sep. 09, 2018).

[103] “HVDC Inertia provision,” *SINTEF.* http://www.sintef.no/en/projects/hvdc-inertia-provision/ (accessed Jun. 13, 2020).

[104] J. Rocabert, A. Luna, F. Blaabjerg, and P. Rodríguez, “Control of Power Converters in AC Microgrids,” *IEEE Trans. Power Electron.*, vol. 27, no. 11, pp. 4734–4749, Nov. 2012, doi: 10.1109/TPEL.2012.2199334.

[105] T. Qoria, T. Prevost, G. Denis, F. Gruson, F. Colas, and X. Guillaud, “Power Converters Classification and Characterization in Power Transmission Systems,” in *2019 21st European Conference on Power Electronics and Applications (EPE ’19 ECCE Europe)*, Genova, Italy, Sep. 2019, p. P.1-P.9, doi: 10.23919/EPE.2019.8914783.

[106] A. M. Bouzid, J. M. Guerrero, A. Cheriti, M. Bouhamida, P. Sicard, and M. Benghanem, “A survey on control of electric power distributed generation systems for microgrid applications,” *Renew. Sustain. Energy Rev.*, vol. 44, pp. 751–766, Apr. 2015, doi: 10.1016/j.rser.2015.01.016.

[107] S. Henninger and J. Jaeger, “Advanced classification of converter control concepts for integration in electrical power systems,” *Int. J. Electr. Power Energy Syst.*, vol. 123, p. 106210, Dec. 2020, doi: 10.1016/j.ijepes.2020.106210.

[108] “IEEE Guide for Planning DC Links Terminating at AC Locations Having Low Short-Circuit Capacities,” IEEE. doi: 10.1109/IEEESTD.1997.85949.

[109] M. Paolone *et al.*, “Fundamentals of power systems modelling in the presence of converter-interfaced generation,” *Electr. Power Syst. Res.*, vol. 189, p. 106811, Dec. 2020, doi: 10.1016/j.epsr.2020.106811.

[110] P. Rodriguez, J. Pou, J. Bergas, J. I. Candela, R. P. Burgos, and D. Boroyevich, “Decoupled Double Synchronous Reference Frame PLL for Power Converters Control,” *IEEE Trans. Power Electron.*, vol. 22, no. 2, pp. 584–592, Mar. 2007, doi: 10.1109/TPEL.2006.890000.

[111] J. Freytes, L. Papangelis, H. Saad, P. Rault, T. Van Cutsem, and X. Guillaud, “On the modeling of MMC for use in large scale dynamic simulations,” in *2016 Power Systems Computation Conference (PSCC)*, Genoa, Italy, Jun. 2016, pp. 1–7, doi: 10.1109/PSCC.2016.7540938.

[112] J. Freytes, P. Rault, F. Gruson, F. Colas, and X. Guillaud, “Dynamic impact of MMC controllers on DC voltage droop controlled MTDC grids,” in *2016 18th European Conference on Power Electronics and Applications (EPE’16 ECCE Europe)*, Karlsruhe, Sep. 2016, pp. 1–10, doi: 10.1109/EPE.2016.7695423.

[113] H. Badihi, Y. Zhang, and H. Hong, “Active power control design for supporting grid frequency regulation in wind farms,” *Annu. Rev. Control*, vol. 40, pp. 70–81, Jan. 2015, doi: 10.1016/j.arcontrol.2015.09.005.

[114] N. R. Ullah, T. Thiringer, and D. Karlsson, “Voltage and Transient Stability Support by Wind Farms Complying With the E.ON Netz Grid Code,” *IEEE Trans. Power Syst.*, vol. 22, no. 4, pp. 1647–1656, Nov. 2007, doi: 10.1109/TPWRS.2007.907523.

[115] Y. Huang, X. Yuan, J. Hu, P. Zhou, and D. Wang, “DC-Bus Voltage Control Stability Affected by AC-Bus Voltage Control in VSCs Connected to Weak AC Grids,” *IEEE J. Emerg. Sel. Top. Power Electron.*, vol. 4, no. 2, pp. 445–458, Jun. 2016, doi: 10.1109/JESTPE.2015.2480859.

[116] Y. Huang, X. Yuan, and J. Hu, “Effect of reactive power control on stability of DC-link voltage control in VSC connected to weak grid,” in *2014 IEEE PES General Meeting | Conference & Exposition*, National Harbor, MD, USA, Jul. 2014, pp. 1–5, doi: 10.1109/PESGM.2014.6939466.

[117] L. Zhang, L. Harnefors, and P. Mitra, “Offshore wind integration to a weak grid by VSC-HVDC links using power-synchronization control: A case study,” in *2014 IEEE PES General Meeting | Conference & Exposition*, National Harbor, MD, USA, Jul. 2014, pp. 1–1, doi: 10.1109/PESGM.2014.6939172.

[118] J. A. Suul, S. D’Arco, P. Rodriguez, and M. Molinas, “Extended stability range of weak grids with Voltage Source Converters through impedance-conditioned grid synchronization,” in *11th IET International Conference on*

AC and DC Power Transmission, Feb. 2015, pp. 1–10, doi: 10.1049/cp.2015.0103.

[119] Z. Jenny Z, “Impact of short circuit ratio and phase locked loop parameters on the small-signal behaviour of a VSC-HVdc converter,” in *2016 IEEE Power and Energy Society General Meeting (PESGM)*, Boston, MA, USA, Jul. 2016, pp. 1–1, doi: 10.1109/PESGM.2016.7741107.

[120] S. Skogestad and I. Postlethwaite, *Multivariable feedback control: analysis and design*, 2nd ed. Hoboken, NJ: John Wiley, 2005.

[121] L. Zhang, L. Harnefors, and H. Nee, “Interconnection of Two Very Weak AC Systems by VSC-HVDC Links Using Power-Synchronization Control,” *IEEE Trans. Power Syst.*, vol. 26, no. 1, pp. 344–355, Feb. 2011, doi: 10.1109/TPWRS.2010.2047875.

[122] L. Harnefors, L. Zhang, and M. Bongiorno, “Frequency-domain passivity-based current controller design,” *IET Power Electron.*, vol. 1, no. 4, p. 455, 2008, doi: 10.1049/iet-pel:20070286.

[123] V. Mariani, F. Vasca, and J. M. Guerrero, “Analysis of droop controlled parallel inverters in islanded microgrids,” in *2014 IEEE International Energy Conference (ENERGYCON)*, Cavtat, Croatia, May 2014, pp. 1304–1309, doi: 10.1109/ENERGYCON.2014.6850591.

[124] E. Rokrok, T. Qoria, A. Bruyere, B. Francois, and X. Guillaud, “Effect of Using PLL-Based Grid-Forming Control on Active Power Dynamics Under Various SCR,” in *IECON 2019 - 45th Annual Conference of the IEEE Industrial Electronics Society*, Oct. 2019, vol. 1, pp. 4799–4804, doi: 10.1109/IECON.2019.8927648.

[125] E. Rokrok, T. Qoria, A. Bruyere, B. Francois, and X. Guillaud, “Classification and dynamic assessment of droop-based grid-forming control schemes: Application in HVDC systems,” *Electr. Power Syst. Res.*, vol. 189, p. 106765, Dec. 2020, doi: 10.1016/j.epsr.2020.106765.

[126] J. He, Y. W. Li, J. M. Guerrero, F. Blaabjerg, and J. C. Vasquez, “An Islanding Microgrid Power Sharing Approach Using Enhanced Virtual Impedance Control Scheme,” *IEEE Trans. Power Electron.*, vol. 28, no. 11, pp. 5272–5282, Nov. 2013, doi: 10.1109/TPEL.2013.2243757.

[127] A. Villa, F. Belloni, R. Chiumeo, and C. Gandolfi, “Conventional and reverse droop control in islanded microgrid: Simulation and experimental test,” in *2016 International Symposium on Power Electronics, Electrical Drives, Automation and Motion (SPEEDAM)*, Capri, Italy, Jun. 2016, pp. 288–294, doi: 10.1109/SPEEDAM.2016.7526020.

[128] J. He, Y. Li, B. Liang, and C. Wang, “Inverse Power Factor Droop Control for Decentralized Power Sharing in Series-Connected-Microconverters-Based Islanding Microgrids,” *IEEE Trans. Ind. Electron.*, vol. 64, no. 9, pp. 7444–7454, Sep. 2017, doi: 10.1109/TIE.2017.2674588.

[129] H. Han, Y. Liu, Y. Sun, M. Su, and J. M. Guerrero, “An Improved Droop Control Strategy for Reactive Power Sharing in Islanded Microgrid,” *IEEE*

Trans. Power Electron., vol. 30, no. 6, pp. 3133–3141, Jun. 2015, doi: 10.1109/TPEL.2014.2332181.

[130] H. Mahmood, D. Michaelson, and J. Jiang, “Accurate Reactive Power Sharing in an Islanded Microgrid Using Adaptive Virtual Impedances,” *IEEE Trans. Power Electron.*, vol. 30, no. 3, pp. 1605–1617, Mar. 2015, doi: 10.1109/TPEL.2014.2314721.

[131] S. Jayalath and M. Hanif, “Generalized LCL-Filter Design Algorithm for Grid-Connected Voltage-Source Inverter,” *IEEE Trans. Ind. Electron.*, vol. 64, no. 3, pp. 1905–1915, Mar. 2017, doi: 10.1109/TIE.2016.2619660.

[132] C. Mahamat, M. Petit, F. Costa, R. Marouani, and A. Mami, “Optimized Design of an LCL Filter for Grid Connected Photovoltaic System and Analysis of the Impact of Neighbors’ Consumption on the System,” *J. Electr. Syst.*, Nov. 2017, Accessed: Apr. 13, 2019. [Online]. Available: https://hal.archives-ouvertes.fr/hal-01676019.

[133] R. Beres, X. Wang, F. Blaabjerg, C. L. Bak, and M. Liserre, “A review of passive filters for grid-connected voltage source converters,” in *2014 IEEE Applied Power Electronics Conference and Exposition - APEC 2014*, Fort Worth, TX, USA, Mar. 2014, pp. 2208–2215, doi: 10.1109/APEC.2014.6803611.

[134] M. Liserre, F. Blaabjerg, and S. Hansen, “Design and Control of an LCL-Filter-Based Three-Phase Active Rectifier,” *IEEE Trans. Ind. Appl.*, vol. 41, no. 5, pp. 1281–1291, Sep. 2005, doi: 10.1109/TIA.2005.853373.

[135] C. Xie, X. Zhao, K. Li, J. Zou, and J. M. Guerrero, “A New Tuning Method of Multiresonant Current Controllers for Grid-Connected Voltage Source Converters,” *IEEE J. Emerg. Sel. Top. Power Electron.*, vol. 7, no. 1, pp. 458–466, Mar. 2019, doi: 10.1109/JESTPE.2018.2833806.

[136] G. Denis, T. Prevost, P. Panciatici, X. Kestelyn, F. Colas, and X. Guillaud, “Improving robustness against grid stiffness, with internal control of an AC voltage-controlled VSC.,” in *2016 IEEE Power and Energy Society General Meeting (PESGM)*, Jul. 2016, pp. 1–5, doi: 10.1109/PESGM.2016.7741341.

[137] T. QORIA *et al.*, “Tuning of AC voltage-controlled VSC based Linear Quadratic Regulation,” *IEEE PES PowerTech*, p. 6, 2019.

[138] T. QORIA, F. GRUSON, F. Colas, X. Kestelyn, and X. Guillaud, “Analysis of the coupling between the outer and inner control loops of a Grid-forming Voltage Source Converter,” *EPE2020 (Accepted)*, Lyon, FRANCE, p. 10, Aug. 2020.

[139] P. Delarue, F. Gruson, and X. Guillaud, “Energetic macroscopic representation and inversion based control of a modular multilevel converter,” in *2013 15th European Conference on Power Electronics and Applications (EPE)*, Lille, France, Sep. 2013, pp. 1–10, doi: 10.1109/EPE.2013.6631859.

[140] Weijia Tang, Daozhuo Jiang, Rui Yin, Yufen Wang, and Yuebin Zhou, “A novel CCSC for circulating current suppression in modular multilevel converters,” in *2016 IEEE Power and Energy Society General Meeting (PESGM)*, Jul. 2016, pp. 1–5, doi: 10.1109/PESGM.2016.7741170.

[141] J. Freytes *et al.*, “Improving Small-Signal Stability of an MMC With CCSC by Control of the Internally Stored Energy,” *IEEE Trans. Power Deliv.*, vol. 33, no. 1, pp. 429–439, Feb. 2018, doi: 10.1109/TPWRD.2017.2725579.

[142] Qingrui Tu, Zheng Xu, and Lie Xu, “Reduced Switching-Frequency Modulation and Circulating Current Suppression for Modular Multilevel Converters,” *IEEE Trans. Power Deliv.*, vol. 26, no. 3, pp. 2009–2017, Jul. 2011, doi: 10.1109/TPWRD.2011.2115258.

[143] S. Samimi, F. Gruson, P. Delarue, F. Colas, M. M. Belhaouane, and X. Guillaud, “MMC Stored Energy Participation to the DC Bus Voltage Control in an HVDC Link,” *IEEE Trans. Power Deliv.*, vol. 31, no. 4, pp. 1710–1718, Aug. 2016, doi: 10.1109/TPWRD.2016.2540926.

[144] T. Qoria, F. Gruson, P. Delarue, P. L. Moigne, F. Colas, and X. Guillaud, “Modeling and Control of the Modular Multilevel Converter connected to an inductive DC source using Energetic Macroscopic Representation,” in *2018 20th European Conference on Power Electronics and Applications (EPE’18 ECCE Europe)*, Sep. 2018, p. P.1-P.10.

[145] S. DrArco, G. Guidi, and J. A. Suul, “Operation of a Modular Multilevel Converter Controlled as a Virtual Synchronous Machine,” in *2018 International Power Electronics Conference (IPEC-Niigata 2018 -ECCE Asia)*, Niigata, May 2018, pp. 782–789, doi: 10.23919/IPEC.2018.8508009.

[146] Z. Lv and Q.-C. Zhong, “Control of modular multilevel converters as virtual synchronous machines,” in *2017 IEEE Power & Energy Society General Meeting*, Chicago, IL, Jul. 2017, pp. 1–5, doi: 10.1109/PESGM.2017.8274551.

[147] C. Verdugo, J. I. Candela, and P. Rodriguez, “Grid support functionalities based on modular multilevel converters with synchronous power control,” in *2016 IEEE International Conference on Renewable Energy Research and Applications (ICRERA)*, Birmingham, United Kingdom, Nov. 2016, pp. 572–577, doi: 10.1109/ICRERA.2016.7884399.

[148] E. Rokrok, T. QORIA, A. Bruyere, B. Francois, H. Zang, and M. M. Belhaouane, “Impact of grid-forming control on the internal energy of a modular multi-level converter,” *EPE2020 (Accepted)*, Lyon, FRANCE, Sep. 2020.

[149] P. Munch, D. Gorges, M. Izak, and S. Liu, “Integrated current control, energy control and energy balancing of Modular Multilevel Converters,” in *IECON 2010 - 36th Annual Conference on IEEE Industrial Electronics Society*, Glendale, AZ, USA, Nov. 2010, pp. 150–155, doi: 10.1109/IECON.2010.5675185.

[150] Kundur, *Power System Stability And Control.* McGraw-Hill, 1994.

[151] T. Qoria, F. Gruson, F. Colas, X. Kestelyn, and X. Guillaud, “Current limiting algorithms and transient stability analysis of grid-forming VSCs,” *Electr. Power Syst. Res.*, vol. 189, p. 106726, Dec. 2020, doi: 10.1016/j.epsr.2020.106726.

[152] T. Qoria, F. Gruson, F. Colas, G. Denis, T. Prevost, and X. Guillaud, “Critical clearing time determination and enhancement of grid-forming converters embedding virtual impedance as current limitation algorithm,” *IEEE J. Emerg. Sel. Top. Power Electron.*, pp. 1–1, 2019, doi: 10.1109/JESTPE.2019.2959085.

[153] H. Saad, X. Guillaud, J. Mahseredjian, S. Dennetiere, and S. Nguefeu, “MMC Capacitor Voltage Decoupling and Balancing Controls,” *IEEE Trans. Power Deliv.*, vol. 30, no. 2, pp. 704–712, Apr. 2015, doi: 10.1109/TPWRD.2014.2338861.

[154] M. Abdelsalam, M. Marei, S. Tennakoon, and A. Griffiths, “Capacitor voltage balancing strategy based on sub-module capacitor voltage estimation for modular multilevel converters,” *CSEE J. Power Energy Syst.*, vol. 2, no. 1, pp. 65–73, Mar. 2016, doi: 10.17775/CSEEJPES.2016.00010.

[155] F. Colas, Qoria Taoufik, X. Guillaud, and F. Gruson, “D3.5 - Local Control for Grid-Forming Converters Experimental Validation,” 2020, doi: 10.13140/RG.2.2.13327.94881.

[156] “EirGrid Group. All-Island Ten Year Transmission Forecast Statement,” *Technical report, EirGrid*, 2016.

Appendices

Appendix A

Park Transformation

The Park transformation consists in using a new coordinates to express the three-phase variables in the static reference frame *abc* with angular frequency defined by $n\omega$ into the rotating frame defined by the axes *dqz*. The *d* axis forms an angle $\theta = n\omega t$ with respect to the fixed vector *a* and the quadrature axis *q* is delayed by 90°. The *d*-*q* axes rotate at an angular speed $n\omega$. This is shown in a graphical description in Fig. A.1.

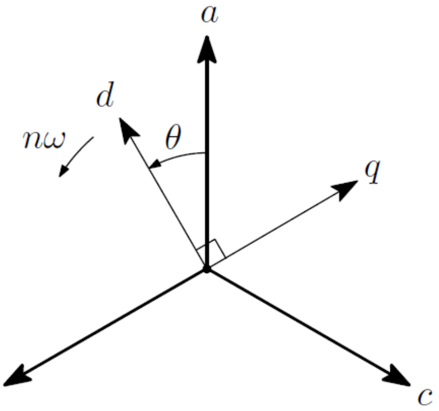

Figure A.1 – Transformation from abc to dqz in a graphical way

The mathematical transformation $P_{n\omega}$ is defined in (A.1). The constant *p* will take the value 2⁄3 if it's desired to maintain the amplitude of the vectors after the transformation (the so-called "Amplitude Invariant Park Transformation"). If the constant *p* takes the value $\sqrt{(2/3)}$, the power is maintained in *abc* and *dqz* frame (the so called "Power Invariant Park Transformation").

$$P_{n\omega} = p\begin{pmatrix} \cos(n\omega t) & \cos\left(n\omega t - \frac{2\pi}{3}\right) & \cos\left(n\omega t + \frac{2\pi}{3}\right) \\ \sin(n\omega t) & \sin\left(n\omega t - \frac{2\pi}{3}\right) & \sin\left(n\omega t + \frac{2\pi}{3}\right) \\ 1/2 & 1/2 & 1/2 \end{pmatrix} \tag{A.1}$$

Clarke Transformation

Another useful transformation widely used in electrical systems is the Clarke transformation. This mathematical transformation projects the three-phase vectors in *abc* frame displaced 120° from each other, onto two stationary axes namely $\alpha\beta$, which are displaced by 90° from each other. The third axis, namely *z*, is the same as for the Park transformation. This transformation is shown in a graphical description in Fig. A.2.

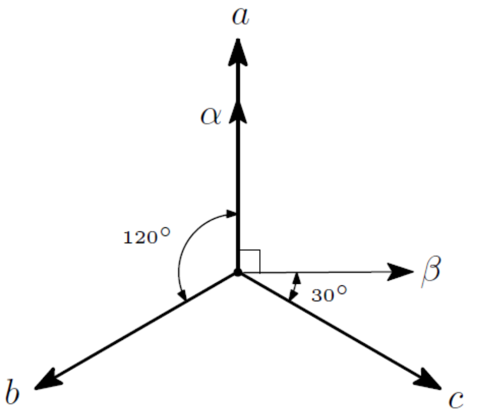

Figure A.2 – Transformation from abc to αβz in a graphical way

The mathematical transformation $C_{\alpha\beta z}$ is defined in (A.2). Similarly as for the Park transformation, the constant p will take the value $2/3$ if it's desired to maintain the amplitude of the vectors after the transformation (the so-called "Amplitude Invariant Clarke Transformation"). If the constant p takes the value $\sqrt{(2/3)}$, the power is maintained in abc and $\alpha\beta z$ frame (the so-called "Power Invariant Clarke Transformation").

$$C_{\alpha\beta z} = p\begin{pmatrix} 1 & -1/2 & -1/2 \\ 0 & -\frac{\sqrt{(3)}}{2} & \frac{\sqrt{(3)}}{2} \\ 1/2 & 1/2 & 1/2 \end{pmatrix} \tag{A.2}$$

Appendix B

Dynamic formulas of active and reactive powers

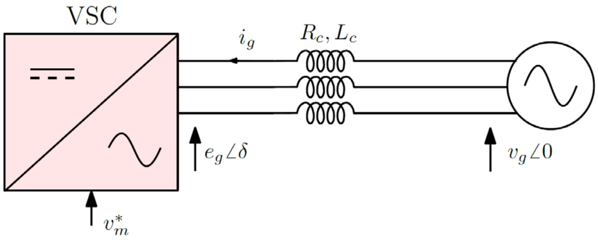

Figure B.1 - VSC connected to an AC system through R-L circuit

The dynamic system is typically developed in a synchronous *d-q* frame with the d-axis chosen aligned with the AC source v_g. The dynamic equations of the main circuit above can be written as:

$$\frac{L_c}{\omega_b}\frac{di_{gd}}{dt} = e_{gd} - v_{gd} - R_c i_{gd} + \omega_g L_c i_{gq} \tag{B.1}$$

$$\frac{L_c}{\omega_b}\frac{di_{gq}}{dt} = e_{gq} - v_{gq} - R_c i_{gq} - \omega_g L_c i_{gd} \tag{B.2}$$

$$e_{gd} = E_g \cos(\delta),\ e_{gq} = E_g \sin(\delta)$$

$$\frac{L_c}{\omega_b}\frac{di_{gd}}{dt} = E_g \cos(\delta) - V_g - R_c i_{gd} + \omega_g L_c i_{gq} \tag{B.3}$$

$$\frac{L_c}{\omega_b}\frac{di_{gq}}{dt} = E_g \sin(\delta) - R_c i_{gq} - \omega_g L_c i_{gd} \tag{B.4}$$

Considering small-variations around the operating point, (B.3) and (B.4) are written:

$$\frac{L_c}{\omega_b}\frac{d\Delta i_{gd}}{dt} = -E_{g0}\sin(\delta_0)\Delta\delta + \Delta E_g \cos(\delta_0) - R_c\Delta i_{gd} + \omega_g L_c \Delta i_{gq} \tag{B.5}$$

$$\frac{L_c}{\omega_b}\frac{d\Delta i_{gq}}{dt} = E_{g0}\cos(\delta_0)\Delta\delta + \Delta E_g \sin(\delta_0) - R_c\Delta i_{gq} - \omega_g L_c \Delta i_{gd} \tag{B.6}$$

(B.5) and (B.6) in Laplace domain are written as:

$$\frac{L_c}{\omega_b}\Delta i_{gd} s = -E_{g0}\sin(\delta_0)\Delta\delta + \Delta E_g \cos(\delta_0) - R_c\Delta i_{gd} + \omega_g L_c \Delta i_{gq} \tag{B.7}$$

$$\frac{L_c}{\omega_b}\Delta i_{gq} s = E_{g0}\cos(\delta_0)\Delta\delta + \Delta E_g \sin(\delta_0) - R_c\Delta i_{gq} - \omega_g L_c \Delta i_{gd} \tag{B.8}$$

$$\Delta i_{gd} = \frac{-E_{g0}\sin(\delta_0)\Delta\delta + \Delta E_g \cos(\delta_0) + \omega_g L_c \Delta i_{gq}}{\frac{L_c}{\omega_b}s + R_c} \tag{B.9}$$

$$\Delta i_{gq} = \frac{E_{g0}\cos(\delta_0)\Delta\delta + \Delta E_g \sin(\delta_0) - \omega_g L_c \Delta i_{gd}}{\frac{L_c}{\omega_b}s + R_c} \tag{B.10}$$

Putting (B.9) in (B.10) and (B.10) in (B.9) yields:

$$\Delta i_{gd} = \frac{-E_{g0}\sin(\delta_0)(\frac{L_c}{\omega_b}s + R_c) + \omega_g L_c E_{g0}\cos(\delta_0)}{\left(\frac{L_c}{\omega_b}s + R_c\right)^2 + \left(\omega_g L_c\right)^2}\Delta\delta + \frac{\omega_g L_c \sin(\delta_0) + \cos(\delta_0)(\frac{L_c}{\omega_b}s + R_c)}{\left(\frac{L_c}{\omega_b}s + R_c\right)^2 + \left(\omega_g L_c\right)^2}\Delta E_g \tag{B.11}$$

$$\Delta i_{gq} = \frac{E_{g0}\cos(\delta_0)\left(\frac{L_c}{\omega_b}s + R_c\right) + E_{g0}\sin(\delta_0)\omega_g L_c}{\left(\frac{L_c}{\omega_b}s + R_c\right)^2 + \left(\omega_g L_c\right)^2}\Delta\delta - \frac{\cos(\delta_0)\omega_g L_c - \sin(\delta_0)(\frac{L_c}{\omega_b}s + R_c)}{\left(\frac{L_c}{\omega_b}s + R_c\right)^2 + \left(\omega_g L_c\right)^2}\Delta E_g \tag{B.12}$$

The active and reactive powers are expressed respectively as follow:

$$\Delta p = \Delta e_{gd} I_{gd_0} + \Delta e_{gq} I_{gq_0} + \Delta i_{gd} E_{gd_0} + \Delta i_{gq} E_{gq_0} \tag{B.13}$$

$$\Delta q = -\Delta e_{qd} I_{gq_0} + \Delta e_{gq} I_{gd_0} + \Delta i_{gd} E_{gq_0} - \Delta i_{gq} E_{gd_0} \tag{B.14}$$

The expressions of the initial values of the grid currents and voltages are deduced from equations (B.3), (B.4), (B.11) and (B.12):

$$I_{gd_0} = \frac{E_{g0}\sin(\delta_0)\omega_g L_c + R_c E_{g0}\cos(\delta_0) - R_c V_g}{\left(R_c\right)^2 + \left(\omega_g L_c\right)^2} \tag{B.15}$$

$$I_{gq_0} = \frac{-E_{g0}\cos(\delta_0)\omega_g L_c + R_c E_{g0}\sin(\delta_0) + V_g \omega_g L_c}{\left(R_c\right)^2 + \left(\omega_g L_c\right)^2} \tag{B.16}$$

$$E_{gd_0} = E_{g0}\cos(\delta_0) \tag{B.17}$$

$$E_{gq_0} = E_{g0}\sin(\delta_0) \tag{B.18}$$

$$\Delta e_{gd} = \frac{L_c}{\omega_b}\Delta i_{gd}s - \omega_g L_c \Delta i_{gq} + R_c \Delta i_{gd} \tag{B.19}$$

$$\Delta e_{gq} = \frac{L_c}{\omega_b}\Delta i_{gq}s + \omega_g L_c \Delta i_{gd} + R_c \Delta i_{gq} \tag{B.20}$$

$$\Delta e_{gd} = \frac{\begin{array}{c}\left[-E_{g0}\sin(\delta_0)\left(\frac{L_c}{\omega_b}\right)^2 s^2 - 2R_c\frac{L_c}{\omega_b}E_{g0}\sin(\delta_0)s - E_{g0}\sin(\delta_0)\left[\left(R_c\right)^2 + \left(\omega_g L_c\right)^2\right]\right]\Delta\delta + \ldots \\ \left[\cos(\delta_0)\left(\frac{L_c}{\omega_b}\right)^2 s^2 + \left[2R_c\frac{L_c}{\omega_b}\cos(\delta_0)\right]s + \cos(\delta_0)\left[\left(R_c\right)^2 + \left(\omega_g L_c\right)^2\right]\right]\Delta E_g\end{array}}{\left(\frac{L_c}{\omega_b}s + R_c\right)^2 + \left(\omega_g L_c\right)^2} \tag{B.21}$$

$$\Delta e_{gq}=\frac{\begin{array}{c}\left[E_{g0}\cos\left(\delta_0\right)\left(\frac{L_c}{\omega_b}\right)^2 s^2+2R_c\frac{L_c}{\omega_b}E_{g0}\cos\left(\delta_0\right)s+E_{g0}\cos\left(\delta_0\right)\left[\left(R_c\right)^2+\left(\omega_g L_c\right)^2\right]\right]\Delta\delta+\ldots\\ \left[\sin\left(\delta_0\right)\left(\frac{L_c}{\omega_b}\right)^2 s^2+\left[2R_c\frac{L_c}{\omega_b}\sin\left(\delta_0\right)\right]s+\sin\left(\delta_0\right)\left[\left(R_c\right)^2+\left(\omega_g L_c\right)^2\right]\right]\Delta E_g\end{array}}{\left(\frac{L_c}{\omega_b}s+R_c\right)^2+\left(\omega_g L_c\right)^2} \tag{B.22}$$

From the equations (B.11-B.12), (B.15-B.18) and (B.21-B.22), the expression of the power matrix is obtained:

$$\begin{bmatrix}\Delta p\\ \Delta q\end{bmatrix}=\begin{bmatrix}T_{p\delta} & T_{pE_g}\\ T_{q\delta} & T_{qE}\end{bmatrix}\begin{bmatrix}\Delta\delta\\ \Delta E_g\end{bmatrix} \tag{B.23}$$

$$T_{p\delta}=\frac{\begin{array}{c}\left[\frac{E_{g0}\left(\frac{L_c}{\omega_b}\right)^2\left(V_g\left(R_c\sin\left(\delta_0\right)+L_c\omega_g\cos\left(\delta_0\right)\right)-E_{g0}L_c\omega_g\right)}{\left(R_c\right)^2+\left(\omega_g L_c\right)^2}\right]s^2+\left[\frac{2R_c\frac{L_c}{\omega_b}E_{g0}\left(V_g\left(R_c\sin\left(\delta_0\right)+L_c\omega_g\cos\left(\delta_0\right)\right)-E_{g0}L_c\omega_g\right)}{\left(R_c\right)^2+\left(\omega_g L_c\right)^2}\right]s+\ldots\\ E_{g0}V_g\left(R_c\sin\left(\delta_0\right)+L_c\omega_g\cos\left(\delta_0\right)\right)\end{array}}{\left(\frac{L_c}{\omega_b}s+R_c\right)^2+\left(\omega_g L_c\right)^2} \tag{B.24}$$

$$T_{pV}=\frac{\begin{array}{c}\left[\frac{E_{g0}\left(\frac{L_c}{\omega_b}\right)^2\left(V_g\left(-R_c\cos\left(\delta_0\right)+L_c\omega_g\sin\left(\delta_0\right)\right)+R_c\right)}{\left(R_c\right)^2+\left(\omega_g L_c\right)^2}\right]s^2+\left[\frac{2R_c\frac{L_c}{\omega_b}\left(V_g\left(-R_c\cos\left(\delta_0\right)+L_c\omega_g\sin\left(\delta_0\right)\right)\right)}{\left(R_c\right)^2+\left(\omega_g L_c\right)^2}+E_{g0}L_c/\omega_b\right]s+\ldots\\ 2R_cE_{g0}+V_g\left(-R_c\cos\left(\delta_0\right)+L_c\omega_g\sin\left(\delta_0\right)\right)\end{array}}{\left(\frac{L_c}{\omega_b}s+R_c\right)^2+\left(\omega_g L_c\right)^2} \tag{B.25}$$

$$T_{q\delta}=\frac{\begin{array}{c}\left[\frac{E_{g0}\left(\frac{L_c}{\omega_b}\right)^2\left(V_g\left(-R_c\cos\left(\delta_0\right)+L_c\omega_g\sin\left(\delta_0\right)\right)+E_{g0}R_c\right)}{\left(R_c\right)^2+\left(\omega_g L_c\right)^2}\right]s^2+\left[\frac{2R_c\frac{L_c}{\omega_b}E_{g0}\left(V_g\left(-R_c\cos\left(\delta_0\right)+L_c\omega_g\sin\left(\delta_0\right)\right)+E_{g0}R_c\right)}{\left(R_c\right)^2+\left(\omega_g L_c\right)^2}+\frac{E_{g0}{}^2L_c}{\omega_b}\right]s+\ldots\\ E_{g0}V_g\left(R_c\cos\left(\delta_0\right)+L_c\omega_g\sin\left(\delta_0\right)\right)\end{array}}{\left(\frac{L_c}{\omega_b}s+R_c\right)^2+\left(\omega_g L_c\right)^2} \tag{B.26}$$

$$T_{qV}=\frac{\begin{array}{c}\left[\frac{\left(\frac{L_c}{\omega_b}\right)^2\left(-V_g\left(R_c\sin\left(\delta_0\right)+L_c\omega_g\cos\left(\delta_0\right)\right)+E_{g0}R_c\right)}{\left(R_c\right)^2+\left(\omega_g L_c\right)^2}\right]s^2+\left[\frac{2R_c\frac{L_c}{\omega_b}\left(-V_g\left(R_c\cos\left(\delta_0\right)+L_c\omega_g\sin\left(\delta_0\right)\right)+E_{g0}L_c\omega_g\right)}{\left(R_c\right)^2+\left(\omega_g L_c\right)^2}\right]s-\ldots\\ V_g\left(R_c\sin\left(\delta_0\right)+L_c\omega_g\cos\left(\delta_0\right)\right)+E_{g0}L_c\omega_g\end{array}}{\left(\frac{L_c}{\omega_b}s+R_c\right)^2+\left(\omega_g L_c\right)^2} \tag{B.27}$$

Appendix C

Linear State-Space model of “Strategy A” based-VSC

$$x_i = [\underbrace{i_{c_d}\ i_{c_q}\ i_{g_d}\ i_{g_d}\ v_{g_d}\ v_{g_q}}_{x_1}\ \underbrace{\zeta_{PLL}\ \delta_{PLL}\ \epsilon_{p_{ac}}\ \delta_m\ \zeta_{TVR_d}\ \zeta_{TVR_q}}_{x_2}],\ \ \Delta u = [v_{e_d}\ v_{e_q}\ p^*\ v_{m_d}\ v_{m_q}]$$

$$A_{11}=\begin{Bmatrix}
-\frac{R_c\omega_b}{L_c} & \omega_b\omega_0 & 0 & 0 & -\frac{\omega_b}{L_c} & 0 \\
-\omega_b\omega_0 & -\frac{R_c\omega_b}{L_c} & 0 & 0 & 0 & -\frac{\omega_b}{L_c} \\
\frac{\omega_b}{C_D} & 0 & -\frac{\omega_b}{C_D} & 0 & 0 & \omega_b\omega_0 \\
0 & \frac{\omega_b}{C_D} & 0 & -\frac{\omega_b}{C_D} & -\omega_b\omega_0 & 0 \\
0 & 0 & -\frac{R_g\omega_b}{L_g} & \omega_b\omega_0 & \frac{\omega_b}{L_g} & 0 \\
0 & 0 & -\omega_b\omega_0 & -\frac{R_g\omega_b}{L_g} & 0 & \frac{\omega_b}{L_g} \\
0 & 0 & -sin(\delta_{PLL0}-\delta_{m0})\ Ki_{PLL} & cos(\delta_{PLL0}-\delta_{m0})\ Ki_{PLL} & 0 & 0 \\
0 & 0 & -sin(\delta_{PLL0}-\delta_{m0})\ Kp_{PLL}\omega_b & cos(\delta_{PLL0}-\delta_{m0})\ Kp_{PLL}\omega_b & 0 & 0 \\
-V_{m0}\omega_c k_i & 0 & 0 & 0 & 0 & 0 \\
0 & 0 & -sin(\delta_{PLL0}-\delta_{m0})\ Kp_{PLL}\omega_b & cos(\delta_{PLL0}-\delta_{m0})\ Kp_{PLL}\omega_b & 0 & 0 \\
R_V\frac{R_c\omega_b}{L_c} & -R_V\omega_b\omega_0 & 0 & 0 & R_v\frac{\omega_b}{L_c} & 0 \\
R_V\omega_b\omega_0 & R_V\frac{R_c\omega_b}{L_c} & 0 & 0 & 0 & R_v\frac{\omega_b}{L_c}
\end{Bmatrix}$$

$$A_{12}=\begin{Bmatrix}
0 & 0 & 0 & 0 & \frac{\omega_b}{L_c} & 0 \\
0 & 0 & 0 & 0 & 0 & \frac{\omega_b}{L_c} \\
0 & 0 & 0 & 0 & 0 & 0 \\
0 & 0 & 0 & 0 & 0 & 0 \\
0 & 0 & 0 & \frac{\omega_b}{L_g}V_e sin(\delta_{m0}) & 0 & 0 \\
0 & 0 & 0 & \frac{\omega_b}{L_g}V_e cos(\delta_{m0}) & 0 & 0 \\
0 & -V_{g_{d0}}cos(\delta_{PLL0}-\delta_{m0})K_{i_{PLL}} & 0 & V_{g_{d0}}cos(\delta_{PLL0}-\delta_{m0})K_{i_{PLL}} & 0 & 0 \\
\omega_b & -V_{g_{d0}}cos(\delta_{PLL0}-\delta_{m0})K_{p_{PLL}}\omega_b & 0 & V_{g_{d0}}cos(\delta_{PLL0}-\delta_{m0})K_{p_{PLL}}\omega_b & 0 & 0 \\
0 & 0 & -\omega_c & 0 & -I_{c_d}\omega_c k_i & -I_{c_q}\omega_c k_i \\
\omega_b & -V_{g_{d0}}cos(\delta_{PLL0}-\delta_{m0})K_{p_{PLL}}\omega_b & 1 & V_{g_{d0}}cos(\delta_{PLL0}-\delta_{m0})K_{p_{PLL}}\omega_b & 0 & 0 \\
0 & 0 & 0 & 0 & -(\frac{R_V\omega_b}{L_c}+\omega_{TVR}) & 0 \\
0 & 0 & 0 & 0 & 0 & -(\frac{R_V\omega_b}{L_c}+\omega_{TVR})
\end{Bmatrix}$$

$$B^T=\begin{Bmatrix}
0 & 0 & 0 & 0 & -\frac{\omega_b}{L_g}cos(\delta_{m0}) & 0 & 0 & 0 & 0 & 0 & 0 & 0 \\
0 & 0 & 0 & 0 & 0 & \frac{\omega_b}{L_g}sin(\delta_{m0}) & 0 & 0 & 0 & 0 & 0 & 0 \\
0 & 0 & 0 & 0 & 0 & 0 & 0 & 0 & \omega_c k_i & 0 & 0 & 0 \\
0 & 0 & 0 & 0 & 0 & 0 & 0 & 0 & 0 & 0 & \omega_{TVR} & 0 \\
0 & 0 & 0 & 0 & 0 & 0 & 0 & 0 & 0 & 0 & 0 & 0
\end{Bmatrix}$$

Appendix D

Calculation of RoCoF and Frequency Nadir

Calculation of RoCoF

The grid frequency with respect to the load change for all control strategies is modeled with 2nd order transfer function with a zero in Laplace domain:

$$\Delta\omega_e(s) = K_1 \frac{(z_1+s)}{(s+\sigma-j\omega_d)(s+\sigma+j\omega_d)} \Delta P_{load}(s) \tag{D.1}$$

With $\sigma = \zeta\omega_n$ and $\omega_d = \omega_n\sqrt{1-\zeta^2}$.

ζ and ω_n denote the damping coefficient and the natural frequency, respectively.

If a step load change is applied to the system, then, the system is written as,

$$\Delta\omega_e(s) = K \frac{(z_1+s)}{s(s+\sigma-j\omega_d)(s+\sigma+j\omega_d)} \tag{D.2}$$

with $K = K_1\Delta P_{load}$

Using the Partial-fraction decomposition, (D.2) is written as,

$$\Delta\omega_e(s) = \frac{A}{s} + \frac{B}{s+\sigma-j\omega_d} + \frac{C}{s+\sigma+j\omega_d} \tag{D.3}$$

With some mathematical developments,

$$A = \frac{z_1}{\sigma^2+\omega_d^2}$$

$$B = \frac{1}{\sigma^2+\omega_d^2}\left(-\underbrace{\frac{z_1}{2}}_{\Re} - j\underbrace{\frac{z_1\sigma-\sigma^2-\omega_d^2}{2\omega_d}}_{\Im}\right)$$

$$C = \frac{1}{\sigma^2+\omega_d^2}\left(-\underbrace{\frac{z_1}{2}}_{\Re} + j\underbrace{\frac{z_1\sigma-\sigma^2-\omega_d^2}{2\omega_d}}_{\Im}\right)$$

In time domain, (D.3) is expressed as,

$$\Delta\omega_e(t) = \frac{K}{\sigma^2+\omega_d^2}\left(z_1 + Be^{(-\sigma-j\omega_d)t} + Ce^{(-\sigma+j\omega_d)t}\right) \tag{D.4}$$

The simplification of (D.4) yields,

$$\Delta\omega_e(t) = \frac{K}{\sigma^2+\omega_d^2}\left[z_1 + e^{-\sigma t}(2\Re\cos(\omega_d t) - 2\Im\sin(\omega_d t)\right] \tag{D.5}$$

(D.5) can also be written as,

$$\Delta\omega_e(t) = \frac{K}{\sigma^2+\omega_d^2}\left[z_1 + e^{-\sigma t}(z_1\cos(\omega_d t) - \left(\frac{z_1\sigma - \sigma^2 - \omega_d^2}{\omega_d}\right)\sin(\omega_d t)\right] \tag{D.6}$$

The RoCof in (Hz) is given by the following expression,

$$\lim_{t\to 0^+} f_b \frac{\Delta\omega_e(t)}{dt} \tag{D.7}$$

The derivative of (D.6) is obtained in the following,

$$\frac{d\Delta\omega_e}{dt} = \frac{K}{\sigma^2+\omega_d^2} e^{-\sigma t}\left[\left(-\sigma^2 - \omega_d^2\right)\cos\omega_d t + \left(z_1\omega_d + \frac{\sigma}{\omega_d}\left(z_1\sigma - \sigma^2 - \omega_d^2\right)\right)\sin\omega_d t\right] \tag{D.8}$$

From (D.8), the final expression of the RoCoF is obtained,

$$\lim_{t\to 0^+} f_b \frac{\Delta\omega_e(t)}{dt} = f_b K \tag{D.9}$$

Calculation of Frequency Nadir

The frequency Nadir is obtained at T_{peak}, which can be deduced from (D.8),

$$\frac{d\Delta\omega_e}{dt} = 0 \tag{D.10}$$

$$\left(-\sigma^2 - \omega_d^2\right)\cos\omega_d t + \left(z_1\omega_d + \frac{\sigma}{\omega_d}\left(z_1\sigma - \sigma^2 - \omega_d^2\right)\right)\sin\omega_d t = 0 \tag{D.11}$$

From (D.11), T_{peak} is obtained,

$$t = T_{peak} = \frac{1}{\omega_d} a\tan\left(\frac{\sigma^2+\omega_d^2}{z_1\omega_d + \frac{\sigma}{\omega_d}\left(z_1\sigma - \sigma^2 - \omega_d^2\right)}\right) \tag{D.12}$$

The frequency Nadir is obtained by putting (D.12) in (D.6),

$$Nadir = \frac{f_b K}{\sigma^2+\omega_d^2}\left[z_1 + e^{-\sigma t}(z_1\cos\left(\omega_d T_{peak}\right) - \left(\frac{z_1\sigma - \sigma^2 - \omega_d^2}{\omega_d}\right)\sin\left(\omega_d T_{peak}\right)\right] \tag{D.13}$$

Appendix E

Linear State-Space model of “Strategy B” based-VSC

$$x_i = [\underbrace{i_{c_d}\ i_{c_q}\ i_{g_d}\ i_{g_d}\ v_{g_d}\ v_{g_q}}_{x_1}\ \underbrace{\zeta_{PLL}\ \delta_{PLL}\ \omega_m\ \delta_m\ \zeta_{TVR_d}\ \zeta_{TVR_q}}_{x_2}],\quad \Delta u = [v_{e_d}\ v_{e_q}\ p^*\ v_{m_d}\ v_{m_q}]$$

$$A_{11}=\left\{\begin{matrix}
-\frac{R_c\omega_b}{L_c} & \omega_b\omega_0 & 0 & 0 & -\frac{\omega_b}{L_c} & 0 \\
-\omega_b\omega_0 & -\frac{R_c\omega_b}{L_c} & 0 & 0 & 0 & -\frac{\omega_b}{L_c} \\
\frac{\omega_b}{C_D} & 0 & -\frac{\omega_b}{C_D} & 0 & 0 & \omega_b\omega_0 \\
0 & \frac{\omega_b}{C_D} & 0 & -\frac{\omega_b}{C_D} & -\omega_b\omega_0 & 0 \\
0 & 0 & -\frac{R_g\omega_b}{L_g} & \omega_b\omega_0 & \frac{\omega_b}{L_g} & 0 \\
0 & 0 & -\omega_b\omega_0 & -\frac{R_g\omega_b}{L_g} & 0 & \frac{\omega_b}{L_g} \\
0 & 0 & -\sin(\delta_{PLL0}-\delta_{m0})\, Ki_{PLL} & \cos(\delta_{PLL0}-\delta_{m0})\, Ki_{PLL} & 0 & 0 \\
0 & 0 & -\sin(\delta_{PLL0}-\delta_{m0})\, Kp_{PLL}\omega_b & \cos(\delta_{PLL0}-\delta_{m0})\, Kp_{PLL}\omega_b & 0 & 0 \\
\frac{-V_{m0}\omega_c k_i}{\omega_b} & 0 & -\sin(\delta_{PLL0}-\delta_{m0})\, Kp_{PLL}\omega_c & \cos(\delta_{PLL0}-\delta_{m0})\, Kp_{PLL}\omega_c & 0 & 0 \\
0 & 0 & 0 & 0 & 0 & 0 \\
R_V\frac{R_c\omega_b}{L_c} & -R_V\omega_b\omega_0 & 0 & 0 & R_v\frac{\omega_b}{L_c} & 0 \\
R_V\omega_b\omega_0 & R_V\frac{R_c\omega_b}{L_c} & 0 & 0 & 0 & R_v\frac{\omega_b}{L_c}
\end{matrix}\right\}$$

$$A_{12}=\left\{\begin{matrix}
0 & 0 & 0 & 0 & \frac{\omega_b}{L_c} & 0 \\
0 & 0 & 0 & 0 & 0 & \frac{\omega_b}{L_c} \\
0 & 0 & 0 & 0 & 0 & 0 \\
0 & 0 & 0 & 0 & 0 & 0 \\
0 & 0 & 0 & \frac{\omega_b}{L_g}V_e\sin(\delta_{m0}) & 0 & 0 \\
0 & 0 & 0 & \frac{\omega_b}{L_g}V_e\cos(\delta_{m0}) & 0 & 0 \\
0 & -V_{g_{d0}}\cos(\delta_{PLL0}-\delta_{m0})K_{i_{PLL}} & 0 & V_{g_{d0}}\cos(\delta_{PLL0}-\delta_{m0})K_{i_{PLL}} & 0 & 0 \\
\omega_b & -V_{g_{d0}}\cos(\delta_{PLL0}-\delta_{m0})K_{p_{PLL}}\omega_b & 0 & V_{g_{d0}}\cos(\delta_{PLL0}-\delta_{m0})K_{p_{PLL}}\omega_b & 0 & 0 \\
\omega_c & -V_{g_{d0}}\cos(\delta_{PLL0}-\delta_{m0})K_{p_{PLL}}\omega_c & -\omega_c & V_{g_{d0}}\cos(\delta_{PLL0}-\delta_{m0})K_{p_{PLL}}\omega_c & \frac{-I_{c_d}\omega_c k_i}{\omega_b} & \frac{-I_{c_q}\omega_c k_i}{\omega_b} \\
0 & 0 & \omega_b & 0 & 0 & 0 \\
0 & 0 & 0 & 0 & -(\frac{R_V\omega_b}{L_c}+\omega_{TVR}) & 0 \\
0 & 0 & 0 & 0 & 0 & -(\frac{R_V\omega_b}{L_c}+\omega_{TVR})
\end{matrix}\right\}$$

$$B^T=\left\{\begin{matrix}
0 & 0 & 0 & 0 & -\frac{\omega_b}{L_g}\cos(\delta_{m0}) & 0 & 0 & 0 & 0 & 0 & 0 & 0 \\
0 & 0 & 0 & 0 & 0 & \frac{\omega_b}{L_g}\sin(\delta_{m0}) & 0 & 0 & 0 & 0 & 0 & 0 \\
0 & 0 & 0 & 0 & 0 & 0 & 0 & 0 & \omega_c k_i & 0 & 0 & 0 \\
0 & 0 & 0 & 0 & 0 & 0 & 0 & 0 & 0 & 0 & \omega_{TVR} & 0 \\
0 & 0 & 0 & 0 & 0 & 0 & 0 & 0 & 0 & 0 & 0 & 0
\end{matrix}\right\}$$

Appendix F

Inertia and System Inertia

Inertia is basically defined as the resistance of a physical object to a change in its state of motion, such as a change in rotation speed and direction. In simple words, the inertia is a tendency to remain unchanged. In the present power system, the inertia is related to the mechanical part of the generators e.g., rotating masse. The rotation speed of these generators is proportionally related to the frequency. Therefore, the inertia offers a resistance to a change of their rotational speed, which contributes positively to the system synchronism and stability. Hence, inertia is considered as a cornerstone parameter in the current power system operation.

Considering a simple example of a single synchronous generator, the swing equation is expressed as follow:

$$2H\frac{d\omega}{dt} = p_m - p_e \tag{F.1}$$

This equation is expressed in per-unit. H denotes the inertia constant in (s). p_m and p_e are the input mechanical power and the electrical power, respectively.

The inertia constant H is derived from the following formula:

$$H = \frac{\frac{1}{2}J\omega_b^2}{S_b} = \frac{E_k}{S_b} \tag{F.2}$$

with J, S_b, ω_b and E_k are the moment of inertia in (kg.m^2), the rated power in (MVA), the base frequency in (rad/s) and the kinetic energy in (J), respectively.

Based on (F.1), one can remark that H presents the resistance to the frequency change during an imbalance between p_m and p_e.

The principle of inertia presented for a single generator is extendable to a multi-generator system. Indeed, in electrical power system, the frequency of each generator is common in steady the state, whereas, in the transient or during disturbances, the frequency of each generator has its own behavior around the center of inertia (COI). However, thanks to the synchronizing forces between the machines, they finally reach the same speed. Because of this inherent synchronization mechanism, all single generators can be aggregated into a single equivalent machine, with an equivalent swing equation that represents the response of all generators (expressed in per unit):

$$2H_{PS}\frac{d\omega_{COI}}{dt} = p_G - p_L \tag{F.3}$$

with H_{PS} is the equivalent inertia constant of the overall power system. It is also called *system inertia*. It is calculated using the following formula:

$$H_{PS} = \frac{\sum H_i S_{bi}}{S_T} = \frac{E_{k_{PS}}}{S_T} \tag{F.4}$$

S_T is the total generation capacity connected to the system.
ω_{COI} is the frequency at center of inertia. It is expressed as following:

$$\omega_{COI} = \frac{\sum H_i S_{bi} \omega_i}{\sum H_i S_{bi}} \tag{F.5}$$

It is important to mention that the conventional power plants based on synchronous generators are the main source of inertia in the power system, but other sources can participate as well, such as storage systems, synchronous comparators and motor loads.

Appendix G

Linear State-Space model of “Strategy C” based-VSC including LC filter (Cascaded Structure)

$$\Delta x = \left[\underbrace{\Delta e_{g_d}\ \Delta e_{g_q}\ \Delta i_{s_d}\ \Delta i_{s_q}\ \Delta i_{g_d}\ \Delta i_{g_q}}_{LCL\ filter}\ \underbrace{\Delta\delta_m\ \Delta\omega_m\ \Delta p_f\ \Delta\delta e_g}_{Outer\ Control}\ \underbrace{\Delta C_{v_d}\ \Delta C_{v_q}\ \Delta C_{c_d}\ \Delta C_{c_q}}_{Inner\ Controllers}\ \underbrace{\Delta\zeta_{TVR_d}\ \Delta\zeta_{TVR_q}}_{TVR} \right]^T .\ \Delta u = \left[\Delta E_g^*\ \Delta V_e\ \Delta p^* \right]^T$$

$$A = \left\{ \begin{matrix}
0 & \omega_0\omega_b & \frac{\omega_b}{C_f} & 0 & -\frac{\omega_b}{C_f} & 0 & 0 & 0 & 0 & 0 & 0 & 0 & 0 & 0 & 0 & 0 \\
-\omega_0\omega_b & 0 & 0 & \frac{\omega_b}{C_f} & 0 & -\frac{\omega_b}{C_f} & 0 & 0 & 0 & 0 & 0 & 0 & 0 & 0 & 0 & 0 \\
-\frac{\omega_b}{L_f}k_{pc}k_{pv} & -\frac{\omega_b}{L_f}k_{pc}C_f\omega_0 & -\left(\frac{\omega_b}{L_f}k_{pc}+\frac{R_f\omega_b}{L_f}\right) & 0 & \frac{\omega_b}{L_f}k_{pc} & 0 & 0 & 0 & 0 & \frac{\omega_b}{L_f}k_{pc}k_{pv} & \frac{\omega_b}{L_f}k_{pc}k_{i_v} & 0 & \frac{\omega_b}{L_f}k_{ic} & 0 & \frac{\omega_b}{L_f}k_{pc}k_{pv} & 0 \\
\frac{\omega_b}{L_f}k_{pc}C_f\omega_0 & -\frac{\omega_b}{L_f}k_{pc}k_{pv} & 0 & -\left(\frac{\omega_b}{L_f}k_{pc}+\frac{R_f\omega_b}{L_f}\right) & 0 & \frac{\omega_b}{L_f}k_{pc} & 0 & 0 & 0 & 0 & 0 & \frac{\omega_b}{L_f}k_{pc}k_{i_v} & 0 & \frac{\omega_b}{L_f}k_{ic} & 0 & \frac{\omega_b}{L_f}k_{pc}k_{pv} \\
\frac{\omega_b}{L_C+L_g} & 0 & 0 & 0 & -\frac{(R_c+R_g)\omega_b}{L_C+L_g} & \omega_0\omega_b & \frac{V_e sin\delta_{m0}\omega_b}{L_C+L_g} & 0 & 0 & 0 & 0 & 0 & 0 & 0 & 0 & 0 \\
0 & \frac{\omega_b}{L_C+L_g} & 0 & 0 & -\omega_0\omega_b & -\frac{(R_c+R_g)\omega_b}{L_C+L_g} & \frac{V_e cos\delta_{m0}\omega_b}{L_C+L_g} & 0 & 0 & 0 & 0 & 0 & 0 & 0 & 0 & 0 \\
0 & 0 & 0 & 0 & 0 & 0 & 0 & \omega_b & 0 & 0 & 0 & 0 & 0 & 0 & 0 & 0 \\
0 & 0 & 0 & 0 & 0 & 0 & 0 & -\omega_c & -\frac{k_i}{\omega_b}\omega_c & 0 & 0 & 0 & 0 & 0 & 0 & 0 \\
\frac{I_{gd_0}}{T_2}-\frac{T_1 I_{gq_0}}{T_2}\omega_0\omega_b+\frac{T_1 E_{gd_0}}{T_2}\frac{\omega_b}{L_C+L_g} & \frac{I_{gq_0}}{T_2}+\frac{T_1 I_{gd_0}}{T_2}\omega_0\omega_b & \frac{T_1 I_{gd_0}}{T_2}\frac{\omega_b}{C_f} & \frac{T_1 I_{gq_0}}{T_2}\frac{\omega_b}{C_f} & \frac{E_{gd_0}}{T_2}-\frac{\omega_b}{C_f}\frac{T_1 I_{gd_0}}{T_2}-\frac{(R_c+R_g)\omega_b}{L_C+L_g}\frac{T_1 E_{gd_0}}{T_2} & -\frac{T_1 I_{gq_0}}{T_2}\frac{\omega_b}{C_f}+\omega_0\omega_b\frac{T_1 E_{gd_0}}{T_2} & \frac{V_e sin\delta_{m0}\omega_b}{L_C+L_g}\frac{T_1 E_{gd_0}}{T_2} & 0 & -\frac{1}{T_2} & 0 & 0 & 0 & 0 & 0 & 0 & 0 \\
\frac{n_q I_{gq_0}}{T_Q} & -\frac{n_q I_{gd_0}}{T_Q} & 0 & 0 & 0 & \frac{n_q E_{gd_0}}{T_Q} & 0 & 0 & 0 & -\frac{1}{T_Q} & 0 & 0 & 0 & 0 & 0 & 0 \\
-1 & 0 & 0 & 0 & 0 & 0 & 0 & 0 & 0 & 1 & 0 & 0 & 0 & 0 & 1 & 0 \\
0 & -1 & 0 & 0 & 0 & 0 & 0 & 0 & 0 & 0 & 0 & 0 & 0 & 0 & 0 & 1 \\
-k_{pv} & -C_f\omega_0 & -1 & 0 & 1 & 0 & 0 & 0 & 0 & k_{p_v} & k_{i_v} & 0 & 0 & 0 & k_{p_v} & 0 \\
C_f\omega_0 & -k_{pv} & 0 & -1 & 0 & 1 & 0 & 0 & 0 & 0 & 0 & 0 & 0 & 0 & 0 & k_{p_v} \\
-\frac{R_V\omega_b}{L_C+L_g} & 0 & 0 & 0 & \frac{R_v(R_c+R_g)\omega_b}{L_C+L_g} & -R_v\omega_0\omega_b & -\frac{R_v V_e sin\delta_{m0}\omega_b}{L_C+L_g} & 0 & 0 & 0 & 0 & 0 & 0 & 0 & -\omega_{TVR} & 0 \\
0 & -\frac{R_V\omega_b}{L_C+L_g} & 0 & 0 & R_v\omega_0\omega_b & \frac{R_v(R_c+R_g)\omega_b}{L_C+L_g} & -\frac{R_v V_e cos\delta_{m0}\omega_b}{L_C+L_g} & 0 & 0 & 0 & 0 & 0 & 0 & 0 & 0 & -\omega_{TVR}
\end{matrix} \right\}$$

$$B = \left\{ \begin{matrix}
0 & 0 & 0 & 0 & 0 & 0 & 0 & 0 & 0 & 0 & 0 & 0 & 0 & 0 & \omega_{TVR} & 0 \\
0 & 0 & 0 & 0 & -\frac{cos\delta_{m0}\omega_b}{L_C+L_g} & \frac{sin\delta_{m0}\omega_b}{L_C+L_g} & 0 & 0 & \frac{T_1 E_{gd_0}}{T_2}\frac{cos\delta_{m0}\omega_b}{L_C+L_g} & 0 & 0 & 0 & 0 & 0 & 0 & 0 \\
0 & 0 & 0 & 0 & 0 & 0 & 0 & \frac{k_i}{\omega_b}\omega_c & 0 & 0 & 0 & 0 & 0 & 0 & 0 & 0
\end{matrix} \right\}$$

Appendix H

Linear State-Space model of “Strategy C” based-VSC including LC filter (Direct Structure)

$$\Delta x = \left[\underbrace{\Delta e_{g_d}\ \Delta e_{g_q}\ \Delta i_{s_d}\ \Delta i_{s_q}\ \Delta i_{g_d}\ \Delta i_{g_q}}_{LCL\ Filter}\ \underbrace{\Delta\delta_m\ \Delta\omega_m\ \Delta p_f\ \Delta\delta e_g}_{Outer\ Control}\ \underbrace{\Delta\zeta_{TVR_d}\ \Delta\zeta_{TVR_q}}_{TVR} \right]^T \quad \Delta u = \left[\Delta E_g^*\ \Delta V_e\ \Delta p^* \right]^T$$

$$A = \left\{ \begin{matrix}
0 & \omega_0\omega_b & \frac{\omega_b}{C_f} & 0 & -\frac{\omega_b}{C_f} & 0 & 0 & 0 & 0 & 0 & 0 & 0 \\
-\omega_0\omega_b & 0 & 0 & \frac{\omega_b}{C_f} & 0 & -\frac{\omega_b}{C_f} & 0 & 0 & 0 & 0 & 0 & 0 \\
-\frac{\omega_b}{L_f} & 0 & R_{LCL_D}\frac{\omega_b}{L_f} & 0 & -R_{LCL_D}\frac{\omega_b}{L_f} & 0 & 0 & 0 & 0 & \frac{\omega_b}{L_f} & \frac{\omega_b}{L_f} & 0 \\
0 & -\frac{\omega_b}{L_f} & 0 & R_{LCL_D}\frac{\omega_b}{L_f} & 0 & -R_{LCL_D}\frac{\omega_b}{L_f} & 0 & 0 & 0 & 0 & 0 & \frac{\omega_b}{L_f} \\
\frac{\omega_b}{L_C+L_g} & 0 & 0 & 0 & -\frac{(R_c+R_g)\omega_b}{L_C+L_g} & \omega_0\omega_b & \frac{V_e sin\delta_{m0}\omega_b}{L_C+L_g} & 0 & 0 & 0 & 0 & 0 \\
0 & \frac{\omega_b}{L_C+L_g} & 0 & 0 & -\omega_0\omega_b & -\frac{(R_c+R_g)\omega_b}{L_C+L_g} & \frac{V_e cos\delta_{m0}\omega_b}{L_C+L_g} & 0 & 0 & 0 & 0 & 0 \\
0 & 0 & 0 & 0 & 0 & 0 & 0 & \omega_b & 0 & 0 & 0 & 0 \\
0 & 0 & 0 & 0 & 0 & 0 & 0 & -\omega_c & -\frac{k_i}{\omega_b}\omega_c & 0 & 0 & 0 \\
\frac{I_{gd_0}}{T_2}-\frac{T_1 I_{gq_0}}{T_2}\omega_0\omega_b+\frac{T_1 E_{gd_0}}{T_2}\frac{\omega_b}{L_C+L_g} & \frac{I_{gq_0}}{T_2}+\frac{T_1 I_{gd_0}}{T_2}\omega_0\omega_b & \frac{T_1 I_{gd_0}}{T_2}\frac{\omega_b}{C_f} & \frac{T_1 I_{gq_0}}{T_2}\frac{\omega_b}{C_f} & \frac{E_{gd_0}}{T_2}-\frac{\omega_b}{C_f}\frac{T_1 I_{gd_0}}{T_2}-\frac{(R_c+R_g)\omega_b}{L_C+L_g}\frac{T_1 E_{gd_0}}{T_2} & -\frac{T_1 I_{gq_0}}{T_2}\frac{\omega_b}{C_f}+\omega_0\omega_b\frac{T_1 E_{gd_0}}{T_2} & \frac{V_e sin\delta_{m0}\omega_b}{L_C+L_g}\frac{T_1 E_{gd_0}}{T_2} & 0 & -\frac{1}{T_2} & 0 & 0 & 0 \\
\frac{n_q I_{gq_0}}{T_Q} & -\frac{n_q I_{gd_0}}{T_Q} & 0 & 0 & 0 & \frac{n_q E_{gd_0}}{T_Q} & 0 & 0 & 0 & -\frac{1}{T_Q} & 0 & 0 \\
-\frac{R_V\omega_b}{L_C+L_g} & 0 & 0 & 0 & \frac{R_v(R_c+R_g)\omega_b}{L_C+L_g} & -R_v\omega_0\omega_b & -\frac{R_v V_e sin\delta_{m0}\omega_b}{L_C+L_g} & 0 & 0 & 0 & -\omega_{TVR} & 0 \\
0 & -\frac{R_V\omega_b}{L_C+L_g} & 0 & 0 & R_v\omega_0\omega_b & \frac{R_v(R_c+R_g)\omega_b}{L_C+L_g} & -\frac{R_v V_e cos\delta_{m0}\omega_b}{L_C+L_g} & 0 & 0 & 0 & 0 & -\omega_{TVR}
\end{matrix} \right\}$$

$$\mathrm{B} = \left\{ \begin{matrix}
0 & 0 & 0 & 0 & 0 & 0 & 0 & 0 & 0 & 0 & \omega_{TVR} & 0 \\
0 & 0 & 0 & 0 & -\frac{cos\delta_{m0}\omega_b}{L_C+L_g} & \frac{sin\delta_{m0}\omega_b}{L_C+L_g} & 0 & 0 & \frac{T_1 E_{gd_0}}{T_2}\frac{cos\delta_{m0}\omega_b}{L_C+L_g} & 0 & 0 & 0 \\
0 & 0 & 0 & 0 & 0 & 0 & 0 & \frac{k_i}{\omega_b}\omega_c & 0 & 0 & 0 & 0
\end{matrix} \right\}$$

Appendix I

RTS Subsystems

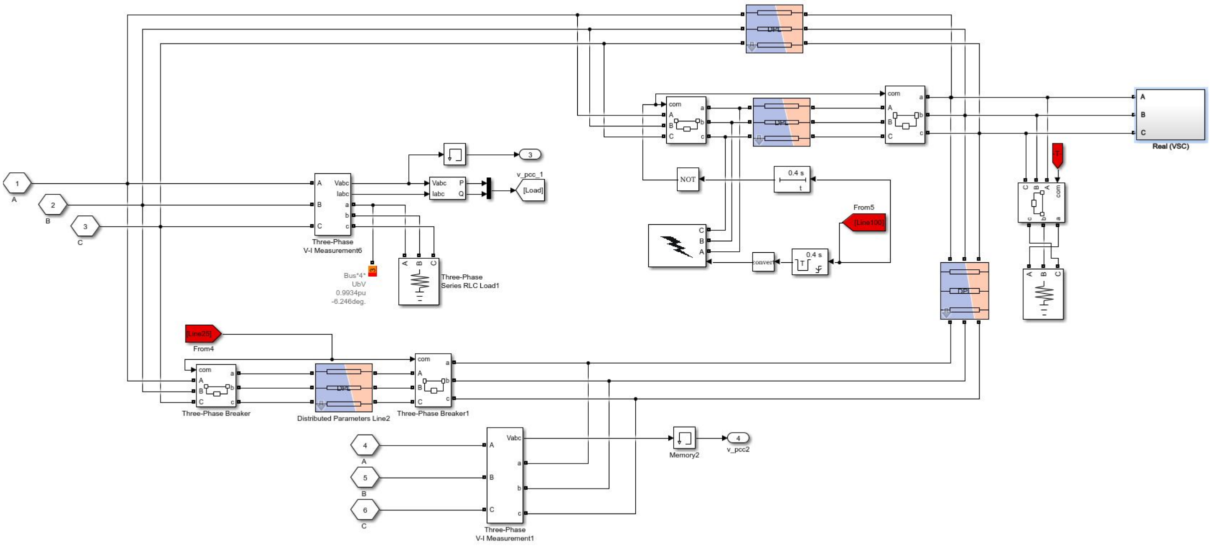

Figure I.1 - SM_MIGRATE

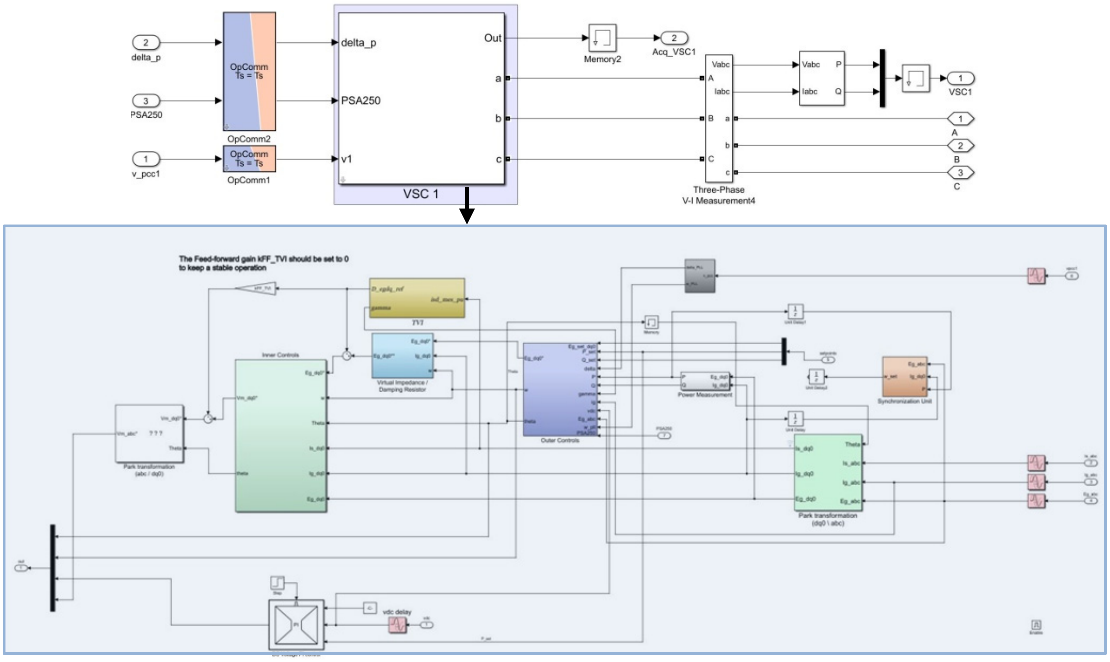

Figure I.2 - SM_C and SM_control

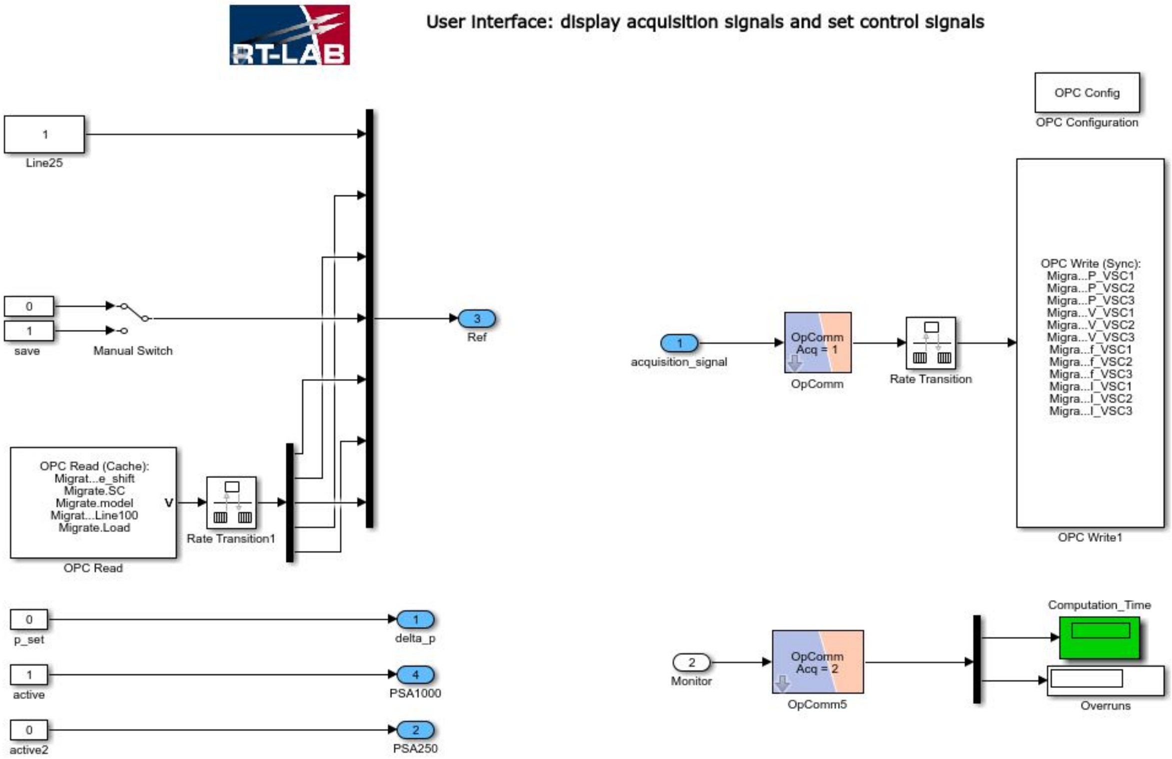

Figure I.3 - SC_user_interface

Résumé étendu en français

Introduction aux réseaux électriques basés sur 100% d’électronique de puissance

Contexte & motivation

Vers un réseau électrique 100% renouvelable: La transition vers un système énergétique basé sur les énergies renouvelables est déjà en cours. La dernière décennie a vu le coût de l'énergie renouvelable baisser continuellement, ce qui la rend compétitive par rapport à l'énergie conventionnelle dans de nombreuses régions du monde. Depuis 2009, les prix des modules solaires photovoltaïques (PV) ont chuté d'environ 80%, tandis que les prix des éoliennes ont baissé de 30 à 40%, ce qui rend la rentabilité des énergies renouvelables plus forte que jamais (IRENA, 2017) [1]. Les avantages les plus cruciaux de la transition vers un système d'énergie 100% renouvelable sont la forte réduction des émissions de gaz à effet de serre (GES) qui en résulte. Pour atteindre la limite de réchauffement climatique, le GIEC (Groupe d'experts intergouvernemental sur l'évolution du climat) souligne la nécessité d'une transition énergétique rapide basée sur une augmentation significative des énergies renouvelables (GIEC, 2018). Plusieurs pays sont déjà sur le point d'atteindre cet objectif. L'Islande, par exemple, fournit 100% de ses besoins en électricité par la géothermie ou l'hydroélectricité. La Norvège (97%), le Costa Rica (93%), le Brésil (76%) et le Canada (62%) sont d'autres pays qui ont des réseaux électriques avec des fractions élevées d'énergies renouvelables basées sur l'hydroélectricité. Les centrales hydroélectriques sont utilisées depuis des décennies pour créer une énergie renouvelable relativement peu coûteuse, mais ces systèmes sont limités par les précipitations naturelles et la topologie géographique. Dans de nombreux pays, la plupart des bons sites pour les grandes ressources hydroélectriques ont déjà été développés, ce qui nécessite une transition vers des sources d'énergie renouvelable intermittente (IRES) (c'est-à-dire des systèmes éoliens et solaires photovoltaïques). Des pays comme le Danemark, l'Irlande et l'Allemagne ont massivement installé des systèmes d'énergie renouvelable intermittente et fonctionnent avec des taux de pénétration annuels de plus de 20% au niveau national [2]. Certains scénarios de l'Association européenne de l'énergie éolienne montrent qu'au cours des dix prochaines années, l'énergie éolienne pourrait satisfaire un cinquième de la demande d'électricité en Europe d'ici 2020, un tiers d'ici 2030 et la moitié d'ici 2050 [3] - [5].

Un certain nombre d'études ont exclu les technologies nucléaires pour déterminer si les systèmes électriques pouvaient s'appuyer à 100% sur des sources d'énergie renouvelables, comme celles du Danemark, des Pays-Bas, de l'Allemagne, de la France, de l'Irlande et du Portugal [6] - [10]. Bien que les premières tendances n'indiquent pas la faisabilité d'une énergie 100% renouvelable, en raison de la production intermittente des sources d'énergie, cependant, la demande résiduelle non fournie par l'IRES peut être compensée par l'une des technologies de production dispatchable, des systèmes de stockage ou de l’inertie stockée dans la partie mécanique des éoliennes.

Un système électrique avec 100% d'énergie renouvelable intermittente est encore un sujet à investiguer. Néanmoins, un scénario avec une zone du système électrique actuel alimenté occasionnellement avec seulement des sources renouvelables intermittentes est de forte probabilité. En fait, étant donné que les générations éolienne et photovoltaïque sont concentrées là où il y a plus de vent et de soleil, une grande partie du système de transmission d'énergie peut perdre la dernière liaison synchrone le reliant au reste du système comme l'illustre la Figure 1. Dans telle situation, les gestionnaires de réseau de transport doivent adapter leur pratique pour faire fonctionner le système en îloté sans générateur synchrone et avec une fiabilité suffisante.

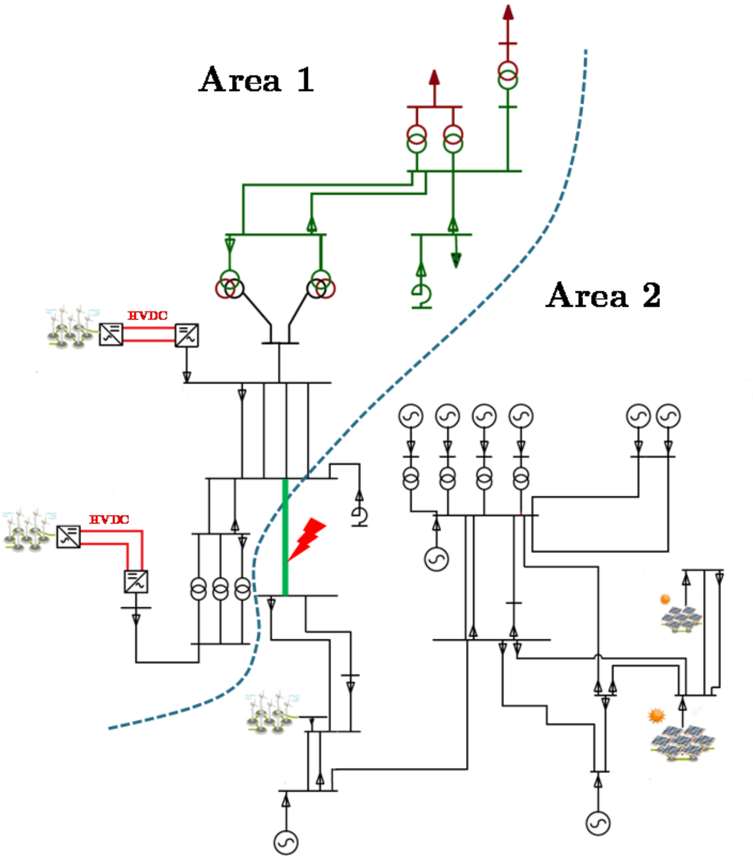

Figure 1 - Représentation du système électrique actuel perdant sa dernière liaison synchrone

Hormis les enjeux liés à la source d'énergie primaire, la gestion de cette énergie elle-même reste un enjeu majeur et où l'électronique de puissance joue un rôle fondamental.

Systèmes électriques et convertisseurs d’électronique de puissance: Les convertisseurs d’électronique de puissance ont été développés pendant des décennies avec de nombreux types d'applications. L'une des premières applications est l'entraînement de machines électriques principalement utilisées pour des applications industrielles. Le début de l'histoire des énergies renouvelables a eu une influence modérée sur le marché des convertisseurs d’électronique de puissance. Très vite, le raccordement des éoliennes et du photovoltaïque via des convertisseurs d’électronique de puissance devient obligatoire. En outre, de nouvelles liaisons de transmission ont dû être établies afin de transporter l'énergie renouvelable de la zone où elle est produite vers la zone où elle est consommée. Une autre raison est l'incitation du marché. En Europe, ENTSO-E, le réseau européen des GRT de l’électricité, planifie le futur réseau avec le plan décennal de développement du réseau (TYNDP) [11], où de nombreuses nouvelles liaisons HVDC sont mentionnées comme indiqué dans la Figure 2.

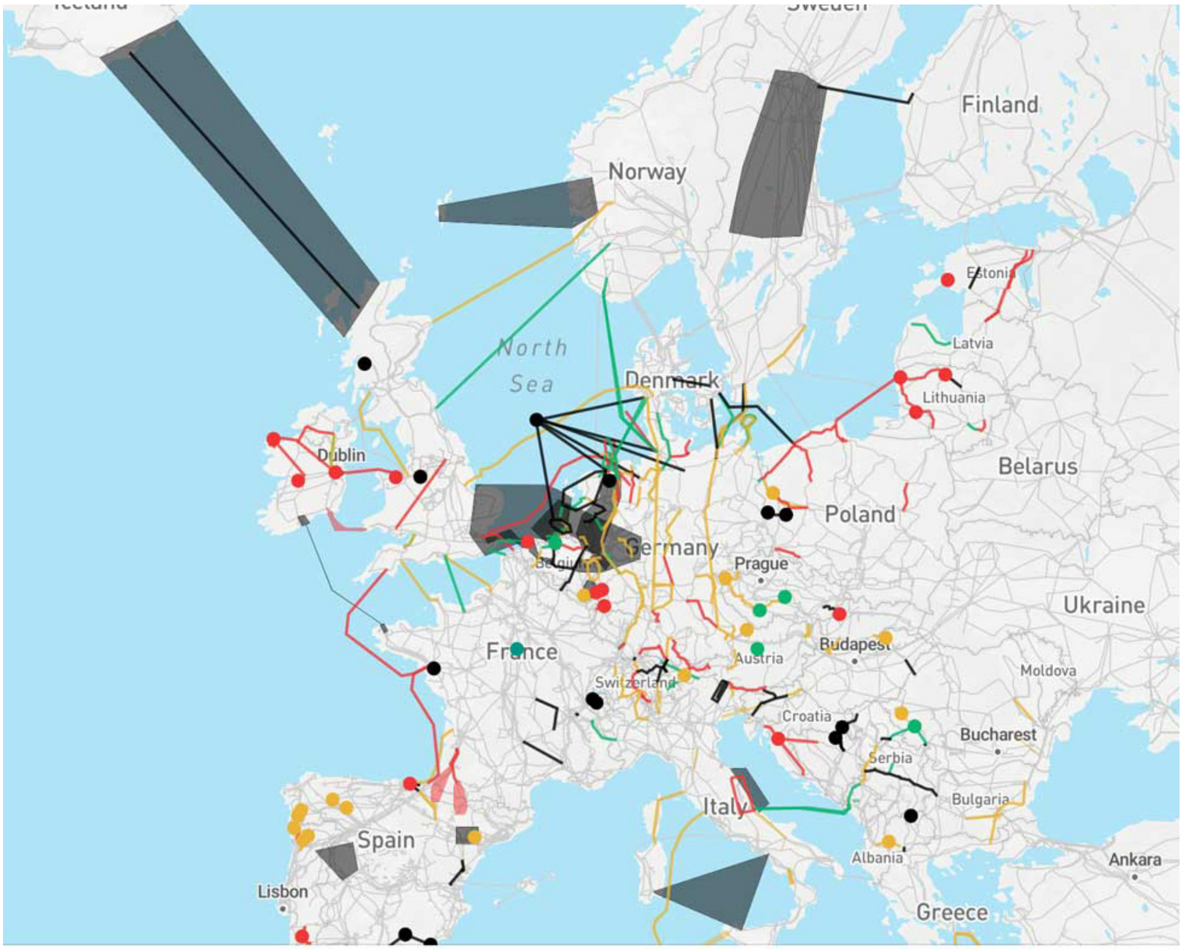

Figure 2 – Liaisons HVDC en Europe

Ces facteurs (c'est-à-dire l'augmentation des IRES et des liaisons HVDC) se traduisent par une augmentation significative des convertisseurs d’électronique de puissance dans le système électrique actuel. Deux types de topologies de convertisseurs de puissance existent dans le système électrique actuel: le convertisseur en source de tension (VSC) basé sur la technologie des transistors et le convertisseur en source de courant (CSC) basé sur la technologie des thyristors, également appelé convertisseurs commutés par la ligne (LCC). En effet, avant d'utiliser des transistors pour l'entraînement de moteur à courant continu ou synchrone, les convertisseurs de puissance à thyristors étaient connectés à une source de courant. En raison du mode de fonctionnement des thyristors, le mode de fonctionnement de la source de courant était obligatoire. Lors du passage à des convertisseurs de puissance à transistor, les deux choix étaient possible, c'est-à-dire la source de courant ou la source de tension. Ce choix a eu une influence sur le type d'interrupteurs, un CSC est censé utiliser un interrupteur composé d'un transistor en série avec une diode, alors que le VSC a besoin d'un transistor en parallèle avec une diode comme le montre la Figure 3.

Dans le cas d'un CSC, les deux interrupteurs en série induisent plus de pertes que dans le cas d'un VSC. Le VSC a été donc choisi pour son efficacité et parce qu'il est plus facile de gérer une source de tension avec un condensateur qu'une source de courant avec une inductance.

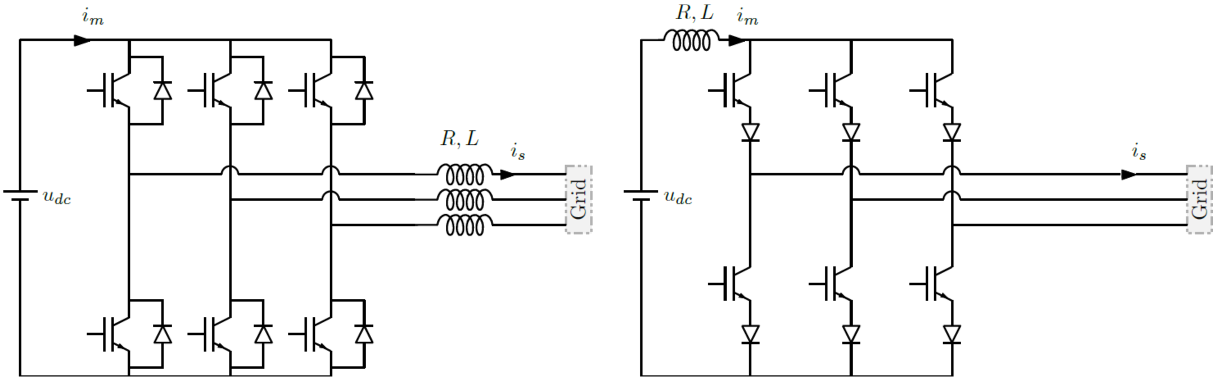

Figure 3 – VSC vs CSC

Un convertisseur est toujours un double modulateur des grandeurs électriques. Dans le cas d'un VSC, la tension du bus DC est modulée pour générer un ensemble de trois tensions côté AC, mais en même temps, les courants AC du réseau sont modulés pour générer le courant DC. Ainsi, cette topologie pourrait être appelée «convertisseur en source de tension continue» ou «convertisseur en source de courant alternatif». La modulation est intrinsèquement symétrique. Cependant, dans les applications pratiques, une seule modulation est utilisée, c'est-à-dire la modulation de tension pour contrôler les courants alternatifs. C'est la raison pour laquelle ce convertisseur est appelé «convertisseur en source de tension».

Pour les applications hautes puissances, la tension du bus DC est limitée par la technologie des câbles. Pendant plusieurs années, la tension nominale du câble DC a dû être fixée à 320 kV entre un pôle et la terre. Désormais, de nouveaux projets sont attendus avec une tension plus élevée de 400 kV à 525 kV. Dans tous les cas, cette tension est censée mettre des centaines de transistors en série. La commutation de centaines de transistors en même temps est extrêmement difficile [12], le concept d'un convertisseur modulaire multiniveau (VSC-MMC) est une solution à ce problème. Il se repose sur une connexion en série de sous-modules élémentaires, qui ne commutent pas en même temps. Les sous-modules peuvent utiliser des topologies demi-pont, pont complet ou hybride [13].

Une pile de N-sous-modules est appelée un demi-bras. Chaque demi-bras est connecté à une inductance dont le but est de limiter la dérivée du courant en cas de défaut DC. Chaque phase comprend deux demi-bras identiques. L'un est connecté au pôle positif du bus DC et l'autre est connecté au pôle négatif du bus DC. Le MMC est composé de trois bras (voir Figure 4). La connexion en série de centaines de sous-modules élémentaires se traduit par une forme d'onde de tension modulée quasi-sinusoïdale comme le montre la Figure 4.

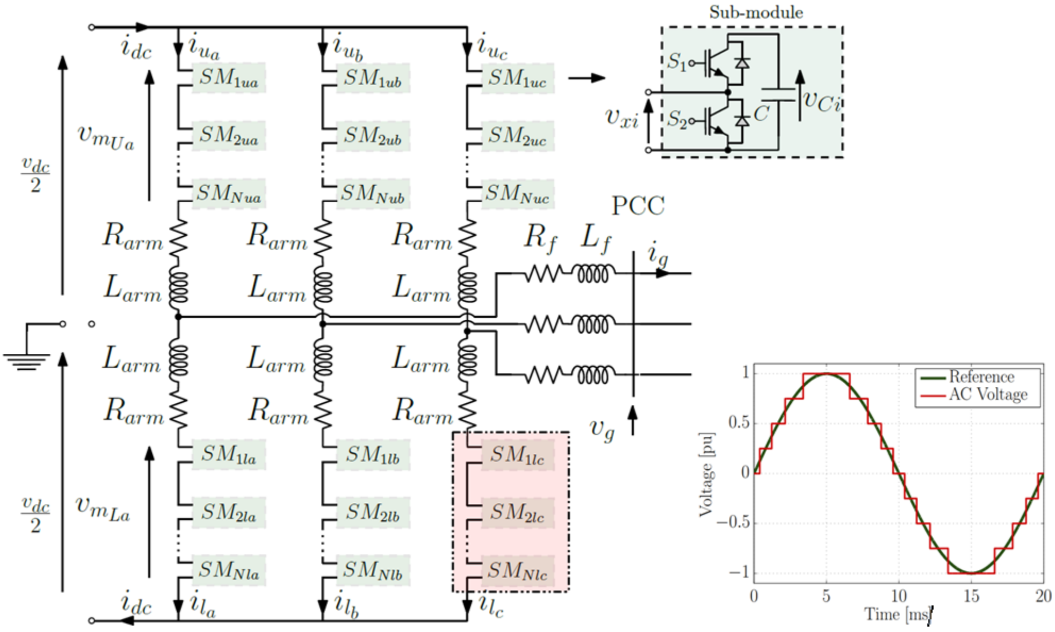

Figure 4 – MMC

Gestion du contrôle des convertisseurs d'électronique de puissance: Lorsque la puissance injectée par ces convertisseurs de puissance n'est pas négligeable par rapport à la puissance nominale du système au PCC, les grandeurs du réseau peuvent être significativement affectées. Par conséquence, les convertisseurs de puissance ne peuvent pas être considérés comme de simples appareils connectés au réseau, mais ils participeront activement au soutien du réseau et affecteront sa stabilité. Il est donc important de surveiller les convertisseurs de puissance connectés au réseau en estimant leurs états (par exemple, angle, tension…), et également de gérer leur échange d'énergie. L'objectif fondamental des convertisseurs de puissance est d'injecter l'énergie éolienne et solaire ou projetée sur des liaisons HVDC au réseau. Cet objectif est atteint grâce à une gestion de contrôle adéquate, c'est-à-dire que les convertisseurs de puissance doivent d'abord être synchronisés avec le réseau principal, puis injecter l'énergie. Le but de l'étage de synchronisation du réseau est de déterminer la phase de la tension du réseau pour contrôler l'échange de puissance entre les systèmes AC et DC, puis, la dynamique de la puissance échangée est spécifiée par un étage de contrôle de puissance. Au finale, des algorithmes efficaces de synchronisation au réseau en plus d'une gestion de puissance adéquate sont des facteurs clés déterminant la qualité complète de la structure de contrôle.

Contrôle Conventionnel Grid-following: Aujourd'hui, les convertisseurs de puissance sont contrôlés sous l’hypothèse qu'une tension alternative avec une amplitude et une fréquence données est maintenue à leurs bornes qu'ils peuvent simplement suivre pour injecter une puissance contrôlée. En pratique, cela se traduit par l'hypothèse que le système alternatif est dominé par des générateurs synchrones formant la tension alternative instantanée. Cette stratégie de contrôle est bien connue sous le nom grid-following. Si une partie du réseau AC dominée par les sources d'énergie renouvelables est déconnectée du réseau AC principal en raison d'un défaut ou d'un déclenchement de ligne, cela entraînera une perte de synchronisme en raison de l'absence d’une tension alternative à suivre.

Une autre conséquence de l'augmentation de la proportion de convertisseurs à base de grid-following est la diminution de l'inertie totale du réseau [14], qui induit une réponse dynamique plus rapide de la fréquence [15]. Le phénomène de faible inertie a déjà été remarqué dans plusieurs régions, comme l'Irlande et le Royaume-Uni. Plus de détails sur ces données sont publiés par ENTSO-E [16]. En fait, un concept «d'inertie synthétique» a été proposé pour les convertisseurs grid-following. Cependant, en raison du retard d'estimation de fréquence et du temps de réponse de la commande, ce concept n'est pas aussi efficace qu'une inertie réelle pour limiter la dérivée de fréquence [17]. De plus, comme le contrôle d'inertie synthétique utilise la dérivée de fréquence pour émuler l'effet d'inertie, cela induit plus de bruit qui peut perturber le fonctionnement du système et mettre en danger la stabilité du système.

Une autre limitation des convertisseurs grid-following est leur incapacité à fonctionner correctement dans des conditions de réseau faibles et en particulier à répondre aux exigences (FRT) [18]. En fait, les grands parcs éoliens sont généralement situés dans des zones éloignées de la zone où la puissance est consommée. Les systèmes de transmission à haute tension qui ont de longues distances de transmission sont utilisés pour fournir de l'énergie éolienne au réseau principal. Les longues lignes ou câbles de transmission se traduisent par une impédance de réseau élevée, et par conséquent, un réseau AC faible. De nombreuses études montrent que le fonctionnement des convertisseurs grid-following est limité et très sensible dans des conditions de réseau faibles. Résultat, un fonctionnement acceptable avec les performances souhaitées ne peut être garanti. [19]. De plus, en cas de défaut, le grid-code impose une injection complète de courant réactif pour supporter la tension du réseau. Cependant, dans le cas d'une plate-forme d'éoliennes en îloté, où aucune puissance réactive n'est requise, ce n'est peut-être pas le bon choix. Pour toutes ces raisons et pour éviter plusieurs limitations du contrôle grid-following, certains pays comme l'Irlande ont fait le choix de limiter à 60% l'intégration des convertisseurs grid-following dans leur réseau [20], [21].
Pour anticiper et se préparer à ces défis, la manière de contrôler les convertisseurs de puissance doit être modifiée afin de répondre aux besoins du système comme avec une machine synchrone.

Convertisseurs d’électronique de puissance et les besoins du système électrique: Les besoins du système électrique listés dans le tableau 1 ont été garantis jusqu'à présent grâce aux caractéristiques physiques des SGs. Par exemple, les SGs ont une inertie en raison de leur masse rotative qui compense le déséquilibre de puissance pendant les transitoires. Les convertisseurs de puissance n'en ont pas et nécessitent donc des systèmes de stockage avec des lois de contrôle adéquates. Un autre exemple est la capacité de surintensité qui est plus grande pour SGs que pour les convertisseurs d’électronique de puissance. En fait, les composants semi-conducteurs pourraient être surdimensionnés pour faire face aux problèmes de surintensité. Cependant, cela engendre un coût et un poids supplémentaires, ce qui rend l'installation des convertisseurs de puissance moins avantageuse. De plus, les convertisseurs de puissance sont actuellement contrôlés en tant que sources de courant. Ils n'imposent pas leur propre tension comme la SG. Par conséquent, ils ne peuvent pas fonctionner en mode autonome.

Tableau 1 - Besoins du système électrique [20]

Service	Fonctionnalités technique	Conditions
Transport d'énergie électrique sur ligne AC	Injection de courants sinusoïdaux triphasés	$\omega_{min} < \omega < \omega_{max}$
Connexion de charge parallèle	Contrôle des tensions RMS des nœuds du réseau	$V_{min} < V(i) < V_{max}$
Sécurité du système	Partage de charge entre générateurs parallèles	$\sum P_{gen}(i) = P_{load}$
Sécurité matérielle	Limitation de surintensité	$I_{gen}(i) < I_{max}$

Dans un futur proche, les convertisseurs de puissance domineront le système AC et remplaceront les SGs. Ainsi, il leur est demandé d'imposer une tension alternative instantanée à leurs bornes, tout en répondant aux mêmes exigences du réseau de transport que les SGs classiques. Cette capacité des convertisseurs de puissance est connue sous le nom «Grid-forming» qui nécessite un changement dans la façon dont les convertisseurs sont contrôlés aujourd'hui.

État de l'art: du Grid-following au Grid-forming

ENTSO-E travaille actuellement sur une nouvelle version du grid-code qui intégrera la notion des convertisseurs grid-forming. Un groupe de travail a déjà publié un rapport technique intitulé «*High Penetration of Power Electronic Interfaced Power Sources and the Potential Contribution of Grid-Forming Converters*» sur ce sujet.

En se référant à la littérature, pour que les convertisseurs de puissance aient une capacité grid-forming, un procédé de contrôle de statisme (droop control) également appelé contrôle de statisme inverse (inverse droop control) pour la synchronisation [22] et la régulation de puissance a été proposée pour imiter les caractéristiques de fonctionnement parallèle des SGs. Il a été proposé à l'origine dans [23] pour les systèmes d'alimentation UPS, et a été développé dans une approche générale pour les convertisseurs parallèles [24], en particulier dans les systèmes Microgrid [25] - [31] et UPS [32], [33]. Par la suite, plusieurs variantes de « droop » ont été proposées pour améliorer la dynamique du système [34] et pour être appliquées dans des réseaux basse tension, dans lesquels l'impédance de ligne est plus résistive [35]. De plus, une méthode virtuelle fréquence-tension est proposée pour résoudre ce problème dans n'importe quelle condition donnée de rapport R/X d'impédance de ligne [36]. D'autre part, le droop control peut encore être appliqué dans les réseaux BT en ajoutant une impédance de sortie virtuelle pour rendre l'impédance de ligne totale plus inductive [37] - [39], pour améliorer la dynamique de puissance active et pour assurer un découplage entre la puissance active et la puissance réactive [40]. De plus, il a également été démontré que l'optimisation du coefficient de gain droop [41] peut aider à améliorer la stabilité du système. Contrairement aux commandes secondaires et tertiaires qui nécessitent des signaux de communication d'un contrôleur central [42] [43] [44], la commande primaire droop control permet un partage de puissance en fonctionnement parallèle uniquement basé sur des mesures locales et sans communication.

Malgré les avantages des stratégies de droop, ils n'ont toujours pas de capacité d'émulation d'inertie, ce qui limite leur applicabilité aux systèmes électriques à petite échelle. Un filtre passe-bas est ajouté pour le droop et permet d'émuler l'effet inertiel [45] - [47] de la même manière qu'une SG. Cependant, cela donne un comportement oscillatoire du système [46]. Par conséquent, une autre solution prometteuse qui remplace la commande droop conventionnelle a été proposée pour imiter non seulement les caractéristiques de régime permanent des SGs, mais également leurs caractéristiques transitoires. Différentes implémentations ont été proposées dans la littérature comme Virtual Synchronous Generator (VSG) [47], [47] - [49], Synchronverter [50] - [54], Virtual Synchronous Machine (VSM) [27], [45], [55] - [59] et VISMA [60], mais tous adoptent l'idée de contrôler le convertisseur pour imiter une SG réel en utilisant ses modèles correspondants. De cette manière, un convertisseur fonctionne de manière équivalente à une SG, notamment en termes de réponse d'inertie [61], [62]. Par conséquent, la VSG peut jouer un rôle important dans les systèmes électriques avec plus d’électronique de puissance à l'avenir. Dans des travaux récents, il est rapporté qu'une unité lead-lag supplémentaire permet au contrôle droop conventionnel de contribuer à l'inertie totale du système et d'améliorer l'amortissement du système [46], [47], et de le rendre mathématiquement équivalent au VSG [46]. Cependant, cette analogie n'est vraie que sous de nombreuses hypothèses qui n'ont pas été discutées dans la littérature.

Outre le VSG et le contrôle de statisme, d'autres lois de contrôle permettant la capacité grid-forming ont été proposées: Virtual Oscillator (VOC) [63] - [68], Matching Control [10] et Inducverter [69]. Il a été prouvé que le VOC est équivaut à un contrôle droop conventionnel [64], [65], [70]. Cependant, cette commande peut être plus avantageuse en cas de déséquilibre et de distorsion de tension du fait de sa caractéristique non linéaire [64], [68]. Le Matching control est une autre façon d'émuler la SG, en créant à travers la commande, un lien entre le bus DC et la fréquence, où le moment d'inertie sera équivalent a la capacité du condensateur et la tension DC sera équivalente à la vitesse de rotation. Cette technique contrôle la fréquence grâce à la variation de la tension continue. Par conséquent, la commande du côté DC avec un contrôleur proportionnel est obligatoire. Grâce à la liaison entre le bus DC et la fréquence, la capacité de partage de charge peut être obtenue de manière similaire à la commande de statisme conventionnelle, où le gain de fréquence est équivalent au gain du contrôleur proportionnel. Le principal inconvénient d'un tel contrôleur réside dans les fonctionnalités tout-en-un, c'est-à-dire (tension continue, contrôle de la fréquence du réseau, partage de puissance et contrôle de la puissance active) gérées avec un seul degré de liberté. Le dernier algorithme, l'Inducverter, fait référence à l'émulation des caractéristiques de la machine à induction, où les convertisseurs peuvent être synchronisés avec le réseau principal sans tenir compte de sa fréquence initiale. Cependant, l'émulation de ce contrôle peut entraîner des problèmes numériques dus à l'action dérivée dans le modèle de la machine.

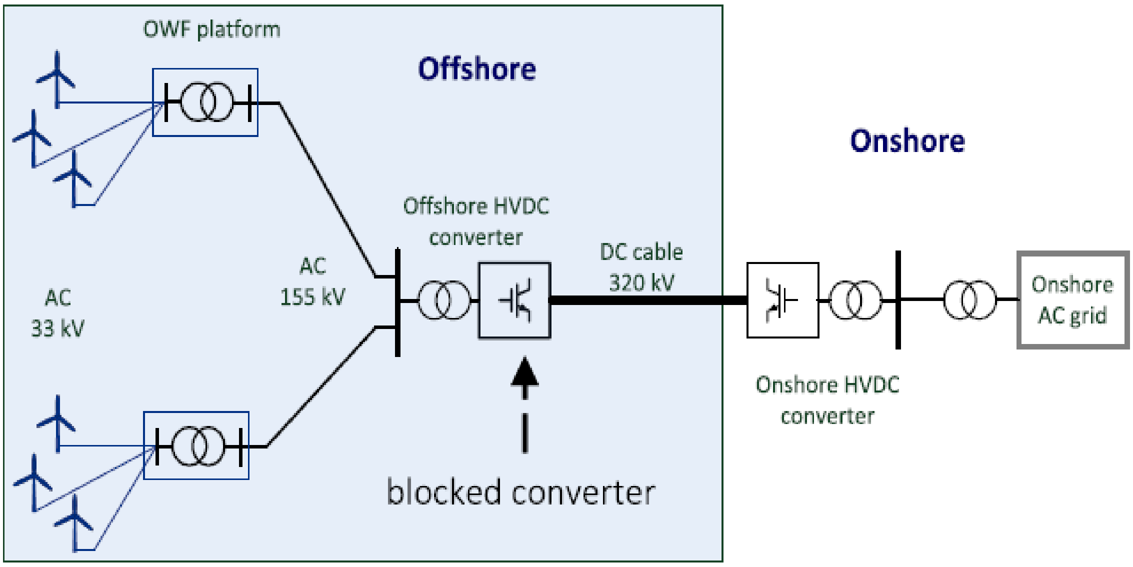

Figure 5 – OWFs connecté au réseau AC via une liaison HVDC

Certains de ces contrôleurs tels que la VSG utilisent la PLL, tandis que la commande droop, la commande droop filtré, VOC, matching-control et Inducverter n'utilisent pas la PLL. Pour certains auteurs [20], l'option sans PLL est avantageuse pour éviter les nombreux problèmes de stabilité provoqués par la PLL avec le contrôle grid-following classique [20], tandis que d'autres auteurs affirment que la PLL n'a pas d'impact majeur sur la stabilité, et que son utilisation est limitée à des fins d'amortissement [58]. Aucune de ces affirmations n'a été prouvée en théorie.

Récemment, un nouveau concept permettant aux convertisseurs de puissance de fonctionner en mode îloté tout en étant une source de courant a été proposé dans [71],

[72]. Le développement de ce contrôle a été motivé par la raison suivante: l'état de blocage du convertisseur HVDC offshore illustré sur la Figure 5 donne une distorsion du point 155 kV et son augmentation d'environ 30%. Ce comportement était lié notamment à la manière dont la boucle de courant est implémentée pour le GSC (Grid Side Converter). Ce comportement a été évité en proposant une commande de tension alternative directe avec un amortisseur transitoire pour le courant du réseau.

Dans la hiérarchie de contrôle, deux niveaux de commandes différents pour les convertisseurs d’électronique de puissance sont caractérisées comme illustré sur la Figure 6: La commande externe interagit avec le réseau externe et la commande interne interagit avec le convertisseur.

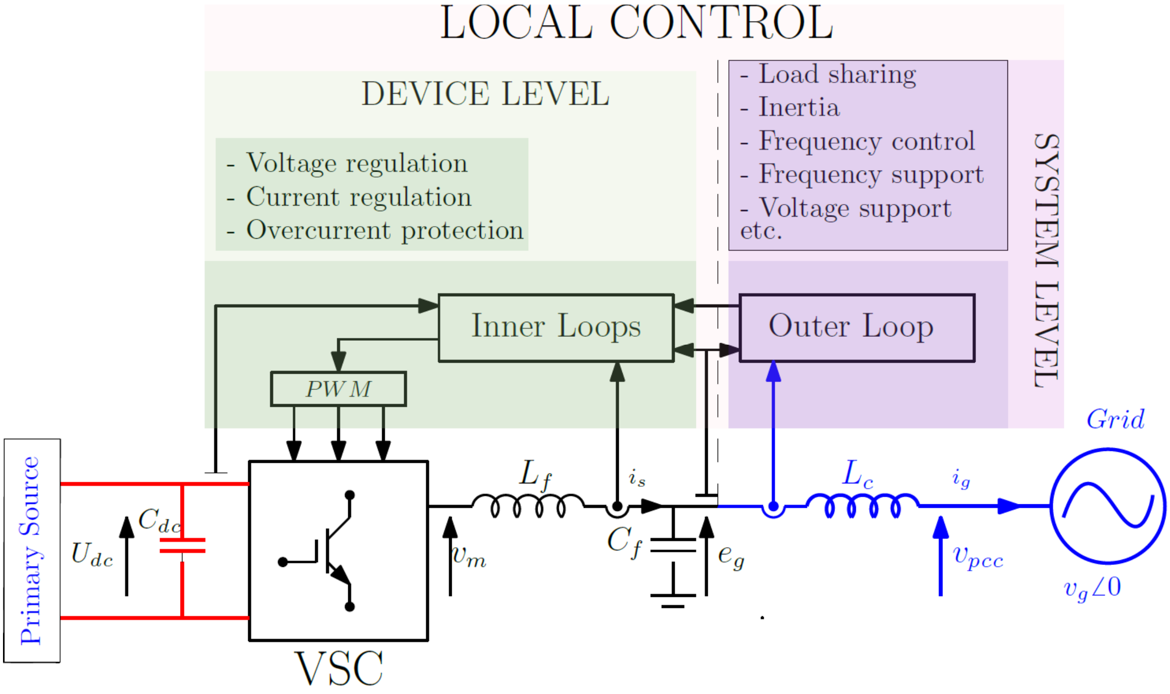

Figure 6 – Hiérarchie du control local

Dans la plupart des références citées précédemment, sauf dans [71], les points focaux étaient sur la commande de boucle externe et son interaction avec le réseau. D'autres recherches se sont principalement intéressées à la conception et au contrôle des boucles de contrôle internes. En fait, une solution courante pour contrôler la tension alternative est basée sur la structure du contrôleur PI en cascade. Cette solution est privilégiée pour les applications industrielles en raison de la simplicité de sa mise en œuvre, et aussi parce qu'elle génère une référence de courant qui sert à protéger le convertisseur [73]. Outre les contrôleurs PI en cascade conventionnels [28], [34], [73] - [77], d'autres stratégies de contrôle ont été utilisées telles que la commande en mode glissant pour la boucle de courant interne et un "H2"/ "H∞" pour boucle de tension alternative [78], régulateur d'ordre fractionnaire [79] et technique LQR [80]. La méthode de [78] vise à concevoir un contrôleur robuste afin d'obtenir des performances élevées, cependant, cette technique est complexe et nécessite un effort de calcul très élevé. La méthode de

[79], a été motivée par sa flexibilité et son grand nombre de degrés de liberté, et enfin, la méthode de [80] a été motivée par sa simplicité. Parmi les stratégies de contrôle interne proposées pour les convertisseurs grid-forming, peu d'études se sont focalisées au contrôle interne dans les applications de forte puissance [73], [78], où la fréquence de commutation est inférieure à 5 kHz. De telles conditions peuvent entraîner une dynamique lente [73], des régions de stabilité restreintes et des interactions entre les boucles de contrôle, ce qui peut conduire à un système instable [81]. Par conséquent, le réglage des paramètres du contrôleur dans de telles conditions est toujours un défi.
Contrairement aux VSC à 2 niveaux, les MMC ne nécessitent pas de filtre LC de sortie, et donc, pas besoin de boucles de régulation de tension alternative. La tension modulée peut être directement entraînée par une consigne de tensions alternatives. Cependant, le MMC contient des condensateurs internes dans chaque sous-module, qui nécessitent des boucles internes pour contrôler l'énergie. La dynamique de ces boucles est proche de celle de la boucle externe, ce qui peut provoquer des interactions entre contrôleurs. Cette question n'a pas été étudiée dans la littérature.

Les convertisseurs grid-forming fonctionnent comme une source de tension derrière une impédance et sont donc très sensibles aux perturbations du réseau qui peuvent engendrer une surintensité. Les stratégies de limitation de courant des VSC grid-forming lors de grandes perturbations ont été étudiées dans de nombreuses références [22], [82] - [89]. Parmi ces travaux, peu de références étendent les études de limitation de courant au grand réseau électrique [87], où d'autres événements peuvent causer des problèmes de surintensité tels que le déclenchement et la refermeture de la ligne. Deux stratégies principales ont été proposées pour les convertisseurs grid-forming afin de limiter le courant lors des transitoires. Une solution est de limiter le courant de référence avec un algorithme de saturation du courant (CSA) [82], [83], [88]. La deuxième solution est l'impédance virtuelle (VI) [71], [84] - [86], [90], [91]. Elle a été mise en œuvre pour émuler l'effet de l'impédance physique lorsque le courant dépasse sa valeur nominale. Cette stratégie de contrôle avait pour but de modifier la référence de tension alternative afin de limiter le courant. Par conséquent, sa réaction contre le défaut dépend du courant ainsi que de la dynamique des régulateurs de tension. Pour une dynamique de contrôle interne lente, l'impédance virtuelle ne peut garantir une limitation de courant pendant le défaut. Une action d'anticipation sur la tension modulée a été proposée pour résoudre ce problème [87]. Une fois le courant limité, la synchronisation post-défaut est extrêmement importante. Cependant, l'impact des techniques de limitation actuelles sur la stabilité transitoire a été marginalement étudié dans la littérature [92] - [97]. En effet, un comportement instable lorsque la protection contre les surintensités est désactivée entraînerait un déclenchement inévitable du convertisseur du réseau pour des raisons de sécurité [18]. Cependant, dans les futurs systèmes électriques, différentes sources d'alimentation doivent faire face aux divers événements et garantir la stabilité. Dans ce contexte, la stabilité transitoire du système est définie comme la capacité du convertisseur de puissance à maintenir le synchronisme après élimination du défaut. Le choix de l'algorithme de limitation de courant a une grande influence sur la stabilité transitoire. Dans [92], [95], le phénomène d'instabilité transitoire utilisant le CSA tout en gardant le contrôle du statisme a été étudié. Pour éviter ce problème d'instabilité, certains articles ont proposé de passer du contrôle de tension, basé sur le contrôle de statisme, au contrôle de courant, basé sur une boucle à verrouillage de phase [22], [98]. Ces méthodes nécessitent un algorithme complexe pour la détection des défauts et les conditions de déclenchement. De plus, comme spécifié par [22], la resynchronisation après défaut ne pouvait être garantie qu'après un re-réglage considérable du contrôleur de tension et du contrôleur de puissance afin d'éviter un effondrement de la tension alternative. Dans [84], les auteurs ont montré à travers des simulations temporelles, la capacité de la VI à assurer une meilleure stabilité transitoire que le CSA en cas de connexion de forte charge. Cependant, ce résultat n'a pas été théoriquement prouvé.

Pour anticiper et se préparer aux futurs défis liés au taux de pénétration élevé des convertisseurs d'électronique de puissance dans les réseaux de transports [16], [99], [100], plusieurs gestionnaires de réseau de transport (GRT) européens et universités se sont réunis pour former un projet européen pour travailler sur ces questions, par exemple, PROMOTioN [101], MIGRATE [102], récemment HVDC Inertial Provision [99], etc. Parmi ces projets, le projet MIGRATE s'intéresse à une forte intégration de convertisseurs d'électronique de puissance jusqu'à 100%. Le projet MIGRATE qui a financé ces travaux est présenté dans le paragraphe suivant.

Le projet MIGRATE: MIGRATE est l'acronyme de Massive InteGRATion of Power Electronic Devices. Il s'agit d'un projet financé par l'UE dans le cadre d'Horizon 2020 de l'Union européenne. Il rassemble plusieurs partenaires. Il y a 11 GRT, 12 universités et un fabricant de 13 pays travaillant ensemble dans ce projet. Leur objectif principal est de proposer des solutions innovantes pour ajuster progressivement le fonctionnement du système HVAC. Les différents objectifs du projet sont abordés dans 8 work packages (Figure 7). Cette thèse fait partie du work package 3 qui vise à développer les contrôles et les opérations d'un réseau avec des appareils 100% basés sur des convertisseurs

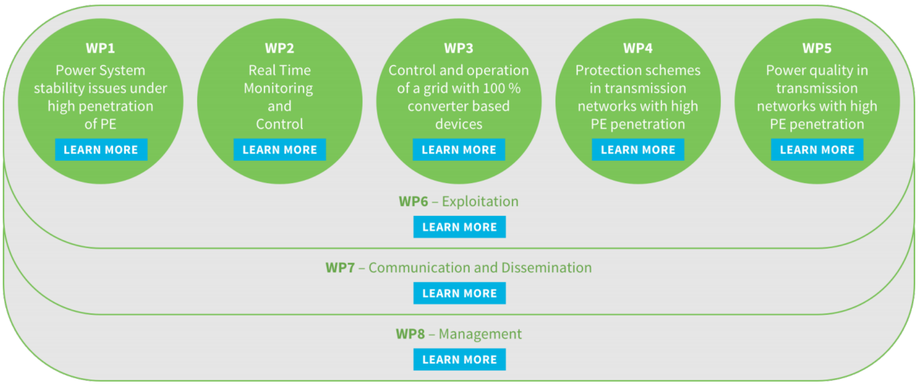

Figure 7 - Les membres et WP du projet MIGRATE

Contributions

Chapitre 2:

Partant de l'objectif fondamental d'un convertisseur de puissance, qui vise à fournir de la puissance active au réseau principal, une première structure de contrôle grid-forming est dérivée (Figure 8).

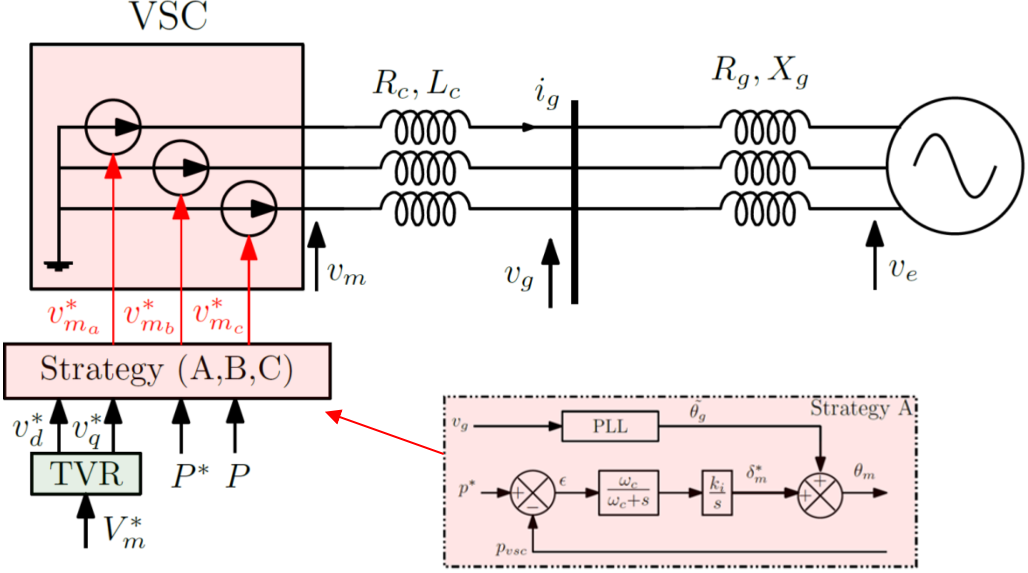

Figure 8 – Stratégie A

Elle se compose d'une boucle de contrôle de puissance robuste qui permet au convertisseur de puissance de garantir une dynamique de puissance active spécifiée quelle que soit la rigidité du réseau AC. Dans ce chapitre, le couplage possible entre la puissance active et la puissance réactive est mis en évidence et limité par un réglage spécifique du régulateur de puissance. De plus, une résistance virtuelle transitoire (TVR) est également implémentée pour surmonter une résonance particulière autour de la fréquence du réseau et amortir la dynamique du courant de réseau.

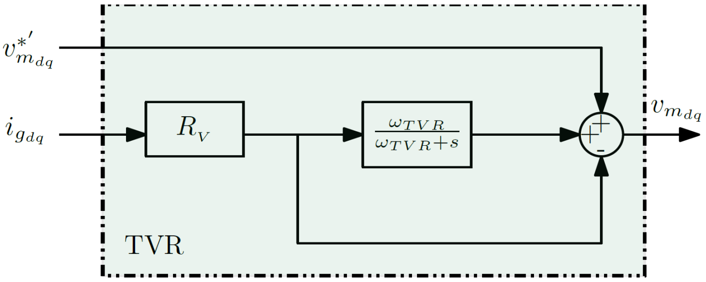

Figure 9 – TVR

Le contrôle proposé est équipé d'une PLL. Il est démontré que l'utilisation de la PLL dans ce contrôle est fondamentalement différente du grid-following. Elle permet de rejeter les perturbations d’angle et améliorer la robustesse du système dans le cas des réseaux faibles (Figure 10).

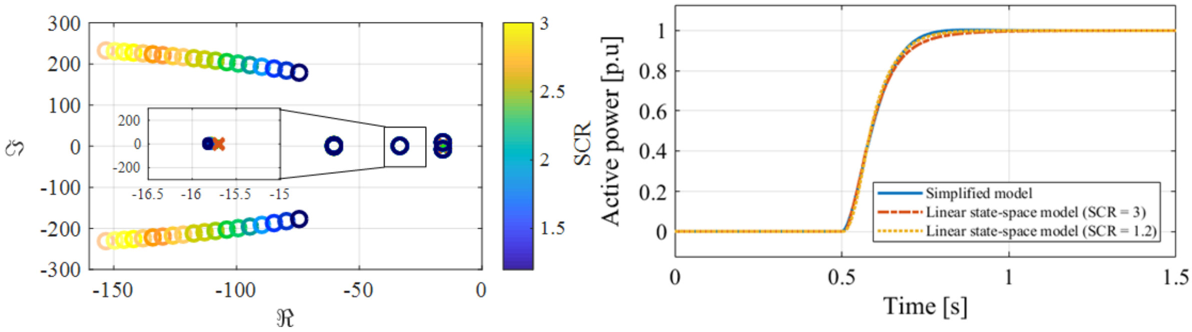

Figure 10 – **Robustesse de la stratégie A en cas de réseau faible**

Chapitre 3:

Dans ce chapitre, trois stratégies de contrôle sont présentées et étudiées. Leur contribution au support du réseau AC et leur stabilité dans plusieurs conditions ont été étudiées. Les principales différences entre eux sont reprises dans le tableau 2.

Tableau 2: Les performances des stratégies de contrôle proposées

	Poursuite de la puissance de référence	**Support de la fréquence**	**Saturation de la puissance active**	**Apport inertiel**	**Robustesse**
Stratégie A	++	++	++	-	++
Stratégie B	++	++	++	++	+
Stratégie C	-	++	-	++	+

À partir du tableau synthétique 2, quelques précisions supplémentaires sont mentionnées:

- **Le VSC basé sur la stratégie A** est capable de fonctionner comme un injecteur de puissance active (c'est-à-dire, suivi de référence de puissance active en régime permanent). Il est robuste au changement topologique du réseau. Le comportement dynamique du système basé sur cette stratégie est stable et respecte les spécifications dynamiques imposées. Il peut contribuer au support de la fréquence de la même manière que les convertisseurs grid-following. Cependant, il ne peut pas être utilisé pour fournir le support inertiel. En conséquence, la prédominance des convertisseurs de puissance basés sur la «stratégie A» n'est pas conforme aux exigences actuelles.

La «stratégie A» peut être équipée d'une saturation de référence de puissance pour éviter que le convertisseur fournisse plus de puissance que sa valeur nominale.

- **Le VSC basé sur la stratégie B** est capable de fonctionner comme un injecteur de puissance active. Il est plus sensible aux changements topologiques du réseau. La dynamique de la puissance active basée sur cette stratégie n'est pas la priorité ultime, puisqu'elle est conçue pour permettre un appui inertiel, par conséquent, la dynamique de puissance active dépend de la constante d'inertie. À l'instar de la «Stratégie A», la «Stratégie B» contribue au support primaire des fréquences.

Cette stratégie de contrôle est également équipée d'une saturation sur la référence de puissance pour éviter que le convertisseur ne dépasse sa puissance nominale.

- **Le VSC basé sur la stratégie C** est un contrôle hybride intégrant un effet inertiel et une fonction de partage de charge «obligatoire». Cependant, la «stratégie C» ne peut pas fonctionner comme un injecteur de puissance active et elle est sensible aux changements topologiques du réseau. La stratégie C ne peut pas être équipée de saturation sur la référence de puissance active. C'est l'un de ses inconvénients majeurs.

Une approche théorique a été développée dans les chapitres 2 et 3, permettant une réduction d'ordre du modèle, c'est-à-dire qu'en mode connecté au réseau, les deux «Stratégie A et B» peuvent être simplement représentés par des systèmes de 2e ordre et «Stratégie C» avec un 2e ou un système de 3e ordre.

Stratégie A:

$$\frac{p_{ac}}{p^*} = \frac{1}{1 + \frac{X_c}{k_i V_m V_e} s + \frac{X_c}{k_i V_m V_e \omega_c} s^2} \tag{1}$$

Stratégie B:

$$\frac{p_{ac}}{p^*} = \frac{1}{1 + \frac{X_c}{k_i V_m V_e} s + \frac{X_c + X_g}{k_i V_m V_e \omega_c} s^2} \tag{2}$$

Stratégie C:

$$\frac{p_{ac}}{p^*} = \frac{1 + T_2 s}{1 + \left(\frac{\omega_c + k_i T_1 \omega_c T_{p\delta}(0)}{k_i \omega_c T_{p\delta}(0)} \right) s + \left(\frac{1 + T_2 \omega_c}{k_i \omega_c T_{p\delta}(0)} \right) s^2 + \frac{T_2}{k_i \omega_c T_{p\delta}(0)} s^3} \tag{3}$$

Ces modèles simplifiés sont d'une grande précision, et permettent de comprendre le comportement dynamique de la puissance active et de la fréquence.

Chapitre 4:

Dans ce chapitre, deux stratégies de commande différentes pour la régulation de tension alternative ont été adoptées pour le convertisseur de source de tension à 2 niveaux:

- Structure de contrôle en cascade avec une nouvelle conception de contrôleurs (Figure 11).
- Contrôle direct de la tension alternative (Figure 12).

Les deux structures de contrôle ont montré leur efficacité pour assurer un fonctionnement stable du système et un comportement dynamique acceptable dans différents cas de réseau, c'est-à-dire; en mode autonome et en mode connecté au réseau. La différence entre les méthodes proposées n'est pas leurs performances, mais leur flexibilité pour atteindre la dynamique souhaitée, c'est-à-dire qu'en raison des interactions de modes provoquées par la boucle de courant dans une structure de contrôle en cascade, il est difficile d'ajuster les gains du contrôleur de manière classique. En effet, toutes les dynamiques doivent être prises en compte pour améliorer la dynamique globale du système et garantir un comportement stable. Alors que, sur la base de la commande de tension alternative directe, aucune boucle de commande de courant n'est requise, seul l'amortissement actif transitoire est utilisé pour éviter la fréquence de résonance du filtre LCL. Cela permet au convertisseur de fonctionner selon son comportement physique de source de tension. De plus, cela permet une plus grande flexibilité pour la conception de la commande et moins d'interactions entre les modes.

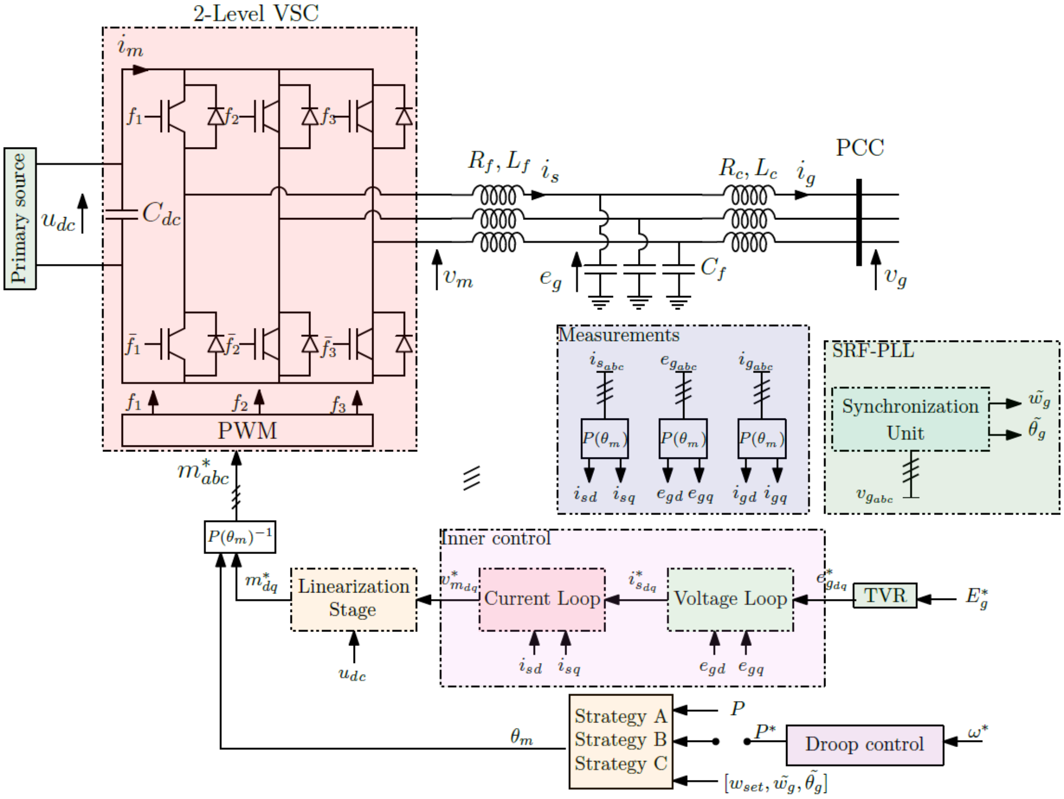

Figure 11 – **Structure de contrôle cascadé**

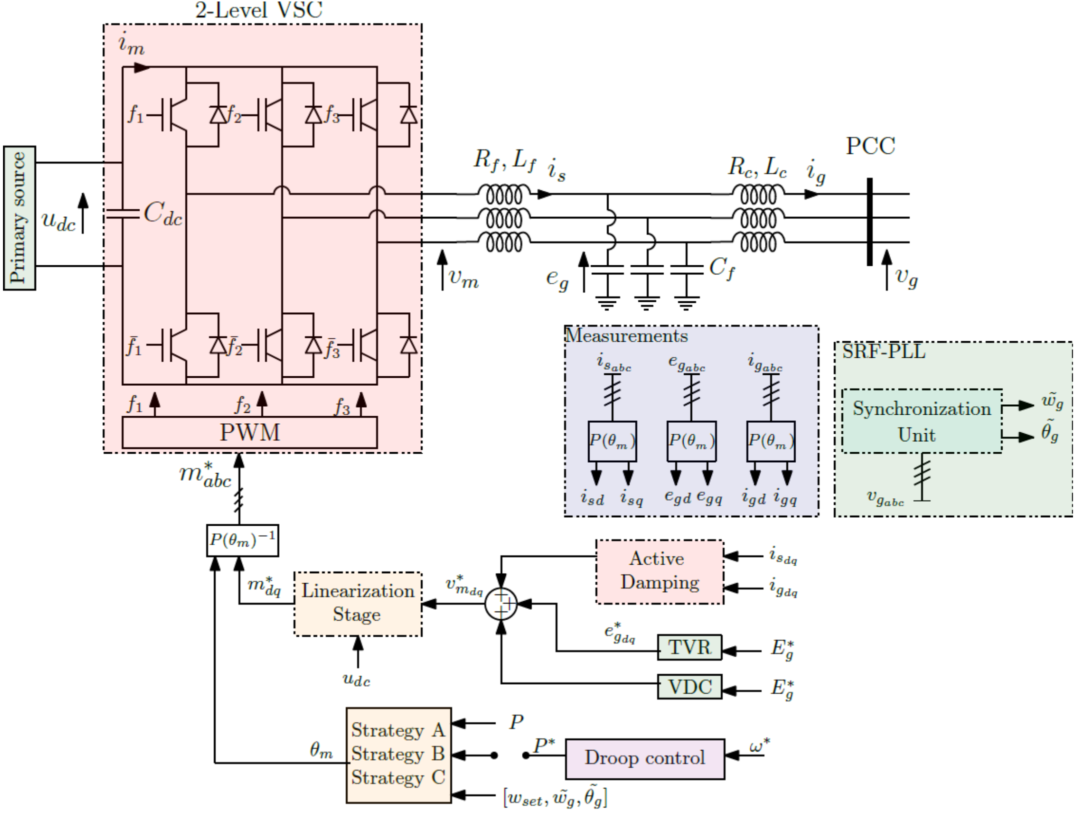

Figure 12 – **Structure de contrôle direct de la tension**

Loin du VSC à 2 niveaux, la commande grid-forming pour MMC a également été étudiée dans ce chapitre. Comme aucun filtre LC de sortie n'est requis, le MMC se comporte simplement comme une source de tension contrôlable avec une onde sinusoïdale de tension alternative de sortie (Figure 13). En plus de la gestion de la tension alternative, une régulation d'énergie de haut niveau est nécessaire pour maintenir les condensateurs sous-modules de la MMC autour de leurs valeurs nominales.

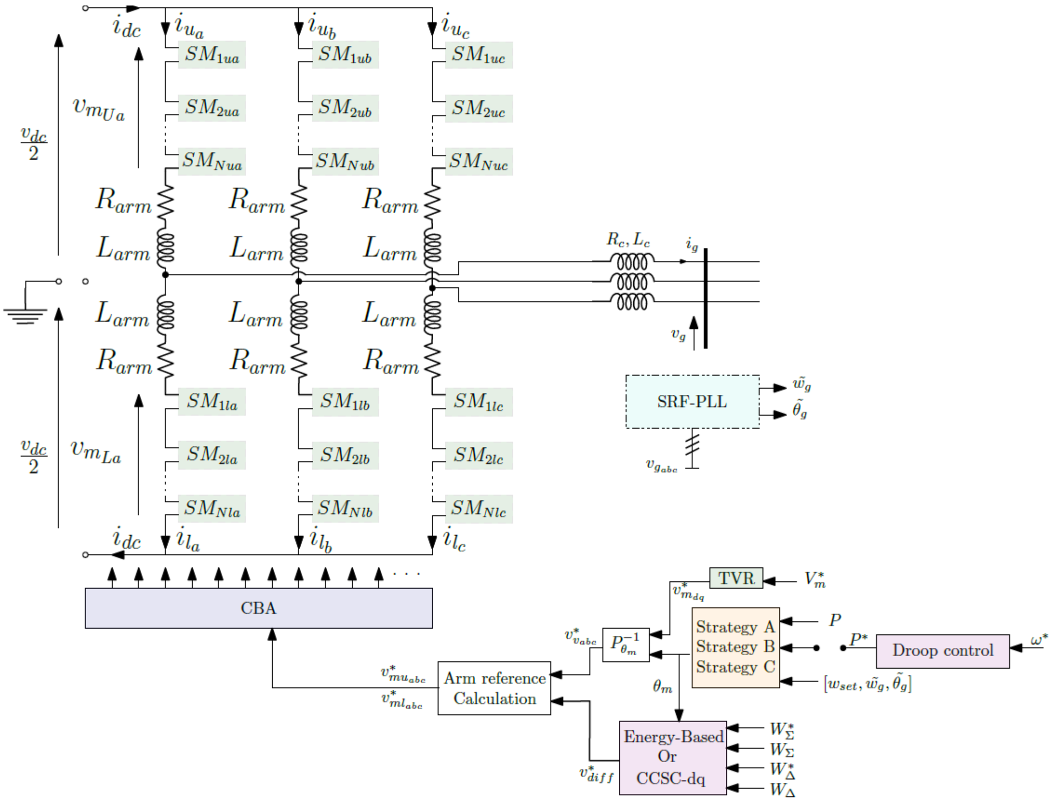

Figure 13 - Grid-forming MMC

Chapitre 5:

Dans ce chapitre, la limitation de courant et la synchronisation post-défaut des convertisseurs grid-forming sont discutées lorsque le système est soumis à de grandes perturbations. Dans ce contexte, un contrôle de limitation de courant hybride (HCLC) est développé sur la base d'une combinaison d'algorithmes d'impédance virtuelle et de la saturation de courant de référence. En fonction de la structure de contrôle interne et de la topologie du convertisseur, le HCLC peut être directement utilisé si une structure de contrôle en cascade est adoptée, tandis qu'une boucle de courant de seuil supplémentaire doit être ajoutée afin de générer des références de courant si une structure de contrôle de tension alternative continue est utilisée.

Après élimination des défauts, la synchronisation du convertisseur de puissance doit être assurée afin d'éviter le déclenchement des convertisseurs. Par conséquent, en négligeant l'effet d'inertie, une formule analytique simple du temps de compensation critique est dérivée basée sur VI ou HCLC et CSA. Il montre l'efficacité du VI et du

HCLC pour assurer une stabilité transitoire plus élevée que CSA et fait également ressortir les principaux paramètres influents sur la stabilité transitoire.

Une méthode pour améliorer le temps de compensation critique et le comportement dynamique a été proposée. Les comparaisons avec la simulation montrent que le modèle simplifié proposé est pertinent pour l'estimation du temps critique d’élimination d défaut et la compréhension du comportement général pendant la période de resynchronisation. Même si l'effet inertiel a été négligé dans cette analyse, les tendances générales resteront efficaces avec un effet inertiel comme le prouvent les simulations temporelles.

Pour montrer le fonctionnement du système dans différentes situations, deux cas de teste avec des topologies à un ou plusieurs convertisseurs ont été proposés pour évaluer la stabilité du système global, y compris les algorithmes proposés. Les résultats obtenus sur la base des cas de grille proposés sont satisfaisants.

Chapitre 6:

Pour valider les stratégies de contrôle proposées, un convertisseur de puissance à petite échelle est développé (Figure 14). Ensuite, l'interopérabilité entre les contrôles proposés est évaluée par une simulation PHIL (Power Hardware In the Loop), où différents cas de test sont réalisés.

Il a été démontré à partir des résultats obtenus que:

- Les contrôleurs locaux proposés fonctionnent de manière stable.
- L'algorithme de limitation de courant proposé peut protéger le convertisseur en cas de défaut triphasé ou de déphasage.
- Différents types de contrôleurs locaux peuvent être interconnectés.
- Un convertisseur grid-forming peut être intégré dans un système électrique réel contenant des machines synchrones classiques.

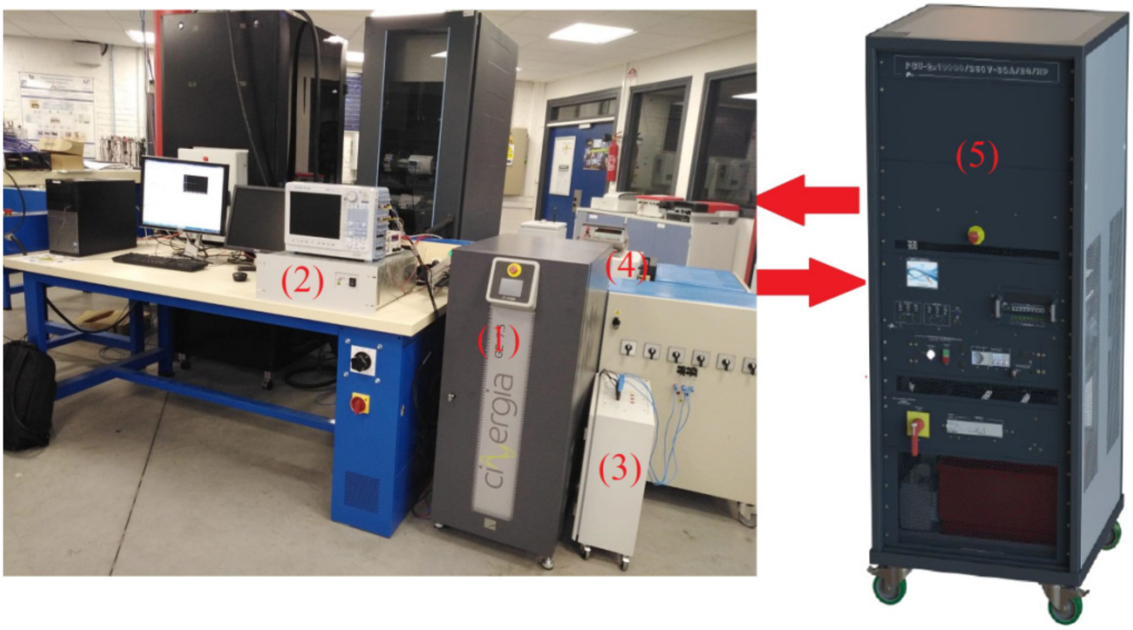

Figure 14 - un VSC 2-niveau à petite échelle

Conclusions générales

La forte pénétration de nouveaux moyens de génération électrique déclenche l'intégration de plus de dispositifs PE dans le système électrique en masse. Il modifie les fondements de l'exploitation et du contrôle des systèmes électriques actuels. Dans le cas d'un système d'alimentation 100% PE, certains convertisseurs connectés au réseau doivent agir comme des sources de tension alternative derrière une impédance. Ces convertisseurs nécessitent des lois de commande différentes afin de répondre aux besoins du système et permettant un fonctionnement stable lors de perturbations importantes. Cette thèse se concentre sur le principe de commande grid-forming utilisé pour les convertisseurs d'électronique de puissance connectés à un réseau de transport. Il revient aux bases de cette commande pour expliquer l'origine de la commande de puissance avec une source de tension.

La fonction principale d'une source d'énergie étant d'injecter de la puissance active dans le réseau, la surveillance des états du réseau est une tâche obligatoire. En d'autres termes, la synchronisation avec le réseau est requise. Cette tâche est fondamentalement différente selon la nature de la source d'alimentation (c.-à-d. Source de courant ou de tension). Dans le cas où le convertisseur fonctionne comme une source de tension, l'auto-synchronisation est réalisée grâce à une boucle de régulation de puissance similaire à une machine synchrone. Contrairement aux idées considérant le grid-forming comme une commande sans PLL, une estimation de l'angle et/ou de la fréquence du réseau à travers une PLL n'est pas obligatoire pour la commande mais elle peut être envisagée. La PLL a toujours été considérée comme une source principale d'instabilité, que les GRT cherchent à éviter à tout prix. Cependant, la PLL n'a pas les mêmes objectifs pour le grid-following que pour le grid-forming. La PLL pour grid-forming n'est pas destinée à garantir la synchronisation, mais à rejeter les perturbations du réseau (Stratégie A) ou à découpler les fonctions de contrôle de puissance et de fréquence (Stratégie B). C'est l'une des idées principales que cette thèse vise à véhiculer.

Contrairement au contrôle grid-following où une dynamique PLL rapide réduit la marge de stabilité du système, une PLL rapide (50 ms) pour grid-forming garantit plus de stabilité et de meilleures performances dynamiques. Ce choix présente un autre avantage majeur prouvé dans le chapitre 3: lorsque la dynamique PLL est rapide, la fréquence du réseau estimée peut être assimilée à la fréquence réelle du réseau, ce qui permet de démontrer certaines similitudes entre la «Stratégie B» (VSM) et les machines synchrones, par ex. les mêmes formulations mathématiques utilisées pour évaluer le RoCoF et l'inertie du système dans le système électrique conventionnel sont toujours valables pour un système 100% PE. Sinon, si la dynamique de la PLL est lente, le concept d'inertie ne sera plus vrai et l'équivalence entre VSM et SM sera erronée.

Les commandes développées dans cette thèse sont inspirées du fonctionnement actuel du réseau électrique, où toutes les sources d'énergie ne sont pas invitées à participer à la fréquence et au support inertiel. Par conséquent, le chapitre 2 propose tout d'abord un contrôle grid-forming robuste qui permet d'injecter la puissance active avec une dynamique spécifiée, quelles que soient la rigidité et la topologie du réseau. Il permet de participer au partage de charge si nécessaire, mais ne permet pas d'émulation d'inertie. La conception de cette commande prend en compte le couplage transitoire entre la puissance active et réactive, et contient une résistance virtuelle transitoire pour amortir les courants du réseau, et ainsi éviter une résonance. Cette résistance virtuelle doit être mise en œuvre quelle que soit la structure de contrôle grid-forming. Si certaines sources d'énergie sont sollicitées pour participer au support de fréquence rapide, deux types de contrôle sont proposés au chapitre 3 «Stratégies B et C» pour répondre à ce besoin. Les deux contrôles permettent un support rapide de la fréquence (contrôle de fréquence primaire et émulation d'inertie). Cependant, avec la stratégie B, le suivi de la consigne de puissance active est toujours possible et le contrôle de fréquence primaire est une fonction optionnelle, alors que, avec la «stratégie C», le contrôle de fréquence primaire est obligatoire. Cela ne permet pas le suivi de la consigne de puissance active en régime permanent.

Selon la topologie du convertisseur de puissance, la connexion au système AC peut être différente. Dans le cas d'un VSC à 2 niveaux, un filtre LC est nécessaire, ce qui nécessite des boucles de contrôle supplémentaires. Habituellement, une structure de boucles de contrôle en cascade est utilisée pour contrôler la tension alternative aux bornes du condensateur, ce qui permet d'éviter une résonance du filtre LCL. De plus, cette structure de contrôle permet la génération d'une référence de courant qui sert à protéger les équipements. Cependant, en raison de la bande passante limitée du convertisseur de puissance dans les applications à haute puissance, le réglage spécifique des contrôleurs en cascade est de la plus haute importance. Dans cette thèse, un réglage basé sur le placement global des pôles est proposé pour placer toutes les valeurs propres du système dans une zone donnée qui respecte certaines contraintes de stabilité et de dynamique. La capacité des gains résultants à garantir un fonctionnement stable a été testée dans différents cas de réseau. De plus, l'ensemble des paramètres garantit un bon découplage entre les boucles de commande intérieure et extérieure comme le démontrent les facteurs de participation du chapitre 4.

Un deuxième procédé a été proposé basé sur la connaissance du système, où, une simple impédance virtuelle quasi-stationnaire est implémentée dans la commande pour compenser la chute de tension aux bornes de l'impédance de sortie. Ensuite, une résistance d'amortissement transitoire virtuelle est ajoutée pour éviter les problèmes d'instabilité liés à la résonance du filtre LCL.

Concernant la topologie MMC, seul un filtre L est nécessaire pour la connexion au réseau. Par conséquent, pas besoin de boucles de contrôle internes. La complexité de la commande MMC est principalement liée à la gestion de son énergie interne dans chaque sous-module. Dans cette thèse, le fonctionnement du MMC a été testé par des simulations temporelles, où le comportement du MMC est analysé dans des conditions normales et anormales. Les résultats obtenus ne révèlent pas d'interactions majeures entre les boucles de contrôle d'énergie et de contrôle de puissance.

La protection des convertisseurs de puissance contre les défauts et leur synchronisation post-défaut est une tâche très importante. Au chapitre 5, deux méthodes bien connues de limitation de courant (CSA et VI) et leur impact sur la stabilité transitoire ont été discutées. Grâce aux approches comparatives et théoriques proposées dans cette thèse, les avantages et les limites de chaque méthode sont mis en évidence. Cette approche conduit à des conclusions fondamentales: la CSA est meilleure pour la limitation de courant, tandis que la VI est meilleure en termes de stabilité transitoire. Sur la base de cette considération, l'hybridation entre les deux stratégies est proposée pour bénéficier de leur avantage dans une stratégie de contrôle unique appelée Hybrid Current Limiting Control (HCLC). Malgré le fait que la stabilité transitoire a été améliorée grâce au HCLC, un risque d'instabilité angulaire reste probable si la durée du défaut est longue. Pour traiter ce problème, un algorithme simple pour améliorer la stabilité transitoire a été proposé. Il consiste à modifier la référence de puissance ou les gains du régulateur de puissance pendant le défaut pour augmenter le temps d'effacement critique. Avec les stratégies B et C, une action de gel supplémentaire sur la PLL est requise.

L'efficacité des contrôleurs développés et des approches théoriques ainsi que cette thèse a été prouvée via différentes expérimentations (système mono et multi-onduleurs). Ces expérimentations ont été basées sur un banc d'essai original à petite échelle utilisant du matériel physique et des principes de simulation en temps réel. Le comportement des convertisseurs de puissance dans différentes topologies de réseau électrique a été simulé avec un simulateur en temps réel. Ensuite, un amplificateur de puissance a été utilisé pour interconnecter des équipements selon le principe PHIL.

HESAM UNIVERSITÉ

Taoufik QORIA

Grid-forming control to achieve a 100% power electronics interfaced power transmission systems

Arts Sciences et Technologies et Métiers

Abstract

The rapid development of intermittent renewable generation and HVDC links yields an important increase of the penetration rate of power electronic converters in the transmission systems. Today, power converters have the main function of injecting power into the main grid, while relying on synchronous machines that guarantee all system needs. This operation mode of power converters is called "Grid-following". Grid-following converters have several limitations: their inability to operate in a standalone mode, their stability issues under weak grids and faulty conditions and their negative side effect on the system inertia.

To meet these challenges, the grid-forming control is a good solution to respond to the system needs and allow a stable and safe operation of power system with high penetration rate of power electronic converters, up to a 100%. Firstly, three grid-forming control strategies are proposed to guarantee four main features: voltage control, power control, inertia emulation and frequency support. The system dynamics and robustness based on each control have been analyzed and discussed. Then, depending on the converter topology, the connection with the AC grid may require additional filters and control loops. In this thesis, two converter topologies have been considered (2-Level VSC and VSC-MMC) and the implementation associated with each one has been discussed. Finally, the questions of the grid-forming converters protection against overcurrent and their post-fault synchronization have been investigated, and then a hybrid current limitation and resynchronization algorithms have been proposed to enhance the transient stability of the system. At the end, an experimental test bench has been developed to confirm the theoretical approach.

Keywords: Power converters, grid-forming control, power system dynamics, small-signal stability analysis, current limitation, transient stability

Résumé

Le développement rapide de la production d'énergie renouvelable intermittente et des liaisons HVDC entraîne une augmentation importante du taux de pénétration des convertisseurs statiques dans les réseaux de transport. Aujourd'hui, les convertisseurs statiques ont pour fonction principale d'injecter une puissance dans le réseau tout en s'appuyant sur des machines synchrones qui garantissent tous les besoins du système électrique. Ce mode de fonctionnement est appelé «Grid-following». Les convertisseurs contrôlés en Grid-following ont plusieurs limitations: leur incapacité à fonctionner en mode autonome, leurs problèmes de stabilité dans des réseaux faibles et en cas de défaut ainsi que leur effet négatif sur l'inertie équivalent du système. Pour relever ces défis, le contrôle en Grid-forming est une bonne solution pour répondre aux besoins du système électrique et permettre un fonctionnement stable et sûr du système même avec un taux de pénétration des convertisseurs statique de 100%. Tout d'abord, trois stratégies de contrôle en Grid-forming sont proposées pour garantir quatre fonctionnalités principales: contrôle de tension, contrôle de puissance, émulation d'inertie et le support de la fréquence. La dynamique et la robustesse du système basées sur chaque contrôle ont été analysées et discutées. Ensuite, selon la topologie du convertisseur, la connexion avec le réseau AC peut nécessiter des filtres et des boucles de contrôle supplémentaires. Dans le cadre de cette thèse, deux topologies de convertisseur ont été envisagées (VSC à 2-niveaux et VSC-MMC) et l'implémentation associée à chacune a été discutée. Enfin, les questions de la protection des convertisseurs Grid-forming contre les surintensités et leur synchronisation post-défaut ont été étudiées, puis, des algorithmes de limitation de courant et de resynchronisation ont été proposés pour améliorer la stabilité transitoire du système. Un banc d'essai a été développé pour confirmer les approches théoriques proposées.

Mots clés: Convertisseur DC/AC-AC/DC, grid-forming contrôle, dynamiques des systèmes électriques, stabilité petit-signaux, limitation de courant, stabilité transitoire